Durham E-Theses

The transport and relaxation of holes in quantum wells

Crow, G.C.

How to cite:

Crow, G.C. (1994) *The transport and relaxation of holes in quantum wells*, Durham theses, Durham University. Available at Durham E-Theses Online: http://etheses.dur.ac.uk/5853/

Use policy

THE TRANSPORT AND RELAXATION

OF HOLES IN QUANTUM WELLS

by

G. C. Crow (B.Sc.)

A thesis submitted in

candidature for the degree of

Doctor of Philosophy

at the University of Durham

May 1994

DECLARATION

The work reported in this thesis has not been previously submitted for any degree and is not currently being submitted towards candidature for any other degree.

The work reported in this thesis was carried out by the candidate.

ACKNOWLEDGEMENTS

"The Sciences do no try to explain,

they hardly even try to interpret,

they mainly make models. By a 'model'

is meant a mathematical construct, which,

with the addition of certain verbal

interpretations, describes observed

phenomena. The justification of such a

mathematical construct is solely and

precisely that it is expected to work".

- John von Neumann

ABSTRACT
THE TRANSPORT AND RELAXATION
OF HOLES IN QUANTUM WELLS
Ph.D. Thesis 1994 Gavin Crow (B.Sc.)

Two properties of holes in InGaAs quantum wells have been investigated and are reported in the thesis - their in-plane mobility at low electric fields, and their capture by a potential well.

Monte Carlo simulations of hole transport in InGaAs-AlGaAs quantum wells of different widths and alloy compositions have been carried out at 77 K, and for field strengths less than $10^5 \, \text{Vm}^{-1}$. Valence bandstructure has been generated using a k.p method in the infinite well approximation, which accounts for mixing between heavy and light hole states. Although less accurate than more detailed k.p calculations which include mixing with the conduction, spin split-off and remote bands, it provides an adequate description of states lying close to the valence band edge, simplifies the calculation of scattering rates and is computationally efficient. The effects of alloy, impurity and phonon scattering have been included. A study of hole transport in 90 Å $In_xGa_{1-x}As$ wells ($0.10 \leq x \leq 0.25$) predicted that the hole mobility should increase with indium concentration, since the reduction in the effective mass of the highest HH1 subband more than compensates for the greater alloy scattering rate. An analysis of wells with 18% indium content and widths in the range 50-150 Å indicated a general increase in the hole mobility with well width but with a local minimum around 120 Å due to intersubband scattering from the HH1 subband to the heavier HH2 subband.

A model for the 'quantum' capture of holes into a square well potential is developed in part two of the thesis. This involves the calculation of transition rates from unbound barrier states above the continuum edge to quasi-two dimensional bound states that form the quantum well subbands. The physical mechanisms and rates for the quantum capture of holes into a 30 Å $In_{0.7}Ga_{0.3}As$-InGaAsP quantum well (suitable for use in lasers operating at 1.55 μm) are discussed. In particular, the role of polar and non-polar optical phonon scattering, acoustic phonon and alloy scattering are considered.

Bound and unbound states have been calculated using an eight band k.p bandstructure model which describes mixing between the heavy and light hole, spin split-off and conduction bands. The quantum well has three subbands which derive from the HH1, HH2 and LH1 zone centre states. By treating quantum capture in a similar way to a barrier transmission problem, the hole capture rate into the well can be expressed in terms of the incident particle flux density. Such local information can be readily incorporated into classical device models, for example those based on Monte Carlo simulation. Heavy and light holes of a particular energy and momentum (both transverse and parallel to the plane of the quantum well) are represented by their appropriate barrier plane wave states. The fraction of the incident amplitude which is transmitted into the well region oscillates as a function of the wavevector normal to the well, and capture is induced by a scattering process, due to phonons or alloy disorder for example. The transition rate is determined by the matrix element between the transmitted wave and the final bound state, hence the capture probability varies as a function of the in-plane wavevector and energy of the unbound state. Peaks in the capture probability are associated with transmission resonances into the well (virtual bound states), but subband mixing is also found to be an important influence.

CONTENTS

Chapter 1

Introduction

The properties of semiconductor crystals are changed when strained. In particular, the application of a uniaxial stress to a semiconductor deforms the lattice and changes the overlap between neighbouring atomic orbitals. As a result, the energy bands are modified and a prominent effect in the valence band is the removal of the degeneracy between the heavy and light hole bands at the band edge. Advances in epitaxial growth techniques have made it possible to reproduce novel strain effects in semiconductor microstructures without the need to apply stress externally.

In principle, the introduction of strain into a quantum well or superlattice is straightforward and can be achieved by growing an epilayer of one material onto a substrate of lesser (greater) lattice constant. For a thin epilayer (~ 100 Å thick), the lattice spacing parallel to the layer plane deforms to that of the substrate, placing the layer under biaxial compression (tension) within its plane. The use of semiconductor alloys allows the fabrication of structures with a continuous range of strains. However, difficulties can arise during the growth process, or subsequently, since the strained layers may relax, creating networks of dislocations. Generally there is a maximum layer thickness that can be grown without forming dislocations, which depends critically upon the total strain energy within the epilayer.

A semiconductor crystal can be described by a set of Cartesian axes. Due to

the elasticity of the material, a biaxial compression of the crystal in the $x - y$ plane results in a relaxation of the lattice along the z axis. The chief effect of this biaxial compression is a reduction in the effective mass of heavy holes within the $x - y$ plane, but the heavy hole band remains heavy along the z direction. This property extends to holes which are bound within a compressive strained quantum well (with the strain field in the $x - y$ plane, growth direction defined by the z axis). The effective mass associated with the highest valence subband is light compared to an equivalent unstrained system, enhancing the hole mobility and offering the prospect of faster two-dimensional hole transport.

In the device context, the increased hole mobility suggests the possibility of fabricating faster p-channel field effect transistors by adopting compressive strained InGaAs-AlGaAs quantum wells instead of bulk GaAs or unstrained GaAs-AlGaAs wells (although the carrier velocity at high fields is generally more important in this respect). By introducing indium into the well, two factors give rise to a reduced in-plane effective mass for holes. First, InAs has a greater lattice constant than GaAs and therefore so has the InGaAs alloy. As a consequence there is compressive strain in the well, and the heavy hole effective mass is reduced as described above. Second, InAs has a lower heavy hole effective mass than GaAs. Therefore, the addition of indium to GaAs produces an alloy with a lower heavy hole mass than GaAs. Another consequence of the lighter mass is that the density of states at the highest valence subband edge is reduced. Semiconductor lasers incorporating compressive strained quantum wells have an advantage over those with unstrained wells, since population inversion may be achieved at smaller current densities.

The first part of the thesis concentrates on hole transport, and in particular the study of InGaAs-AlGaAs quantum wells of different geometries and indium content. It might be expected that on the basis of the arguments discussed above that increased indium in the well will give rise to an increase in the hole mobility. However, the inclusion of indium introduces alloy scattering which acts to reduce the hole mobility. Alloy scattering is a consequence of the difference between the electronic potentials of the indium and gallium atoms, which are randomly distributed on the group III sublattice sites. Monte Carlo simulations of hole transport for a range of quantum wells have been used to provide some insight into the competing factors which determine the average hole mobility.

In any study of the properties of the valence subbands of a quantum well, it is necessary to use a realistic bandstructure model which includes interactions between the bands. For this purpose, all valence subband dispersions are determined using a k.p method which accounts for mixing between states derived from the heavy and light hole bands. Furthermore, the infinite well approximation has been applied, which simplifies calculation and increases the computational efficiency, although at the expense of physical accuracy. This model is described in chapter 2. The effects of compressive and tensile strain upon the valence subbands of a quantum well are discussed, and a comparison is made between the subband mixing profiles of unstrained, compressive and tensile strained quantum wells. In chapter 3, the bandstucture solver is applied to the calculation of the intra- and inter- subband scattering rates of holes in InGaAs-AlGaAs wells with indium contents in the range 10-25 %, and well widths 50-150 Å. The effects of alloy, remote impurity, acoustic and optical phonon scattering are included.

Results from chapter 3 are incorporated into single particle Monte Carlo simulations of hole transport within a quantum well, and the significant features are discussed in chapter 4.

The second part of the thesis reports efforts to devise a model for the trapping of holes into a quantum well. That is, the transition of holes from unbound states in the continuum, to the quasi-two dimensional states on the quantum well subbands. It is believed that the carrier capture times (of picosecond magnitude) are detrimental to the modulation bandwidth of long wavelength (1.55 μm) semiconductor quantum well lasers, in addition to the effects associated with carrier diffusion across the optical confinement region. To ensure a good optical response to high frequency modulation currents, the optimum design for a quantum well is that which enables carriers to be trapped efficiently, but also emits at the desired wavelength and achieves good optical confinement.

Again the **k.p** method is used, but this time in the finite square well approximation, and including the effects of mixing with the conduction and spin split-off bands in addition to that between the heavy and light hole bands. The model is described in chapter 5 and is applied to capture into a 30 Å $In_{0.7}Ga_{0.3}As$-$In_{0.75}Ga_{0.25}As_{0.55}P_{0.45}$ quantum well, as might be used in a 1.55 μm quantum well laser. Rates for capture by acoustic phonon, optical phonon (emission and absorption) and alloy scattering are determined from Fermi's Golden Rule, and the microscopic details of the various capture processes are described. The rates are rewritten in terms of the particle flux associated with the unbound carriers incident upon the well. In this way, the capture probability for a hole of given en-

ergy and momentum into the well can be determined for each of the mechanisms listed above. In chapter 6, alloy and phonon scattering rates are determined for holes which have become trapped by the well. These calculations are necessary for a study of carrier thermalisation between the subbands of the quantum well, for example using Monte Carlo simulation techniques. Such simulations are not discussed in the thesis, but the scattering rates can reveal likely paths and mechanisms for carrier cooling in the well. The work described in chapters 5 and 6 is intended as the first part of a larger study of transport within a semiconductor quantum well laser, and it is expected that the data will eventually be included in an ensemble Monte Carlo simulation of this device.

Finally, conclusions drawn from this work are presented in chapter 7 and suggestions are made for the course of further calculations.

PART ONE

The Parallel Transport Of Holes

In Quantum Wells

Chapter 2

Valence Bandstructure Of Strained

III-V Quantum Wells

2.1 Introduction

Both the electronic and optical properties of a crystal are changed once it is strained. Biaxial strain can be incorporated into a semiconductor quantum well by growing an epilayer of one material between barriers of a wider band-gap material with a different lattice constant. If the well layer is sufficiently thin, the lattice spacing parallel to the layer plane distorts to that of the barrier material, creating a uniform strain field across the well plane. The lattice constant perpendicular to the well plane will be different to that for the barrier, due to the elasticity of the well material. The quantum well is said to be pseudomorphically strained. If the lattice constant of the unstrained well material is less than that for the barriers, then the well is under biaxial tension. The well is said to be under biaxial compression when the lattice constant of the unstrained well material is greater than that for the barriers.

Biaxial strain provides an extra means of influencing the bandstructure of a quantum well, in addition to changes brought about by variation of the well width. The lattice mismatch and therefore the biaxial strain is determined by the composition of the well and barriers. Continuous variation of the strain is possible with the use of alloys.

Biaxial tension in a quantum well causes a reduction of the direct band gap and an increase in the density of states at the valence band maximum. This effect is used to advantage in tensile strained InAsSb-InSb quantum wells for sensitive far-infrared detectors [1].

For a quantum well under biaxial compression, the topmost valence subband becomes light-hole-like in the plane of the well. Consequently both the in-plane hole mass and the density of states are reduced. Compressive strained wells therefore offer the possibility of low threshold current lasers, and the prospect of faster carrier transport than in similar unstrained systems.

One aim of this thesis is to report investigations of the mobility of *holes* at low in-plane electric fields ($\sim 10^5$ Vm^{-1}) in InGaAs-AlGaAs quantum wells, as a function of well width and indium content. In order to do this, details of the quantum well bandstructure and also the intra- and inter- subband scattering rates are needed. An appropriate method for calculating the valence subbands of this and related type I quantum wells is discussed in this chapter.

As well as having highly accurate methods of calculating quantum well bandstructure it is helpful to have a compact bandstructure solver which gives a simple, approximate description of the bands from a small amount of input data. This can then be easily incorporated in transport calculations and used to pick out physical trends as the well parameters are varied. For this purpose states near the valence band edge have been calculated using a four band k.p model in which holes are defined in terms of the heavy and light hole bands. This method requires just three parameters related to the bulk effective masses for

the heavy and light hole bands, and the strain energy due to the lattice mismatch between the well and substrate. Furthermore, the boundary conditions to the problem have been simplified by assuming that the wells are infinite; hence effective masses are only needed for the well material. Although this means the model is less accurate than finite well k.p models which include more bands, it would be expected to give a satisfactory description of the valence subbands for wide band-gap systems with a significant valence band offset - in particular the InGaAs-AlGaAs system. In the following section a brief introduction is given to the k.p method, and it is shown how this is implemented for solving for the heavy and light hole bands of unstrained bulk material. It is then shown how this bulk bandstructure can be applied to the solution of bound states in a quantum well. The model is modified in section 2.3, to include the effect of biaxial strain in the well. Section 2.4 gives both quantitative and qualitative discussion of some generated quantum well bandstructure, the mixing that occurs between the valence subbands and also the effect of biaxial compression and tension upon the quantum well bound states.

2.2 Calculation of the valence bandstructure

2.2a The k.p method and bulk bandstructure

The k.p method is an efficient technique for calculating bandstructure close to the Brillouin zone centre (Γ point). This was first applied to the solution of energy bands in semiconductor materials by Luttinger, Kohn [2, 3, 4], Kane [5, 6, 7], and Dresselhaus et al [8] during the 1950's. Here, the method is introduced

by considering the motion of a single electron through the periodic potential of a bulk crystal lattice. For the moment the spin-orbit interaction is ignored, to simplify the problem. An eigenstate in the bulk material with wavevector $\mathbf{k} = (k_x, k_y, k_z)$ and occupying band n is described by the Schrödinger equation

$$\left(\frac{\mathbf{p}^2}{2m_0} + V(\mathbf{r}) \right) \Psi_{n\mathbf{k}}(\mathbf{r}) = E_{n\mathbf{k}} \Psi_{n\mathbf{k}}(\mathbf{r}), \tag{2.1}$$

$\mathbf{p}$ is the momentum operator, $V(\mathbf{r})$ the crystal potential and m_0 the free electron mass. According to Bloch's theorem, the one-electron wavefunctions $\Psi_{n\mathbf{k}}(\mathbf{r})$ must be of the form

$$\Psi_{n\mathbf{k}}(\mathbf{r}) = u_{n\mathbf{k}}(\mathbf{r}) e^{i\mathbf{k}.\mathbf{r}} \tag{2.2}$$

where the Bloch function $u_{n\mathbf{k}}(\mathbf{r})$ has the symmetry of the primitive unit cell. Writing $\mathbf{p} = -i\hbar\nabla$ in equation 2.1, $u_{n\mathbf{k}}(\mathbf{r})$ is a solution of

$$\frac{1}{2m_0}(\mathbf{p}^2 + 2\hbar\mathbf{k}.\mathbf{p} + \hbar^2\mathbf{k}^2)u_{n\mathbf{k}}(\mathbf{r}) = (E_{n\mathbf{k}} - V(r))u_{n\mathbf{k}}(\mathbf{r}). \tag{2.3}$$

At the zone centre ($\mathbf{k}{=}0$),

$$\left(\frac{\mathbf{p}^2}{2m_0} + V(\mathbf{r}) \right) u_{n0}(\mathbf{r}) = H_0 u_{n0}(\mathbf{r}) = E_{n0} u_{n0}(\mathbf{r}) \tag{2.4}$$

where u_{n0} is the zone centre Bloch function for band n; E_{n0} is the energy of the band edge. If it is assumed that u_{n0}, E_{n0} are known for all bands of the bulk material then, by treating the terms $\frac{\hbar}{m_0}\mathbf{k}.\mathbf{p}$ and $\frac{\hbar^2}{2m_0}\mathbf{k}^2$ as a perturbation, the energy levels $E_{n\mathbf{k}}$ and eigenstates $\Psi_{n\mathbf{k}}$ at small $\mathbf{k}$ can be determined. To second order in $\mathbf{k}$, and to zeroth order in the Bloch functions ($u_{n\mathbf{k}} \sim u_{n0}$), the energy eigenvalue of band n is given as:

$$E_{n\mathbf{k}} = E_{n0} + \frac{\hbar^2\mathbf{k}^2}{2m_0} + \frac{\hbar^2}{m_0^2}\sum_{i \neq n} \frac{|\langle n,0 \mid \mathbf{k}.\mathbf{p} \mid i,0 \rangle|^2}{E_{n0} - E_{i0}} \tag{2.5}$$

9

where the last term includes the momentum matrix elements between Bloch state u_{n0} and all other states u_{i0}. The last term of equation 2.5 implies that, in general, the greater the energy separation of the bands i and n, the smaller the interaction between them. The set of Bloch functions over which it is chosen to expand the bulk eigenfunctions is reduced where possible, so that only the dominant interactions with neighbouring bands are included. The Bloch functions can be derived from the atomic states of the individual atoms which make up the crystal. For example, the conduction band edge is formed from atomic s orbitals, and the uppermost valence states are derived from p orbitals. Higher states in the conduction band are formed from atomic d states. The chosen set of suitable Bloch functions can be considered to define a vector space, hence the wavefunction for a particular bulk eigenstate is described by a vector Ψ, whose components define the quantity of each Bloch state in that solution. The energy bands and eigenfunctions in bulk material are then defined by the matrix equation

$$H\Psi = E\Psi \qquad (2.6)$$

where the Hamiltonian matrix H has the dimensions of the set of basis Bloch functions. The rows of the matrix H are the separate terms for the k.p interactions between the bands in equation 2.5.

In the absence of the spin-orbit interaction, the p states would be sixfold degenerate at the valence band edge for unstrained bulk material (p_x, p_y, p_z and spin-up and spin-down states per orbital). The spin-orbit splitting for GaAs and related III-V compounds is typically > 0.3 eV, and the valence bands are split into states with $J=\frac{3}{2}$ and $J=\frac{1}{2}$ ($J=$ total angular momentum quantum number).

10

There is a fourfold degeneracy between the heavy ($| \frac{3}{2}, \pm\frac{3}{2}\rangle$) and light ($| \frac{3}{2}, \pm\frac{1}{2}\rangle$) hole bands, and the $| \frac{1}{2}, \pm\frac{1}{2}\rangle$ states form the spin split-off band. For this calculation of valence bandstructure the approach of Broido and Sham [9] has been adopted, in which holes are described in terms of the $J=\frac{3}{2}$ states, alone. Interactions with the conduction, spin split-off and remote bands have not been ignored but are absorbed into the k.p matrix elements connecting the heavy and light hole states. The $J=\frac{3}{2}$ Bloch functions can be represented in bra–ket notation, and are listed in table 2.1 below. [X, Y, Z represent the p_x, p_y, p_z orbitals, and $\uparrow$, $\downarrow$ spin-up and spin-down respectively].

Table 2.1 Basis Bloch functions used in the four band k.p model.

$| j\rangle$	$| j, m_j\rangle$	p orbital representation
u_1	$| \frac{3}{2}, \frac{3}{2}\rangle$	$-\frac{1}{\sqrt{2}} | (X + iY) \uparrow\rangle$
u_2	$| \frac{3}{2}, -\frac{1}{2}\rangle$	$\frac{1}{\sqrt{6}} | (X - iY) \uparrow\rangle + \sqrt{\frac{2}{3}} | Z \downarrow\rangle$
u_3	$| \frac{3}{2}, \frac{1}{2}\rangle$	$-\frac{1}{\sqrt{6}} | (X + iY) \downarrow\rangle + \sqrt{\frac{2}{3}} | Z \uparrow\rangle$
u_4	$| \frac{3}{2}, -\frac{3}{2}\rangle$	$\frac{1}{\sqrt{2}} | (X + iY) \downarrow\rangle$

In this basis, the Luttinger-Kohn Hamiltonian matrix describing mixing between the heavy and light hole bands is [10]:

$$
H = \begin{array}{c} \\ | \frac{3}{2}, \frac{3}{2}\rangle \\ | \frac{3}{2}, -\frac{1}{2}\rangle \\ | \frac{3}{2}, \frac{1}{2}\rangle \\ | \frac{3}{2}, -\frac{3}{2}\rangle \end{array} \begin{array}{cccc} | \frac{3}{2}, \frac{3}{2}\rangle & | \frac{3}{2}, -\frac{1}{2}\rangle & | \frac{3}{2}, \frac{1}{2}\rangle & | \frac{3}{2}, -\frac{3}{2}\rangle \\ \left(\begin{array}{cccc} (P+Q) & R & -S & 0 \\ R^\dagger & (P-Q) & 0 & S \\ -S^\dagger & 0 & (P-Q) & R \\ 0 & S^\dagger & R^\dagger & (P+Q) \end{array} \right) \end{array}
\qquad (2.7)
$$

with

$$P = - \left(\frac{\hbar^2}{2m_0} \right) \gamma_{1L}(k_x^2 + k_y^2 + k_z^2)$$

$$Q = - \left(\frac{\hbar^2}{2m_0} \right) \gamma_{2L}(k_x^2 + k_y^2 - 2k_z^2)$$

$$S = - \left(\frac{\hbar^2}{2m_0} \right) 2\sqrt{3}\gamma_{3L}k_z(k_x - ik_y)$$

$$R = \left(\frac{\hbar^2}{2m_0} \right) \left(\sqrt{3}\overline{\gamma}_L(k_x^2 - k_y^2) - 2\sqrt{3}i\gamma_{3L}k_x k_y \right)$$

γ_{1L}, γ_{2L}, γ_{3L} are the Luttinger parameters [3, 4]. Expressions for these are derived from the **k.p** matrix elements between the zone centre Bloch states, including those with the conduction and spin split-off bands. Eppenga et al [11] have shown that the Luttinger parameters can be related to the bulk effective masses for the heavy and light hole bands in the (001) and (111) directions:

$$\gamma_{1L} = \frac{1}{2} \left(\frac{1}{m_{hh(001)}} + \frac{1}{m_{lh(001)}} \right)$$

$$\gamma_{2L} = \frac{1}{4} \left(\frac{1}{m_{lh(001)}} - \frac{1}{m_{hh(001)}} \right)$$

$$\gamma_{3L} = \frac{1}{2} \left(\gamma_{1L} - \frac{1}{m_{hh(111)}} \right)$$

$$\overline{\gamma}_L = \left(\frac{\gamma_{2L} + \gamma_{3L}}{2} \right)$$

An important simplification of the problem can be made by carrying out a unitary transformation of the basis and Hamiltonian [12, 13]. The purpose of this is to reduce the problem to one in which eigenstates are described by just two

12

Bloch components, one heavy and one light hole part. The appropriate operation for the basis set **u** is

$$\mathbf{v} = U\mathbf{u}. \tag{2.8}$$

According to Ahn and Chuang [10], the unitary matrix U takes the general form

$$U = \begin{pmatrix} \alpha^* & 0 & 0 & -\alpha \\ 0 & \beta^* & -\beta & 0 \\ 0 & \beta^* & \beta & 0 \\ \alpha^* & 0 & 0 & \alpha \end{pmatrix}$$

where

$$\alpha = \frac{1}{\sqrt{2}} e^{i(\frac{3\pi}{4} - \frac{3\phi}{2})}, \qquad \beta = \frac{1}{\sqrt{2}} e^{i(\frac{-\pi}{4} + \frac{\phi}{2})}.$$

$\tan\phi = \frac{k_y}{k_x}$. ϕ has been set equal to $\frac{\pi}{2}$. The modified basis **v** is listed in the following table.

Table 2.2 The set of modified basis Bloch functions.

$\mid j\rangle$	band	$\mid j, m_j\rangle$ representation
v_1	heavy hole	$\alpha \mid \frac{3}{2}, \frac{3}{2}\rangle - \alpha^* \mid \frac{3}{2}, -\frac{3}{2}\rangle$
v_2	light hole	$\beta \mid \frac{3}{2}, -\frac{1}{2}\rangle - \beta^* \mid \frac{3}{2}, \frac{1}{2}\rangle$
v_3	light hole	$\beta \mid \frac{3}{2}, -\frac{1}{2}\rangle + \beta^* \mid \frac{3}{2}, \frac{1}{2}\rangle$
v_4	heavy hole	$\alpha \mid \frac{3}{2}, \frac{3}{2}\rangle + \alpha^* \mid \frac{3}{2}, -\frac{3}{2}\rangle$

In table 2.2, the Bloch functions appear as spin-degenerate pairs, that is the heavy hole states v_1, v_4 are both linear combinations of the spin-configurations $m_j = \pm\frac{3}{2}$ and the light hole functions v_2, v_3 are combinations of $m_j = \pm\frac{1}{2}$. The transformation for the Hamiltonian is

$$H' = UHU^\dagger. \tag{2.9}$$

13

The elements of $\mathbb{U}$ have been chosen so that the k.p Hamiltonian is block-diagonalised:

$$H' = \begin{pmatrix} (P+Q) & \overline{R} & 0 & 0 \\ \overline{R}^{\dagger} & (P-Q) & 0 & 0 \\ 0 & 0 & (P-Q) & \overline{R} \\ 0 & 0 & \overline{R}^{\dagger} & (P+Q) \end{pmatrix} \tag{2.10}$$

$\overline{R} = |R| - i|S|$ therefore

$$\overline{R} = -\left(\frac{\sqrt{3}\hbar^2}{2m_0} \right) \left(\sqrt{\gamma_{2L}^2 \left(k_x^2 - k_y^2 \right)^2 + 4\gamma_{3L}^2 k_x^2 k_y^2} - 2i\gamma_{3L} k_z \sqrt{k_x^2 + k_y^2} \right).$$

In the range of small $\mathbf{k}$, the bands in III-V materials are close to isotropic in the $k_x - k_y$ plane [14, 15]. It is therefore reasonable to take an average over the directional dependence of the bandstructure in this plane and set $\gamma_{2L} \sim \gamma_{3L} = \overline{\gamma_L}$. Under this axial approximation $\overline{R}$ reduces to

$$\overline{R} = -\left(\frac{\sqrt{3}\hbar^2}{2m_0} \right) \left(\overline{\gamma}_L k_{\parallel}^2 - 2i\gamma_{3L} k_z k_{\parallel} \right).$$

Now all eigenstates in the bulk are described by three variables $(E, k_{\parallel}, k_z)$ instead of the original four (E, k_x, k_y, k_z). At this point it is useful to explain the significance that these variables will have in the description of the quantum well eigenstates. In the following paragraph, it will be shown that for given energy E and in-plane wavevector $k_{\parallel}$ in the bulk, only a discrete set of wave components k_z propagate through the material and satisfy the Schrödinger equation (2.6). Once holes are confined in the z direction by forming the quantum well, the aim is to construct the envelope functions describing the quantum well eigenstates as linear combinations of the allowed plane wave components k_z for given E and $k_{\parallel}$. By varying E and $k_{\parallel}$, and first solving for the values of k_z, the quantum

14

well eigenstates can be determined by finding suitable linear combinations of the terms $e^{ik_z \cdot z}$ which satisfy the set of boundary conditions defining the well.

Transforming H into H', the Schrödinger equation (2.6) is split into two independent matrix equations:

$$H^U_{2\times2}\Psi^U = E\Psi^U, \qquad (2.11a)$$

$$H^L_{2\times2}\Psi^L = E\Psi^L. \qquad (2.11b)$$

Ψ^U and Ψ^L are defined by the coefficients of Bloch functions v_1, v_2 and v_3, v_4 respectively, for a given bulk solution $(E, k_\parallel, k_z)$. Rearrangement of equations 2.11a and 2.11b yields the secular determinants:

$$\mid H^U_{jj'} - E\delta_{jj'} \mid = 0 \qquad j, j' = 1, 2, \qquad (2.12a)$$

$$\mid H^L_{jj'} - E\delta_{jj'} \mid = 0 \qquad j, j' = 3, 4. \qquad (2.12b)$$

When values are assigned to E, $k_\parallel$ in equations 2.12, it is possible to solve for the wavevector components k_z. Equations 2.12a and 2.12b produce the same eigenvalues, hence identical bandstructure. All bands are therefore doubly degenerate. This is the Kramer's degeneracy, and is restricted to crystals which possess inversion symmetry (see for example the description by Kittel [16]). The inversion asymmetry is small for III-V materials and is therefore neglected [6], so degenerate bands are expected. Equations 2.12 are quartic in k_z, so there are always four solutions, corresponding to states on the heavy and light hole bands. k_z values are therefore indexed k_{z_i} $(i = 1..4)$.

Each bulk wavefunction labelled by $(E, k_\parallel, k_{z_i}$ $(i=1..4))$ and derived from the

15

upper block Hamiltonian may be written as

$$\Psi_i^U(\mathbf{r}_\parallel, z) = \sum_{j=1}^{2} F_{ij} v_j(\mathbf{r}) e^{i(\mathbf{k}_\parallel \cdot \mathbf{r}_\parallel + k_{z_i} \cdot z)}. \tag{2.13a}$$

That for $H_{2 \times 2}^L$ is

$$\Psi_i^L(\mathbf{r}_\parallel, z) = \sum_{j=3}^{4} F_{ij} v_j(\mathbf{r}) e^{i(\mathbf{k}_\parallel \cdot \mathbf{r}_\parallel + k_{z_i} \cdot z)}. \tag{2.13b}$$

F_{ij} is the coefficient of basis state $v_j(\mathbf{r})$ for wavevector k_{z_i}. These are found using:

$$H_i^U \begin{pmatrix} F_{i1} \\ F_{i2} \end{pmatrix} = E \begin{pmatrix} F_{i1} \\ F_{i2} \end{pmatrix} \qquad i = 1..4, \tag{2.14a}$$

$$H_i^L \begin{pmatrix} F_{i3} \\ F_{i4} \end{pmatrix} = E \begin{pmatrix} F_{i3} \\ F_{i4} \end{pmatrix} \qquad i = 1..4. \tag{2.14b}$$

H_i^U, H_i^L are the upper and lower block Hamiltonians with all k_z terms evaluated at k_{z_i}.

2.2b Quantum well bound states

Consider a single well, of width l, with the z axis in Cartesian coordinates defining the growth direction for the quantum well (hence the well lies in the (001) plane). By confining holes in the z direction, the valence bandstructure is no longer three dimensional in k space, and instead eigenstates form a set of subbands in $k_\parallel$ $(k_x - k_y)$ space. Since there is no spatial confinement in any direction within the plane of the quantum well, holes can be represented by a plane wavefront $e^{i\mathbf{k}_\parallel \cdot \mathbf{r}_\parallel}$.

Applying the envelope function approximation, the wavefunction of a bound state at $(E, k_\parallel)$ may be written as a linear combination of the heavy and light hole bulk states at $(E, k_\parallel, k_{z_i}(i = 1..4))$. There are two possible wavefunctions

16

at $(E, k_\parallel)$ since the Hamiltonian has been split into two components; making the subbands doubly degenerate. For the upper block, the wavefunction for a hole at $k_\parallel$ on subband n is:

$$\Psi^U_{n,k_\parallel}(\mathbf{r}_\parallel, z) = \sum_{j=1}^{2} \left(\sum_{i=1}^{4} a_i^U F_{ij} e^{ik_{z_i} z} \right) e^{i\mathbf{k}_\parallel \cdot \mathbf{r}_\parallel} v_j(\mathbf{r}) = \sum_{j=1}^{2} \Phi_j^U(z) e^{i\mathbf{k}_\parallel \cdot \mathbf{r}_\parallel} v_j(\mathbf{r}). \quad (2.15a)$$

That for the lower block is:

$$\Psi^L_{n,k_\parallel}(\mathbf{r}_\parallel, z) = \sum_{j=3}^{4} \left(\sum_{i=1}^{4} a_i^L F_{ij} e^{ik_{z_i} z} \right) e^{i\mathbf{k}_\parallel \cdot \mathbf{r}_\parallel} v_j(\mathbf{r}) = \sum_{j=3}^{4} \Phi_j^L(z) e^{i\mathbf{k}_\parallel \cdot \mathbf{r}_\parallel} v_j(\mathbf{r}). \quad (2.15b)$$

a_i^U and a_i^L are the coefficients of the bulk solutions $(E, k_\parallel, k_{z_i})$ for the upper and lower block quantum well bound states at $(E, k_\parallel)$. $\Phi_j(z)$ is the envelope modulating the lattice-periodic Bloch function $v_j(\mathbf{r})$.

It was stated in the introduction that the quantum well can be approximated by an infinite square well potential, for systems such as GaAs-AlGaAs having a sufficiently large valence band offset. The wavefunctions must therefore vanish outside the well $(| z |> \frac{l}{2})$. Hence the boundary conditions are:

$$\Psi^U = \sum_{i=1}^{4} \sum_{j=1}^{2} a_i^U F_{ij} v_j(\mathbf{r}) e^{i(\mathbf{k}_\parallel \cdot \mathbf{r}_\parallel \pm k_{z_i} \cdot \frac{l}{2})} = 0, \qquad (2.16a)$$

$$\Psi^L = \sum_{i=1}^{4} \sum_{j=3}^{4} a_i^L F_{ij} v_j(\mathbf{r}) e^{i(\mathbf{k}_\parallel \cdot \mathbf{r}_\parallel \pm k_{z_i} \cdot \frac{l}{2})} = 0. \qquad (2.16b)$$

Multiplying each equation by $v_{j'}^*(\mathbf{r})$, integrating over a unit cell at the well boundary and remembering that the Bloch functions are orthogonal to each other i.e.

$$\int_{unit\,cell} v_{j'}^*(\mathbf{r}) v_j(\mathbf{r}) d\mathbf{r} = \delta_{jj'} \qquad (2.17)$$

it follows that

$$\sum_{i=1}^{4} a_i^U F_{ij} e^{ik_{z_i} \frac{l}{2}} = 0 \qquad j = 1, 2, \qquad (2.18a)$$

$$\sum_{i=1}^{4} a_i^U F_{ij} e^{-ik_{z_i} \frac{l}{2}} = 0 \qquad j = 1, 2, \tag{2.18b}$$

$$\sum_{i=1}^{4} a_i^L F_{ij} e^{ik_{z_i} \frac{l}{2}} = 0 \qquad j = 3, 4, \tag{2.18c}$$

$$\sum_{i=1}^{4} a_i^L F_{ij} e^{-ik_{z_i} \frac{l}{2}} = 0 \qquad j = 3, 4. \tag{2.18d}$$

These can be collected into the matrix equations:

$$\begin{pmatrix} F_{11} e^{ik_{z_1} \frac{l}{2}} & F_{21} e^{ik_{z_2} \frac{l}{2}} & F_{31} e^{ik_{z_3} \frac{l}{2}} & F_{41} e^{ik_{z_4} \frac{l}{2}} \\ F_{12} e^{ik_{z_1} \frac{l}{2}} & F_{22} e^{ik_{z_2} \frac{l}{2}} & F_{32} e^{ik_{z_3} \frac{l}{2}} & F_{42} e^{ik_{z_4} \frac{l}{2}} \\ F_{11} e^{-ik_{z_1} \frac{l}{2}} & F_{21} e^{-ik_{z_2} \frac{l}{2}} & F_{31} e^{-ik_{z_3} \frac{l}{2}} & F_{41} e^{-ik_{z_4} \frac{l}{2}} \\ F_{12} e^{-ik_{z_1} \frac{l}{2}} & F_{22} e^{-ik_{z_2} \frac{l}{2}} & F_{32} e^{-ik_{z_3} \frac{l}{2}} & F_{42} e^{-ik_{z_4} \frac{l}{2}} \end{pmatrix} \begin{pmatrix} a_1^U \\ a_2^U \\ a_3^U \\ a_4^U \end{pmatrix} = \begin{pmatrix} 0 \\ 0 \\ 0 \\ 0 \end{pmatrix}, \tag{2.19a}$$

$$\begin{pmatrix} F_{13} e^{ik_{z_1} \frac{l}{2}} & F_{23} e^{ik_{z_2} \frac{l}{2}} & F_{33} e^{ik_{z_3} \frac{l}{2}} & F_{43} e^{ik_{z_4} \frac{l}{2}} \\ F_{14} e^{ik_{z_1} \frac{l}{2}} & F_{24} e^{ik_{z_2} \frac{l}{2}} & F_{34} e^{ik_{z_3} \frac{l}{2}} & F_{44} e^{ik_{z_4} \frac{l}{2}} \\ F_{13} e^{-ik_{z_1} \frac{l}{2}} & F_{23} e^{-ik_{z_2} \frac{l}{2}} & F_{33} e^{-ik_{z_3} \frac{l}{2}} & F_{43} e^{-ik_{z_4} \frac{l}{2}} \\ F_{14} e^{-ik_{z_1} \frac{l}{2}} & F_{24} e^{-ik_{z_2} \frac{l}{2}} & F_{34} e^{-ik_{z_3} \frac{l}{2}} & F_{44} e^{-ik_{z_4} \frac{l}{2}} \end{pmatrix} \begin{pmatrix} a_1^L \\ a_2^L \\ a_3^L \\ a_4^L \end{pmatrix} = \begin{pmatrix} 0 \\ 0 \\ 0 \\ 0 \end{pmatrix}. \tag{2.19b}$$

Rewriting these equations in matrix notation,

$$M^U \mathbf{a}^U = 0, \qquad M^L \mathbf{a}^L = 0.$$

It follows that the allowed eigenstates of the quantum well must therefore satisfy the condition $\mid M^U \mid = 0$, or $\mid M^L \mid = 0$. The valence subbands are obtained by a simple search for zeros of each determinant across a range of $(E, k_\parallel)$ space. Both determinants produce the same bandstructure, as expected because of the double degeneracy of the states, as discussed previously. The a_i^U, a_i^L are the coefficients of the upper and lower block bulk wavefunctions, evaluated at k_{z_i}. It is straightforward to calculate these from the appropriate sets of four equations. Once these are known, they may be combined with the bulk coefficients F_{ij}. In simpler notation, the upper and lower block wavefunctions are therefore:

$$\Psi^U(\mathbf{r}_\parallel, z) = \sum_{j=1}^{2} \sum_{i=1}^{4} \alpha_{ij}^U e^{i(\mathbf{k}_\parallel \cdot \mathbf{r}_\parallel + k_{z_i} \cdot z)} \mid j \rangle, \tag{2.20a}$$

18

$$\Psi^L(\mathbf{r}_{\|}, z) = \sum_{j=3}^{4} \sum_{i=1}^{4} \alpha_{ij}^L e^{i(\mathbf{k}_{\|} \cdot \mathbf{r}_{\|} + k_{z_i} \cdot z)} \mid j\rangle. \tag{2.20b}$$

The envelope functions are generally asymmetric, but if required, (anti)symmetric pairs of envelopes of the original basis functions **u** can be obtained by taking simple linear combinations of these symmetric envelopes.

2.3 The effect of strain on the valence bandstructure

For an epitaxial layer of lattice constant a_{ep}, grown on the (001) planes of a substrate, lattice spacing a_{sub}, the biaxial strain across the interface plane between the layers is

$$\epsilon_{\|} = \left(\frac{a_{sub} - a_{ep}}{a_{ep}} \right). \tag{2.21a}$$

In the valence band, the strain energy ς associated with the lattice mismatch is given by the product of the valence band deformation potential and the net axial strain [17]:

$$\varsigma = -b(\epsilon_z - \epsilon_{\|}). \tag{2.21b}$$

Making the assumption that Poisson's ratio is $\frac{1}{3}$ for GaAs (actual value 0.31 [18]) and related materials, the strain component across the interface plane $\epsilon_{\|}$ is matched by the distortion of the lattice unit cell along the z axis, ϵ_z, hence $\varsigma = 2b\epsilon_{\|}$. The strain energy shifts the band energies; in particular it lifts the degeneracy between the heavy and light hole bands for bulk material [19]. Including this strain splitting, the **k.p** Hamiltonian for the J$=\frac{3}{2}$ basis is [20]:

$$H' = \begin{pmatrix} (P+Q) + \varsigma & \overline{R} & 0 & 0 \\ \overline{R}^{\dagger} & (P-Q) - \varsigma & 0 & 0 \\ 0 & 0 & (P-Q) - \varsigma & \overline{R} \\ 0 & 0 & \overline{R}^{\dagger} & (P+Q) + \varsigma \end{pmatrix}. \tag{2.22}$$
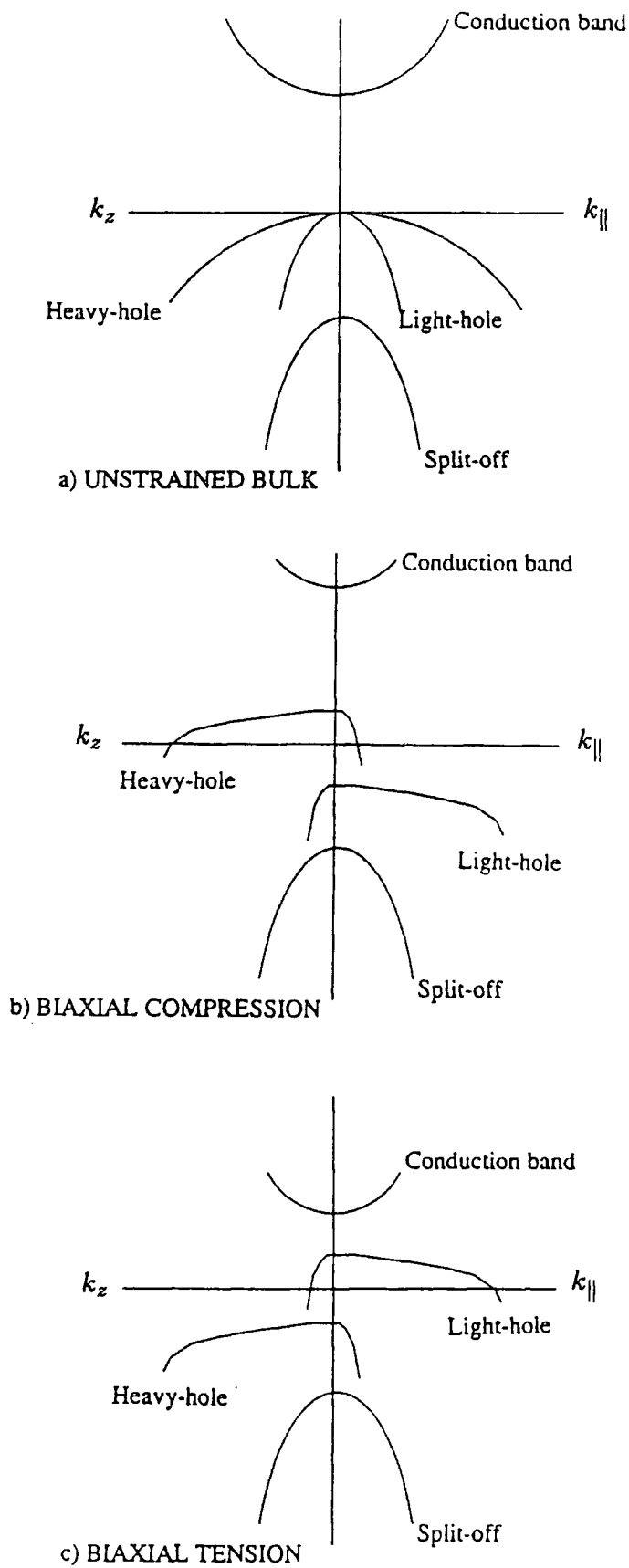
Figure 2.1. Simplified bulk bandstructure of a direct gap semiconductor material.
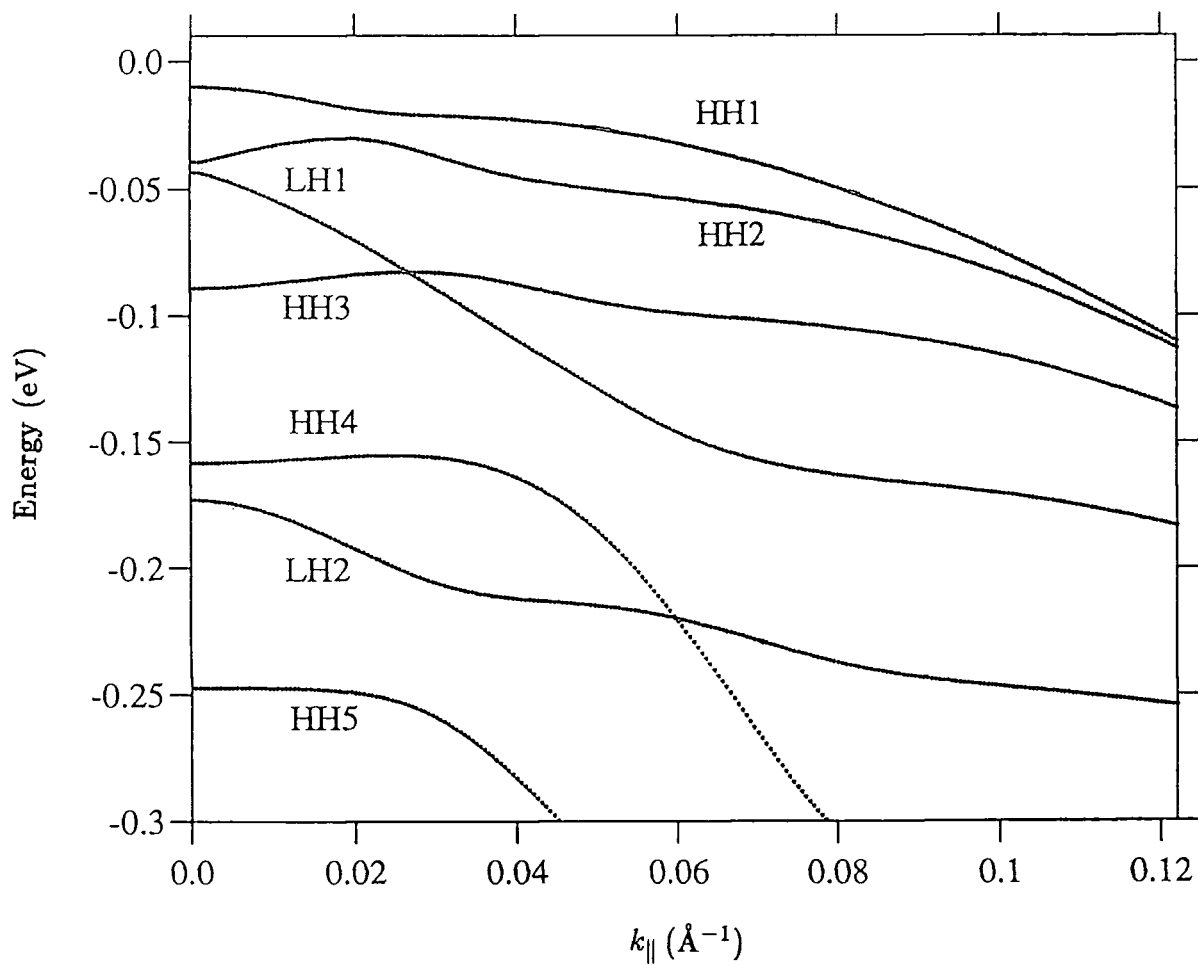
Figure 2.2. In-plane energy dispersions for the highest seven valence subbands of a 100 Å GaAs-AlGaAs infinite quantum well.

Values $\varsigma > 0$ correspond to compressive biaxial strain, and $\varsigma < 0$ to biaxial tension.

It was stated in section 2.1 that biaxial compression of the crystal lattice in the $x - y$ plane gives rise to a highest valence band of reduced in-plane ($k_\parallel$) effective mass. This can be explained using the following simple picture. As a consequence of compression in the $x - y$ plane, the unit cells of the lattice relax along the z axis. This makes the p orbitals more localised between neighbouring atoms on planes in the z direction, but increases the overlap between orbitals on neighbouring sites in the $x - y$ plane and therefore the ease with which a hole can move between lattice sites in this plane; that is holes exhibit a reduced effective mass in this plane. With greater localisation of the p orbitals in the z direction, the holes suffer greater inertia for movement between sites in this direction, and their effective mass along the z axis is increased (figure 2.1b). Biaxial tension produces the converse effect, this time with greater localization of p orbitals between neighbours in the $x - y$ plane, but greater overlap in the z direction (figure 2.1c) [21].

2.4 Analysis of some calculated bandstructures

Figure 2.2 shows the in-plane subband dispersions for an unstrained 100 Å GaAs-AlGaAs quantum well of infinite depth calculated using the method described in section 2.2. The data used to generate this and other bandstructure in this chapter are given in tables 2.3a, b. The bands are markedly non-parabolic and subbands are observed to both cross (e.g. the subbands marked LH1 and

HH3 at $k_\parallel \sim 0.025\text{Å}^{-1}$) and anticross (e.g. HH1 and HH2 at $k_\parallel \sim 0.02\text{Å}^{-1}$; LH1 and HH4 at $k_\parallel \sim 0.05\text{Å}^{-1}$). These features are caused by the interaction between the states in the quantum well, the strength of which can be sufficient for some bands to exhibit an electron-like effective mass at the zone centre, such as the HH2 and HH3 subbands of figure 2.2.

Table 2.3a Lattice constants a_0, valence band deformation potentials b and band effective masses used to generate figures 2.2, 2.4 and 2.6.

(Lattice Temperature = 300 K)

Material	$a_0(\text{Å})$	$b(\text{eV})$	$m_{hh}^{(001)}(m_0)$	$m_{lh}^{(001)}(m_0)$	$m_{hh}^{(111)}(m_0)$
†GaAs	5.653	-1.7	0.38	0.087	0.95
AlAs	5.653	-	-	-	-
•InAs	6.058	-1.8	0.41	0.027	0.917
GaSb	6.095	-1.8	0.30	0.044	0.40
AlSb	6.136	-	-	-	-

Sources of data: † GaAs data [11], • InAs data [18]

Table 2.3b Luttinger parameters used to generate figure 2.2.

γ_{1L}	γ_{2L}	γ_{3L}	$\epsilon_\parallel(\%)$	$\varsigma(\text{meV})$
7.06	2.22	3.01	0.00	0.00

Table 2.3c Luttinger parameters and strain factors

used to generate figures 2.4a..d.

indium content x	γ_{1L}	γ_{2L}	γ_{3L}	$\epsilon_{\parallel}(\%)$	ς (meV)
0.10	7.50	2.42	3.22	-0.70	24.2
0.15	7.75	2.54	3.35	-1.07	36.6
0.20	8.01	2.66	3.48	-1.42	48.8
0.25	8.30	2.80	3.62	-1.77	61.0

Table 2.3d Luttinger parameters and strain factors

used to generate figures 2.6a..d.

arsenic content y	γ_{1L}	γ_{2L}	γ_{3L}	$\epsilon_{\parallel}(\%)$	ς (meV)
0.00	13.03	4.84	5.27	0.68	-24.4
0.05	12.48	4.60	5.07	1.04	-37.5
0.10	12.00	4.36	4.89	1.41	-51.0
0.15	11.51	4.15	4.72	1.78	-63.7

At the zone centre the off-diagonal terms of H^U and H^L (equation 2.10) vanish, decoupling the heavy and light hole bands so that the quantum well eigenstates are purely heavy or light hole in character (that is, the z dependent envelope for all but one of the modified Bloch functions is zero). For the general case of a strained system these eigenstates lie at energies:

$$E_{\text{HHn}}(k_{\parallel} = 0) = \varsigma - n^2 \frac{h^2}{8m_0 l^2}(\gamma_{1L} - 2\gamma_{2L}) \qquad (2.23\text{a})$$

for heavy holes and

$$E_{\text{LHn}}(k_{\parallel} = 0) = -\varsigma - n^2 \frac{h^2}{8m_0 l^2}(\gamma_{1L} + 2\gamma_{2L}) \qquad (2.23\text{b})$$

for light holes. l is the well width, n is an integer corresponding to the mode of the standing wave solution within the well (e.g. $n=1$ represents the even parity ground state, $n=2$ the odd parity first excited state and so on). Subbands are therefore labelled HH1, LH1 etc. according to the character of the zone centre state. In the infinite well model, the normalized zone centre envelopes of both heavy and light holes take the form

$$\begin{cases} \sqrt{\frac{2}{l}}\cos(\frac{n\pi z}{l}) & \text{even parity, } n \text{ odd;} \\ \sqrt{\frac{2}{l}}\sin(\frac{n\pi z}{l}) & \text{odd parity, } n \text{ even.} \end{cases} \qquad (2.24)$$

It is clear from equations 2.23 that the separation of the HHn and LHn energy levels is a function of both the strain and well width whereas the HHn-HHm or LHn-LHm splitting is only well-width dependent.

The magnitudes of the off-diagonal elements of H^U and H^L increase with increasing $k_{\parallel}$ such that any eigenfunction $\Psi_{n,k_{\parallel}}$ is an admixture of the definite parity zone centre envelopes. The strength of the coupling between the HHm

and LHn zone centre eigenfunctions is given from the Hamiltonian H^U (or H^L) [22] as:

$$\langle \mathrm{HHm} \mid \overline{R} \mid \mathrm{LHn} \rangle = -\sqrt{3}\frac{\hbar^2}{2m_0}\langle \mathrm{HHm} \mid \overline{\gamma_L}k_\parallel^2 - 2i\gamma_{3L}k_\parallel k_z \mid \mathrm{LHn} \rangle. \qquad (2.25)$$

Rewriting the operator k_z as $-i\frac{\partial}{\partial z}$,

$$\langle \mathrm{HHm} \mid \overline{R} \mid \mathrm{LHn} \rangle = \frac{\hbar^2}{m_0}\sqrt{3}\gamma_{3L}k_\parallel\langle \mathrm{HHm} \mid \frac{\partial}{\partial z} \mid \mathrm{LHn} \rangle$$

$$-\frac{\hbar^2}{2m_0}\sqrt{3}\overline{\gamma_L}k_\parallel{}^2\langle \mathrm{HHm} \mid \mathrm{LHn} \rangle. \qquad (2.26)$$

$\mid \mathrm{HHm} \rangle$ represents the zone centre envelope for the mth heavy hole subband, and $\mid \mathrm{LHn} \rangle$, that for the nth light hole state. The first term of equation 2.26 involves the momentum matrix element between these states, and the second an overlap integral. Using the normalized definite parity envelopes it is straightforward to show that the coupling is

$$\mid \langle \mathrm{HHm} \mid \overline{R} \mid \mathrm{LHn} \rangle \mid = \begin{cases} \frac{\hbar^2}{2m_0}\frac{8\sqrt{3}\gamma_{3L}k_\parallel}{l}\frac{mn}{|m^2-n^2|}, & m+n \text{ odd}; \\ \frac{\hbar^2}{2m_0}\sqrt{3}\overline{\gamma}_L k_\parallel{}^2, & m = n; \\ 0, & m+n \text{ even}, m \neq n. \end{cases} \qquad (2.27)$$

The above results represent the selection rules for interactions between states in the infinite well and can explain all the crossing/anticrossing phenomena between subbands. Heavy and light hole states sharing the same standing wave mode will interact strongly - their coupling is second order in $k_\parallel$. In addition, this coupling is inversely proportional to the well width l. The last result of equation 2.27 suggests there should be no interaction between the HH3 and LH1 states, nor the HH4 and LH2 states for example, and so these subbands will cross as illustrated in figure 2.2. The crossing phenomenon is unique to the infinite well,

24

and occurs because the zone centre envelopes have $k_z = \frac{n\pi}{l}$, and so vanish at the well edges ($z = \pm\frac{l}{2}$). In the case of a finite well, where the wavefunctions spread into the barriers, there will always be some overlap between any two eigenstates, and therefore anticrossing between all subbands. The selection rules are given in table 2.4 showing the order of each interaction as a function of $k_\parallel$. A box with $k_\parallel^2$ indicates that the interaction is due to the overlap term in equation 2.26, and a box with $k_\parallel$ shows the interaction is due to the momentum matrix element term. A dash indicates the absence of an interaction.

Table 2.4 Selection rules for interactions between

some eigenstates of the infinite well.

	LH1	LH2	LH3	LH4
HH1	$k_\parallel^2$	$k_\parallel$	-	$k_\parallel$
HH2	$k_\parallel$	$k_\parallel^2$	$k_\parallel$	-
HH3	-	$k_\parallel$	$k_\parallel^2$	$k_\parallel$
HH4	$k_\parallel$	-	$k_\parallel$	$k_\parallel^2$
HH5	-	$k_\parallel$	-	$k_\parallel$
HH6	$k_\parallel$	-	$k_\parallel$	-
HH7	-	$k_\parallel$	-	$k_\parallel$
HH8	$k_\parallel$	-	$k_\parallel$	-

Subband mixing can be studied by calculating the overlap integrals between the zone centre states and a set of wavefunctions along each subband. If $\Psi_{m,k_\parallel}$ denotes the wavefunction at in-plane wavevector $k_\parallel$ on the mth valence subband, and $\Psi_{n,0}$ represents the zone centre eigenfunction for the nth band, then the
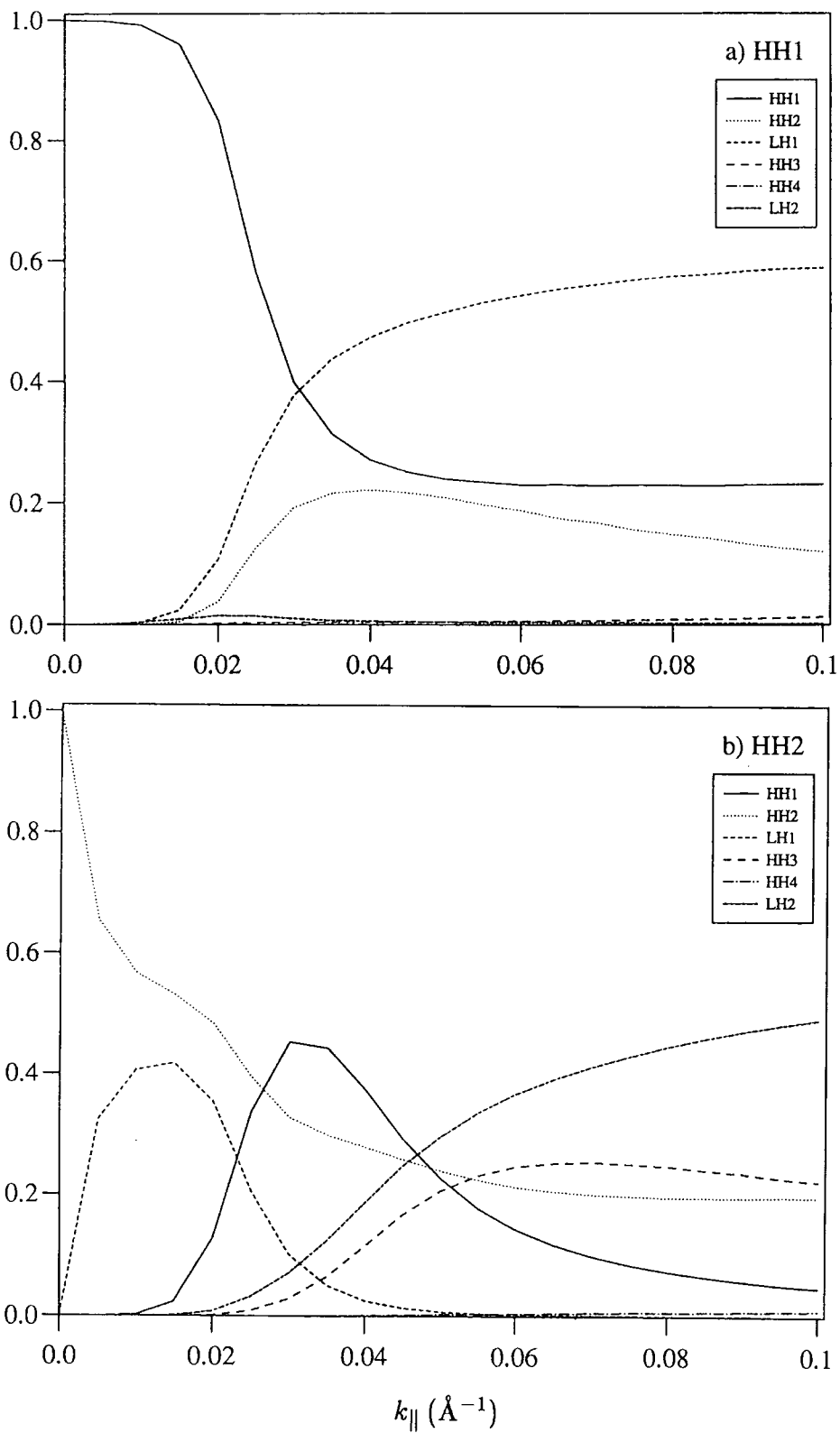
Figures 2.3a, b. The fractional character of the two highest valence subbands of figure 2.2 as a function of $k_{\parallel}$.
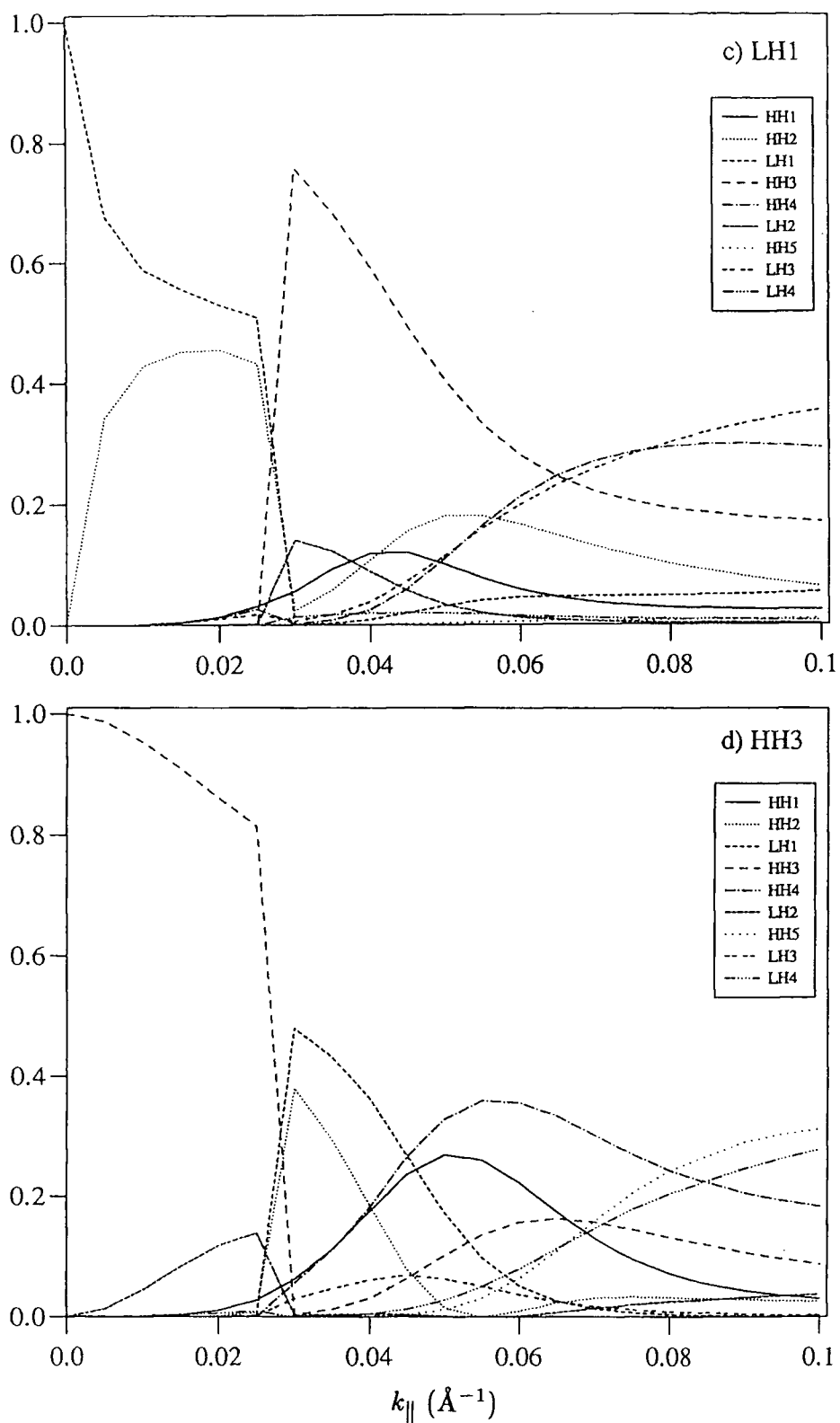
Figures 2.3c, d. The fractional character of the third and fourth highest valence subbands of figure 2.2 as a function of $k_\parallel$, showing the highly mixed character of both bands for $k_\parallel > 0.06\text{Å}^{-1}$. The discontinuity of the curves at $k_\parallel \sim 0.03\text{Å}^{-1}$ is due to crossing between the LH1 and HH3 subbands.

fractional character of state $\Psi_{n,0}$ present in $\Psi_{m,k_\parallel}$ is

$$| \langle m, k_\parallel \mid n, 0 \rangle |^2 = \left| \int_A \int_{-\frac{l}{2}}^{\frac{l}{2}} \Psi_{n,0}^* \Psi_{m,k_\parallel} d\mathbf{r}_\parallel dz \right|^2. \qquad (2.28)$$

The wavefunctions may be written:

$$\Psi_{n,0} = \sum_{j=1}^{2} \sum_{i'=1}^{4} \beta_{i'j} e^{ib_{i'}z} e^{i\mathbf{k}_\parallel \cdot \mathbf{r}_\parallel} \mid j \rangle, \qquad (2.29a)$$

$$\Psi_{m,k_\parallel} = \sum_{j=1}^{2} \sum_{i=1}^{4} \alpha_{ij} e^{ia_i z} e^{i\mathbf{k}_\parallel \cdot \mathbf{r}_\parallel} \mid j \rangle. \qquad (2.29b)$$

Note that in equations 2.29a and 2.29b summation is only made over the Bloch states $j=1,2$ relevant to H^U. By block diagonalising the k.p Hamiltonian and transforming the set of basis Bloch functions, quantum well eigenstates are described completely by the solutions of *either* the upper block Hamiltonian H^U *or* the lower block H^L. The overlap integrals between states $\Psi_{n,0}$ and $\Psi_{m,k_\parallel}$ are the same whether both eigenfunctions are solved using H^U or H^L. The overlap integral between $\Psi_{n,0}$ and $\Psi_{m,k_\parallel}$ is:

$$| \langle m, k_\parallel \mid n, 0 \rangle |^2 = \frac{\left| \int_A \int_{-\frac{l}{2}}^{\frac{l}{2}} \Psi_{n,0}^* \Psi_{m,k_\parallel} d\mathbf{r}_\parallel dz \right|^2}{\left(\int_A \int_{-\frac{l}{2}}^{\frac{l}{2}} \Psi_{n,0}^* \Psi_{n,0} d\mathbf{r}_\parallel dz \right) \left(\int_A \int_{-\frac{l}{2}}^{\frac{l}{2}} \Psi_{m,k_\parallel}^* \Psi_{m,k_\parallel} d\mathbf{r}_\parallel dz \right)}. \qquad (2.30)$$

From table 2.4, the LH1 zone centre state is coupled to the HH1 state with a strength $\sim k_\parallel^2$, and to the HH2 state with strength $\sim k_\parallel$. The HH1 and HH2 states are expected to mix away from the zone centre because of their mutual interaction with the LH1 state. Figures 2.3a, b show the fractional character of states in the HH1 and HH2 subbands as a function of $k_\parallel$. Up to the anticrossing region in figure 2.2 ($k_\parallel \sim 0.025 \text{Å}^{-1}$), the states in the HH1 subband (figure 2.3a)

26

keep much of their HH1 character, but past the anticrossing region, the interaction $\sim k_\parallel^2$ with the LH1 zone centre state dominates. There the HH1 subband has predominantly LH1 character ($\sim 60\%$) but retains some HH1 character ($\sim 20\%$); the remainder being small contributions from HH2 ($\sim 10\%$), HH3 ($\sim 2\%$) and higher order states.

Compared to HH1, the HH2 subband shows a sharper decline in the zone centre component and rise in LH1 character as illustrated in figure 2.3b. This is because the interaction which is first order in $k_\parallel$ is operative in this case. Past the anticrossing at $k_\parallel \sim 0.025 \mathrm{\AA}^{-1}$, the HH1 character of the HH2 subband increases to a peak of $\sim 50\%$ at $k_\parallel \sim 0.03 \mathrm{\AA}^{-1}$, but then the second order coupling to the LH2 state takes over, so that the subband is mostly LH2 in character with a remanent HH2 fraction of ($\sim 20\%$). Considerable HH3 character is also present which is mixed in through LH2.

The mixing of the HH1 and HH2 subbands is straightforward compared with that of higher index subbands, where many more interactions are important. This is illustrated in figures 2.3c and 2.3d, depicting the mixed nature of the LH1 and HH3 subbands. In the vicinity of the zone centre of figure 2.3c, the sharp decline in LH1 character is matched by an increasing fraction of the HH2 state. This complements the character exchange of figure 2.3b. The HH2 and LH1 subbands anticross about the zone centre. It should be noticed in figure 2.3c that near $k_\parallel \sim 0.025 \mathrm{\AA}^{-1}$ the LH1 character drops abruptly and the HH3 character is switched on. The converse is true for figure 2.3d. This marks the crossing of the LH1 and HH3 subbands. It was stated before that the LH1 and
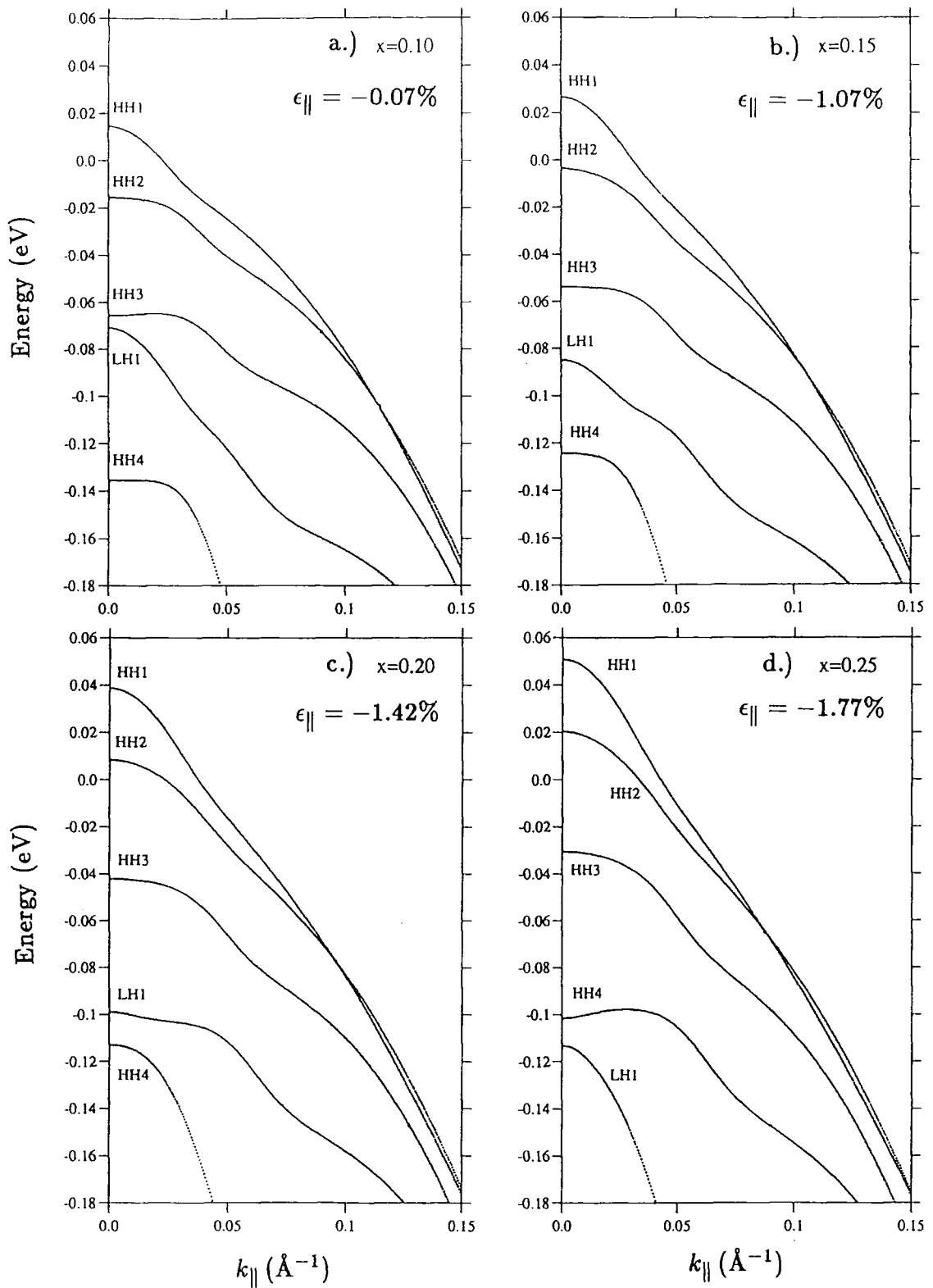
Figures 2.4a..d. In-plane energy dispersions for the highest valence subbands of a 100 Å $In_xGa_{1-x}As$-AlGaAs quantum well as a function of increased indium content x, and therefore increased biaxial compressive strain $\epsilon_{\parallel}$.
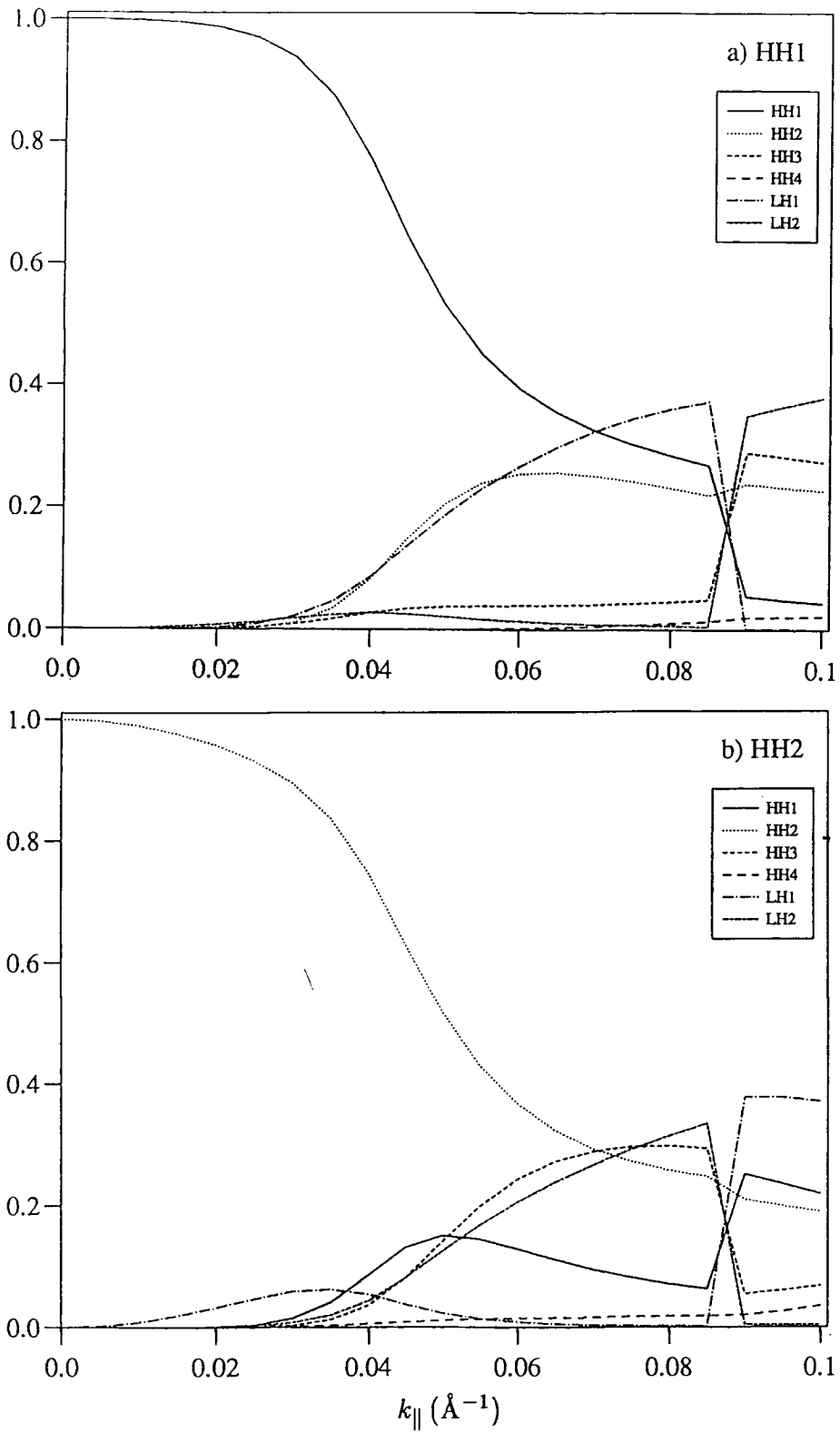
Figures 2.5a, b. The fractional character of the two highest valence subbands for the 100 Å $In_{0.25}Ga_{0.75}As$-AlGaAs quantum well of figure 2.4d as a function of $k_\parallel$. The discontinuity at $k_\parallel \sim 0.09\,\text{Å}^{-1}$ is due to crossing between the HH1 and HH2 subbands.
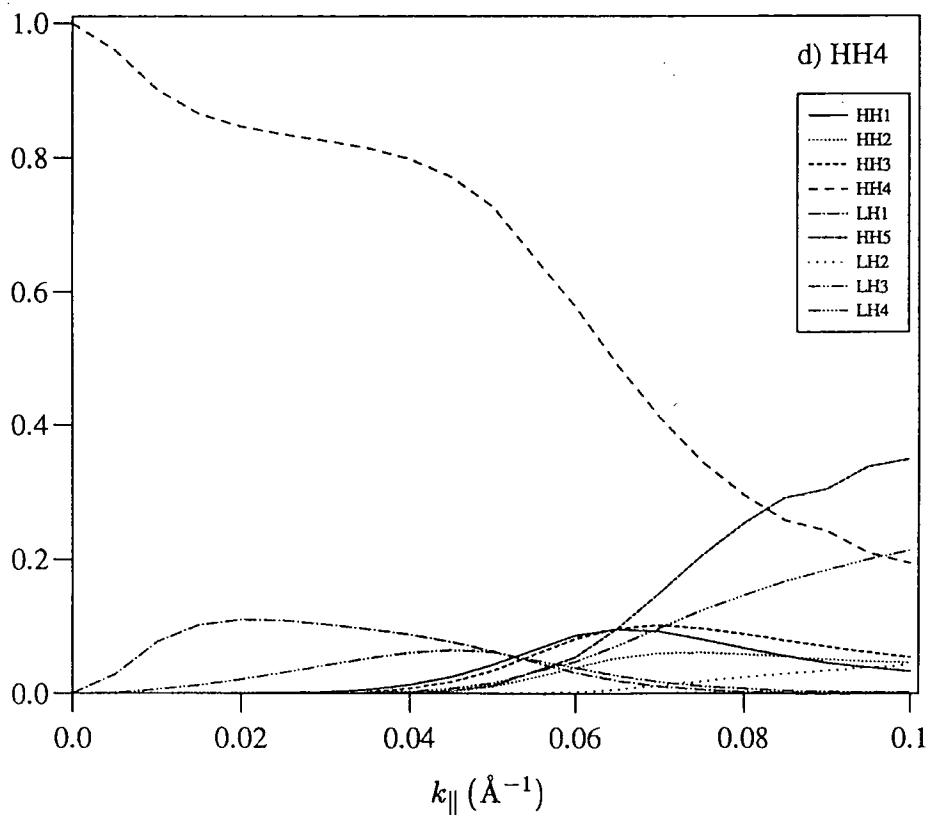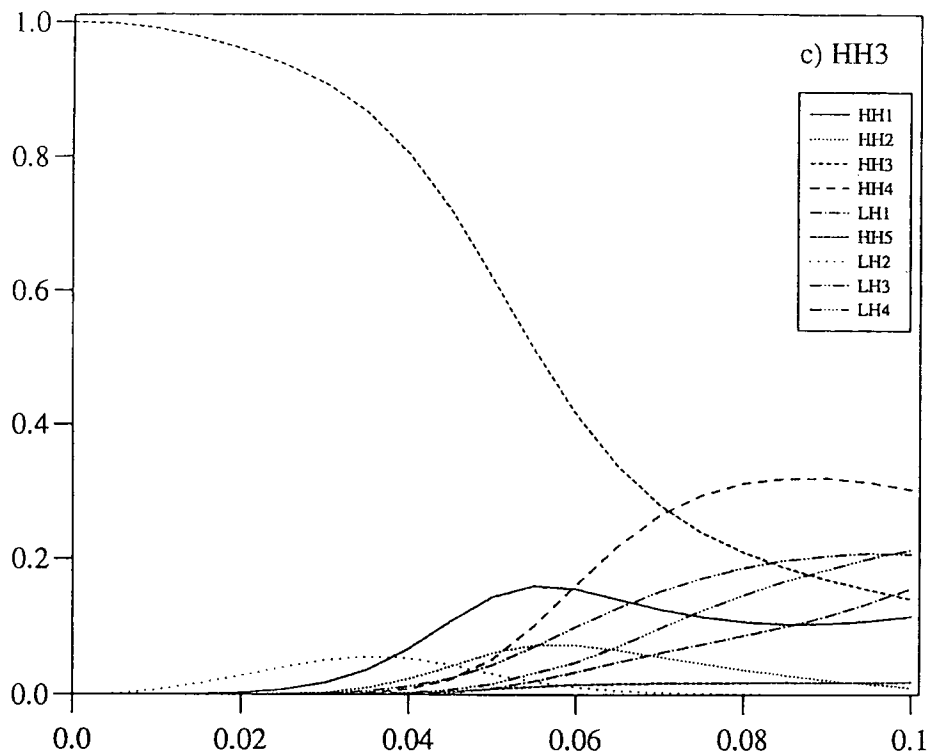
Figures 2.5c, d. The fractional character of the HH3 and HH4 subbands for the 100 Å $In_{0.25}Ga_{0.75}As$-AlGaAs quantum well of figure 2.4d as a function of $k_{\parallel}$.

HH3 zone centre states should not mix. However, the mixing with LH2, LH3 and LH4 states is such that there will be a small fraction of HH3 and LH1 character for states on both these subbands past the crossing point. States on the LH1 subband are seen to have mainly LH3 and LH4 character at large $k_\parallel$, and states on the HH3 band (which is really the continuation of the LH1 band) are made up mostly of HH4, LH4 and HH5.

Strain does not affect the off-diagonal terms in the k.p Hamiltonian (equation 2.22). It does, however, shift the heavy and light hole subband edges relative to each other and in this way can have a strong effect on the exchange of character between bands. Figures 2.4a..d show the dispersions for a 100Å $In_xGa_{1-x}As$-AlGaAs well of infinite depth as a function of increasing indium content x. The addition of indium causes compressive biaxial strain ($\varsigma > 0$) proportional to x in the plane of the quantum well because InAs has a larger lattice constant than GaAs and AlAs, which have very similar constants. The heavy hole states are lifted with respect to the mean valence band energy, while the light hole states are depressed. The curvature of the subbands also becomes greater with x, producing a reduction in the in-plane effective mass for holes.

Figures 2.5a and 2.5b show the character of states on the uppermost HH1 and HH2 valence subbands for the 100Å $In_{0.25}Ga_{0.75}As$-AlGaAs quantum well of figure 2.4d, as a function of $k_\parallel$. Comparing these with the mixing profiles of the 100Å unstrained GaAs-AlGaAs well (figures 2.3a, b) the effect of the compressive strain is to reduce the mixing between the HH1 and HH2 subbands. As a consequence of less mixing, these subbands become more parabolic about

28

the zone centre. Up to $k_\parallel \sim 0.04 \text{Å}^{-1}$, both subbands retain at least 80% of their zone centre character. The HH1 and HH2 subbands become mixed because of their mutual interaction with the LH1 state. Since the strain separates the heavy and light hole states, the magnitude of the off-diagonal elements of the k.p Hamiltonian are reduced with respect to the diagonal elements; in effect the heavy and light hole bands become detached from each other with increased strain, so reduced mixing is to be expected.

Similarly, figures 2.5c and 2.5d showing the character of the HH3 and HH4 subbands indicate little mixing with neighbouring bands up to $k_\parallel \sim 0.05 \text{Å}^{-1}$. However, for $k_\parallel > 0.05 \text{Å}^{-1}$ the HH3 and HH4 subbands anticross and the mixing is strong, the states on the HH3 bands being mostly HH4 ($\sim 30\%$), LH3 ($\sim 20\%$) and LH4 ($\sim 20\%$) character. States on the HH4 subband retain $\sim 20\%$ of the HH4 character, but have $\sim 20\%$ LH4 and also $\sim 30\%$ HH5 character mixed in by interacting with the LH4 band.

For a quantum well under biaxial tension ($\varsigma < 0$), the light hole states are raised in energy whereas the heavy hole states are lowered in energy. Figures 2.6a..d depict the dispersions for four 100Å $\text{GaAs}_y\text{Sb}_{1-y}$-AlSb infinite wells. Increasing the arsenic fraction increases the lattice mismatch between the well and barrier layers and increases the biaxial tension. With increased strain, the uppermost valence subband is LH1, but the mixing with the HH1 and HH2 subbands is such that holes occupying the LH1 band may exhibit an electron-like effective mass in the vicinity of the zone centre, as shown in figures 2.6b and 2.6c. For higher strain still, the separation of the heavy and light hole states reduces the
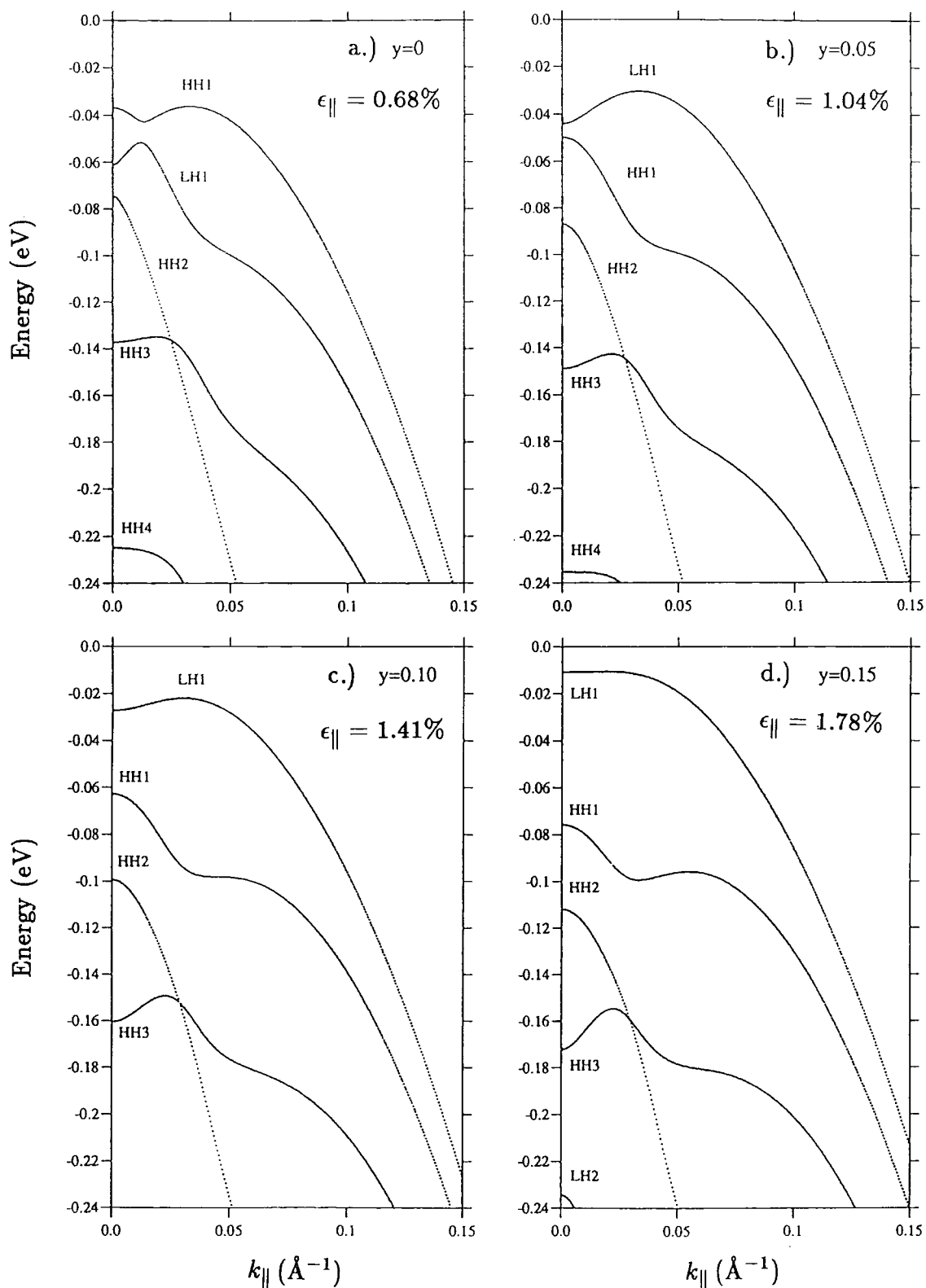
Figures 2.6a..d. In-plane energy dispersions for the highest valence subbands of a 100 Å GaAs$_y$Sb$_{1-y}$-AlSb quantum well as a function of increased arsenic content y and therefore increased biaxial tension $\epsilon_{||}$.
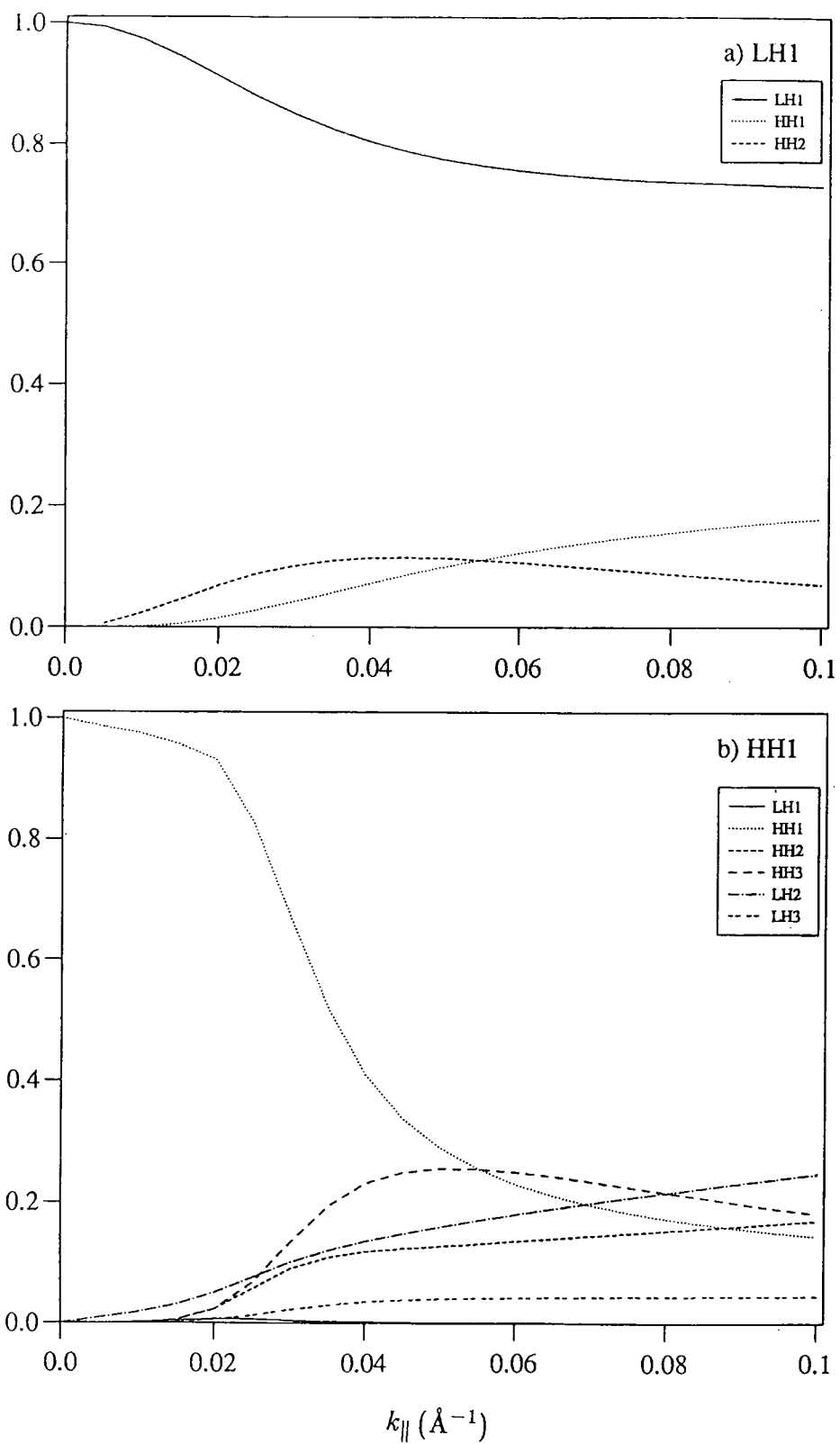
Figures 2.7a, b. The fractional character of the two highest valence subbands for the 100 Å $GaAs_{0.15}Sb_{0.85}$-AlSb quantum well of figure 2.6d as a function of $k_{\parallel}$.
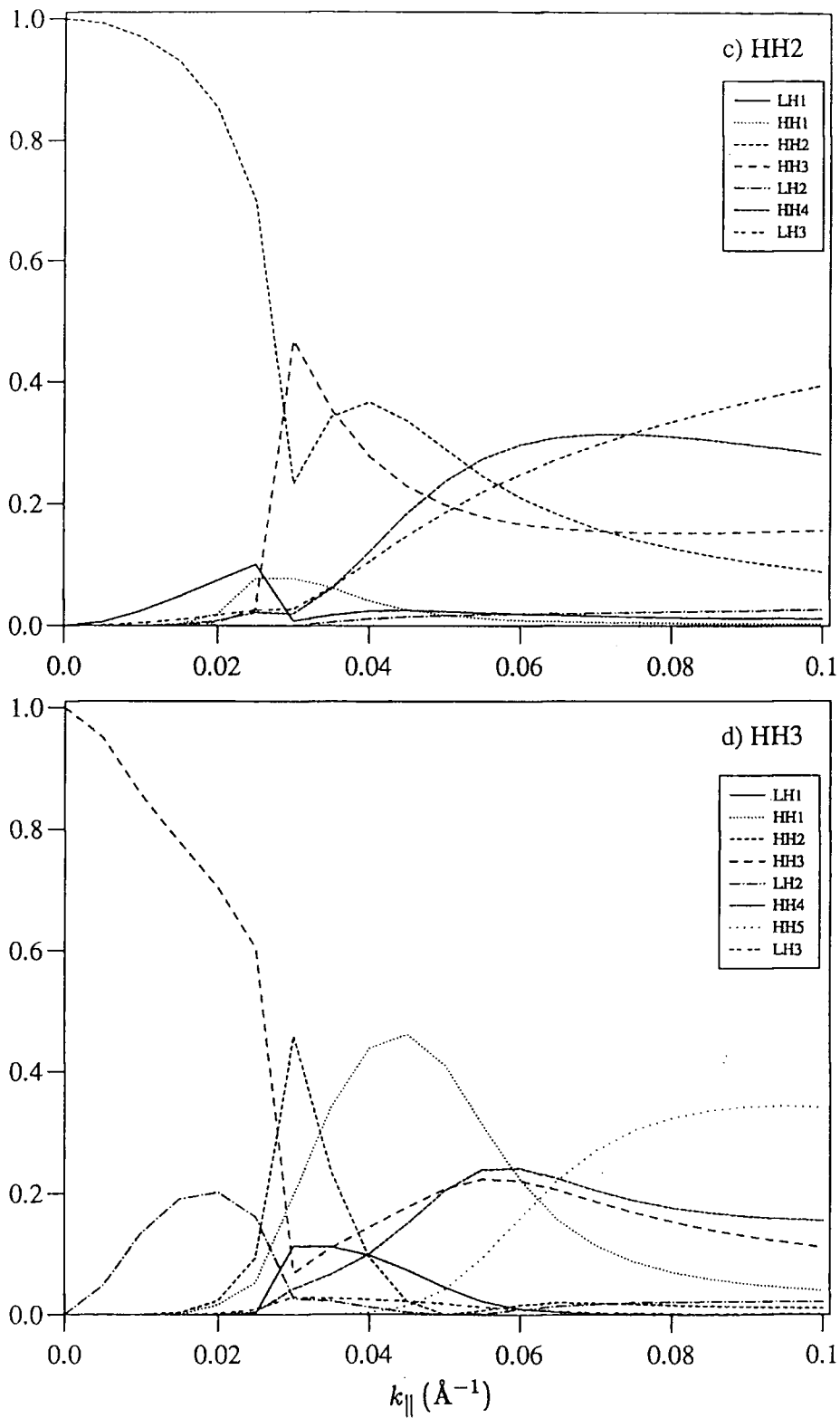
Figures 2.7c, d. The fractional character of the third and fourth highest subbands for the 100 Å GaAs$_{0.15}$Sb$_{0.85}$-AlSb quantum well of figure 2.6d as a function of $k_{\parallel}$. The discontinuity at $k_{\parallel} \sim 0.05$ Å^{-1} is due to crossing between the HH2 and HH3 subbands.

mixing between them, and the LH1 states possess a positive hole mass (figure 2.6d). Figures 2.7a and 2.7b show the fractional character of states on the LH1 and HH1 subbands for the 100Å $GaAs_{0.15}Sb_{0.85}$-AlSb well of figure 2.6d. There is noticeably less mixing between the uppermost LH1 band and heavy hole zone centre states. States on the LH1 band retain at least 70% LH1 character, with a small fraction of HH1 ($\sim$ 10%) and HH2 ($\sim$ 20%) and negligible contribution from higher order interactions. In figure 2.6b, states on the HH1 subband are more strongly mixed with HH2 and HH3 states, through interactions with the LH2 and LH3 states in particular. It is observed that the HH1 band loses much of its zone centre character at $k_{\parallel} \sim 0.03Å^{-1}$, where it undergoes anticrossing with the HH2 subband (marked by the sudden nonparabolicity of the HH1 band in figure 2.7b). By $k_{\parallel} \sim 0.1Å^{-1}$, the HH1 has mostly LH2 character ($\sim$ 30%), with approximately equal fractions of HH1, HH2 and HH3 ($\sim$ 20%).

Figures 2.7c and 2.7d show the mixing profiles for the HH2 and HH3 subbands of figure 2.6d. The interactions with the LH2 and LH3 states dominate, so considerable fractions ($>$ 15%) of HH3, HH4 and HH5 character are mixed into both bands. At $k_{\parallel} \sim 0.1Å^{-1}$, states on the HH2 subband have mostly LH3 and HH4 character ($\sim$ 30%), and those on HH3, mostly HH5 character ($\sim$ 40%), due to the interaction between the HH3 and LH2 zone centre states.

2.5 Conclusion

A four-band $\mathbf{k}.\mathbf{p}$ valence bandstructure calculation for a quantum well has been described in this chapter. This accounts for mixing between the heavy and light hole states. Since an infinite square well potential has been assumed, the model is expected to be reliable only for the wider band-gap systems with a large valence band offset. This model may therefore be applied to GaAs-AlGaAs and related systems, but is clearly not suitable for InGaAs-GaAs and InGaAs-InGaAsP for example, where the valence band offset is typically less than 100meV deep (using data from [18]). The principle advantages of this method over the larger scale $\mathbf{k}.\mathbf{p}$ [23] or pseudopotential [24] methods are in the computational speed and the relative simplicity of the input and output for the calculation. There is a need for only a small amount of input data, and the bandstructure solver is fast since the eigenvalue equation is just a 4×4 matrix, instead of 16×16 for an eight band $\mathbf{k}.\mathbf{p}$ model for instance. In addition, the hole wavefunctions are constructed from a small number of envelopes since the reduced sets of upper or lower block basis Bloch functions contain just two elements. This greatly simplifies the calculation of matrix elements between states. For these three reasons, the method is appropriate for the investigation of the physical influences on hole transport as quantum well parameters are varied. This approach has been used to calculate the intra- and inter- valence subband scattering matrix elements for compressive strained InGaAs-AlGaAs quantum wells, which are the basis of transport simulations as discussed in chapter 3.

The effect of biaxial strain upon the valence bandstructure has been discussed

both qualitatively and quantitatively for the cases of compression (100Å InGaAs-AlGaAs) and tension 100Å (GaAsSb-AlSb), by comparing the mixing between the uppermost subbands of these strained-layer systems with that for an un-strained 100Å GaAs-AlGaAs quantum well. From these calculations, simple rules have been obtained for identifying the mixing properties between sub-bands. The more parabolic a particular subband, then the more detached it is from neighbouring states, and the lower the degree of mixing with them. If a subband is highly non-parabolic, then the mixing is strong, and table 2.4 listing the selection rules for mixing between heavy and light hole states identifies which interactions are dominant.

References

[1] Osbourn G C 1986 *IEEE Journ. Quantum Elec.* 22 1677

[2] Kohn W and Luttinger J M 1954 *Physical Rev.* 96 529

[3] Luttinger J M and Kohn W 1955 *Physical Rev.* 97 869

[4] Luttinger J M 1956 *Physical Rev.* 102 1030

[5] Kane E O 1956 *Journ. Phys. Chem. Solids* 1 82

[6] Kane E O 1956 *Journ. Phys. Chem. Solids* 1 249

[7] Kane E O 1982 *Handbook of Semicond.* 1 193

[8] Dresselhaus G, Kip A F and Kittel C 1955 *Physical Rev.* 98 368

[9] Broido D A and Sham L J 1985 *Phys. Rev. B* 31 888

[10] Ahn D and Chuang S L 1990 *IEEE Journ. Quantum. Elec.* 26 13

[11] Eppenga R, Shuurmans M F H and Colak S
    1987 *Phys Rev. B* 36 1554

[12] Ahn D and Chuang S L 1988 *IEEE Journ. Quantum. Elec.* 24 2400

[13] Chuang S L 1991 *Phys. Rev. B* 43 9649

[14] Altarelli M and Ekenberg U 1985 *Phys. Rev. B* 32 5138

[15] Twardowski A and Hermann C 1987 *Phys. Rev. B* 35 8144

[16] Kittel C 1963 *Quantum Theory of Solids*, Wiley

[17] O'Reilly E P 1989 *Semicond. Sci. Technol.* 4 121

[18] Landolt-Börnstein Neue Serie 1982 *Physics of Group IV Elements
    and III − V Compounds*, Springer-Verlag

[19] Pikus G E and Bir G L 1960 *Sov. Phys. (Solid State)* 1 1502

[20] Suzuki K and Hensel J C 1974 *Phys. Rev. B* 9 4184

[21] O'Reilly E P 1986 *Semicond. Sci. Technol.* 1 128

[22] O'Reilly E P and Witchlow G P 1986 *Phys. Rev. B* 34 6030

[23] Chelikowsy J R and Cohen M L 1976 *Phys. Rev. B* 14 556

[24] Cardona M and Pollak F M 1966 *Phys. Rev.* 142 530

Chapter 3

Scattering Rates For Holes In

InGaAs Quantum Wells

3.1 Introduction

The purpose of this chapter is to present the matrix elements and scattering rates for holes bound in $In_xGa_{1-x}As$-AlGaAs quantum wells of varied geometries and indium concentrations x, using the bandstructure method described in chapter 2. Wells with widths in the range 50-150Å, and strains $\sim$ 0.7-1.8% (that is indium concentrations of 10-25%) have been considered. These data serve as the first part of a study into the in-plane transport properties of holes in quantum wells, and have been incorporated into a Monte Carlo simulation developed by Kelsall [1]. The aim is to predict the effects that compressive strain and spatial confinement have upon the in-plane hole mobility. However, these simulations also serve to test the suitability of the infinite well model for use in a broader range of studies. A brief presentation of details of the simulations is appropriate before describing the scattering rates.

All carrier transport simulations have been carried out at a lattice temperature (T_L) of 77 K, and for low in-plane electric fields < 10^5 Vm^{-1}. Under these conditions, previous simulations had revealed that holes were rarely excited out of the two highest valence subbands [1]. It was therefore sufficient to neglect scattering into other bands, and scattering rates into these bands are not discussed here.

The simulation takes account of alloy and phonon scattering of holes in the quantum well and also charged impurity scattering due to the presence of negatively charged acceptor impurities in the barrier layers. These doped regions serve as supply layers of holes to the quantum well. Three types of phonon scattering are included - acoustic, non-polar optical and polar optical modes; all are treated in the bulk phonon approximation rather than the confined mode scheme [2] (Chamberlain et al have shown that the bulk phonon approximation provides an adequate description of the carrier-phonon coupling in a quantum well [3]). In compound semiconductors the strain associated with the acoustic lattice vibrations produces an additional electric field which acts as an additional scattering potential. The hole-phonon coupling for this so-called piezoelectric scattering is expected to be small at 77 K for InGaAs [4], hence this process has not been included.

The scattering rate expressions for the above processes have been determined by applying Fermi's Golden Rule, and a short description of their derivation is given in section 3.2. The data needed to generate the valence bandstructure for the quantum wells are tabulated in section 3.3. In addition, the scattering matrix elements are described in terms of band mixing effects. A summary of the scattering rates across the range of geometries and strain is given in section 3.4, highlighting those mechanisms which are likely to be most important in the low-field limit.

3.2 Scattering rate formulae

3.2a Alloy scattering

Alloy scattering is an influence on carrier transport in ternary and quaternary semiconductor alloys, and is temperature independent [5, 6]. In the case of $In_xGa_{1-x}As$, this arises from the different electronic potentials which the randomly distributed indium and gallium atoms present to the charge carriers.

By its nature, that is chemical disorder on a microscopic scale, the alloy scattering potential is difficult to probe experimentally. Listed values for both the range and magnitude of the alloy scattering potential are semi-empirical, being chosen to fit carrier mobility data at low temperatures for instance [7].

The scattering potential has frequently been modelled as the difference between the electron affinities of the combined binaries (GaAs and InAs) [5], but the band gap and electronegativity differences have also been used [8, 9]. Basu and Nag [7] have considered the alloy scattering centres to be hard spheres of fixed potential ΔV, where the potential spans a range which is the order of the lattice spacing. (The potential is then some averaged value across its predicted range). A fixed scattering potential across the range of influence is also adopted, but it is assumed that the scattering potential possesses the same symmetry as the lattice site and only exists in the unit cell [9] ($V_{cell} = \frac{a_0^3}{4}$ where a_0 is the interatomic spacing).

The alloy scattering rate is formulated by first considering the matrix element for the interaction with a single scattering centre, and then summing over all available centres in a given volume of the well. According to the Virtual Crys-

tal Approximation [10], the alloy scattering potential may be derived from the difference between the actual and virtual crystal potentials, the virtual potential being the average potential across the indium and gallium sites,

$$< V > = xV_{InAs} + (1 - x)V_{GaAs}. \tag{3.1}$$

V_{InAs} is the potential at an indium site in InGaAs, and V_{GaAs} that for a gallium site. The scattering potentials at indium and gallium sites are respectively,

$$V_s^{In} = V_{InAs} - < V >, \tag{3.2a}$$

$$V_s^{Ga} = V_{GaAs} - < V > . \tag{3.2b}$$

Assuming that the alloy is perfectly random, that is, clustering of the indium and gallium atoms is absent during the growth process, the weighted average of the squares of these individual scattering potentials is

$$< V_s^2 > = x(V_s^{In})^2 + (1 - x)(V_s^{Ga})^2. \tag{3.3}$$

Finally,

$$< V_s^2 > = x(1 - x)(V_{InAs} - V_{GaAs})^2 = x(1 - x)(\Delta V)^2 \tag{3.4}$$

where ΔV is the alloy scattering potential.

After Kelsall and Abram [9], $\Delta V = 0.534$ eV. This result is comparable with figures from Basu et al, who place $\Delta V = 0.529$ eV [11] for $In_{0.5}Ga_{0.5}As$ and also Bastard, who used $\Delta V = 0.6$ eV [12].

Consider intra- or inter- subband elastic scattering from some state $\Psi_{n,k_{||}}$, to a state $\Psi_{n',k'_{||}}$. From first order perturbation theory, the transition rate due to the

interaction with a single scattering centre $V_s(\mathbf{r})$ is:

$$P^{single}_{(n,k_\parallel \to n',k'_\parallel)} = \frac{2\pi}{\hbar} \int \mid \mathrm{m}(k_\parallel, k'_\parallel) \mid^2 \delta(E(k'_\parallel) - E(k_\parallel)) dS_{k'_\parallel}, \qquad (3.5)$$

where $\mathrm{m}(k_\parallel, k'_\parallel)$ is the matrix element between the initial and final states and $dS_{k'_\parallel}$ is the number of final states in an elemental volume of $k_\parallel$ space.

$$\mathrm{m}(k_\parallel, k'_\parallel) = \int_{unit\,cell} \Psi^*_{n',k'_\parallel}(\mathbf{r}_\parallel, z) V_s(\mathbf{r}_\parallel, z_0) \Psi_{n,k_\parallel}(\mathbf{r}_\parallel, z) d\mathbf{r}_\parallel dz. \qquad (3.6)$$

Summing over all scattering centres across unit area of the well A, and its width l, the total scattering rate is

$$P^{AL}_{(n,k_\parallel \to n',k'_\parallel)} = \frac{2\pi}{\hbar} \eta_{In/Ga} \int \int_{-\frac{l}{2}}^{\frac{l}{2}} \mid m \mid^2 dz_0 dS_{k'}. \qquad (3.7)$$

$\eta_{In/Ga}$ is the density of indium/gallium sublattice sites.

In the case of doubly degenerate subbands, the scattering rate from $\Psi_{n,k_\parallel}$ to $\Psi_{n',k'_\parallel}$ is proportional to the average of the four matrix elements connecting both pairs of eigenfunctions. Choosing spin indices 1 and 2 to represent the two eigenfunctions of the initial state, and indices 3 and 4 for the final state, the general form of the total matrix element squared is

$$\mid M \mid^2 = \frac{\mid M_{13} \mid^2 + \mid M_{14} \mid^2 + \mid M_{23} \mid^2 + \mid M_{24} \mid^2}{4}.$$

Since the bands are doubly degenerate, an additional factor of two must be introduced into the density of final states.

In chapter 2 it was chosen to split the **k.p** Hamiltonian into two decoupled upper and lower blocks H^U and H^L, which produce identical subband dispersions. In this scheme, the degenerate eigenfunctions are those determined from each

block, which were named Ψ^U and Ψ^L (equations 2.20a and 2.20b). However, the upper block eigenfunction is defined in terms of Bloch parts which are orthogonal to those appropriate to H^L. Hence, for scattering from a state $\Psi_{n,k_\parallel}$ (with two components $\Psi^U_{n,k_\parallel}$ and $\Psi^L_{n,k_\parallel}$) to $\Psi_{n',k'_\parallel}$ ($\Psi^U_{n',k'_\parallel}$, $\Psi^L_{n',k'_\parallel}$), the matrix elements between $\Psi^U_{n,k_\parallel}$ and $\Psi^L_{n',k'_\parallel}$, also $\Psi^L_{n,k_\parallel}$ and $\Psi^U_{n',k'_\parallel}$ must vanish. Including the factor of two from the density of final states, the total squared matrix element for scattering from $\Psi_{n,k_\parallel}$ to $\Psi_{n',k'_\parallel}$ is

$$| M |^2 = \frac{| M^U |^2 + | M^L |^2}{2},$$

where $| M^U |^2$ and $| M^L |^2$ are the matrix elements between those initial and final wavefunctions derived using H^U and H^L respectively. In fact, it is sufficient to determine the scattering rates using the wavefunctions from *either* the upper *or* lower block, since it is found that $| M^U |^2 = | M^L |^2$.

Choosing the upper block Hamiltonian to describe the initial and final state wavefunctions, these take the form,

$$\Psi_{n,k_\parallel}(\mathbf{r}_\parallel, z) = \frac{1}{\sqrt{A}} \frac{1}{\sqrt{N_I}} \sum_{j=1}^{2} \phi_j(z) e^{i\mathbf{k}_\parallel \cdot \mathbf{r}_\parallel} | j \rangle, \quad \phi_j(z) = \sum_{i=1}^{4} \alpha_{ij} e^{ia_i z}, \qquad (3.8a)$$

$$\Psi_{n',k'_\parallel}(\mathbf{r}_\parallel, z) = \frac{1}{\sqrt{A}} \frac{1}{\sqrt{N_F}} \sum_{j'=1}^{2} \varphi_{j'}(z) e^{i\mathbf{k}_\parallel \cdot \mathbf{r}_\parallel} | j' \rangle, \quad \varphi_{j'}(z) = \sum_{i'=1}^{4} \beta_{i'j'} e^{ib_{i'} z}. \quad (3.8b)$$

The wavefunctions have been normalized such that

$$\int_A \int_{-\frac{l}{2}}^{\frac{l}{2}} | \Psi(\mathbf{r}_\parallel, z) |^2 \, d\mathbf{r}_\parallel dz = 1. \qquad (3.9)$$

N_I, N_F contain the z dependence of the normalization:

$$N_I = \sum_{j=1}^{2} \sum_{i,i'=1}^{4} \alpha^*_{i'j} \alpha_{ij} \begin{cases} l & a_i = a^*_{i'}; \\ \frac{2\sin(a_i - a^*_{i'})\frac{l}{2}}{(a_i - a^*_{i'})} & a_i \neq a^*_{i'}. \end{cases} \qquad (3.10)$$

39

$$N_F = \sum_{j=1}^{2} \sum_{m,m'=1}^{4} \beta_{m'j}^* \beta_{mj} \begin{cases} l & b_m = b_{m'}^*; \\ \dfrac{2\sin(b_m - b_{m'}^*)\frac{l}{2}}{(b_m - b_{m'}^*)} & b_m \neq b_{m'}^*. \end{cases} \qquad (3.11)$$

By choosing the alloy potential to have the symmetry of the primitive unit cell,

$$\int_{cell} v_{j'}(\mathbf{r})^* V_s(\mathbf{r}) v_j(\mathbf{r}) \equiv \langle j' \mid V_s \mid j \rangle = V_s \delta_{jj'}. \qquad (3.12)$$

Applying result (3.12) to the expression for the alloy scattering rate (3.7), after some integration the transition rate due to all scattering centres is

$$P_{(n,k_\parallel \to n',k_\parallel')}^{AL} = \frac{a_0^3 x(1-x)(\Delta V)^2}{4\hbar N_I N_F} \mid M_{AL} \mid^2 \frac{k_\parallel'}{\mid \frac{\partial E}{\partial k_\parallel'} \mid}. \qquad (3.13)$$

$\mid M_{AL} \mid^2$ is the total matrix element arising from the interaction of the envelope functions with the scattering potential, and the last term in (3.13), $k_\parallel' / \mid \frac{\partial E}{\partial k_\parallel'} \mid$ is the reduced density of final states. Specifically,

$$\mid M_{AL} \mid^2 = \sum_{j,j'=1}^{2} \sum_{i,i'=1}^{4} \sum_{m,m'=1}^{4} \beta_{ij}^* \alpha_{i'j} \beta_{mj'} \alpha_{m'j'}^*$$

$$\times \begin{cases} l & a_{i'} + b_m - a_{m'}^* - b_i^* = 0; \\ \dfrac{2\sin(a_{i'} + b_m - a_{m'}^* - b_i^*)\frac{l}{2}}{(a_{i'} + b_m - a_{m'}^* - b_i^*)} & a_{i'} + b_m - a_{m'}^* - b_i^* \neq 0. \end{cases} \qquad (3.14)$$

3.2b Lattice scattering

Acoustic phonon scattering

Intra- and inter-subband transitions by acoustic phonon scattering involve the emission or absorption of longitudinal vibrations with energies of the order $2\hbar v_s k_{\parallel}$ [13], where $k_{\parallel}$ is the in-plane wavevector of the hole (electron) before scattering, and v_s is the average sound velocity through the semiconductor material. Typically this energy is no larger than 1meV, and in the long wavelength phonon limit, acoustic scattering can be assumed to be elastic. Since the valence subbands are isotropic in $k_{\parallel}$-space under the axial approximation, this implies that the initial and final states for intraband scattering are identical, in common with alloy scattering.

Applying Fermi's Golden Rule, the rate for inter- and intra- subband transitions by acoustic (AC) phonon scattering is:

$$P^{AC}_{(n,k_{\parallel}\to n',k'_{\parallel})} = \frac{2\pi}{\hbar} \int \mid \langle k',l' \mid \delta U_{AC} \mid k,l \rangle \mid^2 \delta(E(k',l') - E(k,l))dS_{k',l'}. \quad (3.15)$$

δU_{AC} is the scattering potential for the hole-phonon interaction. The delta function $\delta(E(k',l') - E(k,l))$ represents the conservation of energy in the hole-lattice system, and $dS_{k',l'}$ the incremental density of final states for the hole-lattice system. Since the phonon wavelength is much greater than the lattice spacing, the displacement of the atoms can be represented as a continuous function throughout the crystal. For an atom at some lattice vector r, the displacement may be expressed in terms of the phonon creation (a_q) and annihilation $(a_q^{\dagger})$ operators

[14]. Summing over all possible acoustic modes:

$$u(\mathbf{r}) = \sum_q \sqrt{\frac{\hbar}{2NM\omega_q}} \hat{e}_q (a_q e^{i\mathbf{q}\cdot\mathbf{r}} + a_q^\dagger e^{-i\mathbf{q}\cdot\mathbf{r}}). \qquad (3.16)$$

M is the oscillator mass (the sum of the unit cell atomic masses), $\hat{e}_q$ describes the propagation direction of the lattice vibration with wavevector $\mathbf{q}$. $\hbar\omega_q$ is the phonon energy. The hole-phonon coupling potential is given by the net strain energy associated with the deformation of the lattice:

$$\delta U_{AC} = D_{ac}\nabla u(\mathbf{r}) = iD_{ac} \sum_q \sqrt{\frac{\hbar}{2NM\omega_q}} \hat{e}_q \cdot \mathbf{q} (a_q e^{i\mathbf{q}\cdot\mathbf{r}} - a_q^\dagger e^{-i\mathbf{q}\cdot\mathbf{r}}). \qquad (3.17)$$

The matrix elements for acoustic phonon absorption(ab) and emission(em) are respectively:

$$\langle k', l' \mid \delta U_{AC} \mid k, l \rangle = iD_{ac} \sum_q \sqrt{\frac{\hbar}{2NM\omega_q}} \hat{e}_q \cdot \mathbf{q} \begin{cases} \int \Psi_f^* e^{i\mathbf{q}\cdot\mathbf{r}} \Psi_i \langle l' \mid a_q \mid l \rangle d\mathbf{r} & \text{(ab)}; \\ \int \Psi_f^* e^{-i\mathbf{q}\cdot\mathbf{r}} \Psi_i \langle l' \mid a_q^\dagger \mid l \rangle d\mathbf{r} & \text{(em)}. \end{cases}$$

$$(3.18)$$

Ψ_i and Ψ_f are the initial and final hole eigenfunctions (equations 3.8a, b). Those integrals involving the creation and annihilation operators yield the occupancy of phonon states at wavevector $\mathbf{q}$,

$$\langle l' \mid a_q \mid l \rangle = \sqrt{n_q}, \qquad (3.19a)$$

$$\langle l' \mid a_q^\dagger \mid l \rangle = \sqrt{n_q + 1}, \qquad (3.19b)$$

$$n_q = \frac{1}{e^{\hbar\omega_q/k_B T_L} - 1}.$$

The remaining part of the matrix element of equation 3.18 to be evaluated is the interaction between the hole envelope functions and the acoustic vibrational mode.

This takes the form

$$\int \Psi_f^*(\mathbf{r}) e^{\pm i\mathbf{q}\cdot\mathbf{r}} \Psi_i(\mathbf{r}) d\mathbf{r} = \frac{1}{A\sqrt{N_I N_F}} \int_{-\frac{l}{2}}^{\frac{l}{2}} \left(\sum_{j'=1}^{2} \varphi_{j'}^*(z) \right) e^{\pm i q_z \cdot z} \left(\sum_{j=1}^{2} \phi_j(z) \right) dz$$

$$\times \int_A e^{i(\mathbf{k}_\parallel - \mathbf{k}'_\parallel \pm \mathbf{q}_\parallel)\cdot \mathbf{r}_\parallel} \langle j' \mid j \rangle d\mathbf{r}_\parallel, \tag{3.20}$$

where the $\pm$ represent absorption and emission respectively. Since the Bloch states $\mid j \rangle$ are orthogonal, this reduces to

$$\int \Psi_f^*(\mathbf{r}) e^{\pm i\mathbf{q}\cdot\mathbf{r}} \Psi_i(\mathbf{r}) d\mathbf{r} = \frac{4\pi^2}{A\sqrt{N_I N_F}} \delta(\mathbf{k}_\parallel - \mathbf{k}'_\parallel \pm \mathbf{q}_\parallel) \int_{-\frac{l}{2}}^{\frac{l}{2}} \sum_{j=1}^{2} \varphi_j^*(z) e^{\pm i q_z \cdot z} \phi_j(z) dz. \tag{3.21}$$

The acoustic phonon scattering rate is therefore

$$P_{(n,k_\parallel \rightarrow n',k'_\parallel)}^{AC} = \frac{2\pi D_{ac}^2}{2MN\omega_q N_I N_F} (\hat{\mathbf{e}}_\mathbf{q}\cdot\mathbf{q}_\parallel)^2 \begin{pmatrix} n_q \\ n_q+1 \end{pmatrix} \left(\frac{(2\pi)^2}{A} \delta(\mathbf{k}_\parallel - \mathbf{k}'_\parallel \pm \mathbf{q}_\parallel) \right)^2$$

$$\times \left| \sum_{j=1}^{2} \int_{-\frac{l}{2}}^{\frac{l}{2}} \varphi_j^*(z) e^{\pm i q_z \cdot z} \phi_j(z) dz \right|^2 \delta(E(\mathbf{k}'_\parallel) - E(\mathbf{k}_\parallel)) dS_{k'_\parallel, l''}. \tag{3.22}$$

The delta function $\delta(\mathbf{k}_\parallel - \mathbf{k}'_\parallel \pm \mathbf{q}_\parallel)$ ensures that crystal momentum is conserved in the plane of the quantum well. However, there is no such restriction in the z direction, and so the summation over acoustic phonon modes $\sum_q \mapsto \int_{q_z=-\infty}^{\infty}$. After some integration, using the results

$$\left(\frac{(2\pi)^2}{A} \delta(\mathbf{k}_\parallel - \mathbf{k}'_\parallel \pm \mathbf{q}_\parallel) \right)^2 \equiv \delta_{\mathbf{k}_\parallel \pm \mathbf{q}_\parallel, \mathbf{k}'_\parallel}; \qquad \delta(E(\mathbf{k}'_\parallel) - E(\mathbf{k}_\parallel)) = \frac{\delta(\mathbf{k}_\parallel - \mathbf{k}'_\parallel)}{\mid \frac{\partial E}{\partial k'_\parallel} \mid},$$

the final scattering rate expression is

$$P_{(n,k_\parallel \rightarrow n',k'_\parallel)}^{AC} = \frac{k_B T_L D_{ac}^2}{4\pi\rho\hbar v_s^2 N_I N_F} \frac{k'_\parallel}{\mid \frac{\partial E}{\partial k'_\parallel} \mid} \int_{-\infty}^{\infty} \mid M(q_z) \mid^2 dq_z, \tag{3.23}$$

$$M(q_z) = \sum_{j=1}^{2} \sum_{i,i'=1}^{4} \beta_{i'j}^* \alpha_{ij} \begin{cases} l & a_i - b_{i'}^* \pm q_z = 0; \\ \frac{2\sin(a_i - b_{i'}^* \pm q_z)\frac{l}{2}}{(a_i - b_{i'}^* \pm q_z)} & a_i - b_{i'}^* \pm q_z \neq 0. \end{cases} \tag{3.24}$$

Optical phonon scattering

Both longitudinal (LO) and transverse (TO) optical phonon modes cause deformation potential scattering of holes. The antiphase vibration of oppositely charged ions on the two sublattices creates a local strain field. In addition, the optical phonon modes polarise the ionic charges on neighbouring atoms, creating dipole moments which interact with holes. The deformation potential scattering is referred to as non-polar optical (NPO) scattering, and that due to the charge polarisation is termed polar optical phonon (POP) scattering. The derivation of these are treated in turn, making the simplifying assumption that the LO and TO phonon modes share the same phonon frequency ω_{op} which is independent of the phonon wavevector q.

Non-polar optical phonon scattering

The transition rate for holes by optical deformation potential scattering is:

$$P^{NPO}_{(n,k_{\parallel} \to n',k'_{\parallel})} = \frac{2\pi}{\hbar} \int \mid \langle k',l' \mid \delta U_{NPO} \mid k,l \rangle \mid^2 \delta(E(k',l') - E(k,l))dS_{k',l'}. \quad (3.25)$$

The optical deformation potential δU_{NPO} at some lattice vector r is proportional to the displacement of the centre of mass of the unit cell;

$$\delta U_{NPO} = \sqrt{\frac{\overline{M}}{M_1 + M_2}} D_{op} u(\mathbf{r}).$$

D_{op} is the optical deformation constant, $\overline{M}$ the reduced mass of the atoms on the unit cell, and M_1, M_2 the individual masses. Equation 3.25 only differs from the acoustic phonon rate by a multiplying constant. By comparison, the rate

44

reduces to

$$P^{NPO}_{(n,k_\parallel \to n',k'_\parallel)} = \frac{D^2_{op}}{4\pi\rho\omega_{op}N_I N_F} \frac{k'_\parallel}{|\frac{\partial E}{\partial k'_\parallel}|} \begin{pmatrix} n_q \\ n_q + 1 \end{pmatrix} \int_{-\infty}^{\infty} | M(q_z) |^2 dq_z. \qquad (3.26)$$

$M(q_z)$ is given by equation 3.24. In equation 3.26 the phonon density of states cannot be simplified since the phonon energy is now greater than the thermal energy $k_B T_L$.

Polar optical phonon scattering

The electric polarisation per lattice unit cell is given by

$$P(\mathbf{r}) = \frac{e^* u(\mathbf{r})}{V_{cell}} \qquad (3.27)$$

where e^* is the effective charge associated with the dipole [15],

$$(e^*)^2 = \overline{M} V_{cell} \omega_{op}^2 \epsilon_0 \left(\frac{1}{\epsilon_\infty} - \frac{1}{\epsilon_s} \right).$$

The local charge density associated with this polarisation is given by $\rho(\mathbf{r}) = -\nabla.P(\mathbf{r})$. From Poisson's equation, the perturbing potential is

$$\delta U_{POP} = \frac{iee^*}{\epsilon_0 V_{cell}} \sum_q \sqrt{\frac{\hbar}{2NM'\omega_q}} \frac{1}{q} (a_q e^{i\mathbf{q}\cdot\mathbf{r}} - a_q^\dagger e^{-i\mathbf{q}\cdot\mathbf{r}}). \qquad (3.28)$$

It should be noted that in equation 3.28, the potential is distinct from deformation potential scattering, being inversely proportional to the phonon wavevector q. The polar optical phonon transition rate is

$$P^{POP}_{(n,k_\parallel \to n',k'_\parallel)} = \frac{2\pi}{\hbar} \frac{e^2(e^*)^2}{\epsilon_0^2 V_{cell}^2} \frac{\hbar}{2NM'\omega_q} \sum_q \int \frac{| M(q_z) |^2}{q^2} \delta(E(k',l') - E(k,l)) dS_{k',l'},$$

$$(3.29)$$

$$M(q_z) = \int_A \int_{-\frac{l}{2}}^{\frac{l}{2}} \Psi_f^* e^{\pm i\mathbf{q}\cdot\mathbf{r}} \Psi_i \langle l' | \begin{pmatrix} a_q \\ a_q^\dagger \end{pmatrix} | l \rangle d\mathbf{r}_\parallel dz. \qquad (3.30)$$

45

Equation 3.30 condenses to

$$M(q_z) = (2\pi)^2 \frac{\delta(\mathbf{k}_\parallel - \mathbf{k}'_\parallel \pm \mathbf{q}_\parallel)}{A\sqrt{N_I N_F}} \left(\frac{\sqrt{n_q}}{\sqrt{n_q + 1}} \right) \sum_{j=1}^{2} \sum_{i,i'=1}^{4} \beta^*_{i'j} \alpha_{ij}$$

$$\times \begin{cases} l & a_i - b^*_{i'} \pm q_z = 0; \\ \frac{2\sin(a_i - b_{i'} \pm q_z)\frac{l}{2}}{(a_i - b^*_{i'} \pm q_z)} & a_i - b^*_{i'} \pm q_z \neq 0. \end{cases} \qquad (3.31)$$

Again, momentum conservation is imposed in the well plane, but not in the transverse direction. Furthermore, the $1/q^2$ factor introduces an angular dependence into the scattering rate. From the cosine rule, it is implied that

$$q_\parallel^2 = k_\parallel'^2 + k_\parallel^2 - 2k_\parallel k'_\parallel \cos\theta,$$

where θ is the angle between the wavevectors $k_\parallel$ and $k'_\parallel$. Splitting q into its components $\mathbf{q}_\parallel$, q_z and integrating over $\{0 \leq \theta \leq 2\pi\}$, the rate expression is finally

$$P^{POP}_{(n,k_\parallel \rightarrow n',k'_\parallel)} = \frac{e^2 \omega_{op}}{8\pi^2 \epsilon_0 N_I N_F} \left(\frac{1}{\epsilon_\infty} - \frac{1}{\epsilon_s} \right) \left(\frac{n_{op}}{n_{op} + 1} \right) \frac{k'_\parallel}{\mid \frac{\partial E}{\partial k'_\parallel} \mid}$$

$$\times \int_{-\infty}^{\infty} \frac{2\pi \mid M(q_z) \mid^2 dq_z}{\sqrt{q_z^4 + 2(k_\parallel^2 + k_\parallel'^2)q_z^2 + (k_\parallel^2 - k_\parallel'^2)^2}}, \qquad (3.32)$$

where

$$M(q_z) = \sum_{j=1}^{2} \sum_{i,i'=1}^{4} \beta^*_{i'j} \alpha_{ij} \begin{cases} l & a_i - b^*_{i'} \pm q_z = 0; \\ \frac{2\sin(a_i - b_{i'} \pm q_z)\frac{l}{2}}{(a_i - b^*_{i'} \pm q_z)} & a_i - b^*_{i'} \pm q_z \neq 0. \end{cases} \qquad (3.33)$$

and the integral over q_z is convergent when the limits are $\pm\infty$.

3.2c Remote impurity scattering

The final scattering mechanism to be considered is that by remote negatively charged acceptor impurities in the supply layers for the quantum well. However, in the structure that is modelled in chapter 4, undoped spacer layers are present to separate the doped regions from the well in an effort to reduce the scattering. Charged impurity scattering is modelled here in much the same way as the treatment of alloy scattering in section 3.2a; first the transition probability is determined due to a single point charge, and the total rate is then found by integrating over all impurities per unit area of both doped layers.

Under the screened Coulomb interaction, ionised impurities will redistribute the charge density across the width of the quantum well. Using the Stern-Howard method [16], the charged impurity scattering potential is given by the change in the electrical potential in the quantum well due to the induced charge. As a first order approximation, no change is made to the hole eigenfunctions. For a single negative charge at $(\mathbf{r}_\parallel, z) = (0, z_0)$, the induced charge density associated with the change in the local electrical potential $\Delta\phi$ at some point $(\mathbf{r}_\parallel, z)$ in the well is given by

$$\rho_{ind}(\mathbf{r}_\parallel, z) = -2s\epsilon_r\epsilon_0\xi(z)\int \Delta\phi(\mathbf{r}_\parallel, z)\xi(z)dz. \qquad (3.34)$$

$\xi(z)$ is the normalized hole density across the well and s is the screening constant, given by [16] as

$$s = \frac{p_0 e^2}{2\epsilon_r\epsilon_0 k_B T_L} \frac{1}{ln\left(1 + e^{(E_F - E_0)/k_B T_L}\right)\left(1 + e^{(E_0 - E_F)/k_B T_L}\right)}. \qquad (3.35)$$

p_0 is the areal hole density, E_0 the subband edge energy, and E_F the Fermi level.

Poisson's equation describing the change in the potential at $(r_{\parallel}, z)$ is

$$\nabla^2(\Delta\phi(r_{\parallel}, z)) = -\frac{\rho_{ind}(r_{\parallel}, z)}{\epsilon_r\epsilon_0} + \frac{e\delta(r_{\parallel})\delta(z - z_0)}{\epsilon_r\epsilon_0}. \qquad (3.36)$$

Writing $\Delta\phi(r_{\parallel}, z)$ as a Fourier expansion:

$$\Delta\phi(r_{\parallel}, z) = \frac{1}{(2\pi)^3} \int \Delta\phi_q(z)e^{iq\cdot r_{\parallel}}dq, \qquad (3.37)$$

equation 3.36 can be rewritten in terms of the Fourier components. Adopting the assumption made by Hess [17] that $\xi(z)$ can be approximated by a delta function,

$$\left(\frac{\partial^2}{\partial z^2} - q^2\right)\Delta\phi_q = 2s\delta(z)\Delta\phi_q(0) + \frac{e\delta(z - z_0)}{\epsilon_r\epsilon_0}. \qquad (3.38)$$

To solve equation 3.38, the Green's function is constructed for the term $(\partial^2/\partial z^2 - q^2)$. From Arfken [18], this is

$$G(z, z') = \frac{1}{2q}e^{-q|z - z_0|}.$$

From the formal definition of the Green's function $G(z, z')$, the change in each Fourier component of the electrical potential at $(r_{\parallel}, z)$ is:

$$\Delta\phi_q(z) = -\int G(z, z')\left(2s\delta(z')\Delta\phi_q(0) + \frac{e\delta(z' - z_0)}{\epsilon_r\epsilon_0}\right)dz'. \qquad (3.39)$$

From this,

$$\Delta\phi_q(z = 0) = \frac{-ee^{-q|z_0|}}{2\epsilon_r\epsilon_0(s + q)}. \qquad (3.40)$$

Assuming that the perturbation of the potential energy is constant across the well [17], the ionised impurity scattering potential due to a single remote impurity is

$$e\Delta\phi(r_{\parallel}, z) = \frac{-e^2}{8\pi^2\epsilon_r\epsilon_0} \int \frac{e^{-q|z_0|}}{s + q}e^{iq\cdot r_{\parallel}}dq. \qquad (3.41)$$

48

The transition rate for elastic scattering by a single charged acceptor is therefore

$$P^{single}_{(n,k_\parallel \to n',k'_\parallel)} = \frac{2\pi}{\hbar} \int \mid m(k_\parallel, k'_\parallel) \mid^2 \delta(E(k'_\parallel) - E(k_\parallel)) \frac{A}{(2\pi)^2} d\mathbf{k}'_\parallel, \qquad (3.42)$$

$$m(k_\parallel, k'_\parallel) = \frac{-e^2}{8\pi^2 \epsilon_r \epsilon_0} \int_A \int_{-\frac{l}{2}}^{\frac{l}{2}} \frac{1}{\sqrt{N_I N_F}} \left(\sum_{j=1}^{2} \varphi_j^*(z) \phi_j(z) \right) dz$$

$$\times \frac{1}{A} \int e^{i(\mathbf{k}_\parallel - \mathbf{k}'_\parallel + \mathbf{q}) \cdot \mathbf{r}_\parallel} d\mathbf{r}_\parallel \int \frac{e^{-|q||z_0|}}{(s+q)} dq \qquad (3.43)$$

which simplifies to

$$m(k_\parallel, k'_\parallel) = \frac{-e^2}{2\epsilon_r \epsilon_0 A \sqrt{N_I N_F}} \frac{e^{-|\mathbf{k}'_\parallel - \mathbf{k}_\parallel||z_0|}}{\mid \mathbf{k}'_\parallel - \mathbf{k}_\parallel \mid + s} \int_{-\frac{l}{2}}^{\frac{l}{2}} \sum_{j=1}^{2} \varphi_j^*(z) \phi_j(z) dz. \qquad (3.44)$$

For elastic intraband scattering, $\mid \mathbf{k}'_\parallel - \mathbf{k}_\parallel \mid = 2k_\parallel \sin\theta$ where 2θ is the angle between the initial and final in-plane wavevectors. Summing over all impurities in both supply layers, and assuming that scattering due to stray impurities in the well is negligible, the total scattering rate is

$$P^{CIS}_{(n,k_\parallel \to n',k'_\parallel)} = \frac{N_A e^4}{4\hbar \epsilon_r^2 \epsilon_0^2} \frac{k'_\parallel}{\mid \frac{\partial E}{\partial k'_\parallel} \mid} \frac{\mid M \mid^2}{k'_\parallel} \int_0^\pi \frac{(e^{-4k'_\parallel d \sin\theta} - e^{-4k'_\parallel D \sin\theta})}{\sin\theta(s + 2k'_\parallel \sin\theta)^2} d\theta. \qquad (3.45)$$

$d = d_s + \frac{l}{2}$, $D = d_s + d_a + \frac{l}{2}$. d_s is the width of each spacer layer, d_a the width of the doped layers. M is the overlap integral between the initial and final envelope functions:

$$M = \frac{1}{\sqrt{N_I N_F}} \sum_{j=1}^{2} \int_{-\frac{l}{2}}^{\frac{l}{2}} \varphi_j^*(z) \phi_j(z) dz. \qquad (3.46)$$

In the case of intersubband scattering, $\mid \mathbf{k}'_\parallel - \mathbf{k}_\parallel \mid = \sqrt{k_\parallel^2 + k'^2_\parallel - 2k_\parallel k'_\parallel \cos\theta}$ where θ is the angle between the initial and final in-plane wavevectors. The interband scattering rate due to all scattering centres is

$$P^{CIS}_{(n,k_\parallel \to n',k'_\parallel)} = \frac{N_A e^4}{4\hbar \epsilon_r^2 \epsilon_0^2} \frac{k'_\parallel}{\mid \frac{\partial E}{\partial k'_\parallel} \mid} \mid M \mid^2 \int_0^{2\pi} \frac{(e^{-2\Delta k_\parallel d} - e^{-2\Delta k_\parallel D})}{2\Delta k_\parallel (\Delta k_\parallel + s)^2} d\theta, \qquad (3.47)$$

where $\Delta k_\parallel = \mid k_\parallel - k'_\parallel \mid$. The overlap integrals will be unity for intrasubband processes since the initial and final envelopes are identical under the axial approximation for the bandstructure. The overlap between the initial and final wavefunctions for intersubband processes will be smaller, and their magnitudes will reflect the mixing that occurs between the HH1 and HH2 subbands, mostly through their mutual interaction with the LH1 state. In the limit $k_\parallel \rightarrow 0$, the intraband rate is

$$\frac{N_A \pi e^4 d_a}{\hbar \epsilon_r^2 \epsilon_0^2 s^2} \frac{k'_\parallel}{\mid \frac{\partial E}{\partial k'_\parallel} \mid}.$$

Since the intrasubband scattering rate is inversely proportional to the subband curvature $\frac{\partial E}{\partial k_\parallel}$, then charged impurity scattering (CIS) is likely to be important for low energy holes near the subband edge where a band is flattest, but to be less important once carriers are excited away from the zone centre. As a consequence of the exponential decaying terms within the integrand of equation 3.47, intersubband impurity scattering is expected to be negligible, despite any significant overlap between the eigenfunctions on both bands.

3.3a Variation of scattering matrix elements for

wells with increased indium content

Table 3.1 lists the lattice constants and effective mass data needed to generate the valence subband dispersions of five 90Å $In_x Ga_{1-x}As$-AlGaAs infinite wells with indium concentrations in the range 10-25%. An indium fraction of 0.25 lies near the strain limit for dislocation-free epilayers of 90Å width. According to the Matthews-Blakeslee formula [19], a 90Å well should be able to sustain a maximum strain of $\sim 1.8\%$. For each alloy composition, the bulk effective masses are determined by linear interpolation (Vegard's law). The Luttinger parameters and optical phonon energies $(\hbar\omega_{op})$ are listed in table 3.2.

Figures 3.1a..c depict the two highest valence subbands for 90Å $In_x Ga_{1-x}As$ infinite wells with indium fractions x=0.10, 0.18 and 0.25, indicating the manner in which the subbands change as the indium concentration, and hence the strain in the system, is increased. It may be recalled from chapter 2 that in the bulk, biaxial compressive strain splits the degeneracy at the zone centre between the heavy and light hole bands. When holes are confined in a quantum well, the strain in the well acts to deepen the well for heavy holes and reduce it for light holes. In an infinite well, the same effect causes the heavy hole subbands to be raised in energy compared with that for the unstrained system. The important consequence of the strain splitting is a weakening of the interaction between the HH1, HH2 and LH1 zone centre states. Clearly the curvature of both subbands increases, and the bands become more parabolic in the vicinity of $k_\parallel = 0$ with greater indium content. This favours a higher hole mobility for two reasons - the
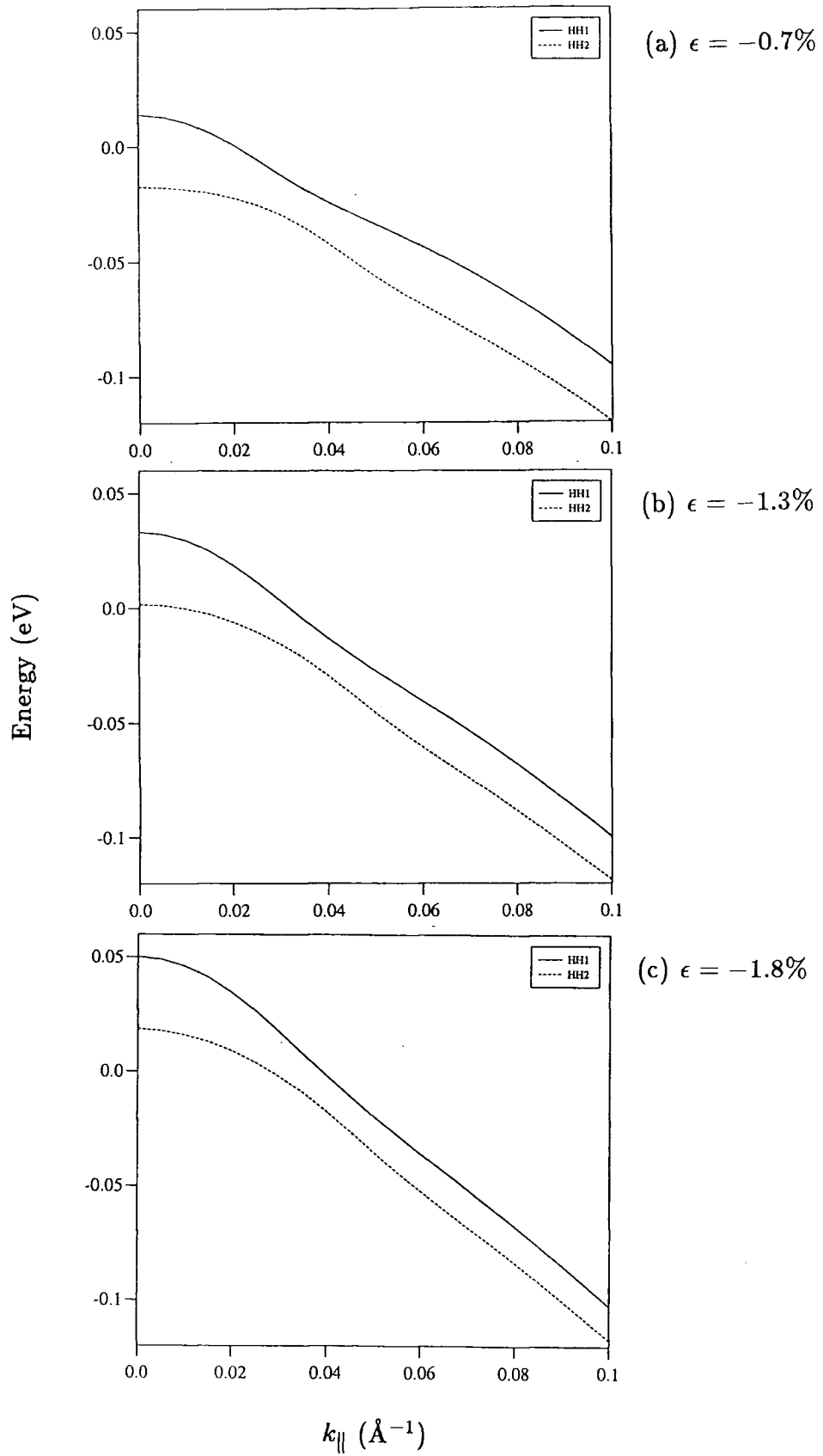
Figure 3.1 In-plane energy dispersions for the first two valence subbands of a 90Å $In_x Ga_{1-x} As$ quantum well: (a) x=0.10, (b) x=0.18, (c) x=0.25.

in-plane effective mass and the density of states are reduced. (The latter implies longer relaxation times between scattering events).

Table 3.1 Material parameters for GaAs, InAs and AlAs at 77 K.

Material	$a_0(\text{Å})$	$b(\text{eV})$	$m_{hh}^{(001)}(m_0)$	$m_{lh}^{(001)}(m_0)$	$m_{hh}^{(111)}(m_0)$	$\bar{\nu}(\text{cm}^{-1})$
GaAs	5.651	-1.7	0.45	0.082	0.57	277
AlAs	5.651	-	-	-	-	-
InAs[†]	6.057	-1.8	0.41	0.024	0.53	228

† The (111) heavy hole mass for InAs is an average of values listed by Adachi [20] and Chuang [21].

Table 3.2 Luttinger parameters, strain factors and optical phonon energies for each of the alloy compositions investigated.

indium content x	γ_{1L}	γ_{2L}	γ_{3L}	$\epsilon_\parallel (\%)$	ς (meV)	$\hbar\omega_{op}$ (meV)
0.10	7.68	2.72	2.96	-0.71	24.4	33.7
0.15	7.95	2.85	3.09	-1.07	36.6	33.4
0.18	8.12	2.93	3.17	-1.27	43.9	33.2
0.20	8.23	2.99	3.23	-1.42	48.7	33.1
0.25	8.54	3.14	3.38	-1.76	60.9	32.8

Table 3.3 Matrix elements plotted in figures 3.3-3.9.

Process	Matrix Element	Reference
Alloy Scattering	$\dfrac{|M_{AL}|^2}{N_I N_F}$	equation 3.13
Acoustic Phonon	$\dfrac{1}{N_I N_F} \int_{-\infty}^{\infty} \| M(q_z) \|^2 \, dq_z$	equation 3.24
Non-Polar Phonon	$\dfrac{1}{N_I N_F} \int_{-\infty}^{\infty} \| M(q_z) \|^2 \, dq_z$	equation 3.24
Polar Phonon	$\dfrac{2\pi}{N_I N_F} \int_{-\infty}^{\infty} \dfrac{|M(q_z)|^2 dq_z}{\sqrt{q_z^4 + 2(k_\parallel^2 + k_\parallel'^2)q_z^2 + (k_\parallel^2 - k_\parallel'^2)^2}}$	equation 3.33
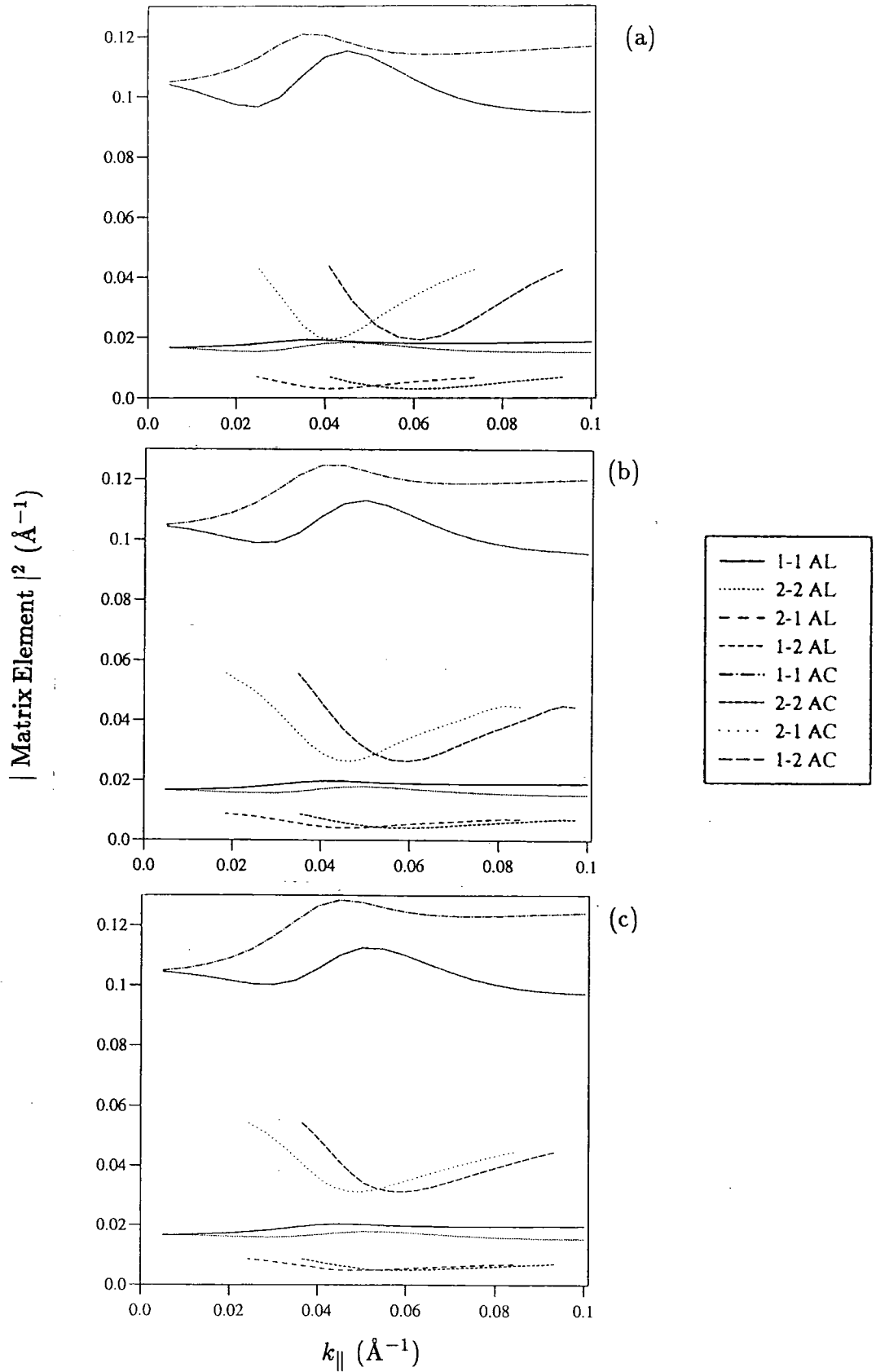
Figure 3.2 Alloy and acoustic phonon scattering matrix elements as a function of in-plane wavevector for the subband dispersions of figure 3.1: (a) x=0.10, (b) x=0.18, (c) x=0.25.
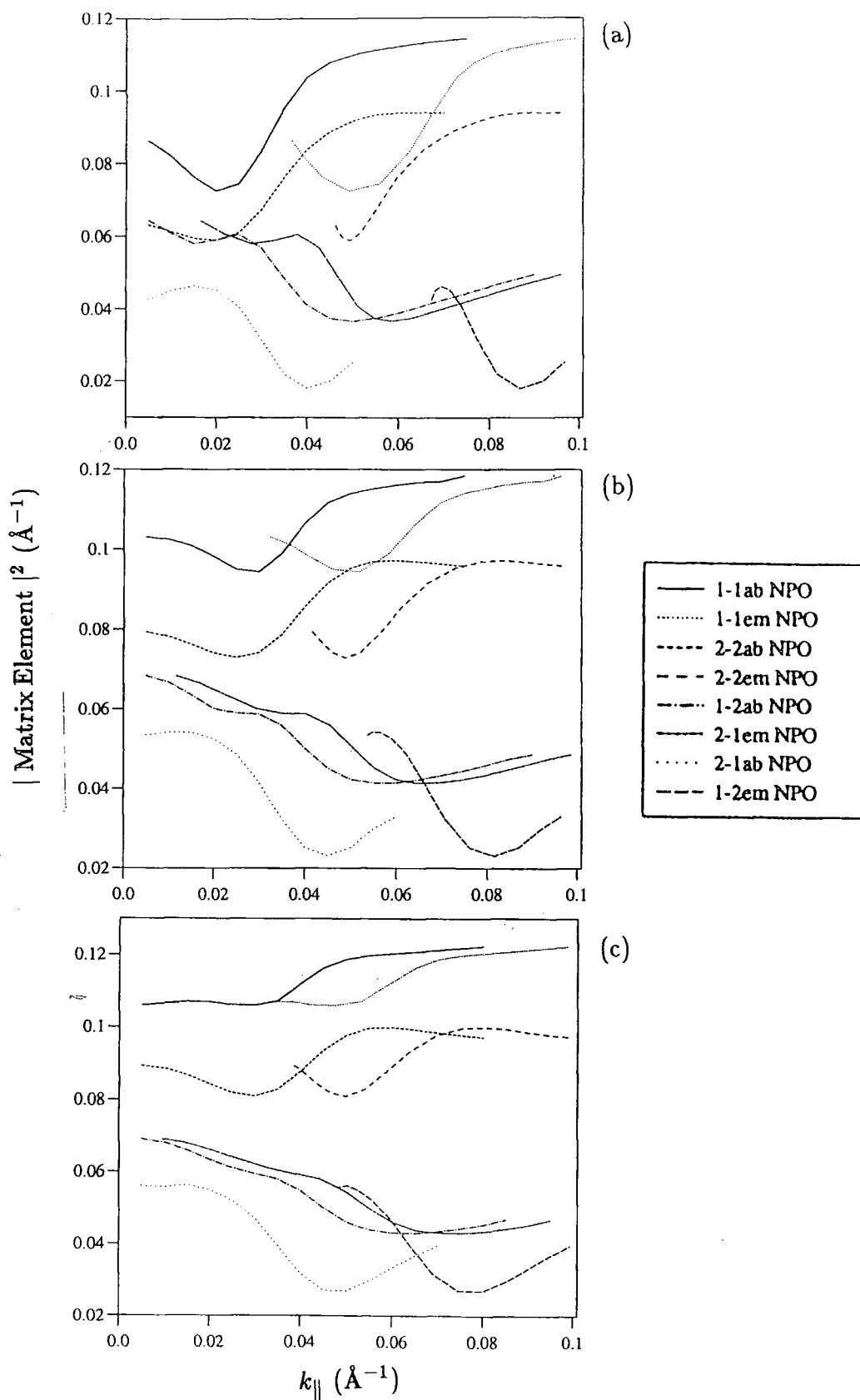
Figure 3.3 Matrix elements for non-polar optical phonon scattering as a function of in-plane wavevector for the subband dispersions of figure 3.1: (a) x=0.10, (b) x=0.18, (c) x=0.25.
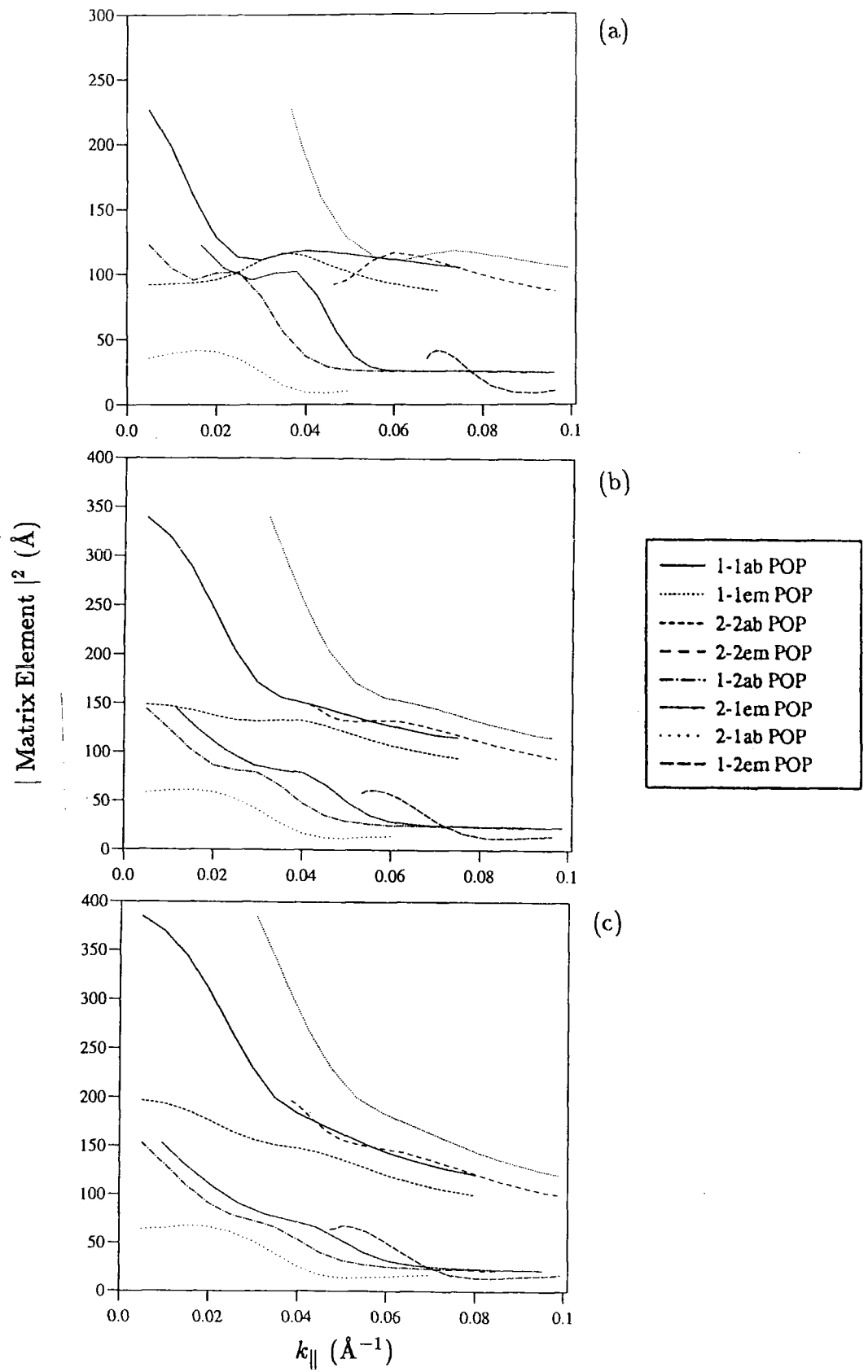
Figure 3.4 Matrix elements for polar optical phonon scattering as a function of in-plane wavevector for the subband dispersions of figure 3.1: (a) x=0.10, (b) x=0.18, (c) x=0.25.
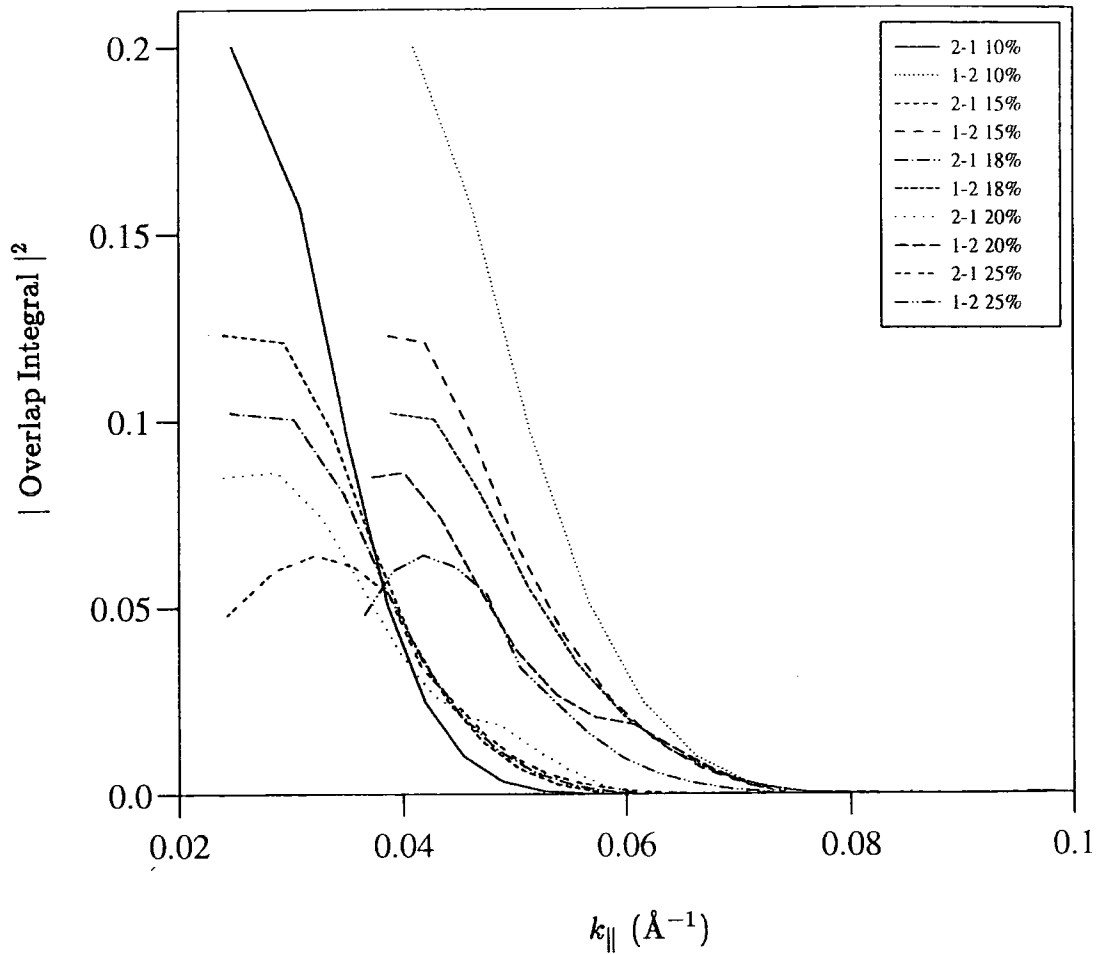
Figure 3.5 Matrix elements for intersubband elastic scattering by remote impurities, as a function of in-plane wavevector for indium contents in the range 10-25%.

Figures 3.2a..c show the alloy and acoustic phonon scattering matrix elements as a function of in-plane wavevector, for the three cases x=0.10, 0.18 and 0.25. The quantities which are plotted are listed in table 3.3. It is apparent that the intra- and inter- subband matrix elements for both processes show similar behaviour as a function of wavevector, and also that there is little change in the magnitude of these matrix elements as a function of strain. In the limit $k_\parallel \to 0$, it is clear that the matrix elements for HH1-HH1 and HH2-HH2 scattering converge to the same value which is independent of the strain, when all three figures are compared. The reason for this is as follows. At $k_\parallel = 0$, the quantum well eigenstates are pure heavy or light hole, and in this limit the matrix elements for acoustic phonon and alloy scattering are respectively $\frac{3\pi}{l}$ [22] and $\frac{3}{2l}$ (at $l =$ 90Å, this gives 0.105Å^{-1} and 0.0167Å^{-1}). At intermediate $k_\parallel \sim 0.05$Å^{-1} the intraband matrix elements oscillate. This is a result of subband mixing. The largest variation occurs in the vicinity of the anticrossing region between the HH1 and HH2 bands, which is no surprise, since this point marks the strongest degree of exchange of character between the HH1 and HH2 subbands. Past the anticrossing, states on both subbands settle to a general mixed character which is largely invariant with $k_\parallel$. Intersubband matrix elements exhibit a minimum for $k_\parallel \sim 0.04 - 0.06$Å^{-1}, where states on the HH1 and HH2 subbands share little heavy or light hole character. In addition, these show a slight increase in magnitude as a function of indium content, and this can be explained by a reduction in the subband mixing with increased strain in the well, and a shift of the anticrossing point to larger $k_\parallel$.

With regard to the behaviour of the optical phonon matrix elements as a func-
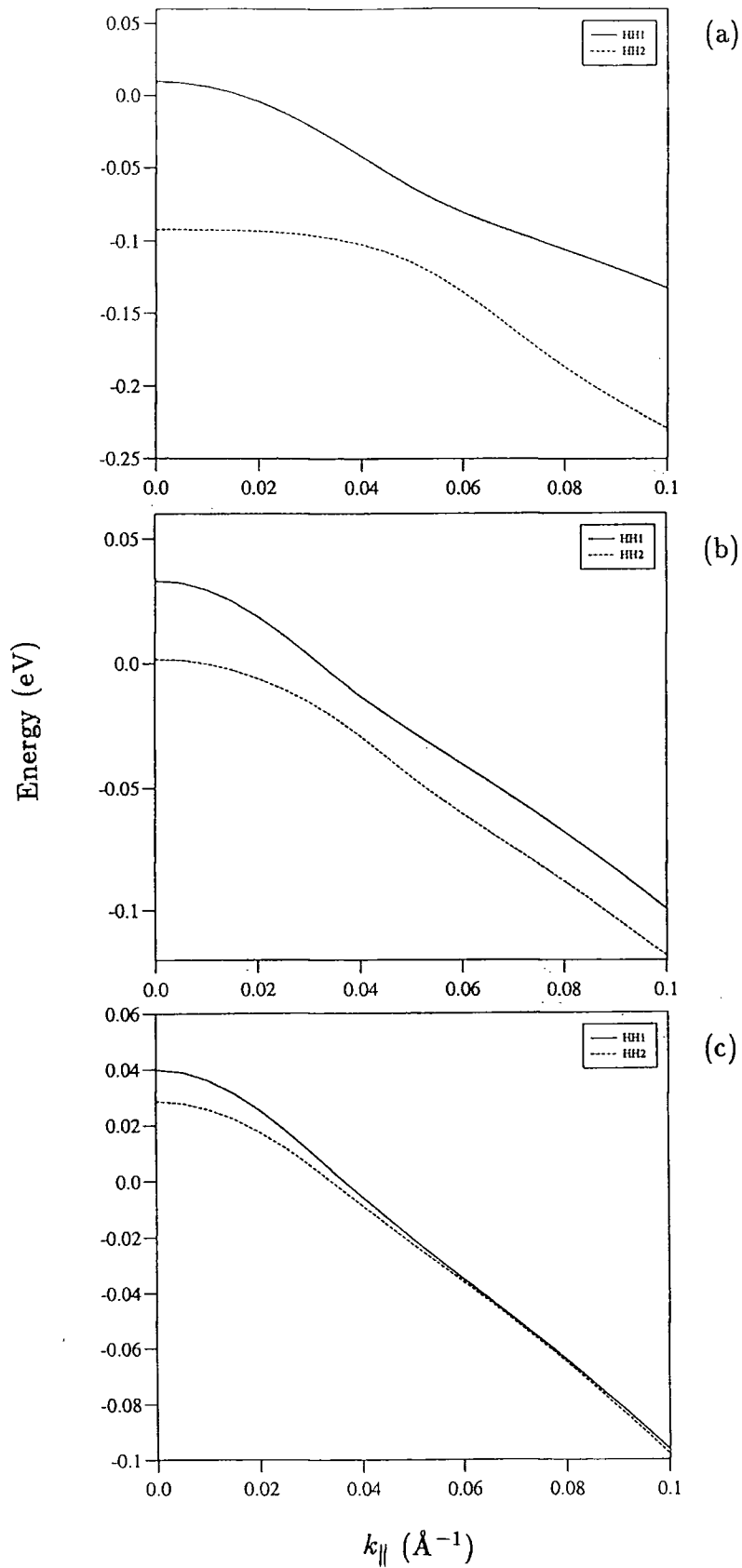
Figure 3.6 In-plane energy dispersions for the first two valence subbands of an $In_{0.18}Ga_{0.82}As$ quantum well: (a) well width=50Å, (b) 90Å, (c) 150Å. The subbands of (c) anticross although this cannot be discerned from the diagram.

tion of indium content, figures 3.3a..c and 3.4a..c show the elements for the non-polar and polar processes, respectively. In both cases, in the vicinity of the zone centre, the intrasubband matrix elements show a general increase with indium content. The increase in the subband curvature is the chief reason for this, on two counts. In the first instance, optical transitions will be made between states which are closer in $k_{\parallel}$ along a given subband, and therefore will generally be similar in character. Secondly, there will be less mixing between the bands until larger wavevector $(k_{\parallel} \sim 0.08\text{Å}^{-1})$ in the higher strain examples. This last factor also explains the flattening of the curves for intrasubband non-polar scattering spanning the range $x = 0.10$ to $x = 0.25$. The intrasubband non-polar matrix elements show an increase with larger $k_{\parallel}$, since at large $k_{\parallel}$ past the anticrossing point, the mixing is complete, and states on a given band adopt a stable, mixed character. This increase is matched by a general decline in the strength of intersubband scattering since the available transitions occur between states on opposite subbands, on the same side of the anticrossing point and, as a rule, these states will have little heavy or light hole nature in common. With regard to figures 3.4a..c, then both intra- and inter- subband polar optical phonon matrix elements decay with increasing in-plane wavevector. This is purely a function of the $1/q_{\parallel}^2$ dependence, as shown by table 3.3.

Figure 3.5 shows the decrease in the magnitude of matrix elements for charged impurity scattering as a function of biaxial strain in the well. The values of these overlap integrals decrease sharply at larger $k_{\parallel}$, and this is expected since the possible transitions will be made between states on the same side of the anticrossing point.
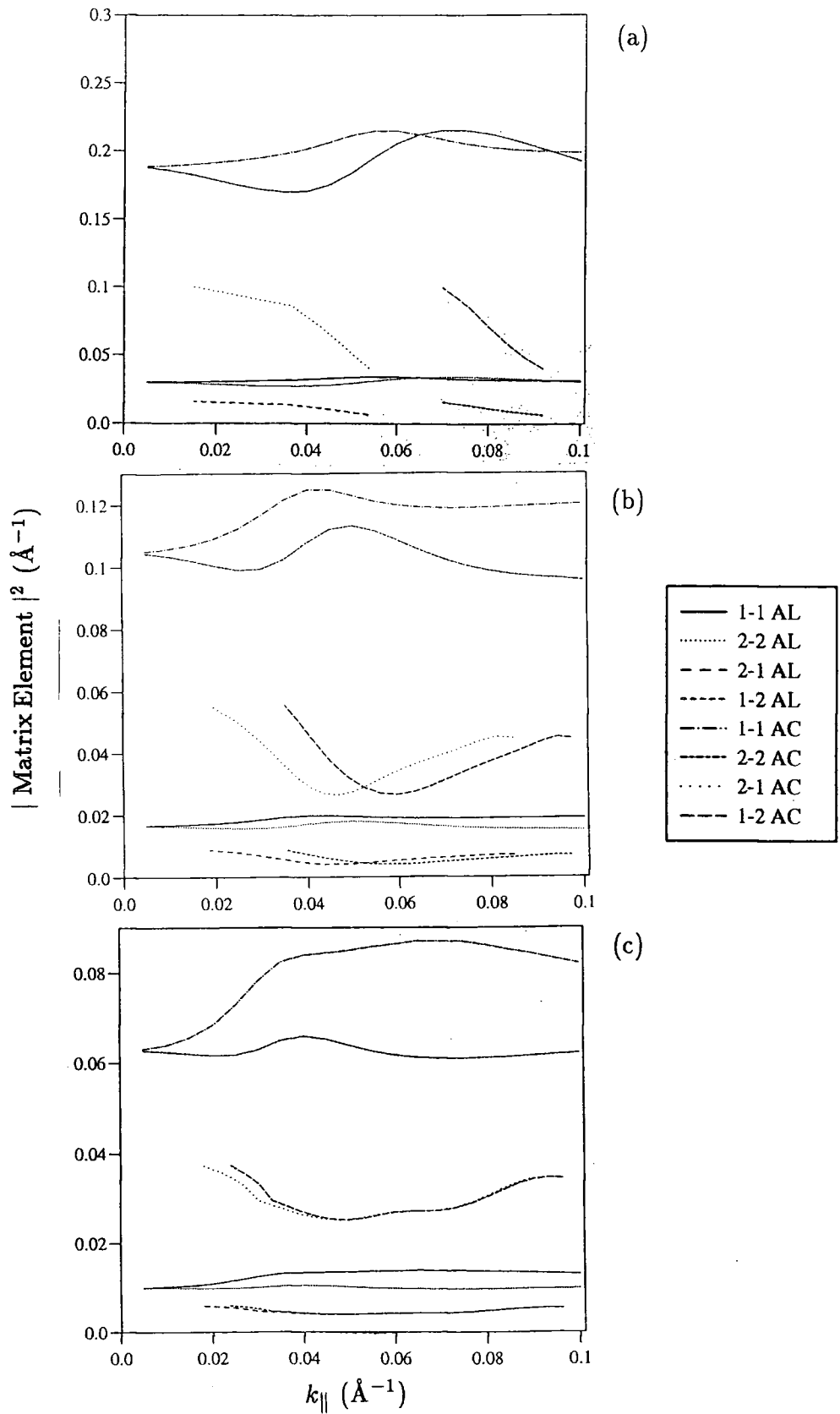
Figure 3.7 Alloy and acoustic phonon scattering matrix elements as a function of in-plane wavevector for the subband dispersions of figure 3.6: (a) well width=50Å, (b) 90Å, (c) 150Å.
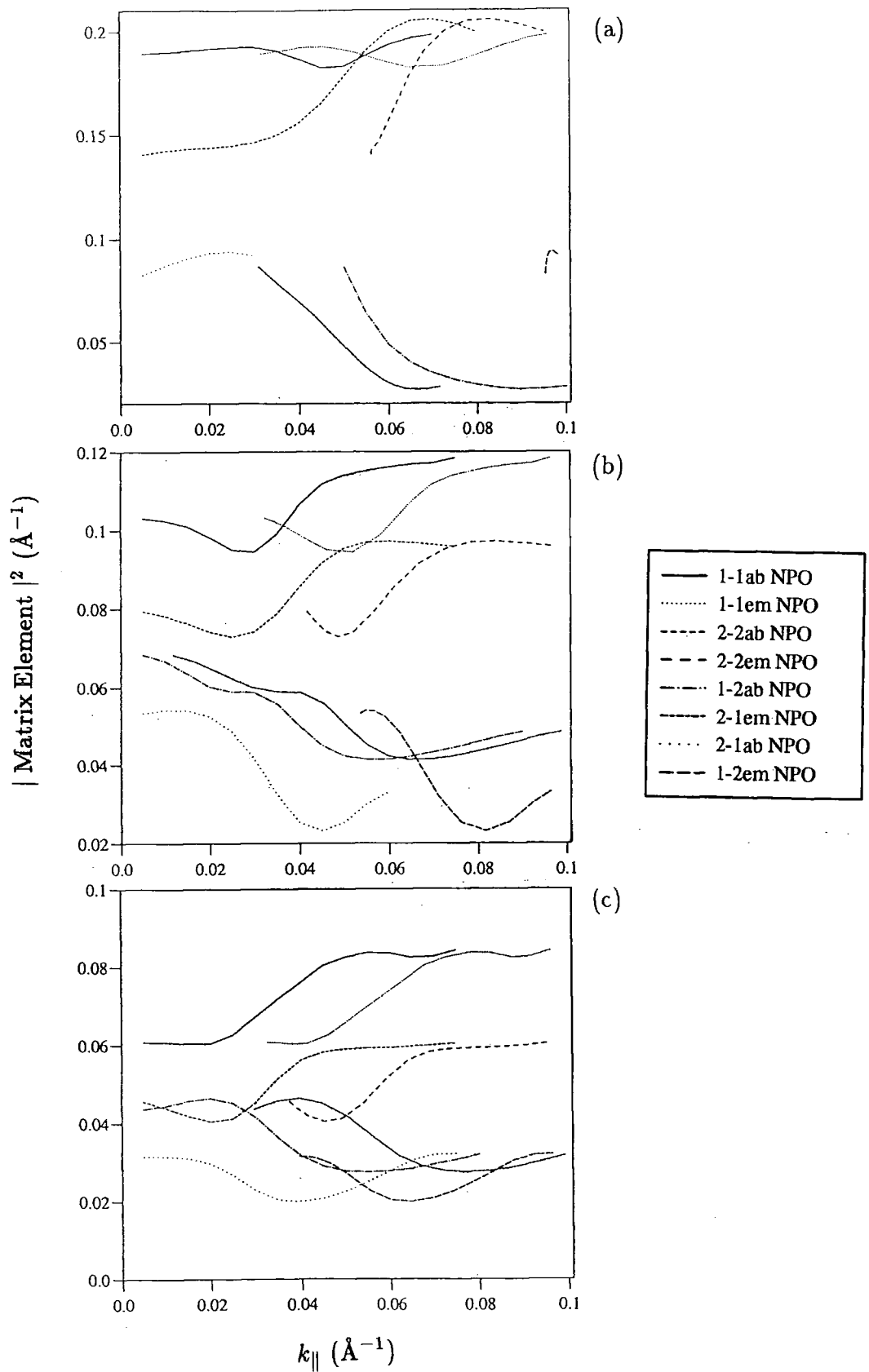
Figure 3.8 Matrix elements for non-polar optical phonon scattering as a function of in-plane wavevector for the subband dispersions of figure 3.6: (a) well width=50Å, (b) 90Å, (c) 150Å.
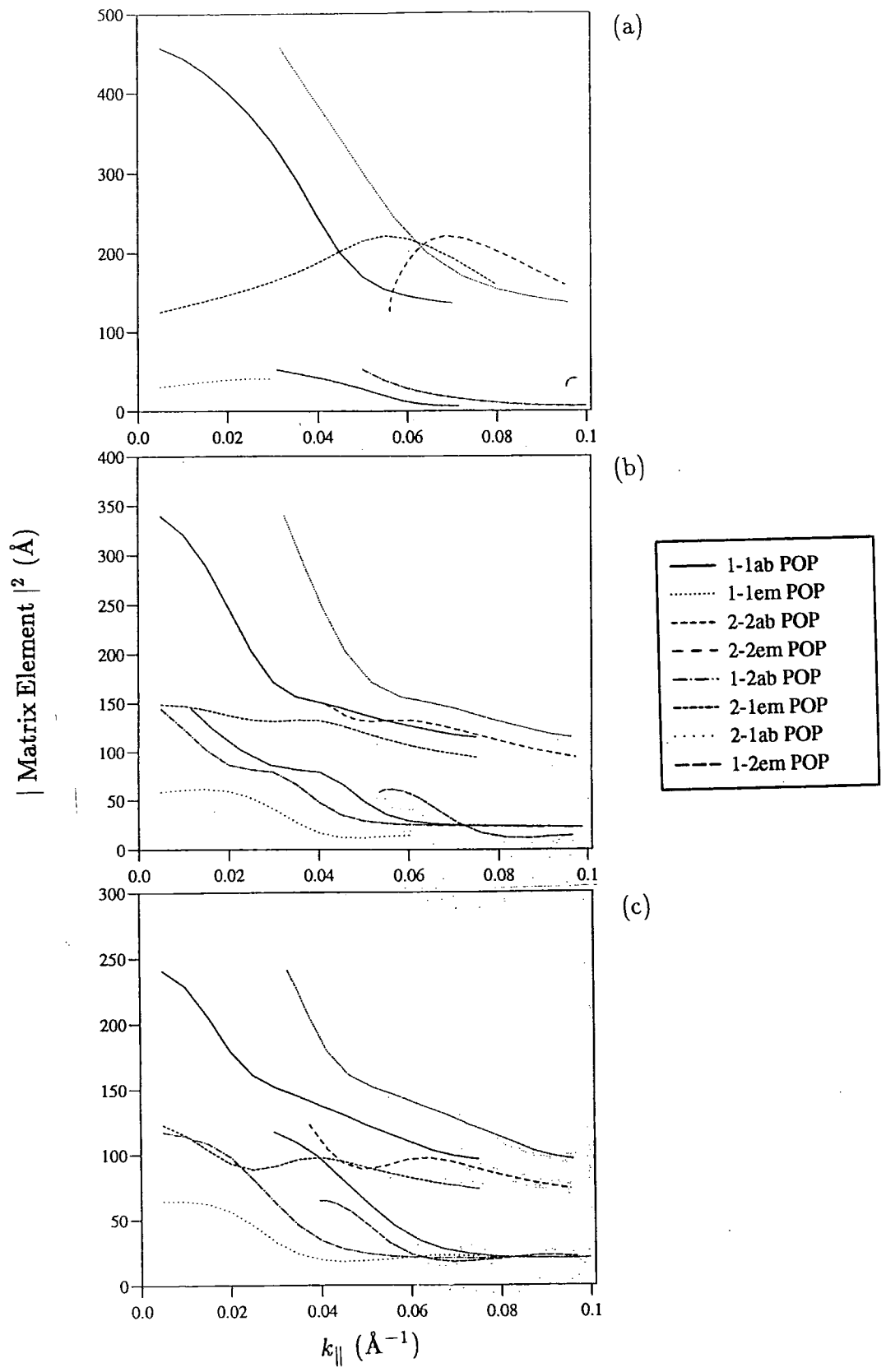
Figure 3.9 Matrix elements for polar optical phonon scattering as a function of in-plane wavevector for the subband dispersions of figure 3.1: (a) well width=50Å, (b) 90Å, (c) 150Å.
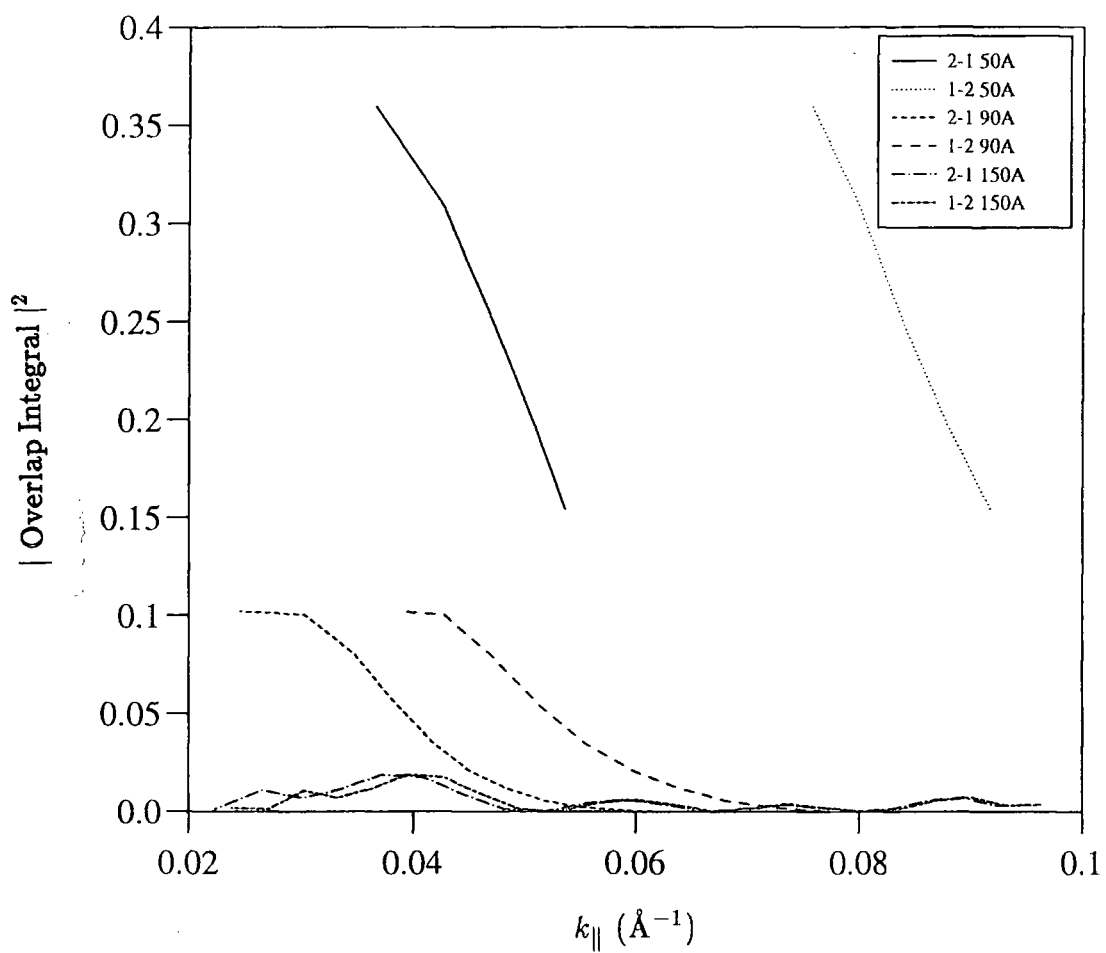
Figure 3.10 Matrix elements for intersubband elastic scattering by remote impurities, as a function of in-plane wavevector for the three wells of figure 3.6.

3.3b Variation of scattering matrix elements with well width

Figures 3.6a..c show the valence subband dispersions for three $In_{0.18}Ga_{0.82}As$ infinite wells of widths 50, 90 and 150Å respectively. The differences between the bandstructures are far greater than the changes resulting from variation of biaxial strain over the range considered. One important property is the subband separation. For the case of the 50Å well, the HH1 and HH2 subband edges are ~ 0.1 eV apart in the infinite well model, but for the 150Å well, the separation is only 10 meV. Also, for the 50Å well, the in-plane effective mass for the HH2 subband is far heavier than that for the HH1 band, whereas in the 150Å example, the subband masses are similar.

The well width dependence of the scattering matrix elements can be thought of as originating in two ways. First, the effect of the localised nature of the envelope functions, which is apparent in the results of Riddoch and Ridley [23] for phonon scattering in a single parabolic subband of an infinite well. The second source of width dependence is subband mixing. A well width dependence is embedded within the interaction Hamiltonian as was seen from equation 2.27; that is the interaction between the HH1 and LH1 zone centre states is simply $\sim k_{\parallel}^2$, but that between the HH2 and LH1 states is of the order $\frac{k_{\parallel}}{l}$.

At the zone centre, it will be recalled that for intraband processes, the alloy and acoustic phonon scattering matrix elements adopt the values $\frac{3}{2l}$ and $\frac{3\pi}{l}$ respectively. Thus, it can be expected that these matrix elements for the 50Å well will be approximately three times the magnitude of those in the 150Å example. Figures 3.7a..c clearly illustrate this. The intersubband matrix elements on the
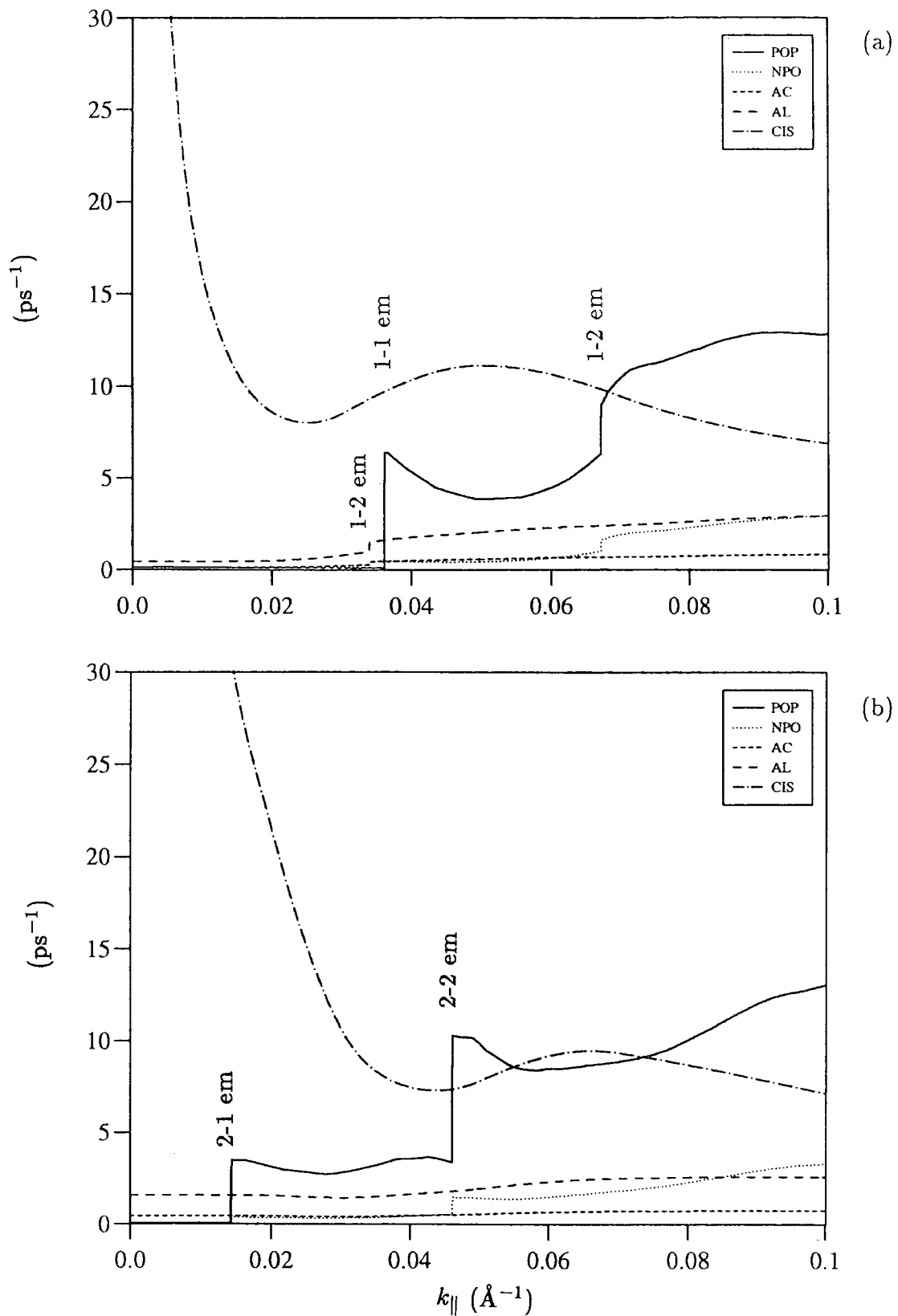
Figure 3.11 Total scattering rates for holes in the HH1 and HH2 subbands of a 90Å $In_{0.10}Ga_{0.90}As$ infinite well as a function of in-plane wavevector: (a) HH1, (b) HH2.
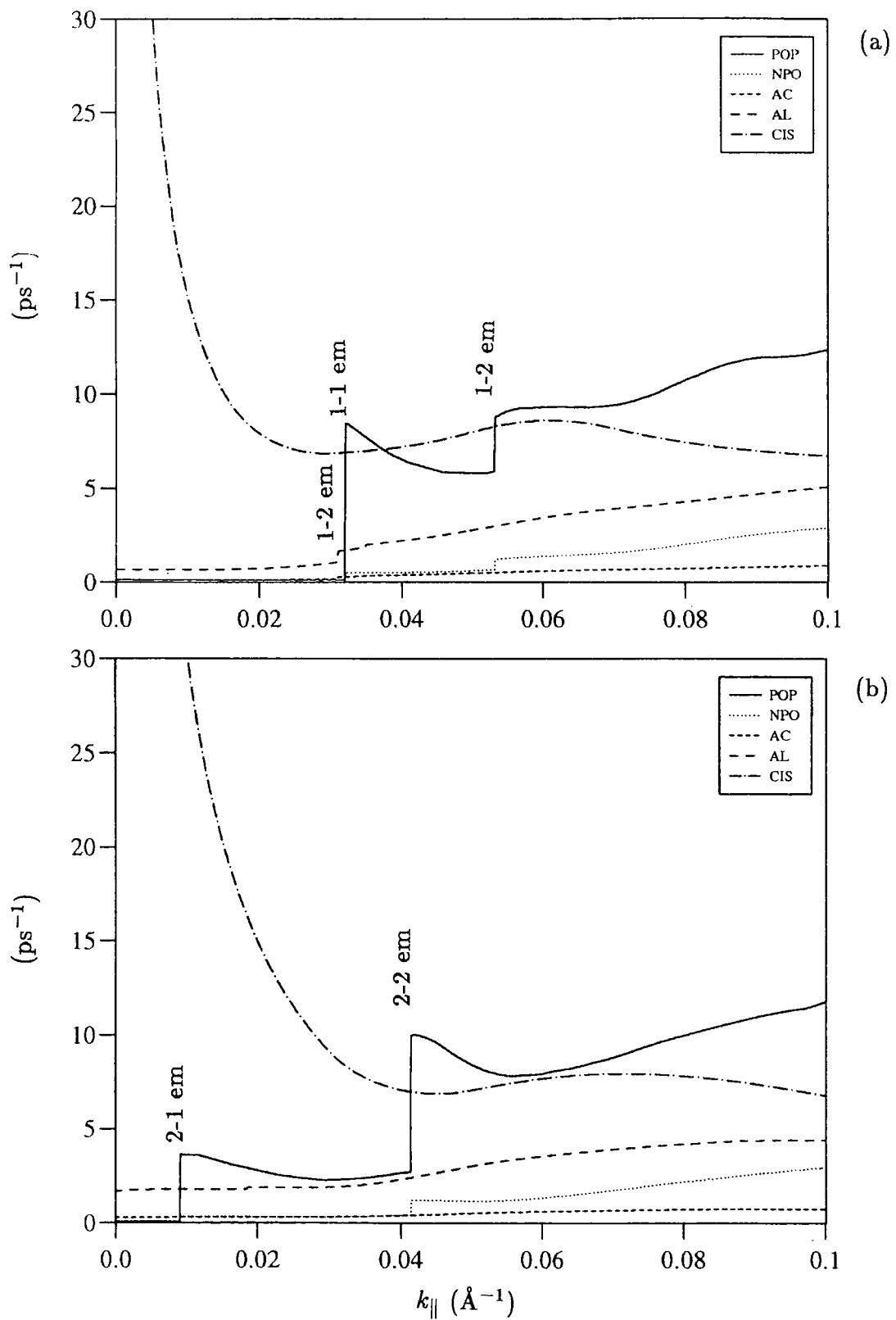
Figure 3.12 Total scattering rates for holes in the HH1 and HH2 subbands of a 90Å $In_{0.18}Ga_{0.82}As$ infinite well as a function of in-plane wavevector: (a) HH1, (b) HH2.
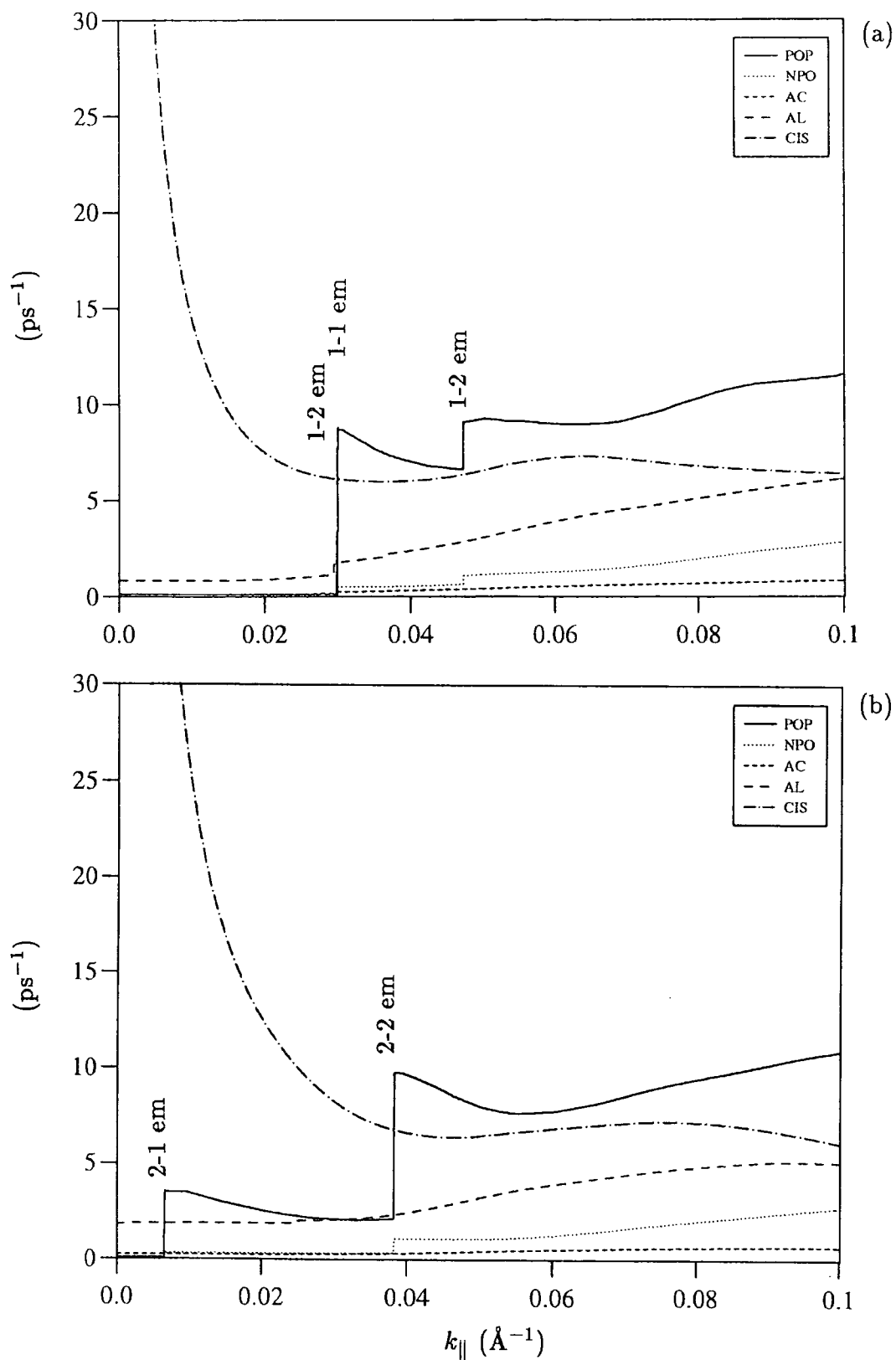
Figure 3.13 Total scattering rates for holes in the HH1 and HH2 subbands of a 90Å $In_{0.25}Ga_{0.75}As$ infinite well as a function of in-plane wavevector: (a) HH1, (b) HH2.

other hand are not expected to show this behaviour, although they do show a general decrease with increasing well width. In the case of narrow wells, the available transitions occur between states lying on opposite sides of the anticrossing point, but for wide wells, both states lie on the same side of the anticrossing. Figures 3.8a..c and 3.9a..c provide a comparison of the non-polar and polar optical matrix elements for the 50 and 150Å wells with the 90Å example shown previously. The overlap integrals for intersubband remote impurity scattering also decrease with increasing well width, as shown in figure 3.10. For these last three processes, this is primarily due to the localised nature of the eigenfunctions.

3.4 Comparison of the hole scattering rates for varied indium content and well width

Figures 3.11a, b..3.13a, b show the scattering rates for the three 90Å wells with indium content 10, 18 and 25%. Necessary data for the rate prefactors are listed in table 3.4. In all three examples, for small $k_\parallel$, intraband remote impurity scattering dominates since it is proportional to $k_\parallel / \frac{\partial E}{\partial k_\parallel} \times \frac{1}{k_\parallel}$. As $k_\parallel$ increases, impurity scattering decreases as the inverse of the subband curvature. Intersubband scattering is negligible in all cases, since the integral over θ in equation 3.47 is small.
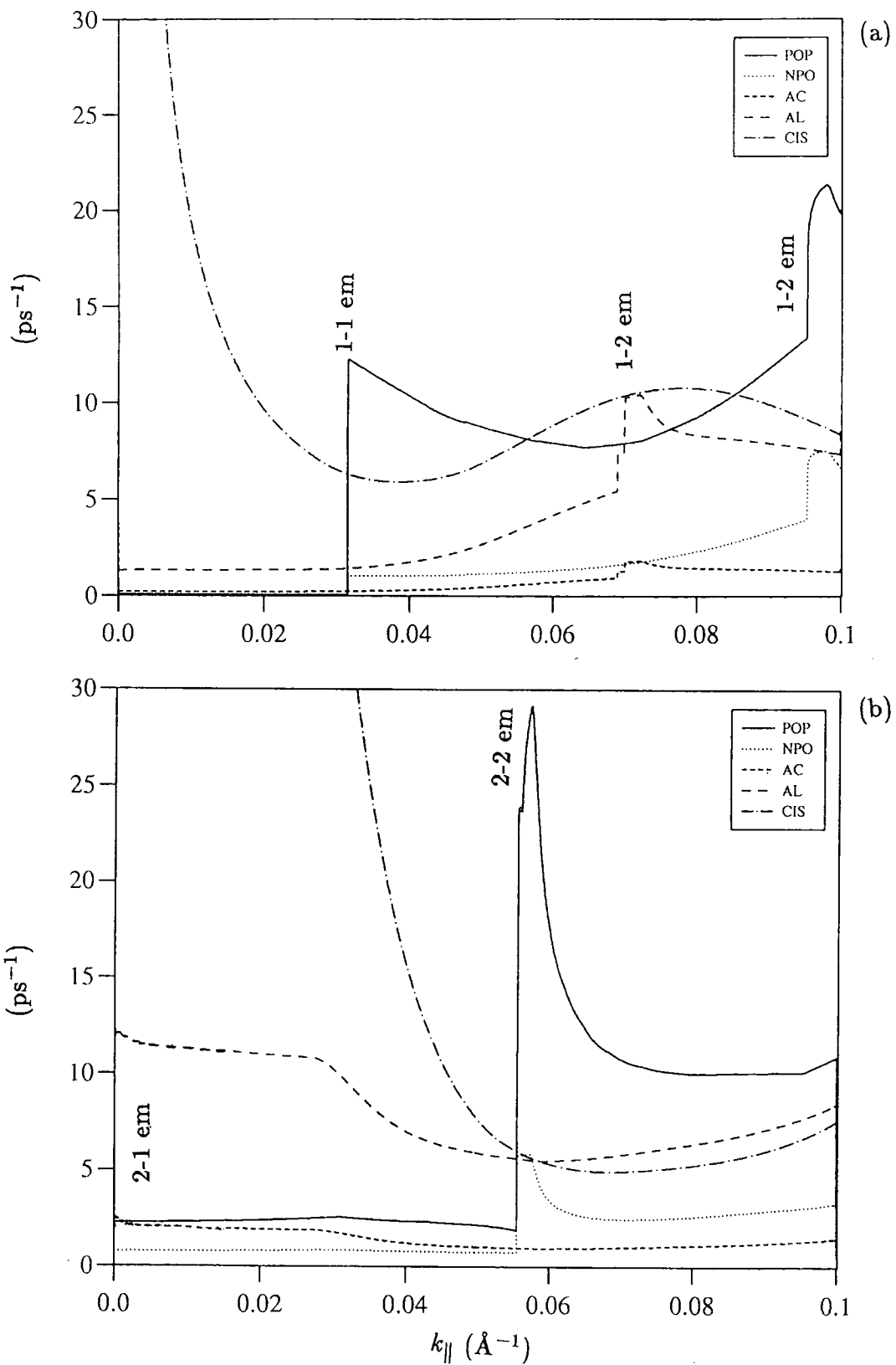
Figure 3.14 Total scattering rates for holes in the HH1 and HH2 subbands of a 50Å $In_{0.18}Ga_{0.82}As$ infinite well as a function of in-plane wavevector: (a) HH1, (b) HH2.
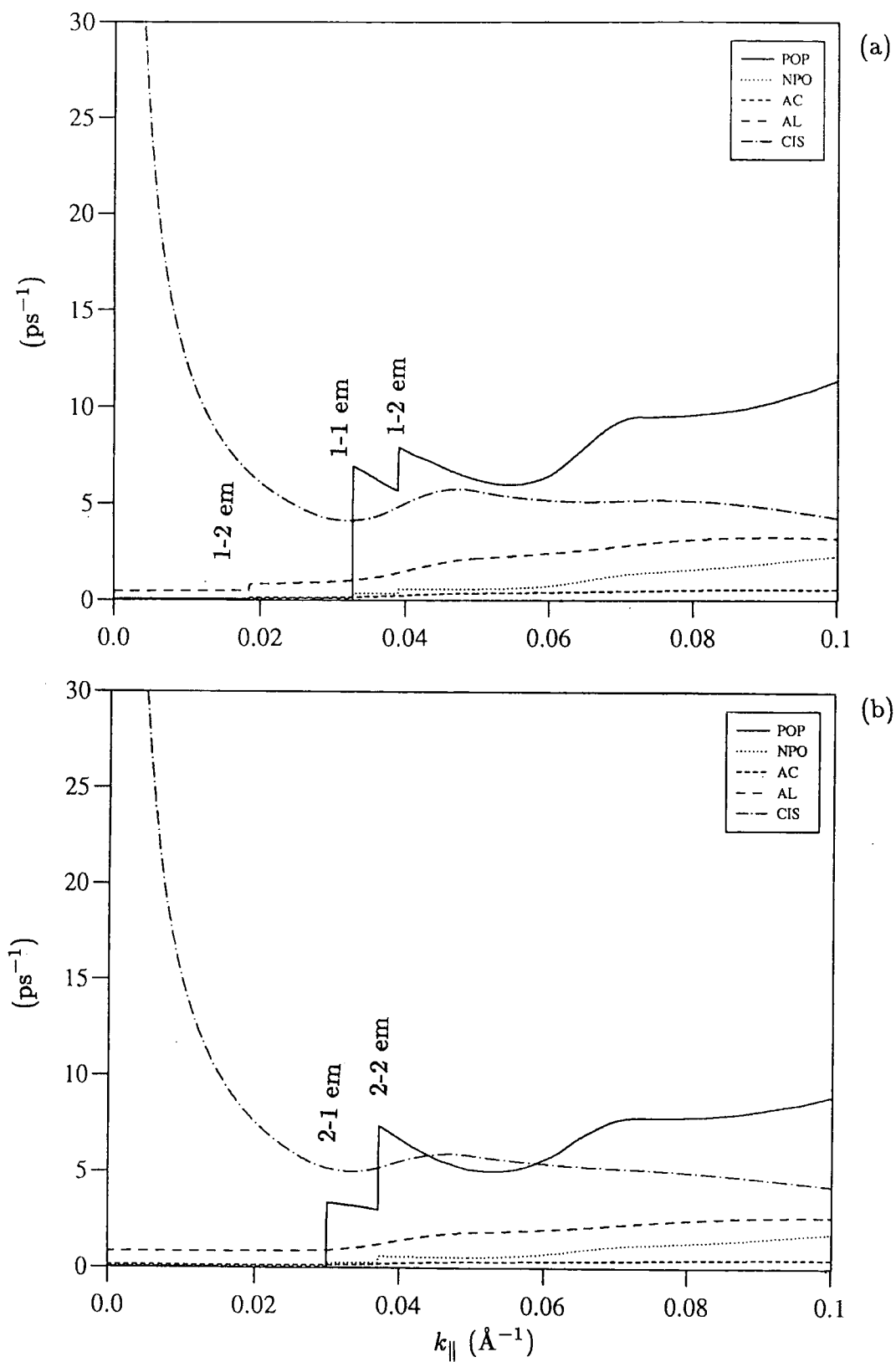
Figure 3.15 Total scattering rates for holes in the HH1 and HH2 subbands of a 150Å $In_{0.18}Ga_{0.82}As$ infinite well as a function of in-plane wavevector: (a) HH1, (b) HH2.

Table 3.4 Parameters for hole scattering rates in $In_xGa_{1-x}As$

at a lattice temperature of T_L=77 K.

x	0.10	0.15	0.18	0.20	0.25
ϵ_s	13.32	13.39	13.43	13.45	13.52
ϵ_∞	11.03	11.09	11.13	11.16	11.24
D_{ac} (eV)	5.00	4.97	4.955	4.94	4.91
ρ (kgm^{-3})	5391.0	5406.0	5415.0	5421.0	5437.0
D_{op} (eVm^{-1})	41.10	41.15	41.18	41.20	41.25
v_s (ms^{-1})	3772.0	3736.0	3714.0	3700.0	3663.0
$\hbar\omega_{op}$ (meV)	33.7	33.4	33.2	33.1	32.8

Sources of data: [20], [24], [25]

There is a clear step-like structure in the polar and non-polar optical phonon rates in all cases; the first discontinuity marking the threshold for intraband transitions by phonon emission, the second marking the onset of interband emission. At $k_\parallel$ below the first threshold, it appears that the scattering rate is zero. This is not the case, but simply that intraband absorption proceeds at a much smaller rate than emission, by a factor $\sim \frac{n_q}{n_q+1}$. As the strain is increased, then the general increase in subband curvature results in a shift of the phonon emission thresholds towards the zone centre. Also, across the range of strain considered, the HH1-HH1 emission rate increases from 6ps^{-1} to 9ps^{-1}. Since the HH2 band is heavier than the HH1 subband, then HH2-HH2 optical transitions will always involve states which are spaced farther apart in $k_\parallel$ than HH1-HH1 events, hence the HH2-HH2 polar optical matrix elements are generally smaller than the HH1-HH1 elements. Despite the larger density of states in the HH2 subband, the

polar optical scattering rates in the HH1 subband are therefore higher than in the HH2 band.

Alloy scattering is the third most important rate in all instances shown, with rates typically 2ps^{-1}. The discontinuity in the alloy scattering rate in the HH1 subband is due to the onset of HH1-HH2 scattering. Significantly, the alloy scattering rate doubles across the range of indium content. Acoustic and non-polar optical phonon scattering would appear to be the least important scattering processes. However, the proportion of carriers which reach the polar optical phonon emission thresholds will depend largely on the magnitude of the applied in-plane electric field. If few carriers pass this threshold, acoustic phonon scattering will account for a greater fraction of all phonon scattering events.

Figures 3.14a, b and 3.15a, b depict the total scattering rates for holes in 50 and 150Å $In_{0.18}Ga_{0.82}As$ wells, respectively. Comparing the rates in the HH1 band, all scattering rates are significantly larger for the narrow well, mostly because of the inverse well width dependence of the matrix elements. The exception to this is charged impurity scattering. For small $k_{\parallel}$, this rate does not differ significantly with well width, because the density of states at the HH1 subband edge varies only marginally. At larger $k_{\parallel} \sim 0.05\text{Å}^{-1}$, the rate for the narrow well is double that for the 150Å example. This is because the HH1 subband is made much heavier due to strong mixing with the HH2 band. The HH1-HH1 optical emission threshold is almost static with well width, since it lies at $k_{\parallel}$ smaller than the anticrossing point. The HH1-HH2 emission threshold on the other hand converges towards the intraband threshold with increasing well width, due to the

decreasing subband separation. In the case of transitions for holes occupying the HH2 subband of the 50Å well, the scattering rates are the largest because of the particularly large density of states in this subband; to be specific the HH2-HH2 emission threshold for polar phonon scattering is $\sim 30\text{ps}^{-1}$, in contrast to 4ps^{-1} for the 150Å well. For wells narrower than 90Å having band separations greater than an optical phonon energy, the HH2-HH1 emission threshold lies at the zone centre. This is significant, since it implies that even if holes do get scattered into the heavier HH2 subband, there will be rapid relaxation back to the HH1 subband.

References

[1] Kelsall R W, Wood A C G and Abram R A
    1991 *Semicond. Sci. Technol.* 6 841

[2] Babiker M 1986 *J. Phys. C : Solid State* 19 683

[3] Chamberlain M P, Hoare D, Kelsall R W and Abram R A
    1992 *Semicond. Sci. Technol.* 7 45

[4] Walukiewicz W, Ruda H E, Logowksi J and Gatos H C
    1984 *Phys. Rev. B* 30 4571

[5] Harrison J W and Hauser J R 1976 *Phys. Rev. B* 13 5347

[6] Chattopadhyay D 1985 *Phys. Rev. B* 31 1145

[7] Basu P K and Nag B R 1983 *Appl. Phys. Lett.* 43 689

[8] Chin V W L, Egan R J and Tansley T L 1991 *J. App. Phys.* 69 3571

[9] Kelsall R W and Abram R A 1992 *Semicond. Sci. Technol.* 7 312

[10] Nordheim L 1931 *Ann. Phys.* 8 607

[11] Basu P K and Bhattacharya K 1986 *J. App. Phys.* 59 992

[12] Bastard G 1984 *Surface Science* 142 284

[13] Ridley B K 1982 *Quantum Processes in Semiconductors*, OUP

[14] Nag B R 1972 *Theory of Electrical Transport in Semiconductors*,
    Pergamon Press

[15] Callen H B 1949 *Phys. Rev.* 76 1394

[16] Stern F and Howard W E 1968 *Phys. Rev.* 163 816

[17] Hess K 1979 *Appl. Phys. Lett.* 35 484

[18] Arfken G 1985 *Mathematical Methods for Physicists 3rd ed.*,
    Academic Press

[19] Matthews J W and Blakeslee A E 1974 *Journal Crystal Growth* 27 118

[20] Adachi S 1982 *J. Appl. Phys.* 53 8775

[21] Chuang S L 1991 *Phys. Rev. B* 43 9649

[22] Price P J 1981 *Ann. Phys.* 133 217

[23] Riddoch F A and Ridley B K 1983 *J. Phys. C : Solid State* 16 6971

[24] Adachi S 1985 *J. Appl. Phys.* 58 R1

[25] Landolt-Börnstein Neue Serie 1982 *Physics of Group IV Elements
    and III − V Compounds*, Springer-Verlag

Chapter 4

Monte Carlo Simulations Of Hole

Transport In InGaAs Quantum Wells

4.1 Introduction

It is well known that III-V quantum well heterostructures with biaxial compressive strain in the well layer produce a ground state valence subband with a reduced in-plane hole effective mass. In principle this can result in an enhanced mobility for the in-plane transport of holes with possible application in devices. For example, the replacement of unstrained GaAs quantum wells by an InGaAs channel could make possible higher speed FETs [1, 2, 3]. With such application in mind, it is the InGaAs-AlGaAs material system which will be examined in this chapter.

The sub-kVcm^{-1} hole mobilities in unstrained p-doped GaAs-AlGaAs quantum wells and superlattices are typically 4-6000 cm^{2}V^{-1}s^{-1} [4, 5]. To date, similar data for In$_x$Ga$_{1-x}$As-GaAs ($x < 0.2$) show little improvement over these figures [6, 7, 8, 9]. In addition, the hole mobility is observed to saturate with increasing in-plane electric field [7]. Likely factors which remove the potential enhancement to the hole mobility are alloy scattering and scattering into a higher order heavier subband [10, 11, 12, 13]. A third possibility is the real space transfer of carriers into the GaAs barrier layers, owing to the small valence band offset between the InGaAs and GaAs layers ($\sim$ 60 meV [3]).

The problem of real space transfer can be reduced by replacing the GaAs barriers by AlGaAs. AlAs has almost the same lattice constant as GaAs hence the same level of strain can be achieved for a particular indium content in the well. However, the band offset between AlGaAs and InGaAs is greater, providing better carrier confinement and limiting carrier escape from the InGaAs channel. Kiehl et al [3] have measured a hole mobility of ~ 5000 cm^{2}V^{-1}s^{-1} at 77 K in In$_{0.12}$Ga$_{0.88}$As-Al$_{0.85}$Ga$_{0.15}$As and In$_{0.12}$Ga$_{0.88}$As-Al$_{0.40}$Ga$_{0.60}$As in comparison to 4000 cm^{2}V^{-1}s^{-1} for a similar GaAs well.

To give a proper assessment of the effect of biaxial compression upon the hole mobility it is necessary to study structures with a range of well widths and levels of biaxial strain, in an attempt to identify those factors which restrict the hole mobility as the well width and indium content are varied. To this end, the infinite well valence bandstructure of chapter 2 and scattering rate calculations of chapter 3 have been used in single particle Monte Carlo transport simulations, to predict the response of holes in strained quantum wells to steady in-plane electric fields. All simulations are carried out at fields less than 10^5Vm^{-1}, well within the limit of the velocity-field saturation.

The geometries of the quantum wells simulated in this chapter are similar to those of samples grown by Fritz et al [9]. Those structures made use of GaAs as the barrier material. The infinite well bandstructure would not be a suitable representation of the InGaAs-GaAs system, so instead AlGaAs has been chosen for the spacer and supply layers because of the larger band gap. The AlGaAs supply layers are considered to be doped with acceptor impurities, to provide

holes for the InGaAs well. These doped regions are separated from the well by undoped spacer layers, which both reduce remote impurity scattering of holes in the well and provide further control of the sheet hole density. The spacer and supply layer widths were chosen to be 150Å and 125Å respectively [9, Table 1, sample 3]. For this structure, the acceptor concentration was $2 \times 10^{17} \text{cm}^{-3}$, and the areal hole density was $2 \times 10^{11} \text{cm}^{-2}$.

The average drift velocities in the ground state and second valence subbands are determined from the sum over all energy changes during each carrier free flight [14]

$$\langle v_{1,2}^{\text{drift}} \rangle = \frac{1}{eET_{1,2}} \sum_{i=1}^{N_{1,2}} (\Delta E)_i, \qquad (4.1)$$

where E is the electric field strength, $(\Delta E)_i$ the energy change of the hole during the ith simulation free flight, of a total number of events N in a given subband. T_1 and T_2 are the accumulated flight times within each band. The hole mobility $\langle \mu \rangle$ is determined by the average of the drift velocities in each subband and the fractional occupation of each band during the simulation:

$$\langle \mu \rangle = \frac{1}{E} \left(v_1^{\text{drift}} P_1 + v_2^{\text{drift}} P_2 \right). \qquad (4.2)$$

P_1 and P_2 denote the occupancy of the HH1 and HH2 subbands respectively.

Section 4.2 provides an analysis of simulations carried out to investigate the hole mobility as a function of indium content in the well. The expected behaviour of the hole mobility as a function of well width is presented in section 4.3.

4.2 Variation of hole mobility with indium concentration

To study the variation of hole mobility with indium concentration at a lattice temperature of 77 K, single particle Monte Carlo simulations of steady-state hole transport in 90Å $In_xGa_{1-x}As$-AlGaAs quantum wells were performed with indium fractions x=0.10, 0.15, 0.18, 0.20 and 0.25. The transport simulations indicated that the hole mobility increases with indium content, despite the increase in alloy scattering. (figure 4.1). The main reason for this is the reduction in the HH1 and HH2 subband masses (figure 4.2). The valence band bulk masses of InAs are less than for GaAs, and the greater the indium content, the lower the in-plane heavy hole mass, irrespective of the compressive strain. The distribution of scattering events for fields $\sim 10^4 Vm^{-1}$ were as follows. For all levels of strain considered, intraband impurity scattering accounted for at least 90% of scattering events. Of the remainder, alloy scattering was found to be the second most important mechanism, as highlighted by figure 4.3. Relatively few carriers were excited up to the optical phonon emission threshold (at $k_\parallel \sim 0.03Å^{-1}$). This is reflected in the fact that the optical phonon emission and absorption processes were found to carry equal weight, and that the average energy of carriers in the HH1 subband was little more than 10meV ($k_\parallel \sim 0.02Å^{-1}$) above the subband edge. In all, polar optical phonons accounted for no more than $\sim$ 1.5% of scattering events. The small excitation of holes, and the presence of the strong HH1-HH1 phonon emission threshold meant that the proportion of carriers reaching the threshold for optical phonon emission into the HH2 subband was negligible. Acoustic phonon and non-polar optical scattering were the least
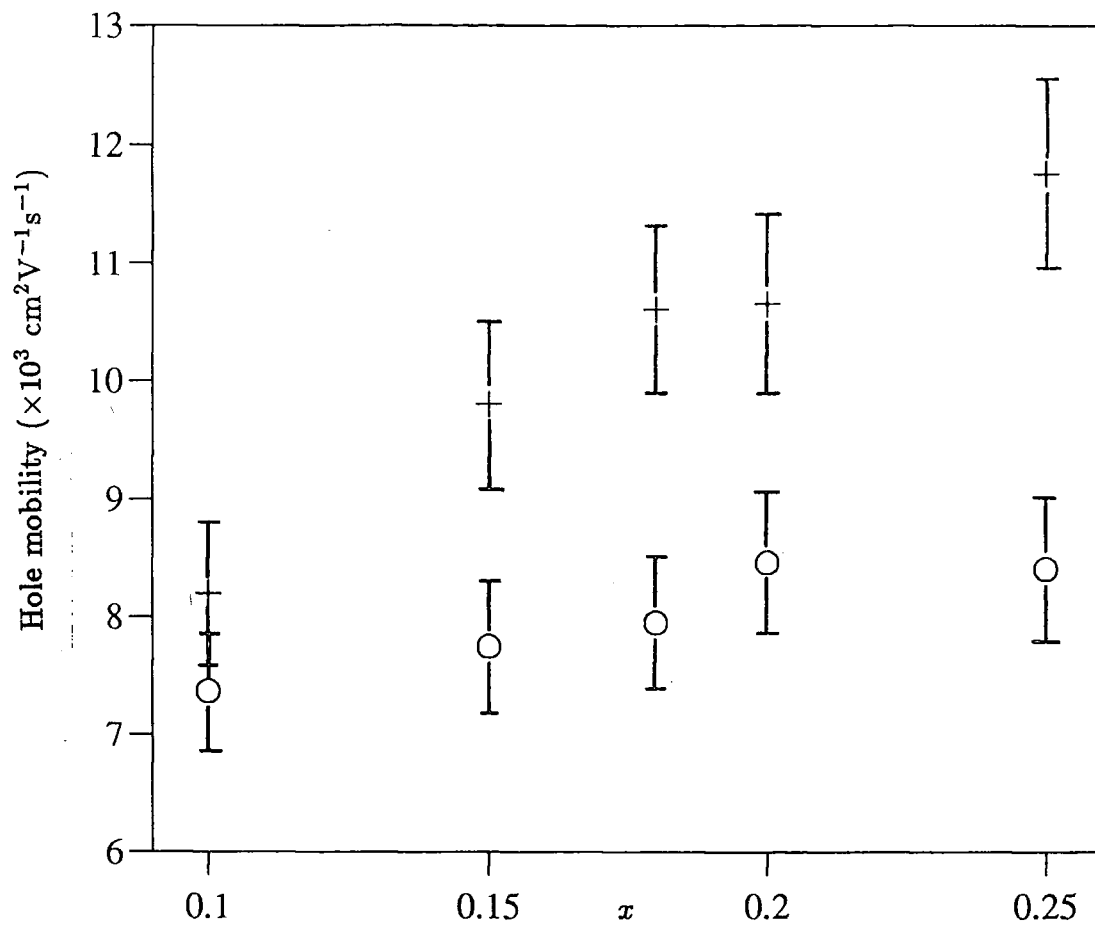
Figure 4.1 77 K hole mobility versus indium fraction x for $In_xGa_{1-x}As$ quantum wells of width 90 Å: o, mobility as a function of strain; +, mobility including both strain and reduction in bulk effective mass.
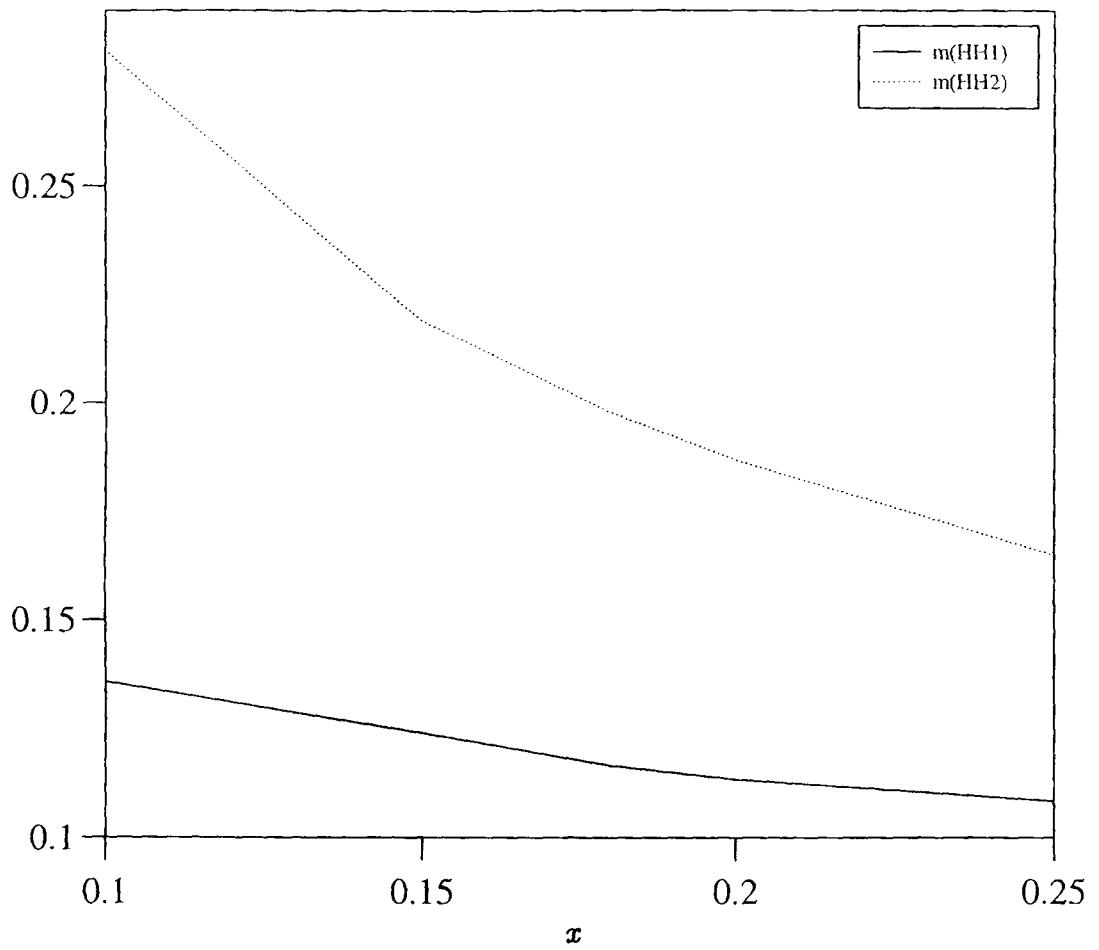
Figure 4.2 Subband edge effective masses for the HH1 and HH2 subbands as a function of indium fraction for $In_xGa_{1-x}As$ quantum wells of width 90 Å.
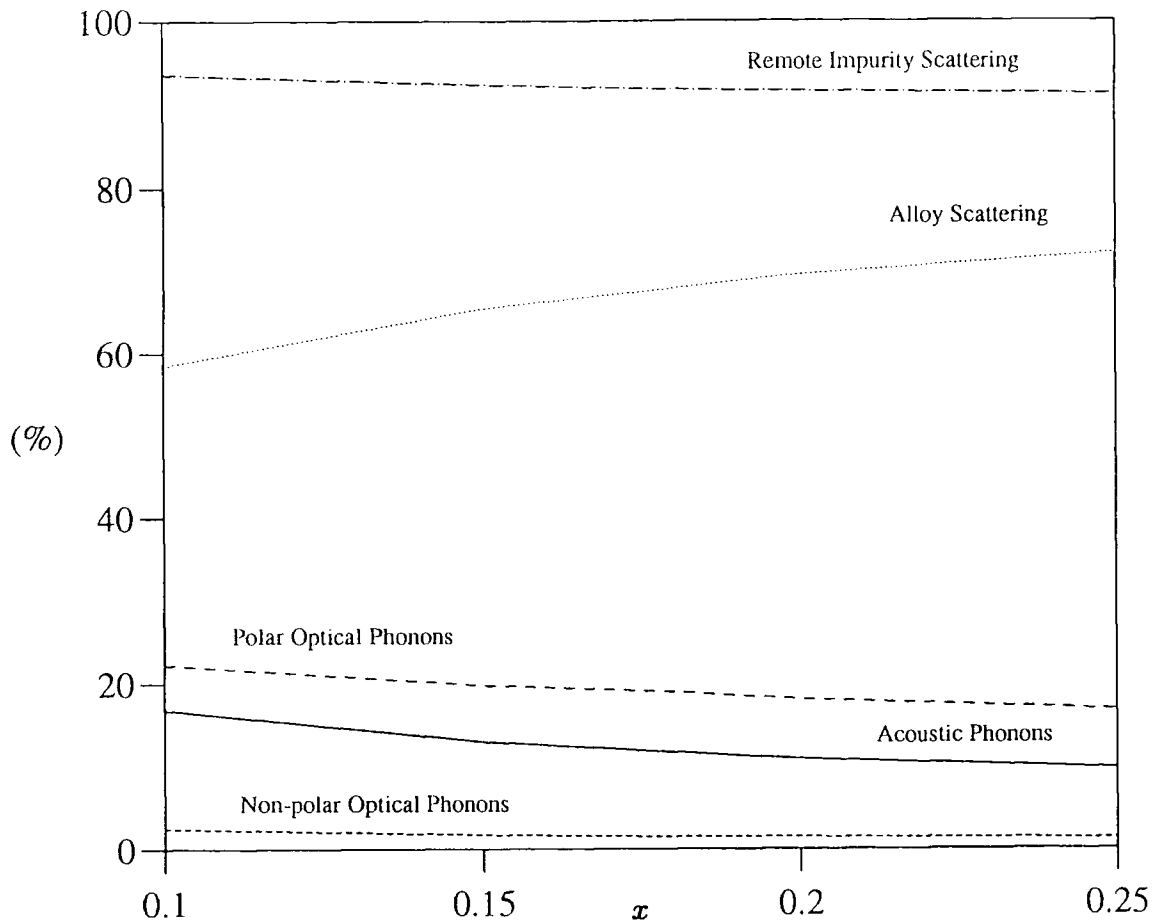
Figure 4.3 The distribution of scattering events in the HH1 subband as a function of indium content x for 90 Å $In_xGa_{1-x}As$ wells. Charged impurity scattering is shown as a fraction of all scattering events. Alloy and phonon scattering are shown as a fraction of the remainder.

important for these field strengths at 77 K, contrary to previous opinion [6].

The fractional occupation of the HH2 subband was found to be no more than 4% ($x = 0.10$) for the 90Å quantum wells - a direct consequence of the low excitation into, and fast relaxation from the HH2 band (the HH1-HH2 subband separation is of the order of the optical phonon energy). In fact, the population of the HH2 subband fell to 2% as the indium fraction was increased to $x = 0.25$, due mostly to increased HH2-HH1 polar optical emission, alloy and acoustic phonon scattering, in descending order of importance. (The HH2-HH1 optical phonon emission threshold lies closer to the Brillouin zone centre with increased strain; hence that fraction of carriers which do get scattered into the HH2 subband readily relax from it).

Figure 4.1 also shows hole mobility data published previously [15]. This data did not account for the change in the bulk valence band masses with indium content. Instead, all bandstructure was calculated using the Luttinger parameters $\gamma_{1L} = 6.85$, $\gamma_{2L} = 2.56$, $\gamma_{3L} = 2.60$ [16]. As such the results predict the increase in the hole mobility which would result from biaxial strain alone. The bands generally give heavier hole masses than the more recent calculations, which are in closer agreement with experiment ($m^*_{HH1} \sim 0.15$ for $x = 0.2$) [3, 6, 10]. In addition, the subband separation was less ($\sim 20\mathrm{meV}$); hence there was greater population of the heavier HH2 band ($\sim 10\%$). Because of greater intersubband scattering, and the heavier subband masses, the mobilities are consistenly lower than those from the more recent simulations.

4.3 Variation of hole mobility with well width

In the second investigation, $In_{0.18}Ga_{0.82}As$ quantum wells with widths in the range 50-150 Å were studied. It will be recalled from chapter 3, that the differences between the bandstructures produced by the well width variation are far greater than the changes resulting from the range of biaxial strain considered. One important feature is the subband separation. For the case of the 50Å well, the HH1 and HH2 subband edges are separated by 0.1 eV, but for the 150Å example this separation is only 11 meV. Also, for the 50Å well, the in-plane hole effective mass for the HH2 subband is eight times that of the HH1 subband, whereas in the 150Å case the effective masses of both subbands are similar. The zone centre effective mass of the HH1 subband remains almost unchanged at ~ 0.12 across the range of well widths. Figures 4.4a, b depict the subband edge separation and the ratios of the zone centre masses for the HH1 and HH2 subbands as a function of well width, showing how the mass ratio approaches unity as the subbands converge.

In low-field hole transport few carriers will be excited into the remote second subband of the 50Å well and therefore the greater effective mass of that band will not have a significant effect on the average hole mobility. In contrast, the proximity of the HH1 and HH2 subbands for the 150Å well implies that there will be considerable scattering into the HH2 subband. However, in this instance, holes occupying the HH2 subband possess much the same in-plane mass as those in the HH1 subband. The increase in the HH2 mass as the quantum well becomes narrower results in a larger density of states, which acts to increase the scattering
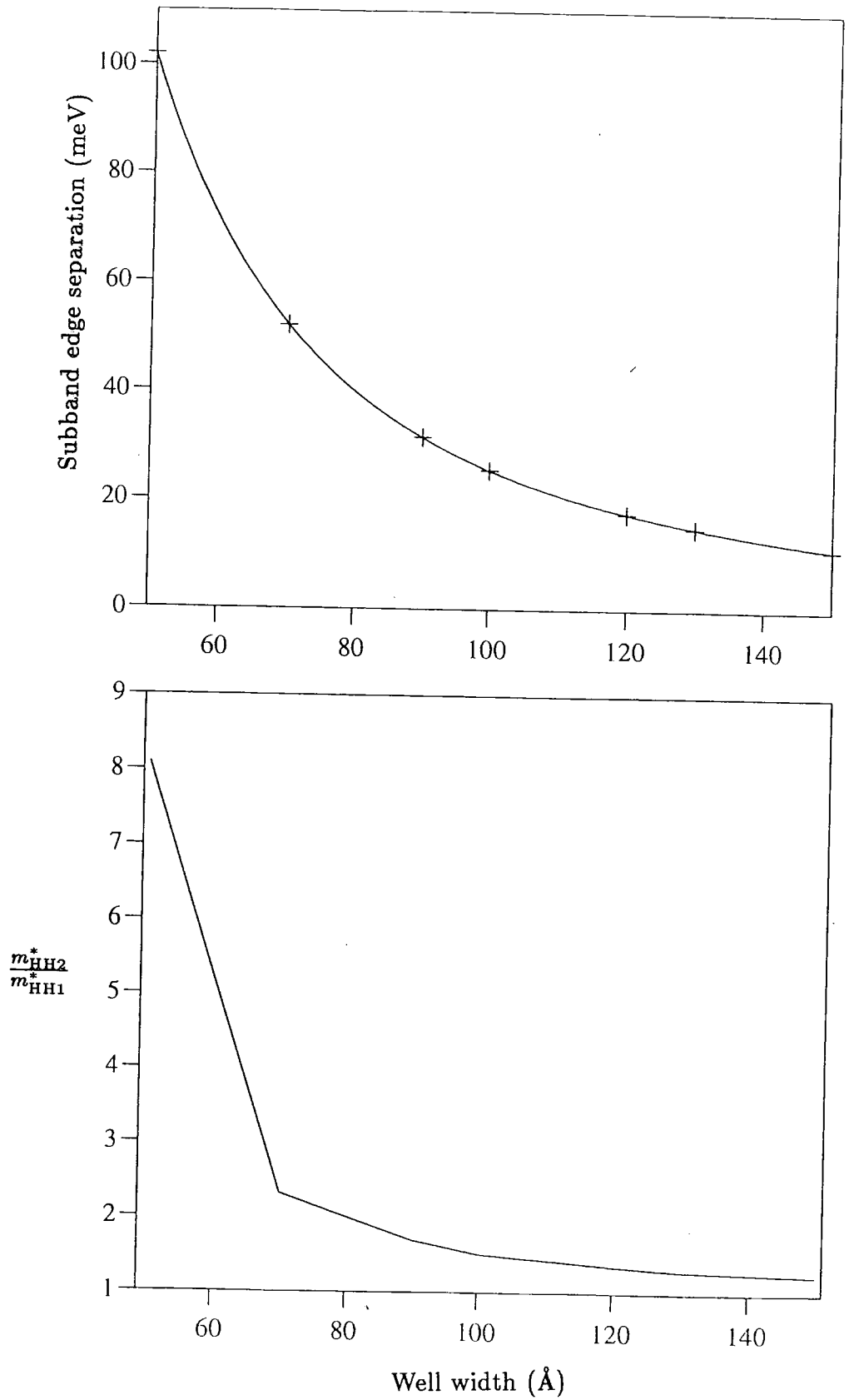
Figure 4.4 (a) HH1 and HH2 subband edge separation, and (b) the ratio of the zone centre effective masses as a function of well width for $In_{0.18}Ga_{0.82}As$ quantum wells.
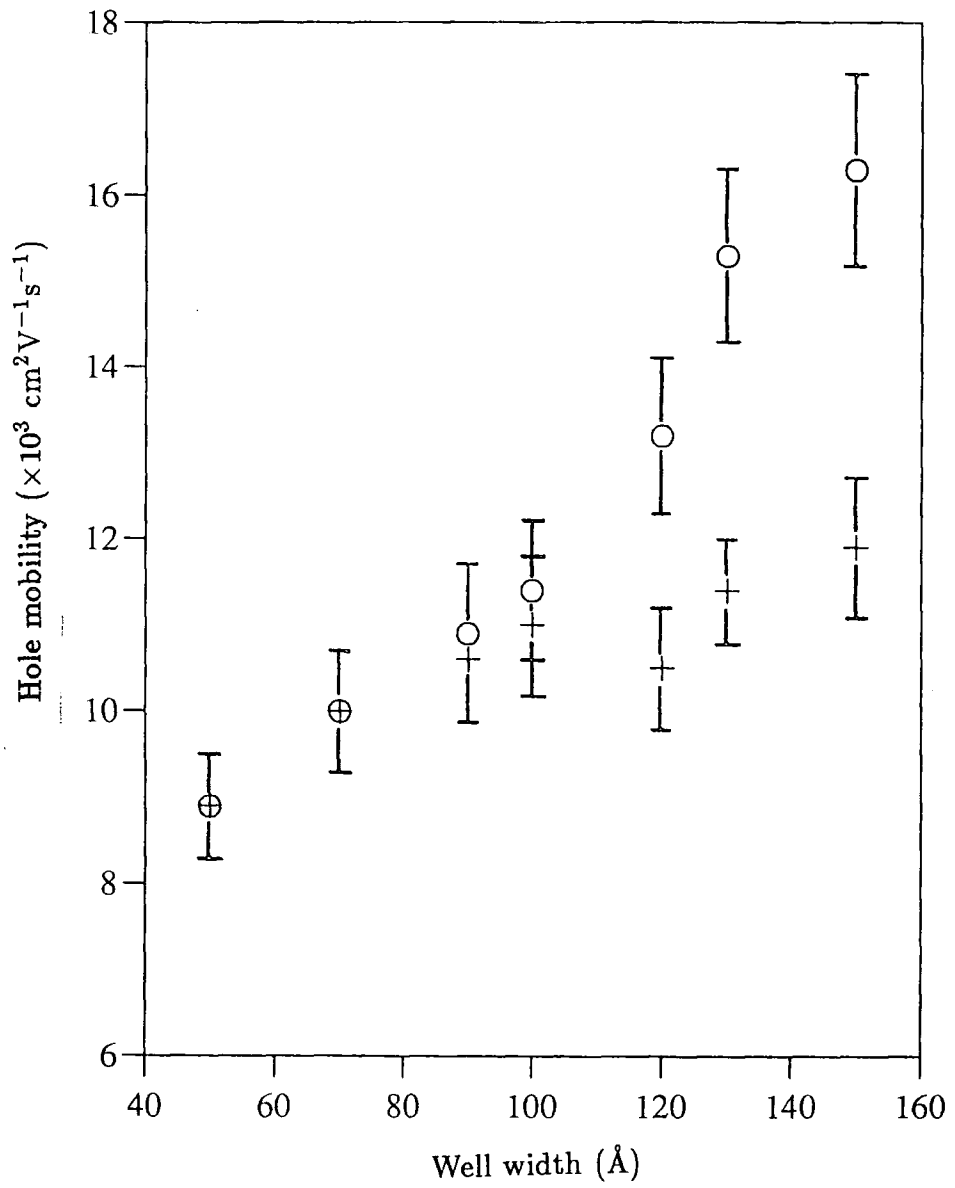
Figure 4.5 77 K hole mobility versus well width for $In_{0.18}Ga_{0.82}As$ quantum wells: o, one subband approximation; +, two subband approximation.
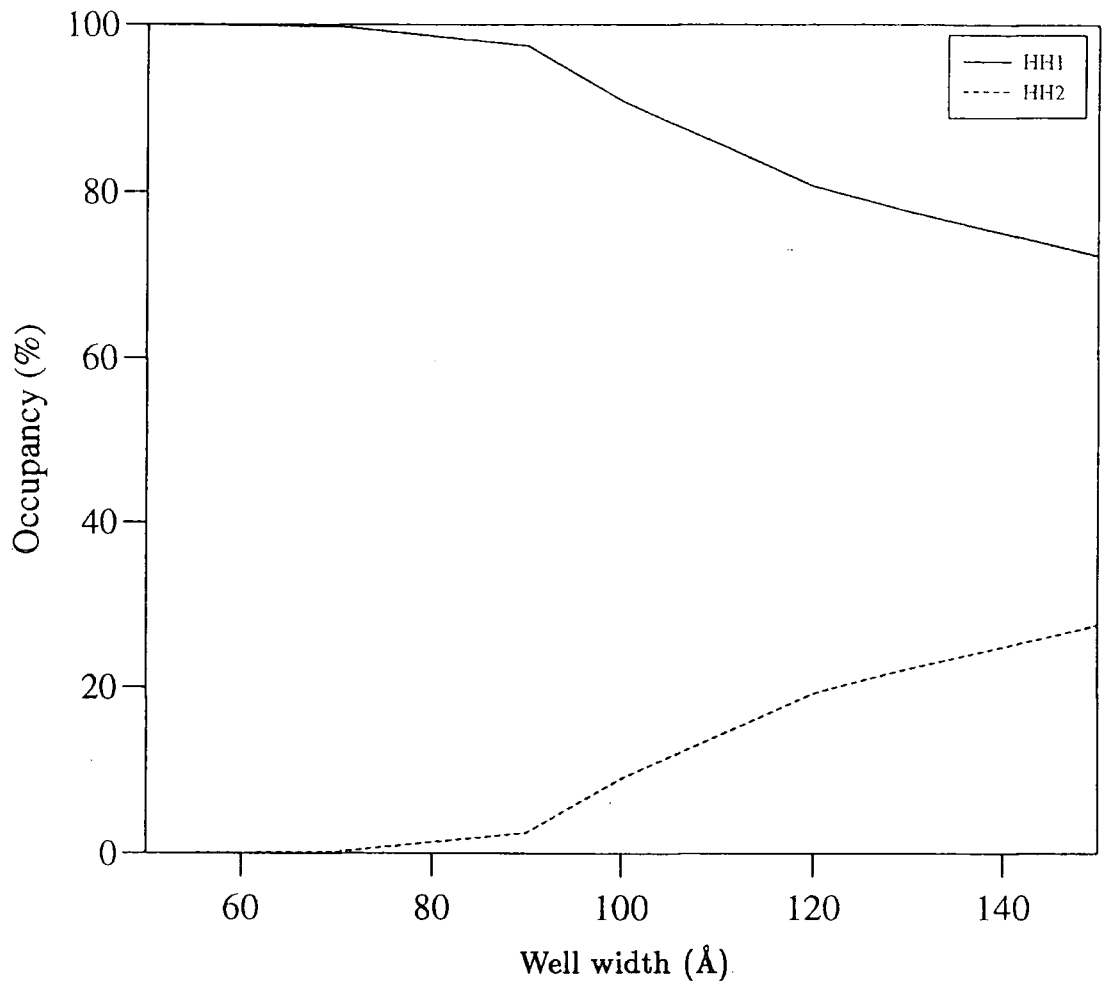
Figure 4.6 Percentage of holes in the HH2 subband versus well width for an $In_{0.18}Ga_{0.82}As$ quantum well at 77 K and with an applied electric field of 10^4 Vm^{-1}.

rates to that subband and the strength of intraband scattering. In addition, the scattering rates increase with decreasing well width, through the contribution from the scattering matrix elements. This is primarily due to the localised nature of the hole envelope functions, but is also a result of the reduced coupling between the HH2 and LH1 zone centre states for wider wells (the HH1 and HH2 subbands are mixed by their mutual interaction with the LH1 zone centre state).

The analysis of the bandstructure and scattering matrix elements of chapter 3 indicates that the hole mobility should increase with well width. The mobilities obtained from the simulations for the set of $In_{0.18}Ga_{0.82}As$ wells are given in figure 4.5 and show the expected general trends. There is, however, a local minimum in the hole mobility for wells $\sim$ 120Å wide, which can be explained as follows. For the narrowest well studied, it has already been pointed out that there is negligible excitation of holes to the second subband. With increasing well width, and therefore reduced subband separation, holes are seen to be more readily scattered into the HH2 band, as illustrated by figure 4.6. For a 120Å well, there is considerable population of the HH2 subband ($\sim$ 19%). However, the important characteristic of this case is that it combines a significant second subband population with a hole mass for that subband which is comparatively heavy at 1.4 times the mass in HH1. At larger well widths, the HH2 population increases but the effective mobility of this subband also increases. For the wells with an appreciable HH2 subband occupancy, scattering within the HH2 subband is dominated by intrinsic charged impurity and alloy scattering. Of the phonon processes, polar optical HH2-HH1 emission and intraband acoustic scattering are important.

Also in figure 4.5 are the results of simulations that were carried out using a one-subband approximation (i.e. just the HH1 subband). The aim was to see what mobilities might have been obtained if intersubband scattering was omitted and all holes had a common in-plane effective mass. For wells less than 100Å thick, the curves for the one- and two-subband approximations converge, reflecting the fact that in this regime the second subband plays a minor role, but at the onset of intersubband scattering for wider wells, the presence of the second subband suppresses the hole mobility.

The 150Å well width marks the limit of the validity of the two-band approximation. Around this well width, scattering into the third (HH3) subband becomes likely, since it lies 19meV below the HH2 subband edge. According to Andersson et al [17] and the Matthews-Blakeslee model [18], this well width is also near the critical layer thickness for growing dislocation-free layers of InGaAs for this level of strain.

Using the valence bandstructure parameters given by O'Reilly and Witchlow [16], the results are qualitatively similar to those discussed above, but the population of the HH2 subband becomes significant at a well width of 80Å, and the local minimum in the hole mobility occurs at a 90Å layer width.

4.4 Conclusions

Results from the low-field transport simulations for 90Å $In_xGa_{1-x}As$-AlGaAs quantum wells ($0.10 \leq x \leq 0.25$) predict that a greater hole mobility is to be expected as the indium content is increased. This arises from the reduction in the in-plane hole effective mass for the HH1 subband (due to the larger compressive biaxial strain and the reduced masses in the bulk) which more than compensates for the effect of increased alloy scattering within the well. The predicted increase in the hole mobility with strain for InGaAs-AlGaAs is $\sim 4000\,cm^2/(Vs\%)$. This compares with the experimental value of around $5000\,cm^2/(Vs\%)$ for InGaAs-GaAs determined by Fritz et al [6].

The variation of the hole mobility with well width shows interesting effects derived from the competing factors which enhance or reduce the hole mobility. The general trend was for the hole mobility to increase with well width, but a local minimum in the mobility was observed for wells ~ 120Å wide because of the combination of significant transfer into the second subband and the relatively large effective mass of that subband.

Scattering of holes at sub-kVcm^{-1} fields is dominated by intrinsic alloy and charged impurity scattering. Optical phonon scattering, in particular, was not seen to cause a significant reduction of the hole mobility. This is due to the low excitation of carriers away from the subband edge states at these field strengths.

The particular drawback of applying the infinite well model to these transport simulations is the artificially low in-plane effective mass and large subband sepa-

ration in comparison with finite well models, which means that all hole mobilities are consistently larger than experimental values, and that the onset of intersubband scattering occurs for wider wells than expected. The explanation for this is as follows. Total confinement reduces the uncertainty in the position of the holes within the well, and hence the eigenstates lie at higher energies than they would if the well was finite and the hole wavefunctions were permitted to spread into the barriers.

A second limitation is that transport studies at high electric fields would be unreliable since the model does not allow carrier escape into the barriers. However, the model does give an acceptably useful, simple and accurate description of the HH1-LH1-HH2 mixing and, at least qualitatively, the predictions from the infinite well model are adequate. The threshold well width for appreciable population of the second subband is that at which the subband edge separation is less than the optical phonon energy (~ 30 meV). In experimental structures this condition will be met at smaller well widths than the infinite well model predicts. Since many of the experimental structures referred to in the introduction incorporate wells ~ 100Å thick, the factors described above may explain why existing parallel transport data for holes in InGaAs shows little improvement against those for similar unstrained systems.

References

[1] Osbourn G C 1986 *Phys. Rev. B* 27 5126

[2] Schirber J E, Fritz I J and Dawson L R 1985 *Appl. Phys. Lett.* 46 187

[3] Kiehl R A, Shtrikman H and Yates I 1991 *Appl. Phys. Lett.* 58 954

[4] Mendez E E and Wang W I 1985 *Appl. Phys. Lett.* 46 1159

[5] Störmer H L, Gossard A C, Weigmann W, Blondel R and Baldwin K
1984 *Appl. Phys. Lett.* 44 139

[6] Fritz I J, Doyle B L, Schirber J E, Jones E D, Dawson L R and
Drummond T J 1986 *Appl. Phys. Lett.* 49 581

[7] Reddy M, Grey R, Claxton P A, Woodhead J
1990 *Semicond. Sci. Technol.* 5 628

[8] Fritz I J, Dawson L R, Drummond T J, Schirber J E and Biefeld R M
1986 *Appl. Phys. Lett.* 48 139

[9] Fritz I J, Drummond T J, Osbourn G C, Schirber J E and Jones E D
1986 *Appl. Phys. Lett.* 48 1678

[10] Drummond T J, Zipperian T E, Fritz I J, Schirber J E and Plut T A
1986 *Appl. Phys. Lett.* 49 461

[11] Hjalmarson H P 1989 *Appl. Phys. Lett.* 54 2215

[12] Hjalmarson H P, Fritz I J and Dawson L R
1989 *Solid. State. Elec.* 32 1777

[13] Kelsall R W and Abram R A 1992 *Semicond. Sci. Technol.* 7 B312

[14] Fawcett W, Boardmann A D and Swain S
1970 *Journ. Phys. Chem. Sol.* 31 1963

[15] Crow G C, Kelsall R W and Abram R A
1993 *Semicond. Sci. Technol.* 8 219

[16] O'Reilly E P and Witchlow G P 1986 *Phys. Rev. B* 34 6030

[17] Andersson T J, Chen Z G, Kulakovskii V D, Uddin A and
Vallin J T 1987 *Appl. Phys. Lett.* 51 752

[18] Matthews J W and Blakeslee A E 1974 *J. Crystal Growth* 27 118

PART TWO

The Relaxation Of Holes

In Quantum Wells

Chapter 5

The Quantum Capture Of Holes

By A Square Well Potential

5.1 Introduction

In quantum mechanical terms, the quantum capture of carriers into a semiconductor quantum well is the transition of carriers from bulk-like continuum states, to the quasi-two dimensional bound states. It is believed that carriers make these transitions by the emission of polar optical phonons [1] or by non-polar optical phonon scattering [2]. Capture induced by impurity scattering in the barrier material has also been considered [3].

Carrier capture is an important process in the operation of quantum well lasers and has attracted much interest in recent years [4, 5]. Here the relevant processes are carrier diffusion across the confinement layers, the trapping rate, and once captured, carrier thermalisation to the ground state of the quantum well. Unless the carrier injection into the bound states contributing to the stimulated emission is sufficiently fast, the high speed performance of the laser will be impaired.

In their semiclassical studies of capture by polar optical phonon emission, Schichijo et al [6] and Tang et al [7] conclude that wide wells are necessary to ensure fast capture, and that wells narrower than the phonon limited mean free path are inefficient traps. More recent calculations by Bastard et al [1] predict that the electron and hole capture times oscillate as a function of well

width. These fluctuations are attributed to the binding of additional states as the well width is increased, and also to the presence of virtual bound states or 'transmission resonances' within an optical phonon energy of the continuum edge.

The concept of a virtual bound state may be illustrated by considering the one dimensional problem of the scattering of a plane wavefront at a potential step. Quantum mechanics shows that the reflection probability at the interface oscillates as a function of the energy associated with the wave. If a second potential step is introduced into the problem, creating a potential well, the wave which is transmitted past the first interface subsequently undergoes multiple reflections at both interfaces [8]. Constructive interference of the reflected waves occurs at energies for which the wavelength in the well layer is approximately a half integer multiple of the well width. This results in states with an enhanced probability density in the vicinity of the well. There is some experimental evidence that such states exist. Bastard et al [9] have studied the excitation spectroscopy of a double GaAs-AlGaAs well structure, and observe a spectral line at a wavelength consistent with that calculated for a light hole virtual bound state using an eight band **k.p** model. Bastard suggests that quantum wells designed to have a virtual bound level in the vicinity of the continuum edge will serve as better carrier traps. Kozyrev and Shik [2] have performed complementary calculations, but for non-polar optical phonon emission, predicting similar oscillations in the capture rate with well width.

Direct experimental measurement of the carrier capture time into a quantum

well is not possible. However, the electron and hole capture times can be estimated by time resolved measurement of photonic emissions. Carrier capture results in an increase of the photoluminescence and spontanous emission intensity from the well at the expense of that from the barriers. The rise time for the emission intensity from the well provides an estimate of the electron capture time, whereas the rate of decay of the emission intensity from the barriers provides a measure of the hole capture rate. Time resolved photoluminescence studies carried out for InGaAs-InGaAsP quantum wells by Deveaud et al [10] suggest that the capture time is approximately one picosecond for electrons and subpicosecond for holes. (The hole capture time may be shorter because of the higher density of final states in the valence band [1]). This group has also shown that 9 Å wells collect carriers as efficiently as wider 150 Å wells. Hirayama et al [11] have measured similar capture times from spontaneous emission studies of InGaAs-InGaAsP quantum wells.

There is a significant discrepancy between the experimental results and the predicted values, which place the capture times for electrons and holes at around a few tens of picoseconds. A subpicosecond capture time appears to be in keeping with existing rate equation models of semiconductor lasers [11], hence it seems likely that it is the current theory which is at fault.

Apart from Bastard's k.p model, which successfully predicted the presence of a virtual bound state [9], other models [1, 2, 3, 12, 13] have treated the wavefunctions for both electrons and holes using the parabolic band approximation. This is a particularly poor assumption for the valence band since holes exhibit

mixed character, as discussed previously in chapter 2.

The aim of this chapter is to report on the development of a detailed model for hole capture into a quantum well using realistic k.p bandstructure. This compares the capture rates for polar optical, non-polar optical and acoustic phonon scattering, and also alloy scattering. The capture process is treated in a similar way to a barrier transmission problem. In this way, the capture *rate* can be adapted to construct the capture *probability* (the fraction of the incident particle current which becomes trapped by the well). Expressed in this form, the capture data is better suited for use in semiclassical transport models. The calculations are restricted to a quantum well system which is currently being investigated by GEC-Marconi (Caswell) for inclusion in a $1.55\,\mu$m multiple quantum well laser. This consists of 30Å $In_{0.7}Ga_{0.3}As$ wells separated by layers of $In_{0.75}Ga_{0.25}As_{0.55}P_{0.45}$ ($1.25\,\mu$m band gap) which serve as the barriers and separate confinement heterostructure. The InGaAsP layers are lattice matched to InP, the outer cladding material of the device. The wells are under a biaxial compressive strain of 1.2%; the InGaAsP layers are unstrained. This hole capture model is applied to an investigation of the trapping properties of a single 30Å $In_{0.7}Ga_{0.3}As$ well bounded by $In_{0.75}Ga_{0.25}As_{0.55}P_{0.45}$ barriers of equal width. To be representative of the confinement layers of a quantum well laser, a distance of 1μm has been chosen for the sum of the barrier and well widths.

5.2 Solution to the hole capture problem

There are two ways of constructing the wavefunctions of the unbound holes in the barrier region. They may be regarded as standing waves extended across the confinement region which are perturbed by the quantum well, as described by Bastard et al, or Ru and Li, for example [3, 14]. The alternative is to model a carrier as an incoming plane wave of energy E, in-plane wavevector $k_\parallel$, and transverse component k_z incident upon the well, and determine what fraction of this wave is reflected and transmitted at the well-barrier boundary [2, 8, 12]. Both models are limited by the assumption that at the instant of capture, the holes can be represented by coherent wavefunctions across the confinement volume. This is a somewhat simplified approach, since the holes can be expected to suffer carrier-carrier and phonon scattering during their transit across the confining layers; but without this approximation, the problem is particularly complicated.

In either picture, Fermi's Golden Rule can be used to determine the rate of scattering between the unbound and bound states; that is the rate of capture of carriers by the well. In the incoming wave model, the trapping efficiency of the well can be expressed in terms of the fraction of the incident particle flux density which is absorbed per unit area of the well per unit time. The situation is then comparable to perpendicular transport experiments [12].

The two methods are essentially equivalent, but by constructing the capture rate per unit incident particle flux, the plane wave model can be viewed in a *local* sense allowing a relaxation of the fact that scattering in the confinement is neglected.

5.3 The k.p solution for unbound and bound states

The wavefunctions for all unbound and bound states in the valence band have been constructed using the envelope function approximation, writing them as an expansion over eight Bloch functions $| j \rangle$ representing electron states at Γ. This basis set includes spin-up and spin-down conduction band states, and the corresponding pairs of states for the heavy hole, light hole and spin split-off bands. These are listed in table 5.1.

Table 5.1 Basis Bloch functions of

the eight band k.p model.

$\| j \rangle$	s-, p- orbital representation
$\| 1 \rangle$	$\| S \uparrow \rangle$
$\| 2 \rangle$	$\frac{1}{\sqrt{2}} \| (X + iY) \uparrow \rangle$
$\| 3 \rangle$	$\frac{1}{\sqrt{6}} \| (X + iY) \downarrow \rangle - \sqrt{\frac{2}{3}} \| Z \uparrow \rangle$
$\| 4 \rangle$	$\frac{1}{\sqrt{3}} \| (X + iY) \downarrow \rangle + \| Z \uparrow \rangle$
$\| 5 \rangle$	$\| S \downarrow \rangle$
$\| 6 \rangle$	$\frac{1}{\sqrt{2}} \| (X - iY) \downarrow \rangle$
$\| 7 \rangle$	$\frac{-1}{\sqrt{6}} \| (X - iY) \uparrow \rangle - \sqrt{\frac{2}{3}} \| Z \downarrow \rangle$
$\| 8 \rangle$	$\frac{-1}{\sqrt{3}} \| (X - iY) \uparrow \rangle - \| Z \downarrow \rangle$

The wavefunctions are matched across the well-barrier boundaries by assuming that the Bloch functions are identical for the InGaAs and InGaAsP layers. The basis set, and the 8 × 8 Hamiltonian matrix describing interactions between the Bloch functions have been derived by Eppenga et al [15], Smith and Mailhiot [16]. Terms describing the effects of biaxial strain in the well layer were derived

by Wood [17].

Table 5.2 Bandstructure parameters for the

Hamiltonian of figure 5.1.

(Lattice Temperature $T_L = 300\,\text{K}$)

	[†]$\text{In}_{0.7}\text{Ga}_{0.3}\text{As}$	[°]$\text{In}_{0.75}\text{Ga}_{0.25}\text{As}_{0.55}\text{P}_{0.45}$
$a_0(\text{Å})$	5.9374	5.8687
E_g (eV)	0.5848	0.9919
Δ (eV)	0.3635	0.2533
s	-13.51	-4.54
γ_1	-2.60	-0.276
γ_2	-2.55	-1.210
γ_3	-1.839	-0.730
P	5.12	4.795
l (eV)	-3.4	-
m (eV)	1.7	-
c (eV)	-6.93	-
ϵ_{xx}	-0.0117	-
ϵ_{zz}	0.0117	-

Sources of data: † GaAs data [15], InAs data [18]

• InGaAsP data [19]

79

$$H_0 = $$

	$\lvert 1\rangle$	$\lvert 2\rangle$	$\lvert 3\rangle$	$\lvert 4\rangle$	$\lvert 5\rangle$	$\lvert 6\rangle$	$\lvert 7\rangle$	$\lvert 8\rangle$
$\lvert 1\rangle$	$sk_\parallel^2 + E_g + \epsilon_1$	$\frac{iP}{\sqrt{3}}(k_x+ik_y)$	0	0	0	0	$\frac{-iP}{\sqrt{6}}(k_z^2-k_y^2)$	$\frac{-iP}{\sqrt{3}}(k_z-ik_y)$
$\lvert 2\rangle$	$\frac{-iP}{\sqrt{3}}(k_z-ik_y)$	$-(\gamma_1+\gamma_2)k_\parallel^2+\epsilon_2$	0	0	0	0	$\sqrt{3}\gamma_2(k_z^2-k_y^2)-2\sqrt{3}i\gamma_3k_zk_y$	$\sqrt{6}\gamma_2(k_z^2-k_y^2)-2\sqrt{6}i\gamma_3k_zk_y$
$\lvert 3\rangle$	0	0	$(\gamma_2-\gamma_1)k_\parallel^2+\epsilon_3$	$-\sqrt{2}\gamma_2k_\parallel^2+\epsilon_6$	0	0	$-\sqrt{3}\gamma_2(k_z^2-k_y^2)+2\sqrt{3}i\gamma_3k_zk_y$	$-\sqrt{3}\gamma_2(k_z^2-k_y^2)-2\sqrt{3}i\gamma_3k_zk_y$
$\lvert 4\rangle$	0	0	$-\sqrt{2}\gamma_2k_\parallel^2+\epsilon_6$	$-\gamma_1k_\parallel^2-\Delta+\epsilon_4$	$\frac{iP}{\sqrt{3}}(k_z+ik_y)$	$\frac{-iP}{\sqrt{6}}(k_z-ik_y)$	$-\sqrt{6}\gamma_2(k_z^2-k_y^2)+2\sqrt{6}i\gamma_3k_zk_y$	$-\sqrt{6}\gamma_2(k_z^2-k_y^2)-2\sqrt{6}i\gamma_3k_zk_y$
$\lvert 5\rangle$	0	0	0	$\frac{iP}{\sqrt{6}}(k_z+ik_y)$	$sk_\parallel^2+E_g+\epsilon_1$	$\frac{-iP}{\sqrt{3}}(k_z-ik_y)$	$\frac{iP}{\sqrt{3}}(k_z-ik_y)$	0
$\lvert 6\rangle$	0	0	0	0	$\frac{iP}{\sqrt{3}}(k_z+ik_y)$	$-(\gamma_1+\gamma_2)k_\parallel^2+\epsilon_2$	0	0
$\lvert 7\rangle$	$\frac{iP}{\sqrt{6}}(k_z+ik_y)$	$\sqrt{3}\gamma_2(k_z^2-k_y^2)+2\sqrt{3}i\gamma_3k_zk_y$	0	0	0	0	$(\gamma_3-\gamma_1)k_\parallel^2+\epsilon_3$	$-\sqrt{2}\gamma_2k_\parallel^2+\epsilon_6$
$\lvert 8\rangle$	$\frac{iP}{\sqrt{3}}(k_z+ik_y)$	$\sqrt{6}\gamma_2(k_z^2-k_y^2)+2\sqrt{6}i\gamma_3k_zk_y$	0	0	0	0	$-\sqrt{2}\gamma_2k_\parallel^2+\epsilon_6$	$-\gamma_1k_\parallel^2-\Delta+\epsilon_4$

$$H_1 = $$

	$\lvert 1\rangle$	$\lvert 2\rangle$	$\lvert 3\rangle$	$\lvert 4\rangle$	$\lvert 5\rangle$	$\lvert 6\rangle$	$\lvert 7\rangle$	$\lvert 8\rangle$
$\lvert 1\rangle$	0	0	$-iP\sqrt{\frac{2}{3}}$	$\frac{iP}{\sqrt{3}}$	0	0	0	0
$\lvert 2\rangle$	0	0	$2\sqrt{3}\gamma_3(k_z-ik_y)$	$-\sqrt{6}\gamma_3(k_z-ik_y)$	0	0	0	0
$\lvert 3\rangle$	$iP\sqrt{\frac{2}{3}}$	$2\sqrt{3}\gamma_3(k_z+ik_y)$	0	0	0	0	0	$-3\sqrt{2}\gamma_3(k_z-ik_y)$
$\lvert 4\rangle$	$\frac{-iP}{\sqrt{3}}$	$-\sqrt{6}\gamma_3(k_z+ik_y)$	0	0	0	0	$3\sqrt{2}\gamma_3(k_z-ik_y)$	0
$\lvert 5\rangle$	0	0	0	0	0	0	$-iP\sqrt{\frac{2}{3}}$	$\frac{iP}{\sqrt{3}}$
$\lvert 6\rangle$	0	0	0	0	0	0	$2\sqrt{3}\gamma_3(k_z-ik_y)$	$-\sqrt{6}\gamma_3(k_z-ik_y)$
$\lvert 7\rangle$	0	0	0	$3\sqrt{2}\gamma_3(k_z+ik_y)$	$iP\sqrt{\frac{2}{3}}$	$2\sqrt{3}\gamma_3(k_z-ik_y)$	0	0
$\lvert 8\rangle$	0	0	$-3\sqrt{2}\gamma_3(k_z+ik_y)$	0	$\frac{-iP}{\sqrt{3}}$	$-\sqrt{6}\gamma_3(k_z-ik_y)$	0	0

$$H_2 = $$

	$\lvert 1\rangle$	$\lvert 2\rangle$	$\lvert 3\rangle$	$\lvert 4\rangle$	$\lvert 5\rangle$	$\lvert 6\rangle$	$\lvert 7\rangle$	$\lvert 8\rangle$
$\lvert 1\rangle$	s	0	0	0	0	0	0	0
$\lvert 2\rangle$	0	$2\gamma_2-\gamma_1$	0	0	0	0	0	0
$\lvert 3\rangle$	0	0	$-(\gamma_1+2\gamma_2)$	$2\sqrt{2}\gamma_3$	0	0	0	0
$\lvert 4\rangle$	0	0	$2\sqrt{2}\gamma_3$	$-\gamma_1$	0	0	0	0
$\lvert 5\rangle$	0	0	0	0	s	0	0	0
$\lvert 6\rangle$	0	0	0	0	0	$2\gamma_2-\gamma_1$	0	0
$\lvert 7\rangle$	0	0	0	0	0	0	$-(\gamma_1+2\gamma_2)$	$2\sqrt{2}\gamma_2$
$\lvert 8\rangle$	0	0	0	0	0	0	$2\sqrt{2}\gamma_2$	$-\gamma_1$

Figure 5.1 Components of the eight band k.p Hamiltonian, including the effect of biaxial strain. (For a definition of terms refer to tables 5.1 and 5.2).

Table 5.3 Strain terms of the k.p Hamiltonian.

$\epsilon_1 = (2\epsilon_{xx} + \epsilon_{zz})c$
$\epsilon_2 = \epsilon_{xx}(l + m) + m\epsilon_{zz}$
$\epsilon_3 = \frac{l}{3}(\epsilon_{xx} + 2\epsilon_{zz}) + \left(\frac{5\epsilon_{xx} + \epsilon_{zz}}{3}\right) m$
$\epsilon_4 = \left(\frac{2\epsilon_{xx} + \epsilon_{zz}}{3}\right)(l + 2m)$
$\epsilon_5 = \frac{\sqrt{2}}{3}(\epsilon_{xx} - \epsilon_{zz})(l - m)$

The first step towards calculating the unbound states is to solve the bulk band-structure for the barrier and extract all real wavevector solutions for a given hole energy above the continuum edge of the quantum well. For a hole of energy E and in-plane wavevector component $k_{\parallel}$, the transverse wavevector components k_z can be determined by rearranging the Schrödinger equation into an eigenvalue equation where k_z is the eigenvalue. The time-independent Schrödinger equation for the hole in bulk material is

$$H\Psi(\mathbf{r}_{\parallel}, z) = E\Psi(\mathbf{r}_{\parallel}, z) \tag{5.1}$$

where $\Psi(\mathbf{r}_{\parallel}, z)$ is the bulk wavefunction. Separating H into components independent, linear and quadratic in k_z,

$$H = H_0 + H_1 k_z + H_2 k_z^2. \tag{5.2}$$

The 8 × 8 matrices H_0, H_1 and H_2 are listed in figure 5.1 and the relevant bandstructure parameters are defined in tables 5.2 and 5.3. (The Hamiltonian has been written using the units convention $\frac{\hbar^2}{2m_0} = 1$). Absorbing E into the matrix H_0 to form H_0', and multiplying the equation by H_2^{-1} then

$$(-H_2^{-1}H_0' - H_2^{-1}H_1 k_z)\Psi(\mathbf{r}_{\parallel}, z) = k_z^2\Psi(\mathbf{r}_{\parallel}, z). \tag{5.3}$$

Combining this with the trivial equation $k_z \Psi(\mathbf{r}_\parallel, z) = k_z \Psi(\mathbf{r}_\parallel, z)$,

$$\left| \begin{pmatrix} 0_{8\times8} & I_{8\times8} \\ -H_2^{-1}H'_{0_{8\times8}} & -H_2^{-1}H_{1_{8\times8}} \end{pmatrix} - k_z I_{16\times16} \right| = 0. \qquad (5.4)$$

I is the identity matrix, and 0 the zero matrix. It is straightforward to solve

for the sixteen k_z eigenvalues numerically using the NAG computing routine

F02AKF. Eigenvalues will either be real, corresponding to propagating plane

wave solutions, or complex evanescent waves (at energies in the band gap for

example). For states on the doubly degenerate heavy hole bands, there will be

four real k_z solutions, corresponding to left- and right- travelling waves for the

degenerate pair of solutions. For $E_{\text{valence band edge}} > E > E_{\text{spin split-off band edge}}$

there will be **eight** real k_z solutions representing hole states on the heavy and

light hole bands, and likewise **twelve** real solutions for states deeper in the va-

lence band where $E < E_{\text{spin split-off band edge}}$. For each k_{z_i} there is a corresponding

eigenvector

$$\begin{pmatrix} \Psi_i \\ k_{z_i}^B \Psi_i \end{pmatrix} = \begin{pmatrix} F_{i1}^B \\ \cdot \\ \cdot \\ F_{i8}^B \\ k_{z_i}^B F_{i1}^B \\ \cdot \\ \cdot \\ k_{z_i}^B F_{i8}^B \end{pmatrix}.$$

Each element F_{ij}^B defines the coefficient of the zone centre Bloch state $|\, j \rangle$ in the

bulk solution at $(E, k_\parallel, k_{z_i}^B)$ in the barrier material. For any k_z solution there will

be two eigenvectors, corresponding to the two spin degenerate pairs of solutions

that make up each band. The NAG routine produces the pairs of eigenvectors

at random phase to one another, which can be orthonormalised. All wavevectors

which propagate or decay in the direction of positive z are grouped into indices

$i = 1..8$, and those which are biased to negative z are grouped $i = 9..16$. The bulk bandstructure at $(E, k_\parallel)$ for the well material is found in the same way. By considering each barrier wave separately, it is possible to observe how an individual heavy, or light hole state interacts with the quantum well.

Writing the unbound state wavefunction in a general form, allowing ingoing and outgoing plane waves, and outgoing evanescent waves in both barriers,

$$\Psi^B_{(left)} = \sum_{j=1}^{8} \left(\sum_{ingoing\,plane} g^B_n F^B_{nj} e^{it^B_n z} + \sum_{\substack{outgoing\,plane, \\ evanescent}} a^B_i F^B_{ij} e^{is^B_i z} \right) e^{ik_\parallel \cdot r_\parallel} \mid j \rangle,$$

(5.5a)

$$\Psi^W_{(well)} = \sum_{j=1}^{8} \sum_{i=1}^{16} a^W_i F^W_{ij} e^{is^W_i z} e^{ik_\parallel \cdot r_\parallel} \mid j \rangle,$$

(5.5b)

$$\Psi^B_{(right)} = \sum_{j=1}^{8} \left(\sum_{ingoing\,plane} h^B_n F^B_{nj} e^{it^B_n z} + \sum_{\substack{outgoing\,plane, \\ evanescent}} a^B_i F^B_{ij} e^{is^B_i z} \right) e^{ik_\parallel \cdot r_\parallel} \mid j \rangle.$$

(5.5c)

To obtain a solution corresponding to one incoming barrier wave, just one of the coefficients g^B_n or h^B_n is set to unity, and the rest to zero. The thirty two unknown a^B_i and a^W_i coefficients which define the reflected and transmitted waves are then determined from the boundary conditions. One set of conditions is that the envelope function associated with each basis state is continuous across both well-barrier interfaces, which gives:

$$\sum_n g^B_n F^B_{nj} e^{-it^B_n \frac{l}{2}} + \sum_{i=1}^{8} a^B_i F^B_{ij} e^{-is^B_i \frac{l}{2}} = \sum_{i=1}^{16} a^W_i F^W_{ij} e^{-is^W_i \frac{l}{2}} \qquad j = 1..8, \quad (5.6a)$$

$$\sum_n h^B_n F^B_{nj} e^{it^B_n \frac{l}{2}} + \sum_{i=9}^{16} a^B_i F^B_{ij} e^{is^B_i \frac{l}{2}} = \sum_{i=1}^{16} a^W_i F^W_{ij} e^{is^W_i \frac{l}{2}} \qquad j = 1..8. \quad (5.6b)$$

Condensing these equations into matrix form:

$$\mathbf{i} + \overline{C}_{16\times16}\mathbf{a}^B = C_{16\times16}\mathbf{a}^W \tag{5.7}$$

where

$$\mathbf{a}^B = \begin{pmatrix} a_1^B \\ \cdot \\ \cdot \\ \cdot \\ a_{16}^B \end{pmatrix}, \mathbf{a}^W = \begin{pmatrix} a_1^W \\ \cdot \\ \cdot \\ \cdot \\ a_{16}^W \end{pmatrix}, \mathbf{i} = \begin{pmatrix} \sum_n g_n^B F_{n1}^B e^{-it_n^B \frac{l}{2}} \\ \cdot \\ \sum_n g_n^B F_{n8}^B e^{-it_n^B \frac{l}{2}} \\ \sum_n h_n^B F_{n1}^B e^{it_n^B \frac{l}{2}} \\ \cdot \\ \sum_n h_n^B F_{n8}^B e^{it_n^B \frac{l}{2}} \end{pmatrix}.$$

Integration of the Schrödinger equation through each interface gives the other set of matching conditions for the wavefunctions [15]:

$$\left(H_2^B \frac{\partial}{\partial z} + \frac{1}{2} H_1^B \right) \Psi^B \big|_{z=\pm\frac{l}{2}} = \left(H_2^W \frac{\partial}{\partial z} + \frac{1}{2} H_1^W \right) \Psi^W \big|_{z=\pm\frac{l}{2}}. \tag{5.8}$$

Hence for $j = 1..8$,

$$\sum_n g_n^B \sum_{m=1}^8 M_{jmn}^B F_{nm}^B e^{-it_n^B \frac{l}{2}} + \sum_{i=1}^8 a_i^B \sum_{m=1}^8 M_{jmi}^{\prime B} F_{im}^B e^{-is_i^B \frac{l}{2}}$$

$$= \sum_{i=1}^{16} a_i^W \sum_{m=1}^8 M_{jmi}^{\prime W} F_{im}^W e^{-is_i^W \frac{l}{2}}, \tag{5.9a}$$

$$\sum_n h_n^B \sum_{m=1}^8 M_{jmn}^B F_{nm}^B e^{it_n^B \frac{l}{2}} + \sum_{i=9}^{16} a_i^B \sum_{m=1}^8 M_{jmi}^{\prime B} F_{im}^B e^{is_i^B \frac{l}{2}}$$

$$= \sum_{i=1}^{16} a_i^W \sum_{m=1}^8 M_{jmi}^{\prime W} F_{im}^W e^{is_i^W \frac{l}{2}}, \tag{5.9b}$$

where

$$M_{jmn}^B = \left(iH_2^B(j,m)t_n^B + \frac{1}{2} H_1^B(j,m) \right),$$

$$M_{jmn}^{\prime B/W} = \left(iH_2^{B/W}(j,m)s_n^{B/W} + \frac{1}{2} H_1^{B/W}(j,m) \right).$$

83

$H_2^{B/W}(j,\,m)$ represents the element of the matrix H_2 on the jth row and m^{th} column, and likewise for $H_1^{B/W}(j,\,m)$. Collecting these into matrix form,

$$\mathbf{i}' + \overline{P}_{16\times16}\mathbf{a}^B = P_{16\times16}\mathbf{a}^W \tag{5.10}$$

where

$$\mathbf{i}' = \begin{pmatrix} \sum_n g_n^B \sum_{m=1}^8 M_{1mn}^B F_{nm}^B e^{-it_n^B \frac{l}{2}} \\ \cdot \\ \cdot \\ \sum_n g_n^B \sum_{m=1}^8 M_{8mn}^B F_{nm}^B e^{-it_n^B \frac{l}{2}} \\ \sum_n h_n^B \sum_{m=1}^8 M_{1mn}^B F_{nm}^B e^{it_n^B \frac{l}{2}} \\ \cdot \\ \cdot \\ \sum_n h_n^B \sum_{m=1}^8 M_{8mn}^B F_{nm}^B e^{it_n^B \frac{l}{2}} \end{pmatrix}.$$

Rearranging equations (5.7) and (5.10)

$$\mathbf{a}^W = (\overline{C}^{-1}C - \overline{P}^{-1}P)^{-1}(\overline{C}^{-1}\mathbf{i} - \overline{P}^{-1}\mathbf{i}'), \tag{5.11a}$$

$$\mathbf{a}^B = (C^{-1}\overline{C} - P^{-1}\overline{P})^{-1}(P^{-1}\mathbf{i} - C^{-1}\mathbf{i}'), \tag{5.11b}$$

which define the wavefunction completely. Once the terms of the matrices C, $\overline{C}$, P and $\overline{P}$ have been calculated, it is relatively straightforward to solve for $\mathbf{a}^W$ and $\mathbf{a}^B$. The appropriate matrix inversions are achieved using the NAG routine F04ADF.

The procedure for solving the quantum well bound states is much the same as that for the continuum states. The bulk bandstructure is determined for some trial $(E,\,k_\parallel)$, and linear combinations of the bulk solutions are matched across the interfaces. For bound states, the appropriate evanescent solutions are chosen in the barriers on each side of the well such that the wavefunction decays into the barriers, and the probability density remains finite everywhere. The

wavefunction in the well and barriers is:

$$\Psi^B_{(left)} = \sum_{j=1}^{8} \sum_{i=1}^{8} a^B_i F^B_{ij} e^{i s^B_i z} e^{i \mathbf{k}_\parallel \cdot \mathbf{r}_\parallel} \mid j \rangle, \tag{5.12a}$$

$$\Psi^W_{(well)} = \sum_{j=1}^{8} \sum_{i=1}^{16} a^W_i F^W_{ij} e^{i s^W_i z} e^{i \mathbf{k}_\parallel \cdot \mathbf{r}_\parallel} \mid j \rangle, \tag{5.12b}$$

$$\Psi^B_{(right)} = \sum_{j=1}^{8} \sum_{i=9}^{16} a^B_i F^B_{ij} e^{i s^B_i z} e^{i \mathbf{k}_\parallel \cdot \mathbf{r}_\parallel} \mid j \rangle. \tag{5.12c}$$

Applying the matching conditions for the envelope functions across the well-barrier boundaries, for $j = 1..8$,

$$\sum_{i=1}^{8} a^B_i F^B_{ij} e^{-i s^B_i \frac{l}{2}} = \sum_{i=1}^{16} a^W_i F^W_{ij} e^{-i s^W_i \frac{l}{2}}, \tag{5.13a}$$

$$\sum_{i=9}^{16} a^B_i F^B_{ij} e^{i s^B_i \frac{l}{2}} = \sum_{i=1}^{16} a^W_i F^W_{ij} e^{i s^W_i \frac{l}{2}}, \tag{5.13b}$$

$$\sum_{i=1}^{8} a^B_i \sum_{m=1}^{8} M'^B_{jmi} F^B_{im} e^{-i s^B_i \frac{l}{2}} = \sum_{i=1}^{16} a^W_i \sum_{m=1}^{8} M'^W_{jmi} F^W_{im} e^{-i s^W_i \frac{l}{2}}, \tag{5.13c}$$

$$\sum_{i=9}^{16} a^B_i \sum_{m=1}^{8} M'^B_{jmi} F^B_{im} e^{i s^B_i \frac{l}{2}} = \sum_{i=1}^{16} a^W_i \sum_{m=1}^{8} M'^W_{jmi} F^W_{im} e^{i s^W_i \frac{l}{2}}. \tag{5.13d}$$

which combine to give:

$$\overline{C} \mathbf{a}^B = C \mathbf{a}^W, \tag{5.14a}$$

$$\overline{P} \mathbf{a}^B = P \mathbf{a}^W. \tag{5.14b}$$

Column vectors $\mathbf{a}^W$ and $\mathbf{a}^B$ take the same form as listed in equation 5.7. Valid solutions for these exist so long as

$$\mid \overline{P}^{-1} P C^{-1} \overline{C} - I_{16 \times 16} \mid = 0. \tag{5.15}$$

This condition identifies allowed energy states. By scanning a range of $E - \mathbf{k}_\parallel$ space and listing all zeros of the determinant in equation 5.15, the quantum well

85
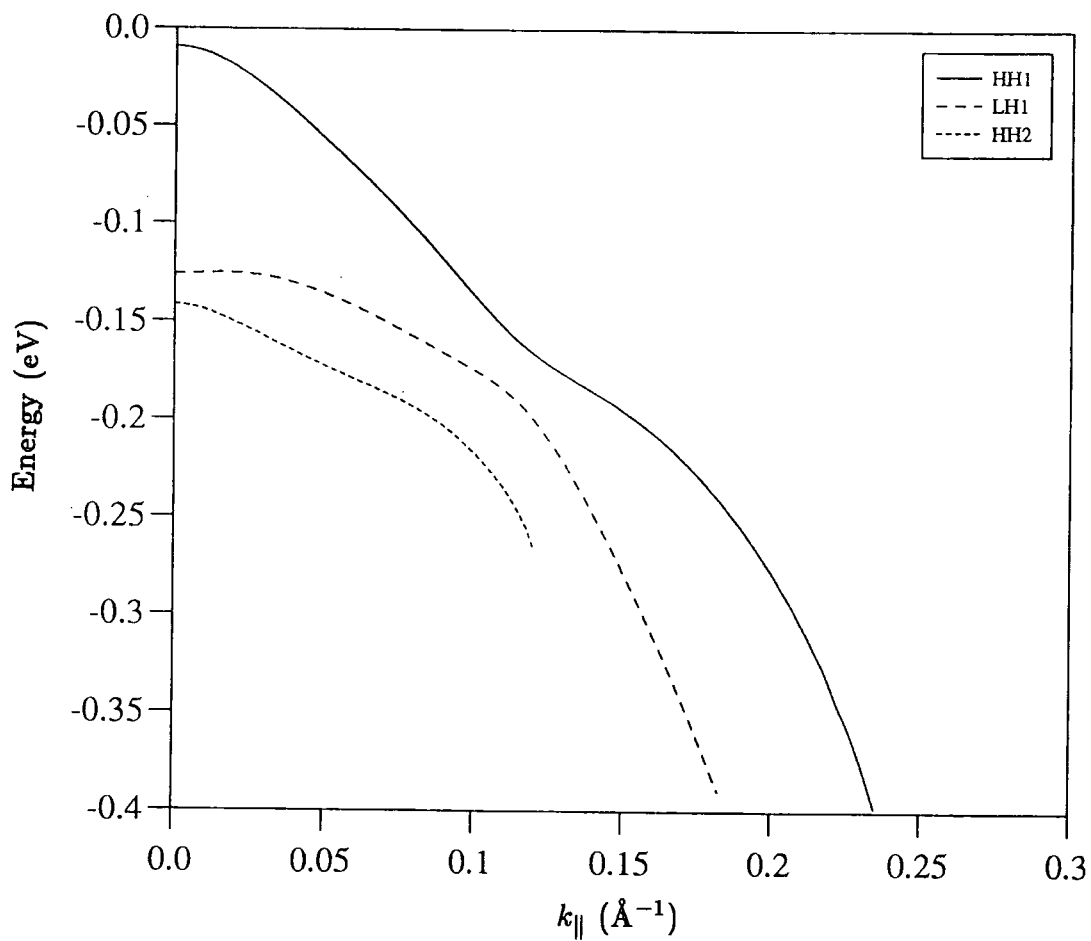
Figure 5.2 The valence subband dispersions for a 30Å $In_{0.7}Ga_{0.3}As$-$In_{0.75}Ga_{0.25}As_{0.55}P_{0.45}$ quantum well. The biaxial compressive strain in the well is 1.2%.
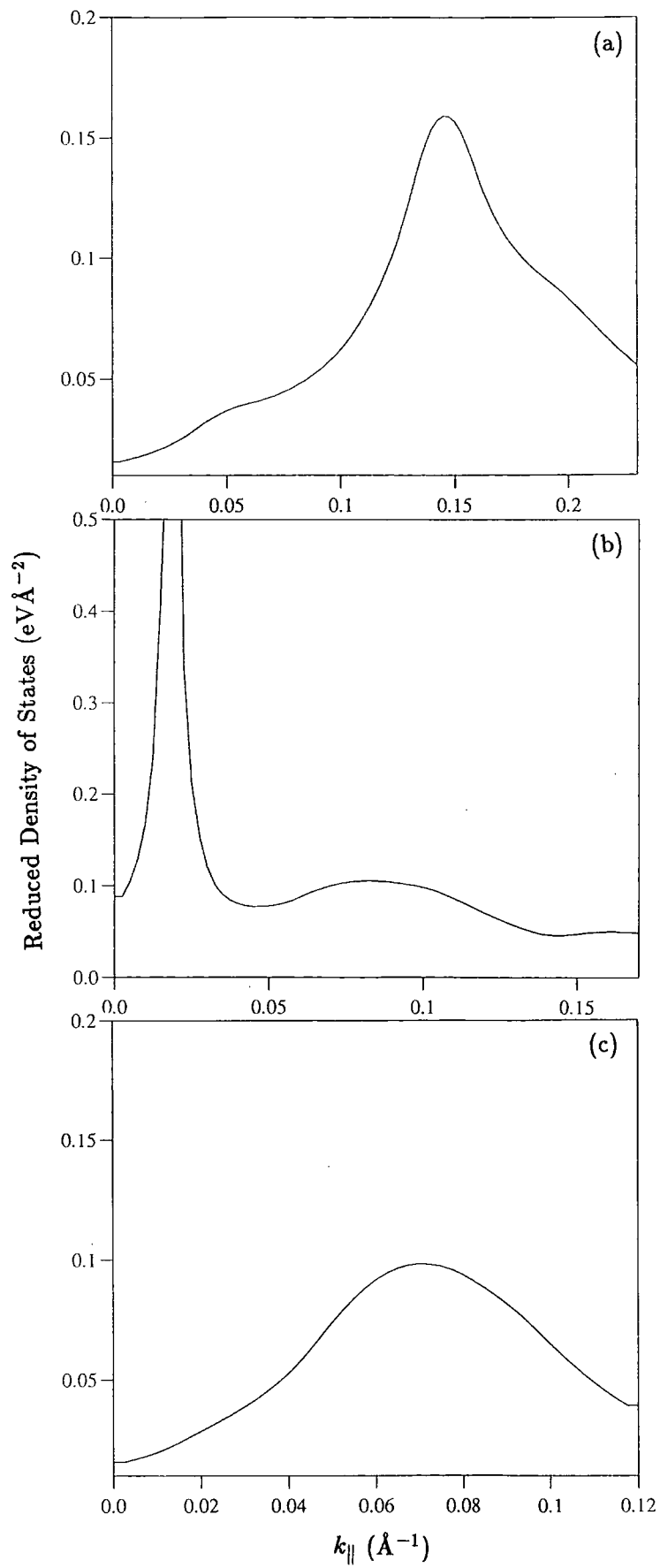
Figure 5.3 Density of states $\frac{k_\parallel}{\frac{\partial E}{\partial k_\parallel}}$ for the (a) HH1, (b) LH1 and (c) HH2 subbands as a function of in-plane wavevector $k_\parallel$.
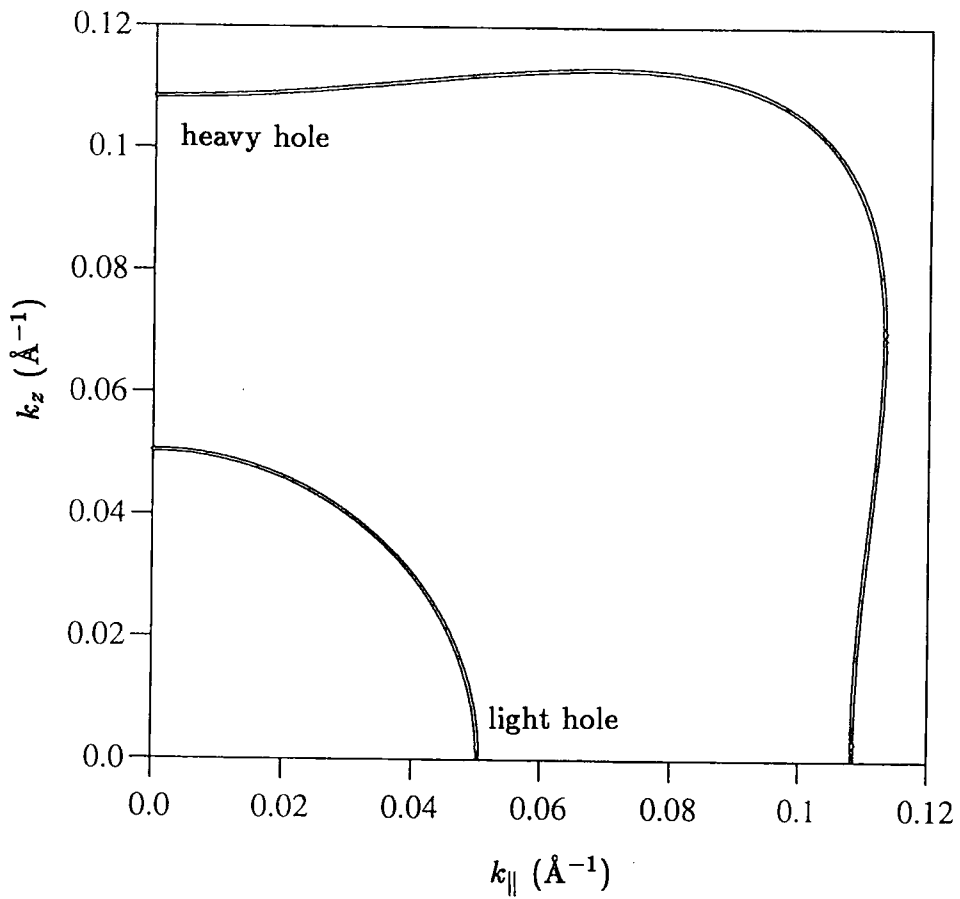
Figure 5.4 Cross-section through the constant energy surfaces of bulk $In_{0.75}Ga_{0.25}As_{0.55}P_{0.45}$, illustrating the warping of the heavy hole band.

Values for negative k_z are obtained by reflection in the axes.

subbands can be obtained. The search for energies was carried out using an iterative technique developed by Walmsley [20].

As with the unbound states, the bound state wavefunctions appear as degenerate pairs. The envelope functions for these solutions are not in general orthogonal, but for calculational convenience can be combined to form two orthogonal wavefunctions with envelopes of definite parity.

The valence bandstructure of the 30 Å $In_{0.7}Ga_{0.3}As$-$In_{0.75}Ga_{0.25}As_{0.55}P_{0.45}$ well is shown in figure 5.2. The subbands are almost isotropic in the k_x-k_y plane, and so the bands are suitably represented by the single variable $k_\parallel$. The subbands are non-parabolic due to mixing, and this is reflected in the fluctuating reduced density of states $k_\parallel / \mid \frac{\partial E}{\partial k_\parallel} \mid$ for each band (figure 5.3).

5.4 Unbound-bound scattering matrix elements

In the quantum capture process by optical phonon emission, holes may only make transitions into bound states lying within an optical phonon energy of the continuum edge. Within this energy range the initial states of the holes can be considered to result from scattering of the incoming barrier states by the quantum well. Holes approaching the well in the spin split-off band cannot be captured directly since this band lies out of the energy range. Figure 5.4 shows the form of part of the constant energy surfaces for bulk $In_{0.75}Ga_{0.25}As_{0.55}P_{0.45}$. The heavy hole band is warped with an effective mass which becomes heavier away from the principal axes. At $k_\parallel = 0$, k_z has two magnitudes, one corresponding to a light

hole state, the other to a state on the heavy hole band (the heavy and light hole bands are degenerate at $k_{\parallel} = 0$ for unstrained InGaAsP). At intermediate $k_{\parallel}$ only heavy hole plane wave states exist. For larger $k_{\parallel}$, $\mid k_z \mid$ is again double-valued, but both solutions are derived from the heavy hole band.

Consider a transition from an unbound state $\Psi^u_{k_{\parallel}}$, to a final state $\Psi^b_{n,k'_{\parallel}}$ on the nth subband. Rewriting equations (5.5a..c) in condensed notation,

$$\Psi^u_{(left)} = \sum_{j=1}^{8} \sum_{i=1}^{8} \left(\eta^B_{ijh} e^{it^B_i z} + \epsilon^B_{ijh} e^{is^B_i z} \right) e^{ik_{\parallel} \cdot r_{\parallel}} \mid j \rangle \qquad h = 1, 2, \qquad (5.16a)$$

$$\Psi^u_{(well)} = \sum_{j=1}^{8} \sum_{i=1}^{16} \epsilon^W_{ijh} e^{is^W_i z} e^{ik_{\parallel} \cdot r_{\parallel}} \mid j \rangle \qquad h = 1, 2, \qquad (5.16b)$$

$$\Psi^u_{(right)} = \sum_{j=1}^{8} \sum_{i=9}^{16} \left(\eta^B_{ijh} e^{it^B_i z} + \epsilon^B_{ijh} e^{is^B_i z} \right) e^{ik_{\parallel} \cdot r_{\parallel}} \mid j \rangle \qquad h = 1, 2. \qquad (5.16c)$$

Similarly for equations (5.12a..c),

$$\Psi^b_{(left)} = \sum_{j=1}^{8} \sum_{i=1}^{8} \alpha^B_{ijh'} e^{ia^B_i z} e^{ik_{\parallel} \cdot r_{\parallel}} \mid j \rangle \qquad h' = 3, 4, \qquad (5.17a)$$

$$\Psi^b_{(well)} = \sum_{j=1}^{8} \sum_{i=1}^{16} \alpha^W_{ijh'} e^{ia^W_i z} e^{ik_{\parallel} \cdot r_{\parallel}} \mid j \rangle \qquad h' = 3, 4, \qquad (5.17b)$$

$$\Psi^b_{(right)} = \sum_{j=1}^{8} \sum_{i=9}^{16} \alpha^B_{ijh'} e^{ia^B_i z} e^{ik_{\parallel} \cdot r_{\parallel}} \mid j \rangle \qquad h' = 3, 4. \qquad (5.17c)$$

Since the unbound and bound wavefunctions are doubly spin-degenerate, the net scattering matrix element between the initial unbound states (with spin indices $h = 1, 2$) and final bound energy states (spin indices $h' = 3, 4$) is given by (recall chapter 3):

$$\mid M \mid^2 = \frac{\mid M_{13} \mid^2 + \mid M_{14} \mid^2 + \mid M_{23} \mid^2 + \mid M_{24} \mid^2}{2}. \qquad (5.18)$$

The pairs of eigenfunctions for a bulk plane wave at energy E and with wavevector components $k_\|$, k_z, or with components $k_\|$, $-k_z$ are made up of the same weightings of the basis states. It follows that the modulus of the matrix element squared for scattering from a heavy or light hole wave incident from the left hand barrier is identical to that for the corresponding wave incident from the right hand barrier. In the application of Fermi's Golden Rule, the unbound and bound states are normalised across a chosen region of space. The appropriate normalisation constants for unit area in the plane of the quantum well and a distance of $L = 1\,\mu\mathrm{m}$ transverse to it, are respectively for unbound and bound states:

$$N_U = \int_{-\frac{L}{2}}^{-\frac{l}{2}} \mid \Psi^u_{(left)}(z) \mid^2 dz + \int_{-\frac{l}{2}}^{\frac{l}{2}} \mid \Psi^u_{(well)}(z) \mid^2 dz + \int_{\frac{l}{2}}^{\frac{L}{2}} \mid \Psi^u_{(right)}(z) \mid^2 dz,$$

(5.19)

$$N_B = \int_{-\frac{L}{2}}^{-\frac{l}{2}} \mid \Psi^b_{(left)}(z) \mid^2 dz + \int_{-\frac{l}{2}}^{\frac{l}{2}} \mid \Psi^b_{(well)}(z) \mid^2 dz + \int_{\frac{l}{2}}^{\frac{L}{2}} \mid \Psi^b_{(right)}(z) \mid^2 dz.$$

(5.20)

5.4a Alloy scattering

Allowing for the possibility of capture by alloy scattering (including scattering centres in the barriers in addition to those in the well), the scattering rate into subband n from either a heavy or a light hole barrier state is:

$$P^{AL}_{(k_\|,k_z \to n,k'_\|)} = \frac{1}{4\hbar} \sum_{h=1}^{2} \sum_{h'=3}^{4} \frac{1}{2} \mid M_{AL} \mid^2 \frac{k'_\|}{\mid \frac{\partial E}{\partial k'_\|} \mid},$$

$$\mid M_{AL} \mid^2 = a_0^3 x(1-x)(\Delta V)^2 \mid M^{well}_{AL} \mid^2 + a_0'^3 (\Delta U)^2 (\mid M^{left}_{AL} \mid^2 + \mid M^{right}_{AL} \mid^2).$$

(5.21)

$$| \mathrm{M}_{AL}^{well} |^2 = \frac{1}{N_U N_B} \sum_{j,j'=1}^{8} \sum_{i,i'=1}^{16} \sum_{m,m'=1}^{16} \alpha_{ijh'}^{W*} \epsilon_{i'jh}^{W} \alpha_{mj'h'}^{W} \epsilon_{m'j'h}^{W*}$$

$$\times \begin{cases} l & s_{i'}^{W} + a_m^{W} - s_{m'}^{W*} - a_i^{W*} = 0; \\ \frac{2\sin(s_{i'}^{W}+a_m^{W}-s_{m'}^{W*}-a_i^{W*})\frac{l}{2}}{(s_{i'}^{W}+a_m^{W}-s_{m'}^{W*}-a_i^{W*})} & a_{i'}^{W} + b_m^{W} - a_{m'}^{W*} - b_i^{W*} \neq 0. \end{cases} \qquad (5.22\text{a})$$

$$| \mathrm{M}_{AL}^{left} |^2 = \frac{1}{N_U N_B} \sum_{j,j'=1}^{8} \sum_{i,i'=1}^{8} \sum_{m,m'=1}^{8}$$

$$\alpha_{i'jh'}^{B*} \eta_{ijh}^{B} \alpha_{m'j'h'}^{B} \eta_{mj'h}^{B*} \left(\frac{e^{-i(t_i^B - a_{i'}^{B*} - t_m^{B*} + a_{m'}^{B})\frac{l}{2}} - e^{-i(t_i^B - a_{i'}^{B*} - t_m^{B*} + a_{m'}^{B})\frac{L}{2}}}{i(t_i^B - a_{i'}^{B*} - t_m^{B*} + a_{m'}^{B})} \right)$$

$$+\alpha_{i'jh'}^{B*} \eta_{ijh}^{B} \alpha_{m'j'h'}^{B} \epsilon_{mj'h}^{B*} \left(\frac{e^{-i(t_i^B - a_{i'}^{B*} - s_m^{B*} + a_{m'}^{B})\frac{l}{2}} - e^{-i(t_i^B - a_{i'}^{B*} - s_m^{B*} + a_{m'}^{B})\frac{L}{2}}}{i(t_i^B - a_{i'}^{B*} - s_m^{B*} + a_{m'}^{B})} \right)$$

$$+\alpha_{i'jh'}^{B*} \epsilon_{ijh}^{B} \alpha_{m'j'h'}^{B} \eta_{mj'h}^{B*} \left(\frac{e^{-i(s_i^B - a_{i'}^{B*} - t_m^{B*} + a_{m'}^{B})\frac{l}{2}} - e^{-i(s_i^B - a_{i'}^{B*} - t_m^{B*} + a_{m'}^{B})\frac{L}{2}}}{i(s_i^B - a_{i'}^{B*} - t_m^{B*} + a_{m'}^{B})} \right)$$

$$+\alpha_{i'jh'}^{B*} \epsilon_{ijh}^{B} \alpha_{m'j'h'}^{B} \epsilon_{mj'h}^{B*} \left(\frac{e^{-i(s_i^B - a_{i'}^{B*} - s_m^{B*} + a_{m'}^{B})\frac{l}{2}} - e^{-i(s_i^B - a_{i'}^{B*} - s_m^{B*} + a_{m'}^{B})\frac{L}{2}}}{i(s_i^B - a_{i'}^{B*} - s_m^{B*} + a_{m'}^{B})} \right),$$

$$(5.22\text{b})$$

$$| \mathrm{M}_{AL}^{right} |^2 = \frac{1}{N_U N_B} \sum_{j,j'=1}^{8} \sum_{i,i'=9}^{16} \sum_{m,m'=9}^{16}$$

$$\alpha_{i'jh'}^{B*} \eta_{ijh}^{B} \alpha_{m'j'h'}^{B} \eta_{mj'h}^{B*} \left(\frac{e^{i(t_i^B - a_{i'}^{B*} - t_m^{B*} + a_{m'}^{B})\frac{L}{2}} - e^{i(t_i^B - a_{i'}^{B*} - t_m^{B*} + a_{m'}^{B})\frac{l}{2}}}{i(t_i^B - a_{i'}^{B*} - t_m^{B*} + a_{m'}^{B})} \right)$$

$$+\alpha_{i'jh'}^{B*} \eta_{ijh}^{B} \alpha_{m'j'h'}^{B} \epsilon_{mj'h}^{B*} \left(\frac{e^{i(t_i^B - a_{i'}^{B*} - s_m^{B*} + a_{m'}^{B})\frac{L}{2}} - e^{i(t_i^B - a_{i'}^{B*} - s_m^{B*} + a_{m'}^{B})\frac{l}{2}}}{i(t_i^B - a_{i'}^{B*} - s_m^{B*} + a_{m'}^{B})} \right)$$

$$+\alpha_{i'jh'}^{B*} \epsilon_{ijh}^{B} \alpha_{m'j'h'}^{B} \eta_{mj'h}^{B*} \left(\frac{e^{i(s_i^B - a_{i'}^{B*} - t_m^{B*} + a_{m'}^{B})\frac{L}{2}} - e^{i(s_i^B - a_{i'}^{B*} - t_m^{B*} + a_{m'}^{B})\frac{l}{2}}}{i(s_i^B - a_{i'}^{B*} - t_m^{B*} + a_{m'}^{B})} \right)$$

$$+\alpha_{i'jh'}^{B*} \epsilon_{ijh}^{B} \alpha_{m'j'h'}^{B} \epsilon_{mj'h}^{B*} \left(\frac{e^{i(s_i^B - a_{i'}^{B*} - s_m^{B*} + a_{m'}^{B})\frac{L}{2}} - e^{i(s_i^B - a_{i'}^{B*} - s_m^{B*} + a_{m'}^{B})\frac{l}{2}}}{i(s_i^B - a_{i'}^{B*} - s_m^{B*} + a_{m'}^{B})} \right). \qquad (5.22\text{c})$$

In equation 5.21, a_0' is the lattice parameter for the InGaAsP. As in chapter 3, the alloy scattering potential for InGaAs, ΔV is taken as 0.534 eV. According to Littlejohn et al [21], the alloy potential factor for InGaAsP is given by

$$(\Delta U(In_xGa_{1-x}As_yP_{1-y}))^2 = x(1-x)y^2(\Delta V_{InGaAs})^2$$

$$+x(1-x)(1-y)^2(\Delta V_{InGaP})^2$$

$$+y(1-y)x^2(\Delta V_{InAsP})^2$$

$$+y(1-y)(1-x)^2(\Delta V_{GaAsP})^2. \qquad (5.23)$$

Applying this formula, using the values for ΔV_{InGaP} etc. listed in [21], $(\Delta U)^2$ $\sim 0.081\,\mathrm{eV}^2$.

5.4b Phonon induced capture

For acoustic (elastic approximation) and non-polar optical phonon scattering, the capture rates are respectively:

$$P^{AC}_{(k_\parallel,k_z \to n,k'_\parallel)} = \frac{k_B T_L D_{ac}^2}{4\pi\rho\hbar v_s^2} \frac{k'_\parallel}{\mid \frac{\partial E}{\partial k'_\parallel} \mid} \sum_{h=1}^{2} \sum_{h'=3}^{4} \frac{1}{2} \int_{-\infty}^{\infty} \mid M(q_z) \mid^2 dq_z, \qquad (5.24)$$

$$P^{NPO}_{(k_\parallel,k_z \to n,k'_\parallel)} = \frac{D_{op}^2}{4\pi\rho\omega_{op}} \left(\begin{array}{c} n_q \\ n_q+1 \end{array} \right) \frac{k'_\parallel}{\mid \frac{\partial E}{\partial k'_\parallel} \mid} \sum_{h=1}^{2} \sum_{h'=3}^{4} \frac{1}{2} \int_{-\infty}^{\infty} \mid M(q_z) \mid^2 dq_z, \qquad (5.25)$$

where the symbols are as defined in chapter 3. The matrix elements squared are given by

$$\mid M(q_z) \mid^2 = \frac{1}{N_U N_B} \mid I_{(left)}(q_z) + I_{(well)}(q_z) + I_{(right)}(q_z) \mid^2 \qquad (5.26)$$

where

$$I_{(well)} = \sum_{j=1}^{8} \sum_{i'=1}^{16} 2\epsilon_{ijh}^{W} \alpha_{i'jh'}^{W*} \frac{\sin(s_i^{W} - a_{i'}^{W*} \pm q_z)\frac{l}{2}}{i(s_i^{W} - a_{i'}^{W*} \pm q_z)},$$

$$I_{(left)} = \sum_{j=1}^{8} \sum_{i'=1}^{8} \epsilon_{ijh}^{B} \alpha_{i'jh'}^{B*} \frac{e^{-i(s_i^B - a_{i'}^{B*} \pm q_z)\frac{l}{2}} - e^{-i(s_i^B - a_{i'}^{B*} \pm q_z)\frac{L}{2}}}{i(s_i^B - a_{i'}^{B*} \pm q_z)}$$

$$+\eta_{ijh}^{B} \alpha_{i'jh'}^{B*} \frac{e^{-i(t_i^B - a_{i'}^{B*} \pm q_z)\frac{l}{2}} - e^{-i(t_i^B - a_{i'}^{B*} \pm q_z)\frac{L}{2}}}{i(t_i^B - a_{i'}^{B*} \pm q_z)},$$

$$I_{(right)} = \sum_{j=1}^{8} \sum_{i'=9}^{16} \epsilon_{ijh}^{B} \alpha_{i'jh'}^{B*} \frac{e^{i(s_i^B - a_{i'}^{B*} \pm q_z)\frac{L}{2}} - e^{i(s_i^B - a_{i'}^{B*} \pm q_z)\frac{l}{2}}}{i(s_i^B - a_{i'}^{B*} \pm q_z)}$$

$$+\eta_{ijh}^{B} \alpha_{i'jh'}^{B*} \frac{e^{i(t_i^B - a_{i'}^{B*} \pm q_z)\frac{L}{2}} - e^{i(t_i^B - a_{i'}^{B*} \pm q_z)\frac{l}{2}}}{i(t_i^B - a_{i'}^{B*} \pm q_z)},$$

where $\pm q_z$ denote phonon absorption and emission respectively. Values for the crystal density ρ and other material data in the rate prefactors are listed in table 5.3. The Fermi's Golden Rule capture rate by polar optical phonons is

$$P_{(k_\parallel, k_z \to n, k_\parallel')}^{POP} = \frac{e^2 \omega_{op}}{8\pi^2 \epsilon_0} \left(\frac{1}{\epsilon_\infty} - \frac{1}{\epsilon_s} \right) \binom{n_q}{n_q + 1} \frac{k_\parallel'}{\mid \frac{\partial E}{\partial k_\parallel'} \mid}$$

$$\times \sum_{h=1}^{2} \sum_{h'=3}^{4} \frac{1}{2} \int_{-\infty}^{\infty} \frac{2\pi \mid M(q_z) \mid^2}{\sqrt{q_z^4 + 2(k_\parallel^2 + k_\parallel'^2)q_z^4 + (k_\parallel^2 - k_\parallel'^2)^2}} dq_z, \qquad (5.27)$$

where

$$\mid M(q_z) \mid^2 = \frac{1}{N_U N_B} \mid I_{(left)}(q_z) + I_{(well)}(q_z) + I_{(right)}(q_z) \mid^2 . \qquad (5.28)$$

Table 5.3 Parameters for hole capture rates for $In_{0.7}Ga_{0.3}As$

at a lattice temperature $T_L=300\,K$.

ϵ_s	14.14
ϵ_∞	11.84
D_{ac} (eV)	4.65
ρ (kgm^{-3})	5575.0
D_{op} (eVm^{-1})	41.7
v_s (ms^{-1})	3326.0
$\hbar\omega_{op}$ (meV)	30.1

5.5 Carrier trapping efficiency of the well

In section 5.4 the scattering matrix elements were determined by normalising the unbound and bound states within a volume of real space. By choosing this volume to be that of the total confinement region AL, the probability of capture $P_{(k_{||},k_z \to n,k_{||})}$ into a well of width l from any given unbound state is of the order $\frac{l}{L}$.

However, if hole capture data were to be applied to a simulation of relaxation within a quantum well laser, by Monte Carlo techniques for instance, it would be desirable to have capture data which depends on the conditions in the vicinity of the well and is independent of the dimensions of the confinement region. That way, the data could be applied universally across a range of structures of different confinement widths. Indeed, if the holes are frequently scattered in their passage across the confinement region, a quantum mechanical model of the whole system is inappropriate and the dimensions of the confinement region will only influence

the capture rate through classical transport factors such as diffusion currents and local carrier densities.

Another way to look at the problem is to consider the fraction of incident hole current which is captured by the well. This information can be regarded as local to the well and can readily be employed in a classical model of transport and well capture for the whole device. Within this approach, heavy or light holes incident on the well are represented by a plane wave which is taken to describe the quantum mechanical propagation of the particle since its last scattering before arriving at the well. The particle current associated with such a wave is given by the quantum mechanical flux. In section 5.4 the wavefunction describing the incident, reflected and transmitted waves was normalised to unity in the confinement volume but the result can still be used in this new approach. The incident plane wave part of the wavefunction has the form $(AN_U)^{-\frac{1}{2}}e^{i\mathbf{k}\cdot\mathbf{r}}$, where N_U was defined in equation 5.19 and the associated current density j_i is

$$j_i = \frac{v_z}{AN_U} = \frac{1}{\hbar AN_U}\frac{\partial E}{\partial k_z},$$ (5.29)

where v_z is the velocity transverse to the well plane for holes of wavevector $(k_{\parallel}, k_z)$. The capture probability per unit area of the well is $A^{-1}P_{(k_{\parallel},k_z\to n,k'_{\parallel})}$ and may be expressed as a fraction $p(k_{\parallel}, k_z)$, of the rate per unit area j_i at which holes are incident on the well:

$$p(k_{\parallel}, k_z) = \frac{P_{(k_{\parallel},k_z\to n,k'_{\parallel})}}{A.j_i}.$$ (5.30)

This is a useful figure of merit for the carrier capture properties of the well. Now $A^{-1}P_{(k_{\parallel},k_z\to n,k'_{\parallel})}$ is the capture rate per unit area when $(AN_U)^{-1}$ holes per unit
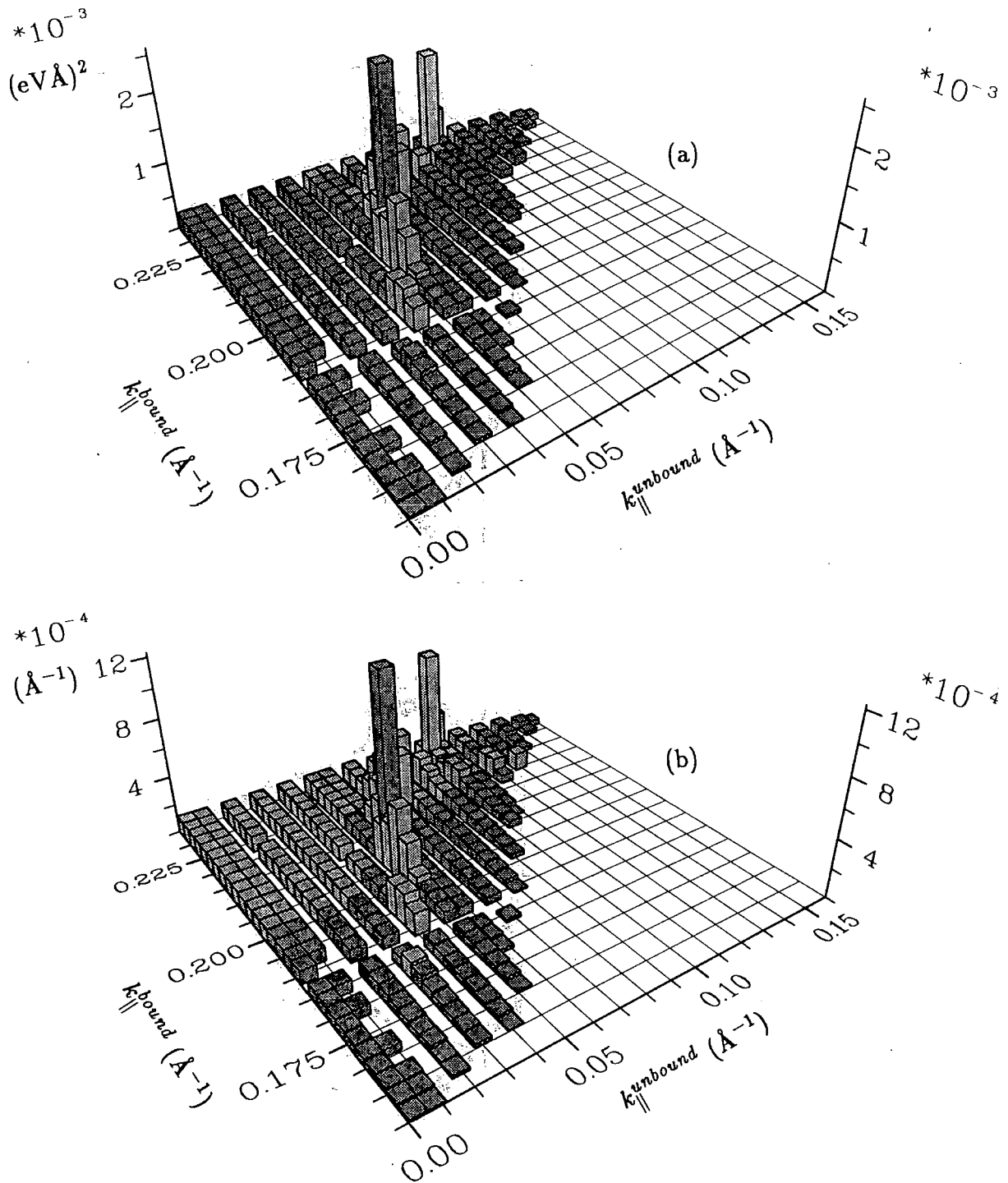
Figure 5.5 Moduli squared of matrix elements plotted against $k_{\parallel}^{bound}$ and $k_{\parallel}^{unbound}$ for (a) alloy, and (b) acoustic phonon scattering from heavy hole unbound states into the HH1 subband of figure 5.2.
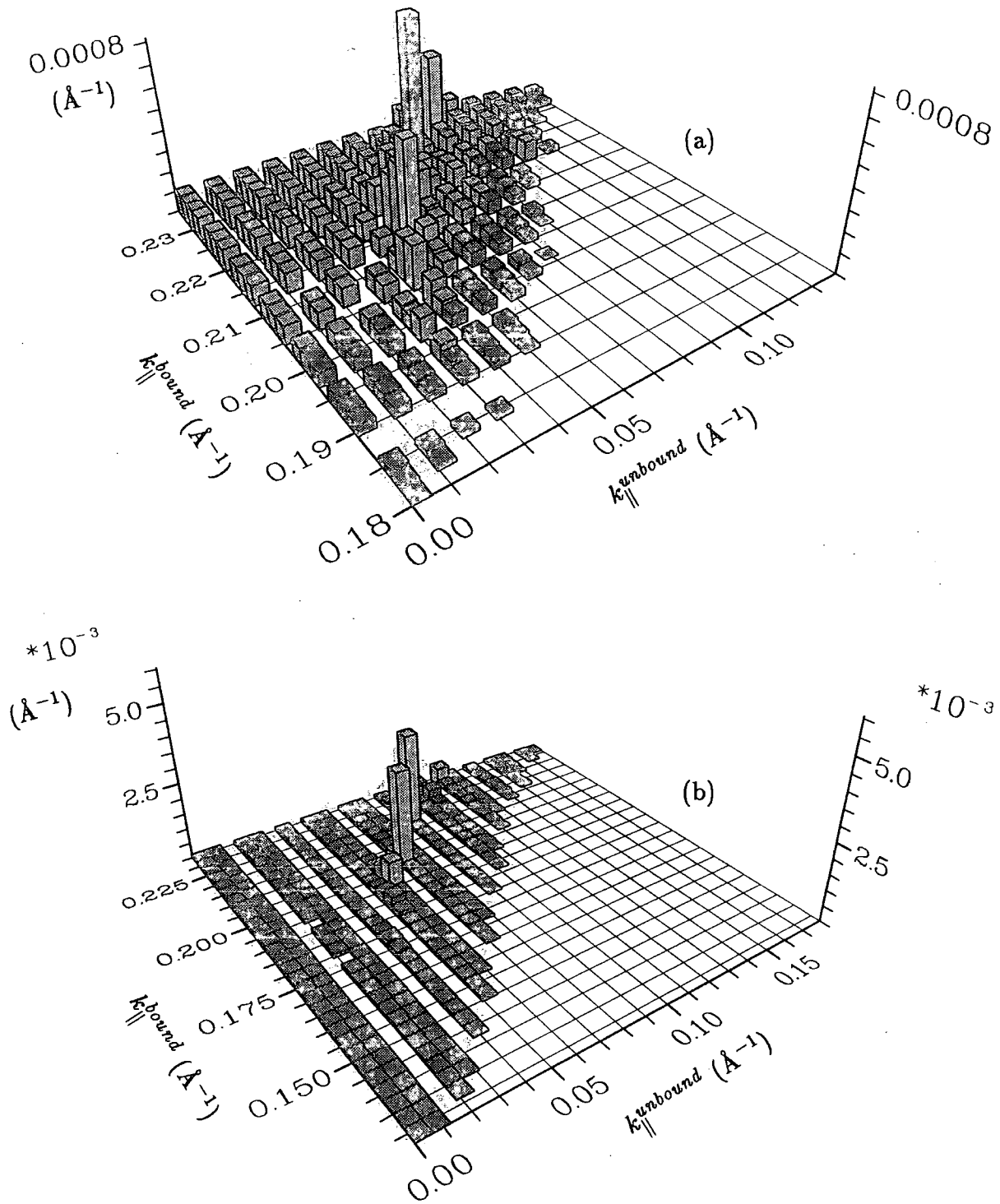
Figure 5.6 Moduli squared of matrix elements plotted against $k_{\parallel}^{bound}$ and $k_{\parallel}^{unbound}$ for (a) non-polar optical phonon absorption, and (b) non-polar optical phonon emission from heavy hole unbound states into the HH1 subband of figure 5.2.
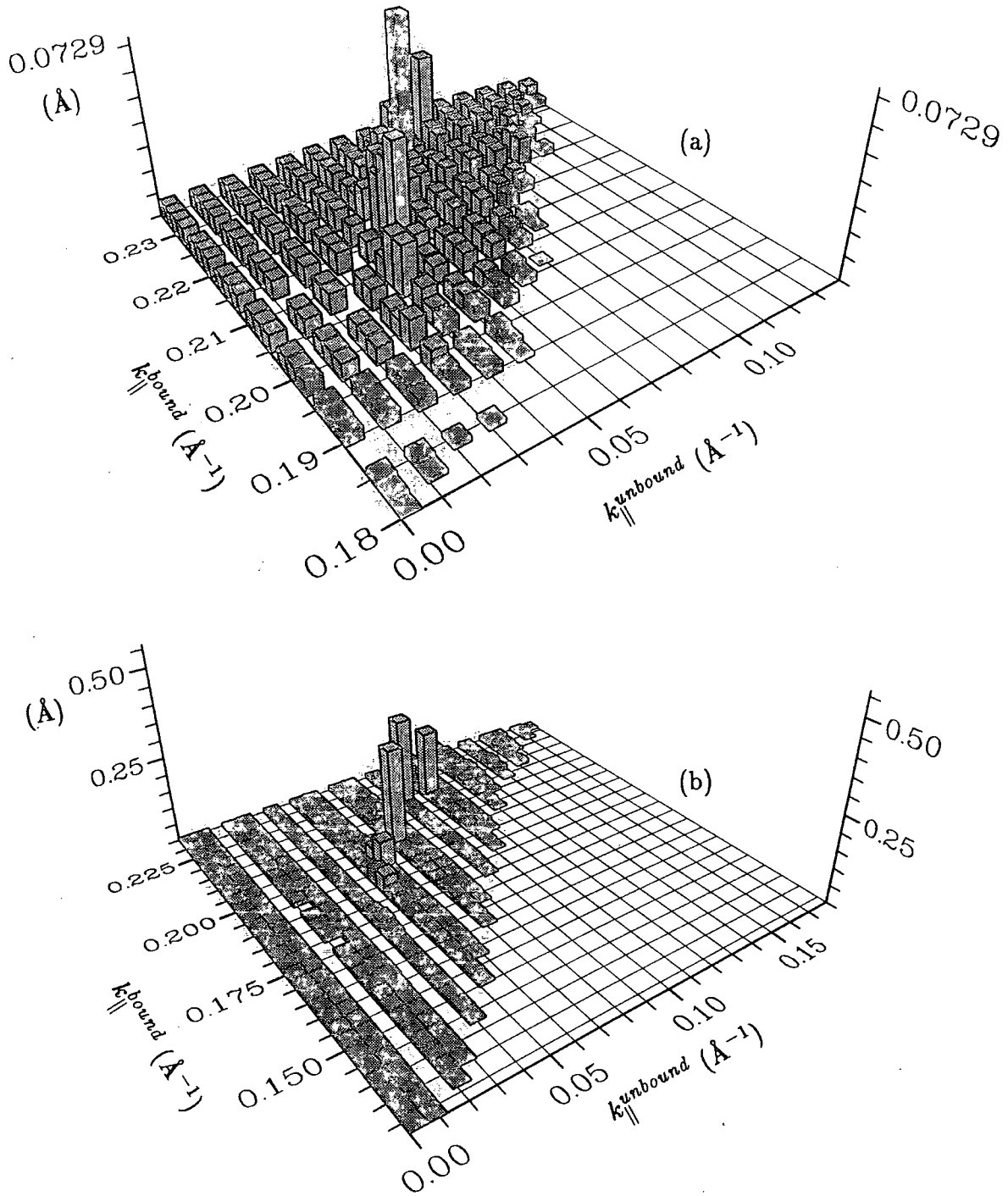
Figure 5.7 Moduli squared of matrix elements plotted against $k_{\parallel}^{bound}$ and $k_{\parallel}^{unbound}$ for (a) polar optical phonon absorption, and (b) polar optical phonon emission from heavy hole unbound states into the HH1 subband of figure 5.2.
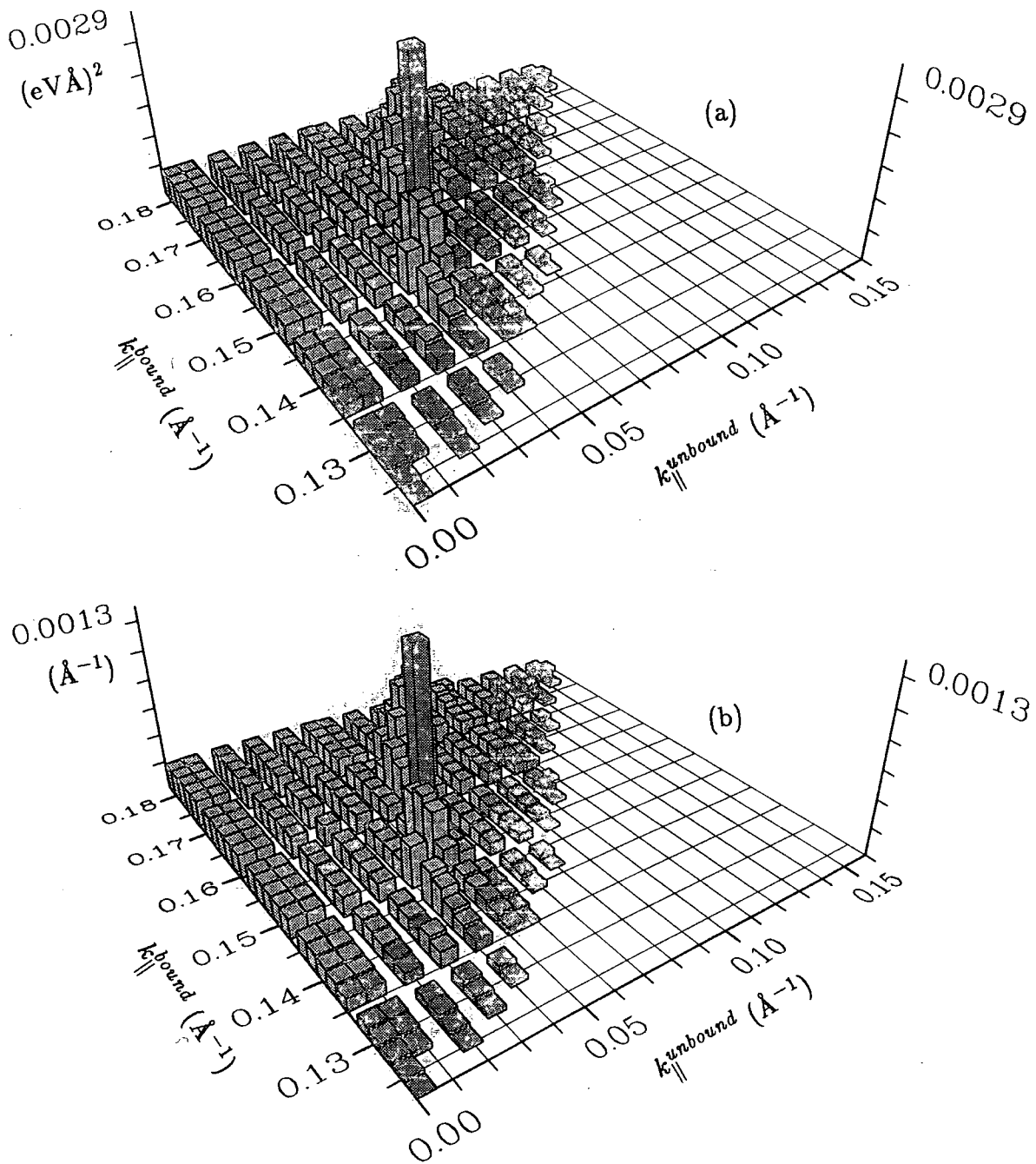
Figure 5.8 Moduli squared of matrix elements plotted against $k_{\parallel}^{bound}$ and $k_{\parallel}^{unbound}$

for (a) alloy, and (b) acoustic phonon scattering from heavy hole unbound states into the LH1 subband of figure 5.2.
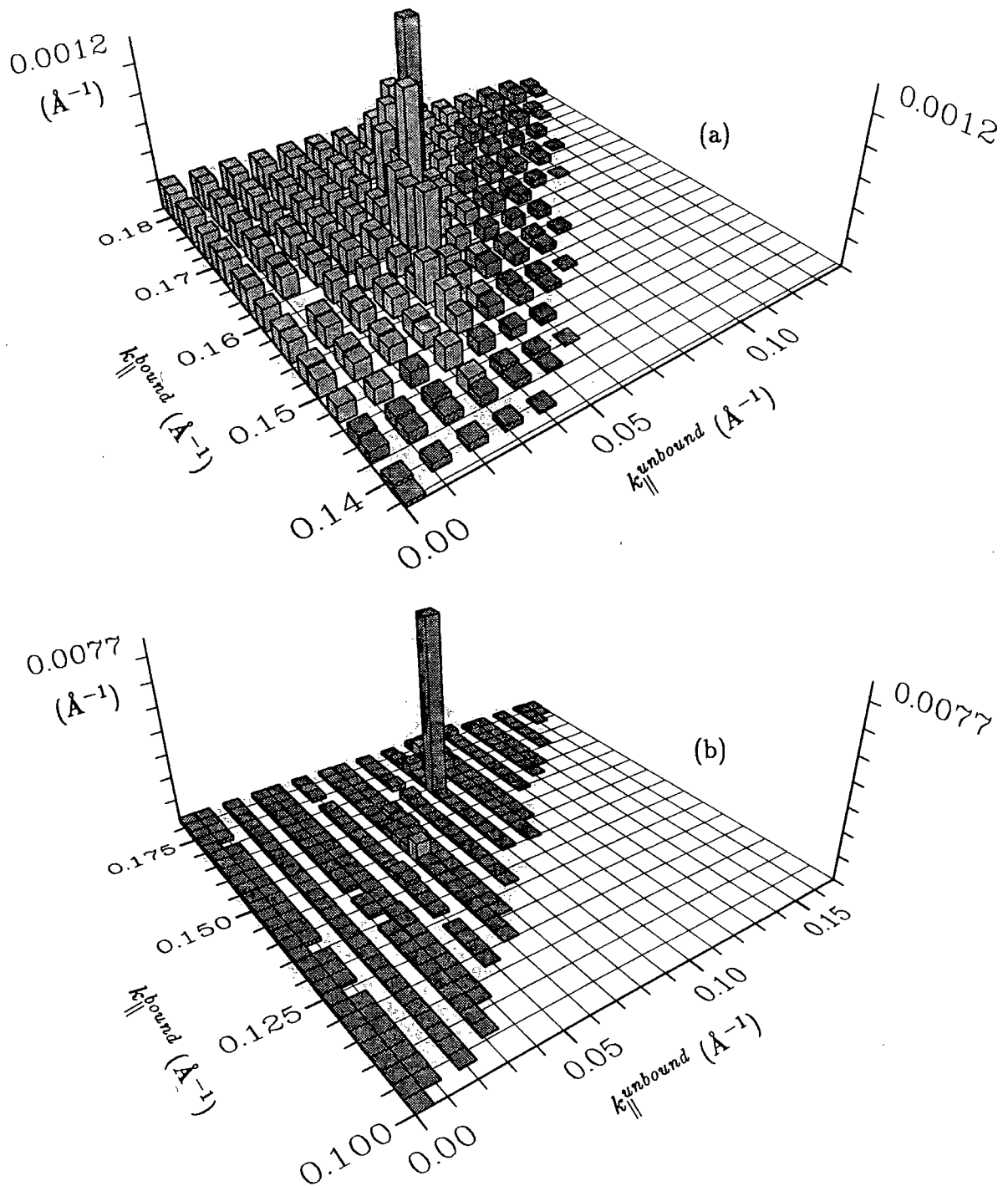
Figure 5.9 Moduli squared of matrix elements plotted against $k_{\parallel}^{bound}$ and $k_{\parallel}^{unbound}$ for (a) non-polar optical phonon absorption, and (b) non-polar optical phonon emission from heavy hole unbound states into the LH1 subband of figure 5.2.
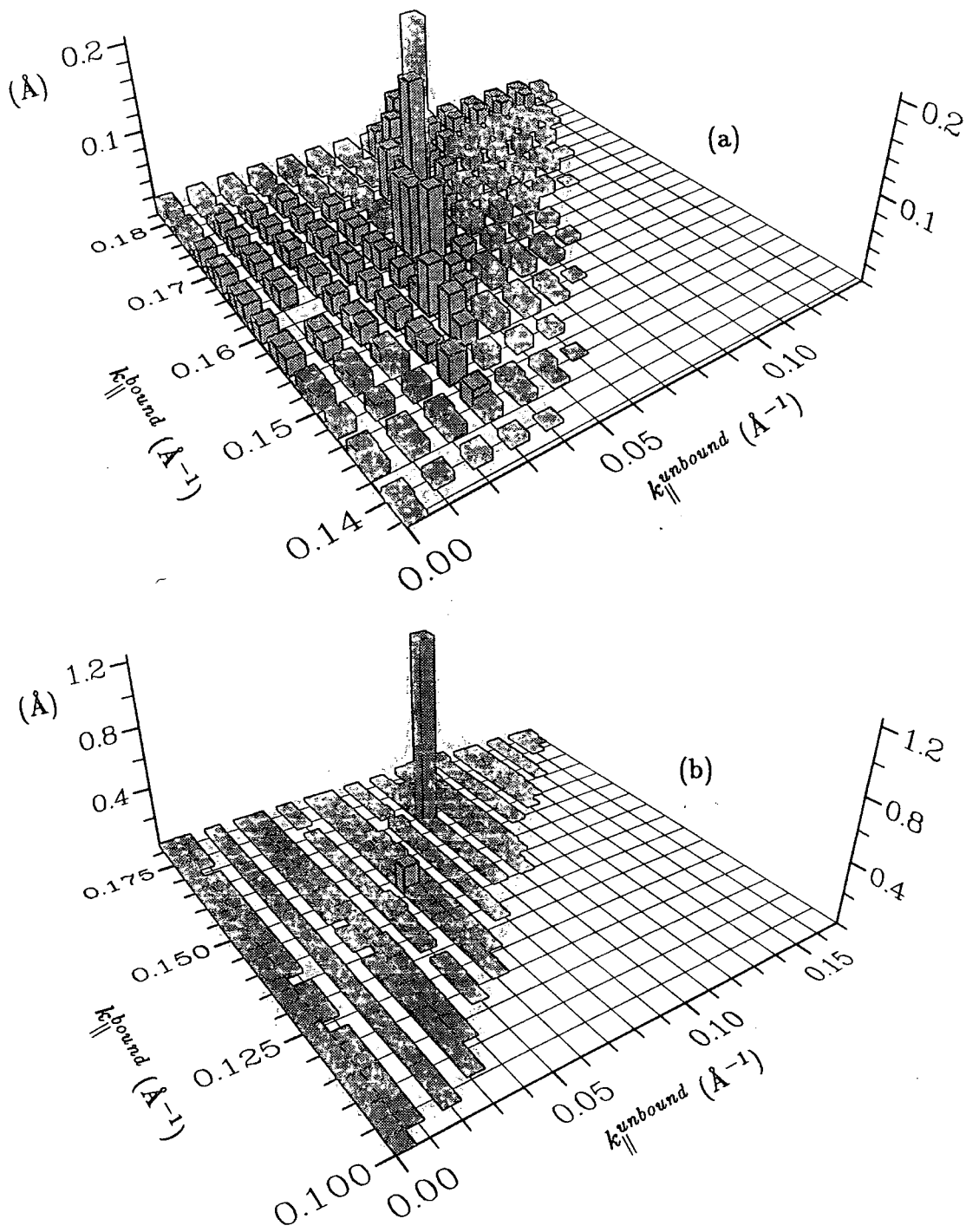
Figure 5.10 Moduli squared of matrix elements plotted against $k_\parallel^{bound}$ and $k_\parallel^{unbound}$ for (a) polar optical phonon absorption, and (b) polar optical phonon emission from heavy hole unbound states into the LH1 subband of figure 5.2.
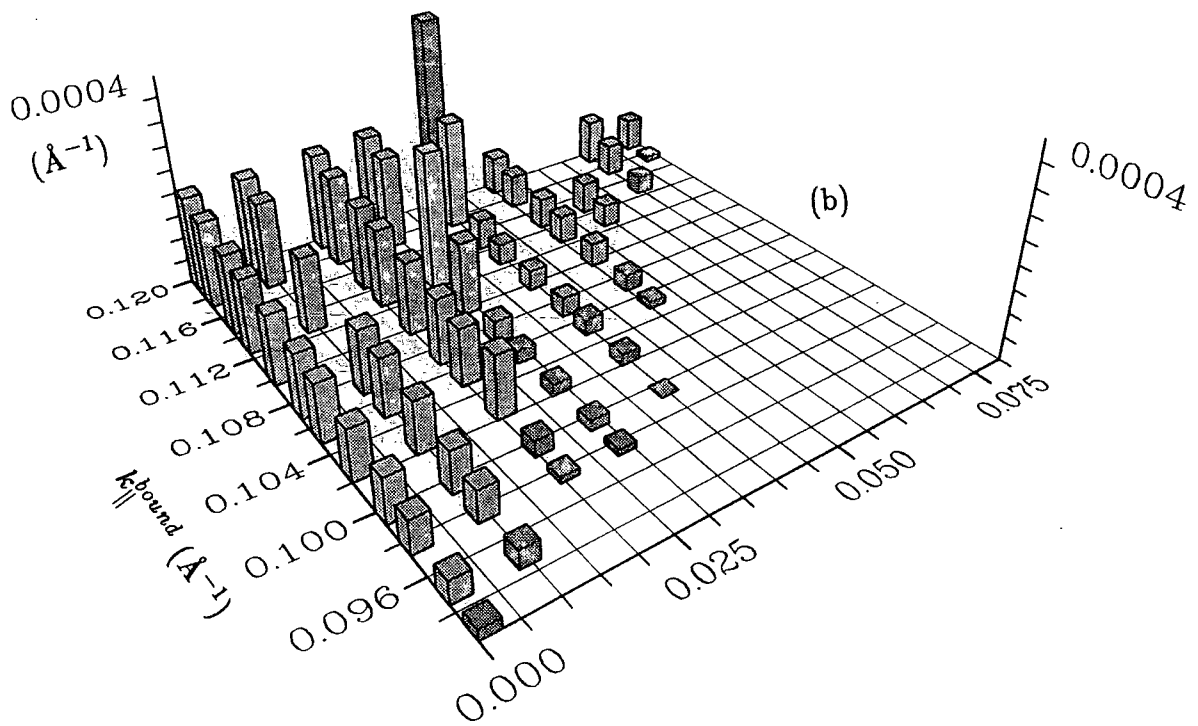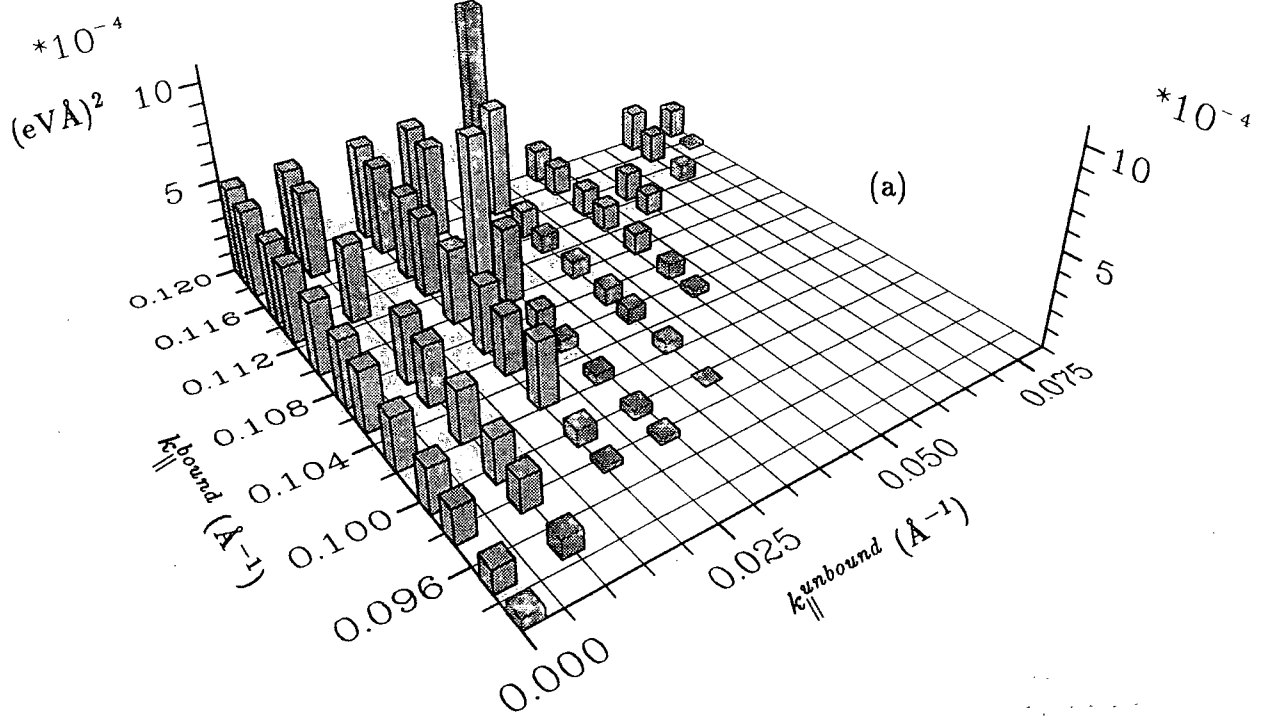
Figure 5.11 Moduli squared of matrix elements plotted against $k_{\parallel}^{bound}$ and $k_{\parallel}^{unbound}$ for (a) alloy, and (b) acoustic phonon scattering from heavy hole unbound states into the HH2 subband of figure 5.2.
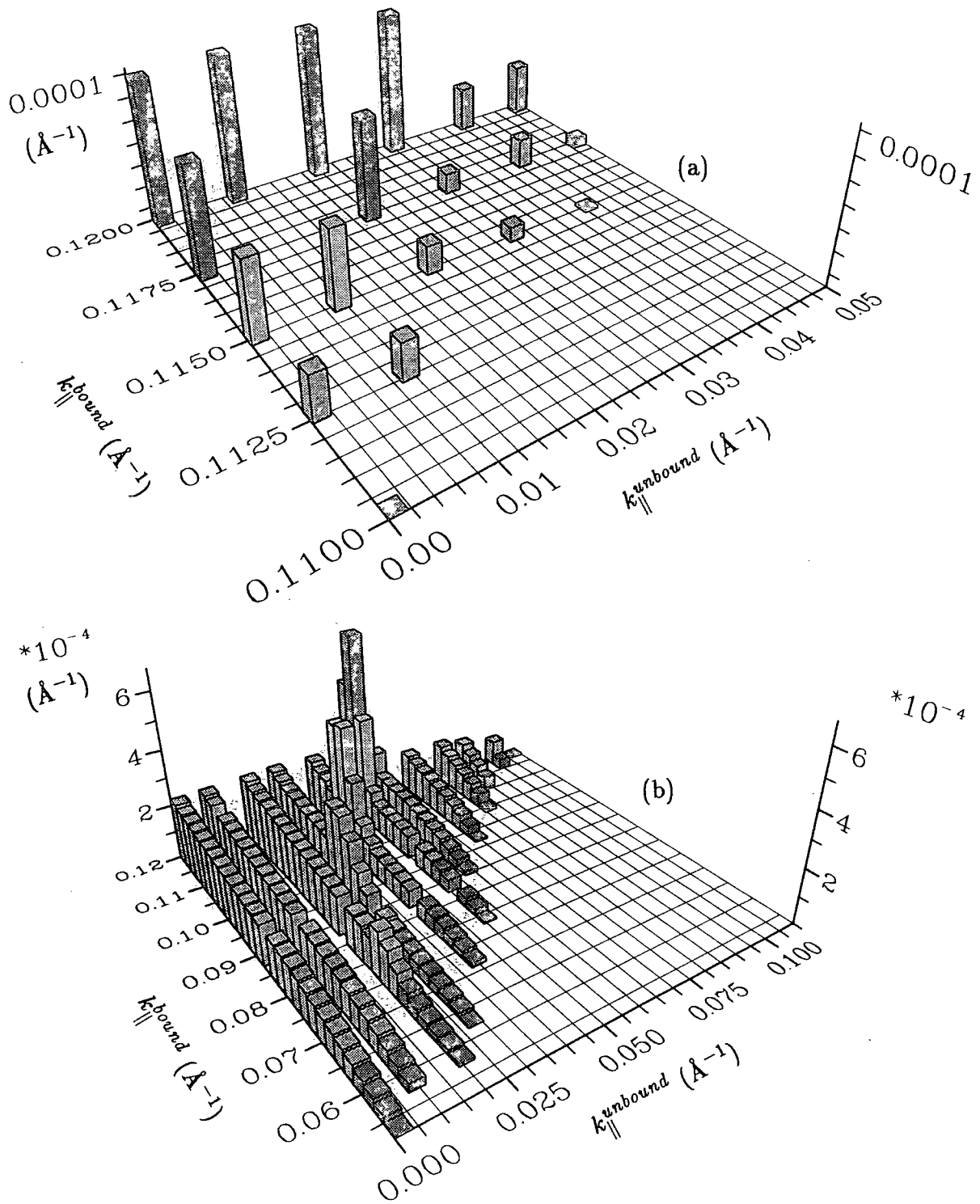
Figure 5.12 Moduli squared of matrix elements plotted against $k_{\parallel}^{bound}$ and $k_{\parallel}^{unbound}$ for (a) non-polar optical phonon absorption, and (b) non-polar optical phonon emission from heavy hole unbound states into the HH2 subband of figure 5.2.
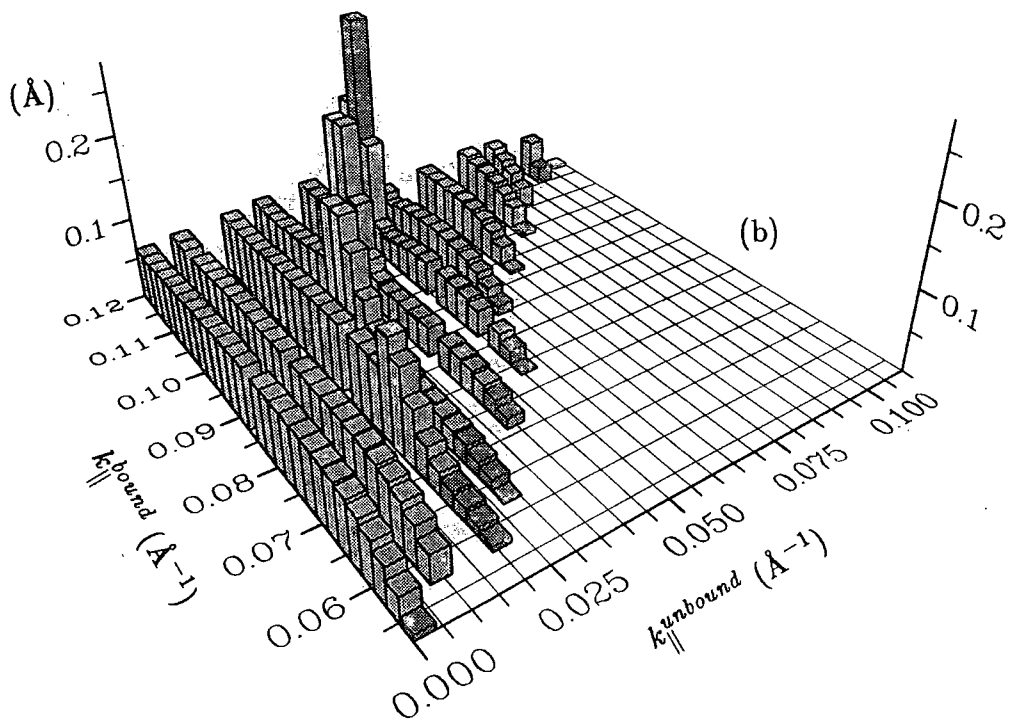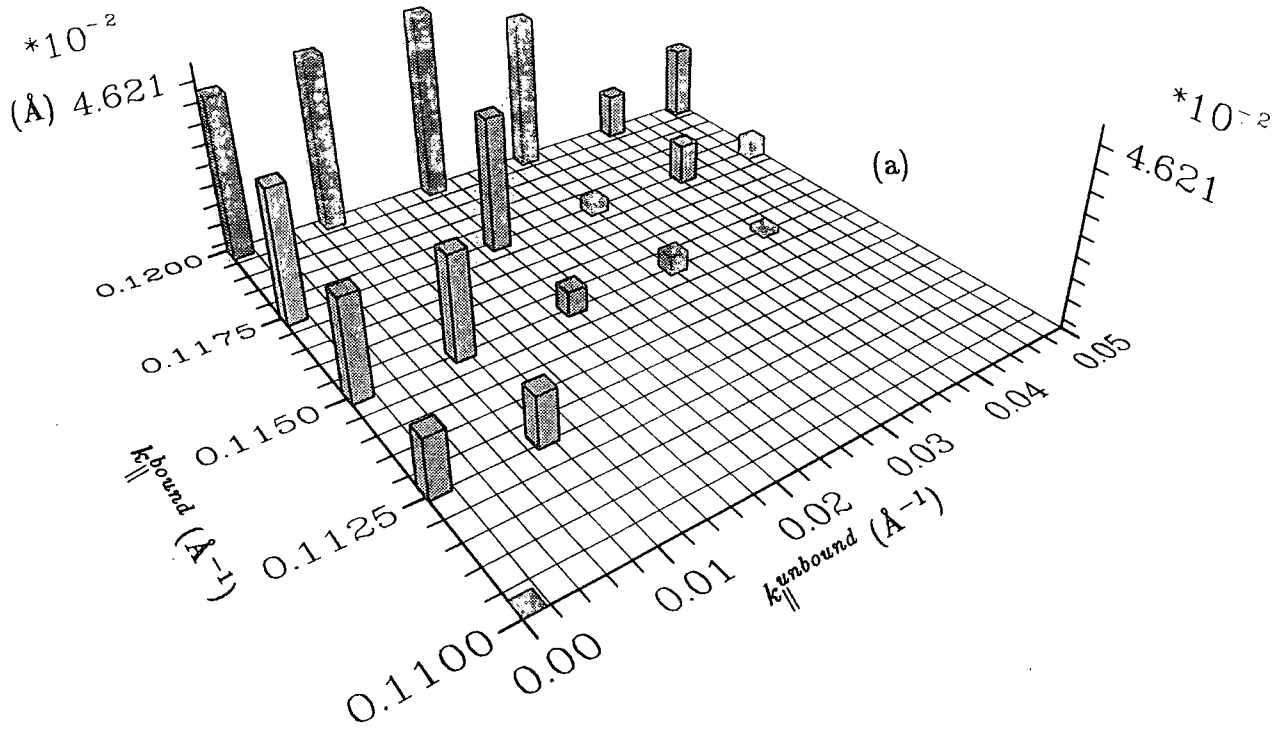
Figure 5.13 Moduli squared of matrix elements plotted against $k_{\parallel}^{bound}$ and $k_{\parallel}^{unbound}$ for (a) polar optical phonon absorption, and (b) polar optical phonon emission from heavy hole unbound states into the HH2 subband of figure 5.2.
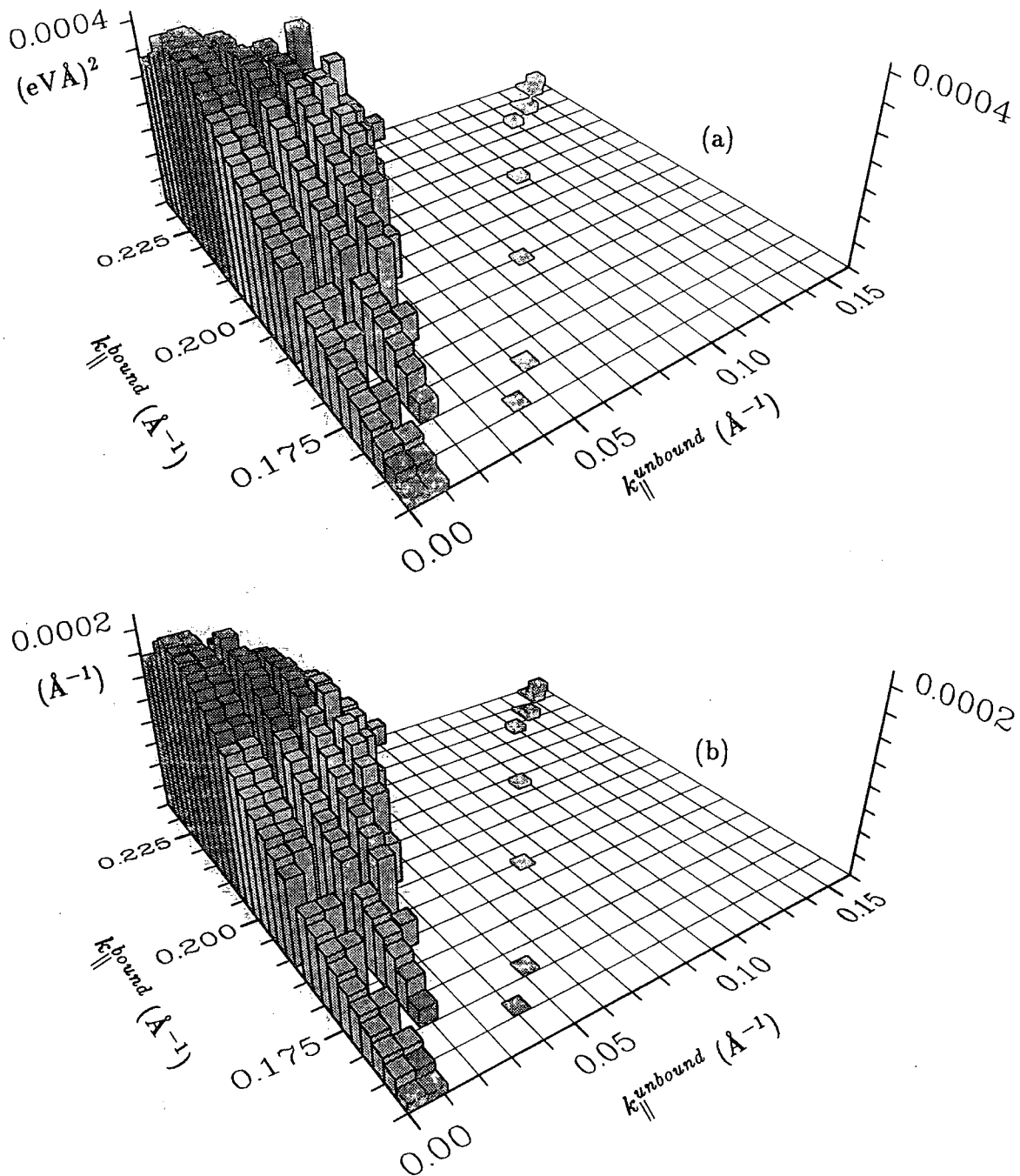
Figure 5.14 Moduli squared of matrix elements plotted against $k_{\parallel}^{bound}$ and $k_{\parallel}^{unbound}$ for (a) alloy, and (b) acoustic phonon scattering from light hole unbound states into the HH1 subband of figure 5.2.
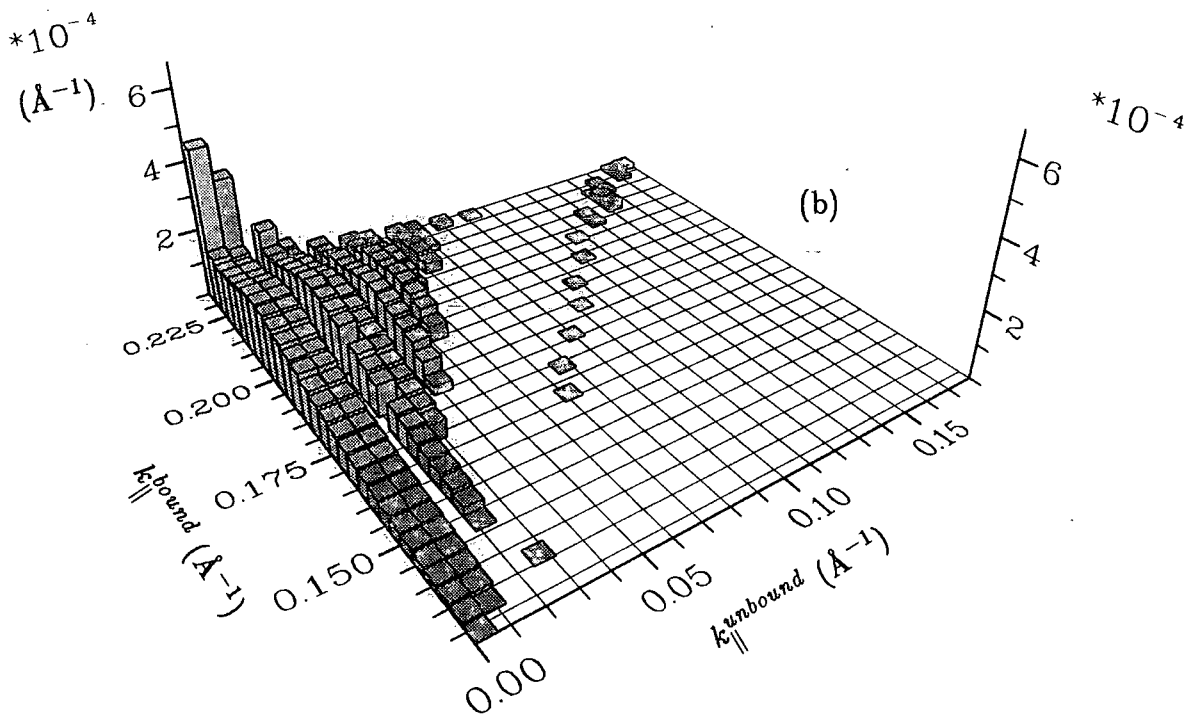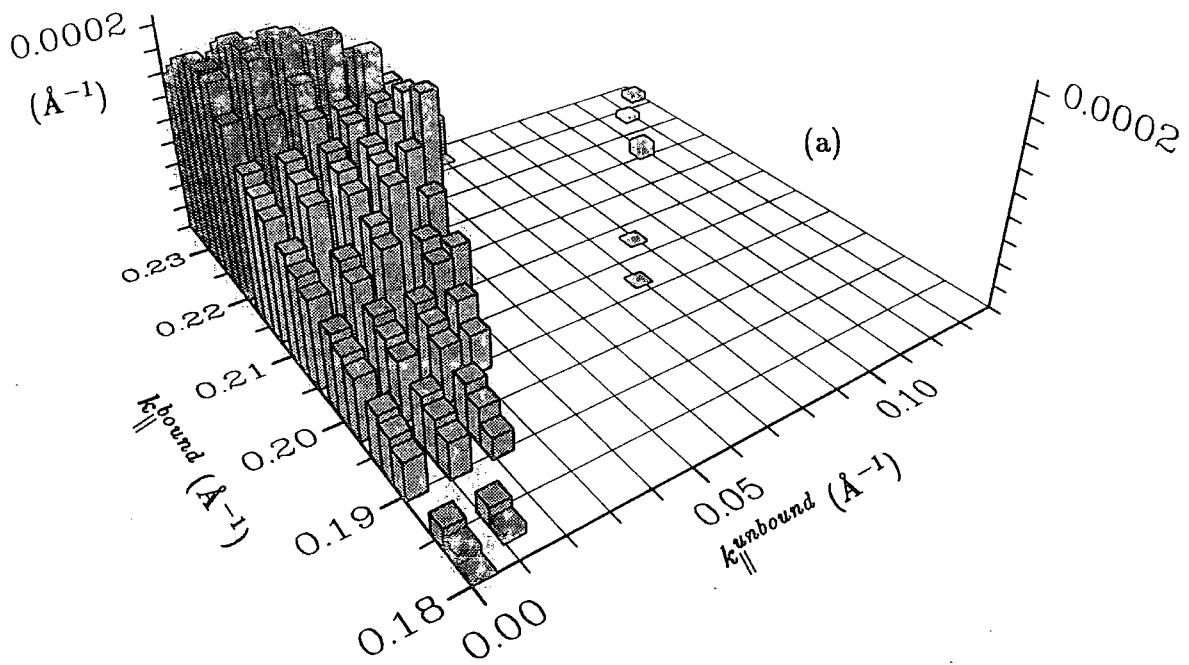
Figure 5.15 Moduli squared of matrix elements plotted against $k_\parallel^{bound}$ and $k_\parallel^{unbound}$ for (a) non-polar optical phonon absorption, and (b) non-polar optical phonon emission from light hole unbound states into the HH1 subband of figure 5.2.
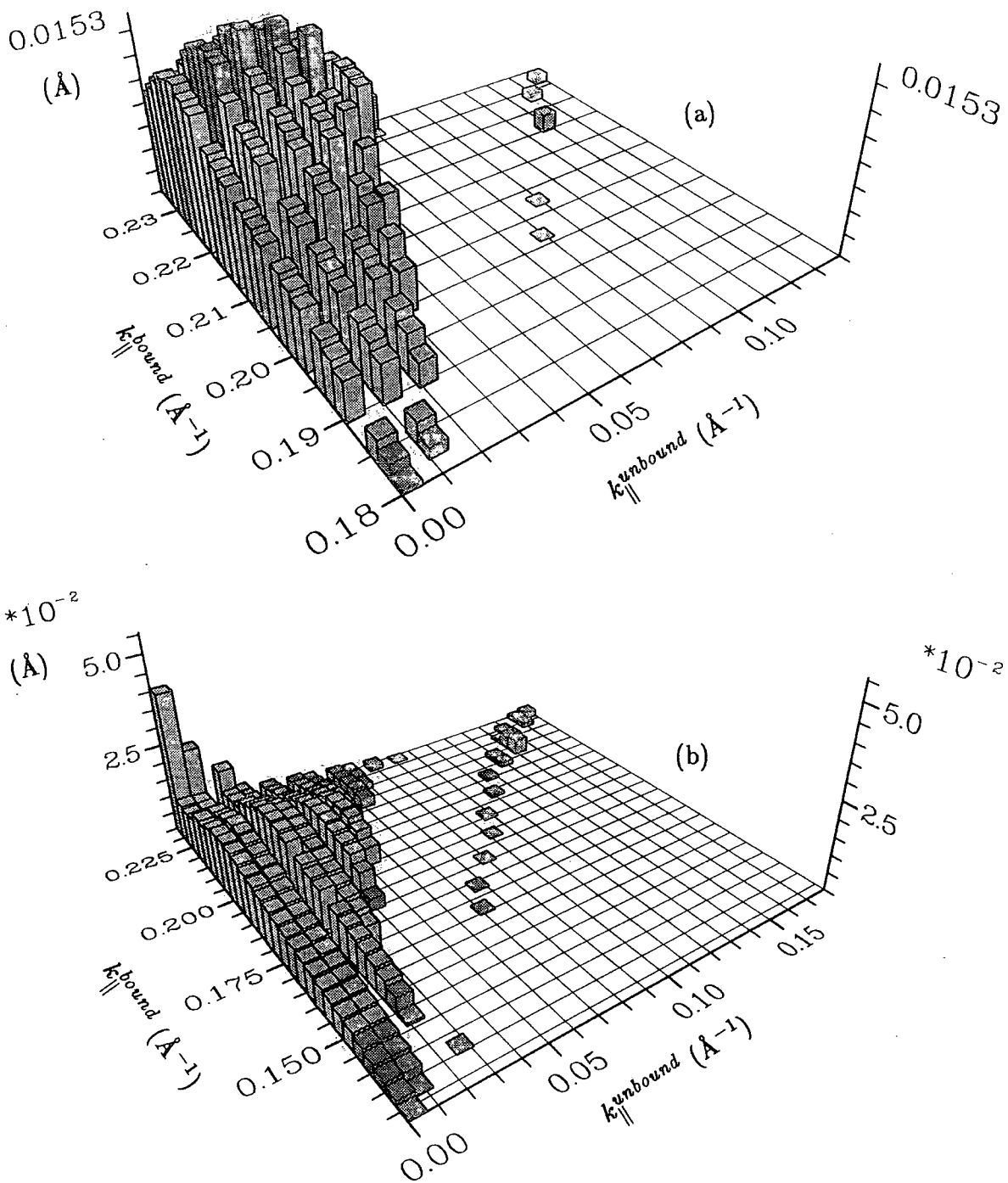
Figure 5.16 Moduli squared of matrix elements plotted against $k_{\parallel}^{bound}$ and $k_{\parallel}^{unbound}$ for (a) polar optical phonon absorption, and (b) polar optical phonon emission from light hole unbound states into the HH1 subband of figure 5.2.
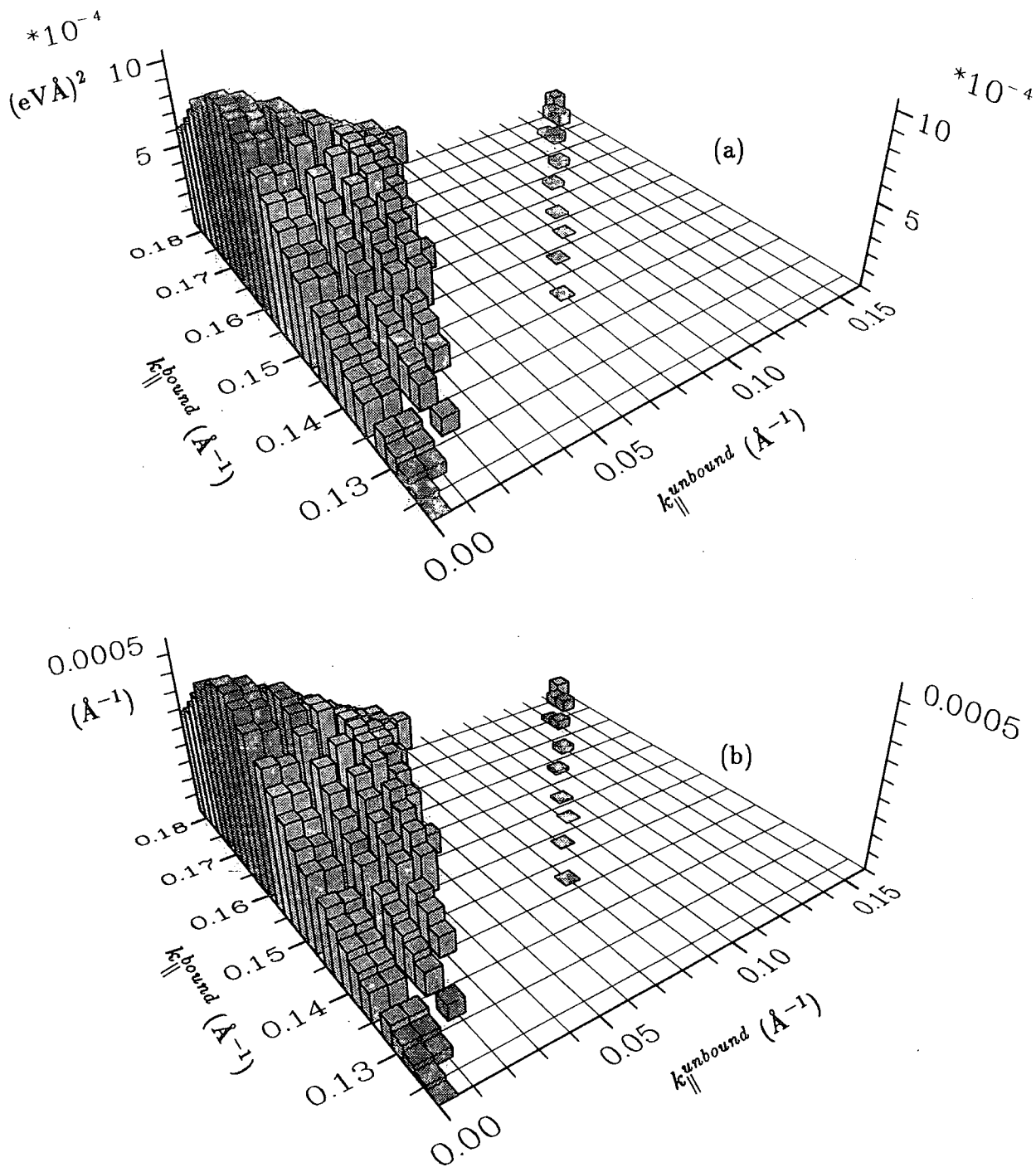
Figure 5.17 Moduli squared of matrix elements plotted against $k_{\parallel}^{bound}$ and $k_{\parallel}^{unbound}$ for (a) alloy, and (b) acoustic phonon scattering from light hole unbound states into the LH1 subband of figure 5.2.
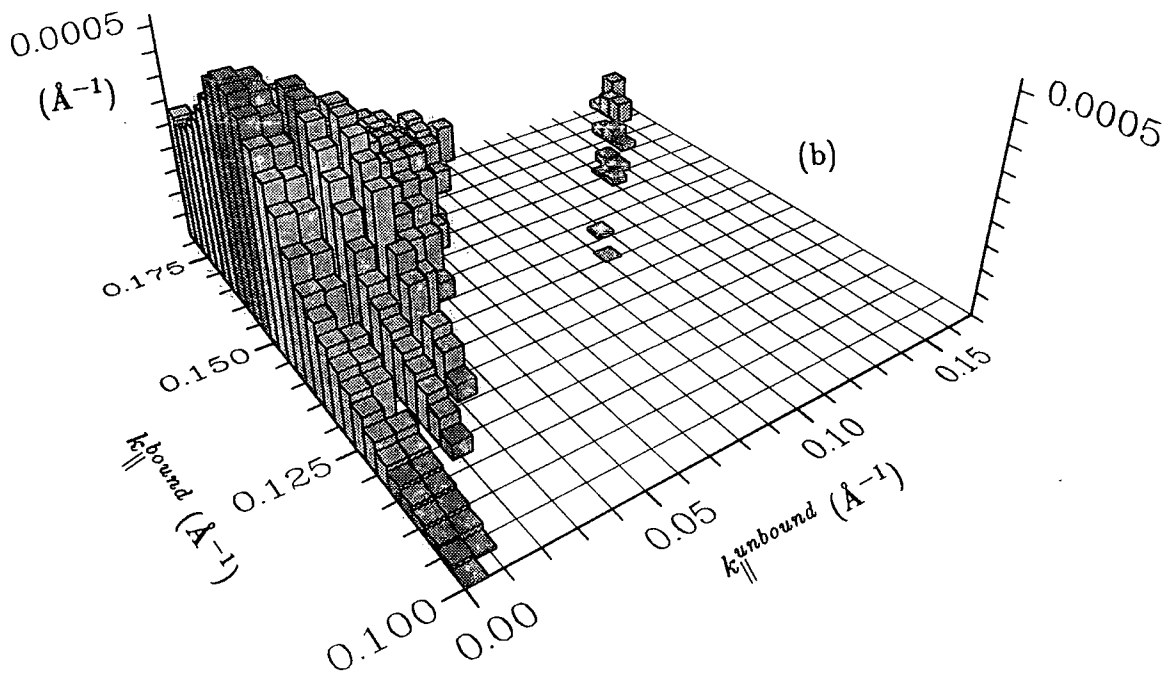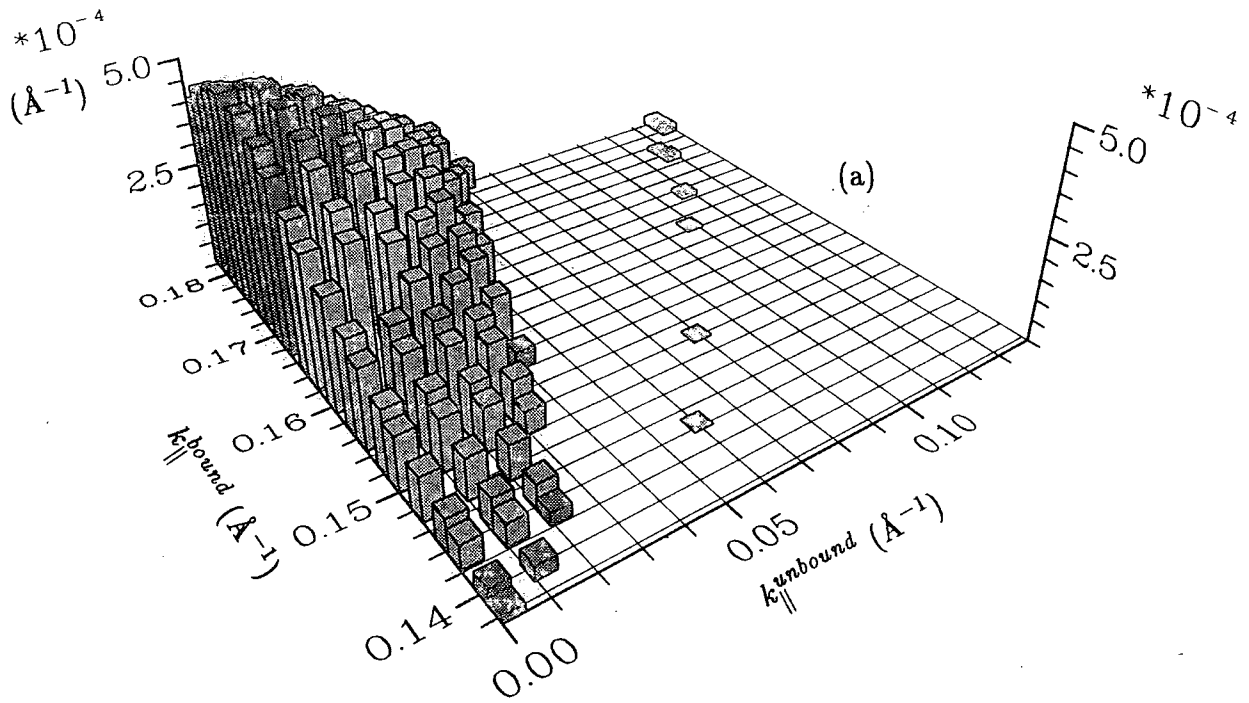
Figure 5.18 Moduli squared of matrix elements plotted against $k_{\parallel}^{bound}$ and $k_{\parallel}^{unbound}$ for (a) non-polar optical phonon absorption, and (b) non-polar optical phonon emission from light hole unbound states into the LH1 subband of figure 5.2.
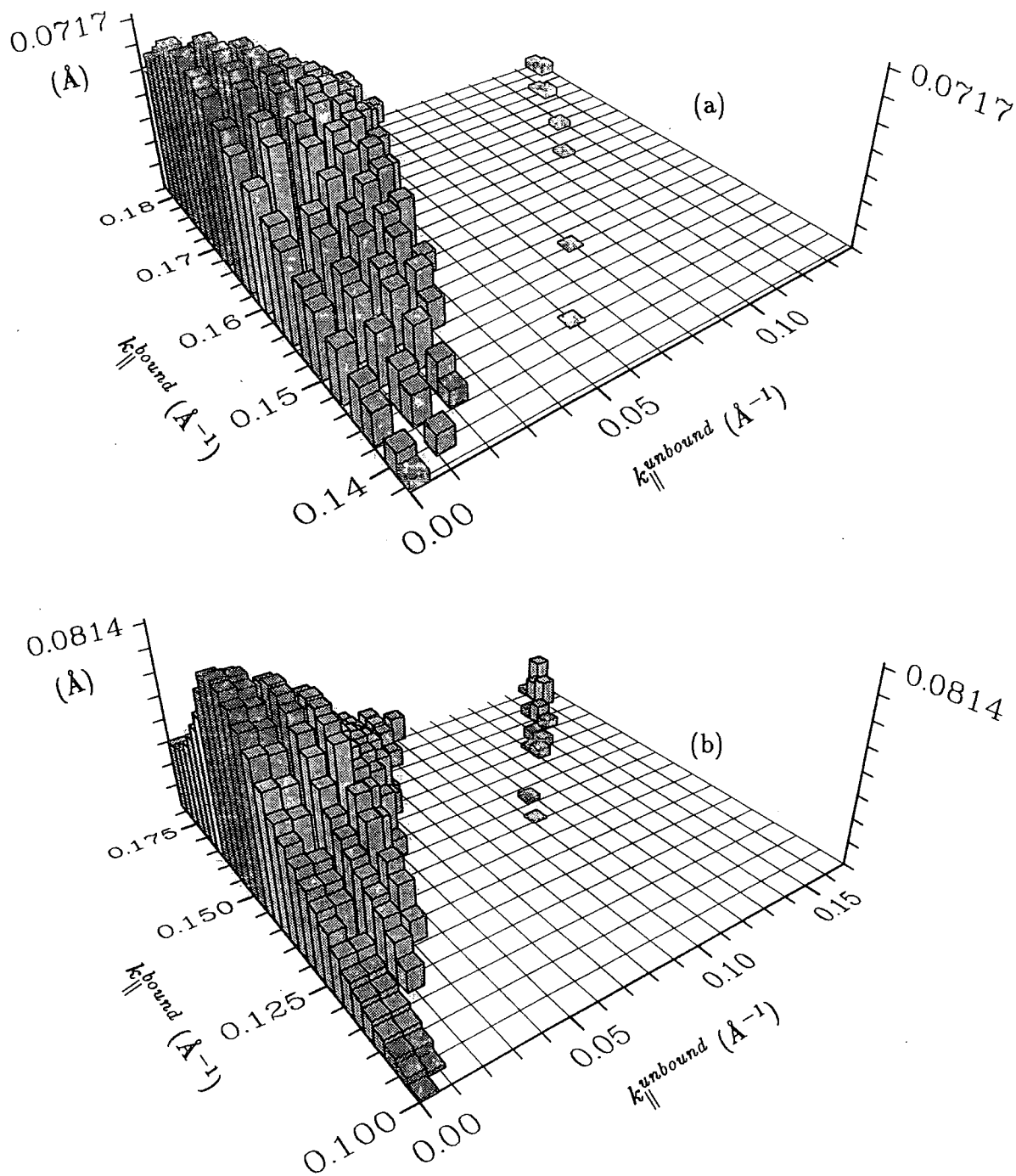
Figure 5.19 Moduli squared of matrix elements plotted against $k_{\parallel}^{bound}$ and $k_{\parallel}^{unbound}$ for (a) polar optical phonon absorption, and (b) polar optical phonon emission from light hole unbound states into the LH1 subband of figure 5.2.
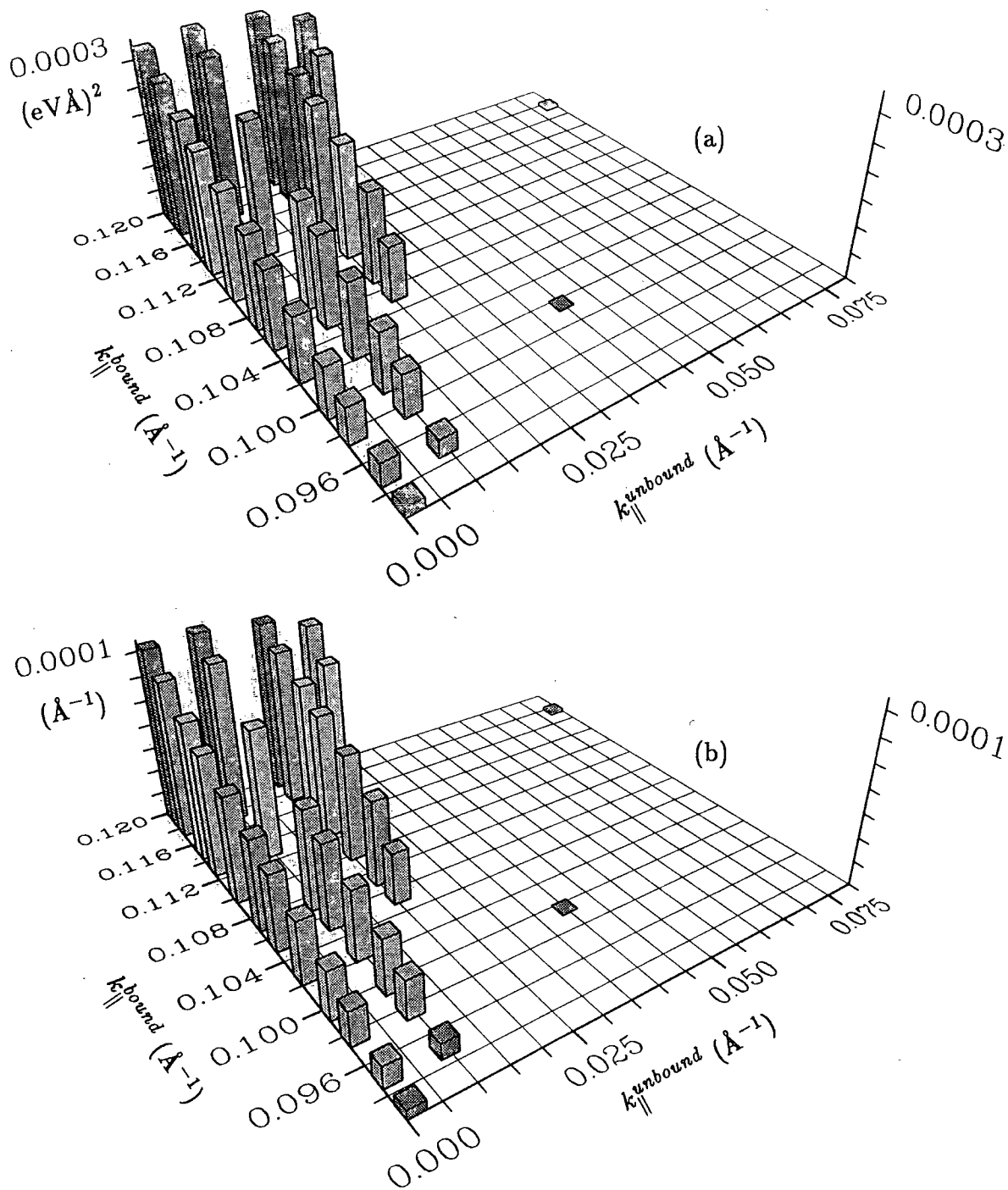
Figure 5.20 Moduli squared of matrix elements plotted against $k_{\parallel}^{bound}$ and $k_{\parallel}^{unbound}$ for (a) alloy, and (b) acoustic phonon scattering from light hole unbound states into the HH2 subband of figure 5.2.
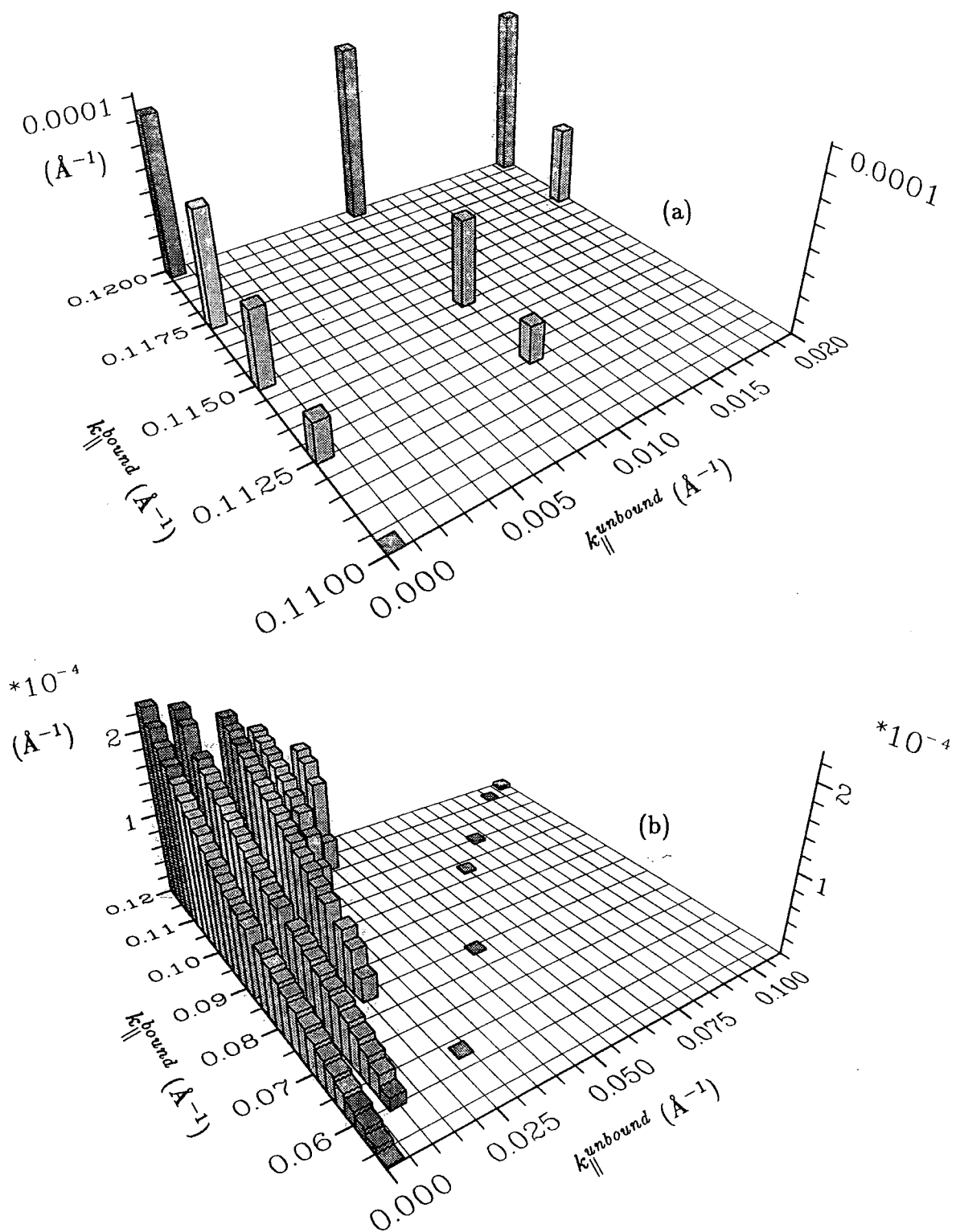
Figure 5.21 Moduli squared of matrix elements plotted against $k_\parallel^{bound}$ and $k_\parallel^{unbound}$ for (a) non-polar optical phonon absorption, and (b) non-polar optical phonon emission from light hole unbound states into the HH2 subband of figure 5.2.
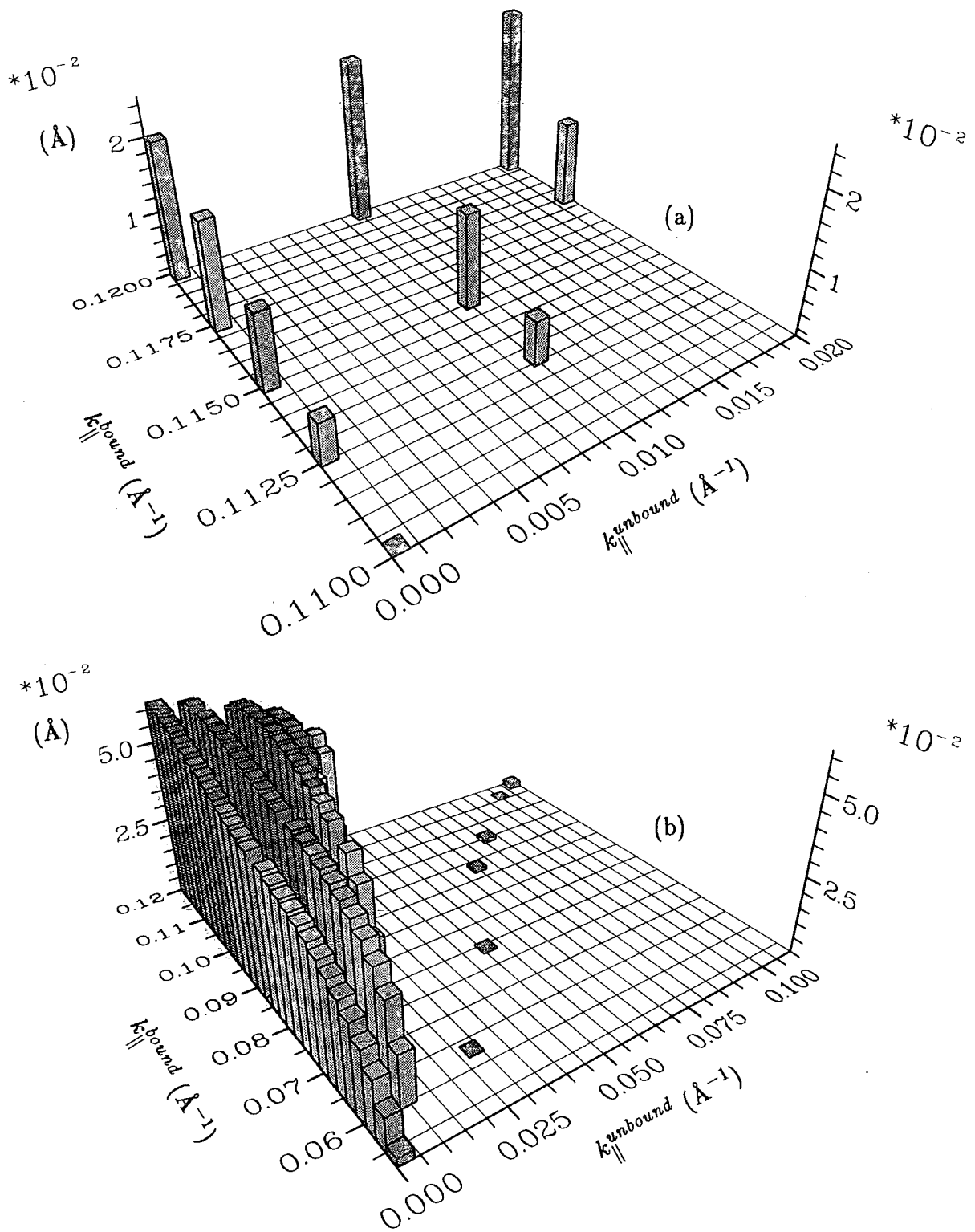
Figure 5.22 Moduli squared of matrix elements plotted against $k_\parallel^{bound}$ and $k_\parallel^{unbound}$ for (a) polar optical phonon absorption, and (b) polar optical phonon emission from light hole unbound states into the HH2 subband of figure 5.2.

volume in state $(k_\parallel, k_z)$ contribute to the current density. It follows that if m holes per unit volume in state $(k_\parallel, k_z)$ were to make up the current, the capture rate per unit area would be

$$\frac{m}{(AN_U)^{-1}} A^{-1} P_{(k_\parallel, k_z \to n, k'_\parallel)} = mN_U P_{(k_\parallel, k_z \to n, k'_\parallel)}. \qquad (5.31)$$

If the heavy and light holes are distributed in k-space with state occupancy $f_{hh(lh)}(k_\parallel, k_z)$ the mean capture rate can be obtained by averaging over all wavevectors. Accordingly, the capture rate per unit area becomes

$$A^{-1} < P(k_\parallel \to n, k'_\parallel) > = \frac{1}{8\pi^3} \int \int f_{hh(lh)}(k_\parallel, k_z) N_U(k_\parallel, k_z) P_{(k_\parallel, k_z \to n, k'_\parallel)} d\mathbf{k}_\parallel dk_z.$$

$$(5.32)$$

However, the distribution function $f_{hh(lh)}(k_\parallel, k_z)$ can only be obtained from a transport model of the whole structure which, amongst other things, takes account of the details of the carrier injection and their recombination in the well and elsewhere in the device, and is beyond the scope of this thesis.

5.6 Matrix elements and capture probabilities

The scattering matrix elements for capture from heavy and light hole unbound states into the HH1, LH1 and HH2 subbands of figure 5.2 are depicted in figures 5.5-5.22. The quantities which are plotted in these figures are listed in table 5.4. Capture is due to alloy and acoustic phonon scattering, non-polar optical phonon absorption and emission, and polar optical phonon absorption and emission. In all these figures, the matrix elements (squared) are shown as a function of the in-plane wavevector of the bound state $(k_\parallel^{bound})$ and the in-plane wavevector component of the unbound state $(k_\parallel^{unbound})$. The sense of increasing $k_\parallel^{bound}$ is also

that of increased energy of the initial unbound hole state. Since the transmitted wave amplitude generally increases as a function of the energy of the hole in the barrier, the scattering matrix elements show a general increase in magnitude for scattering into bound states higher within the quantum well (i.e. for greater $k_\parallel$ in the subbands). In contrast, the larger $k_\parallel^{unbound}$ for a hole of given energy, the smaller is the associated transverse wavevector k_z and the matrix elements generally decrease with increasing wavevector of the unbound state, as a consequence of the reduced transmission into the well.

Table 5.4 Matrix elements plotted in figures 5.5-5.22.

Process	Matrix Element	Equation
Alloy Scattering	$\sum_{h=1}^{2}\sum_{h'=3}^{4} \frac{1}{2}\mid M_{AL}\mid^2$	5.21
Acoustic Phonon	$\sum_{h=1}^{2}\sum_{h'=3}^{4} \frac{1}{2}\int_{-\infty}^{\infty}\frac{\mid I_{(left)}+I_{(well)}+I_{(right)}\mid^2 dq_z}{N_U N_B}$	5.26
Non-Polar Phonon	$\sum_{h=1}^{2}\sum_{h'=3}^{4} \frac{1}{2}\int_{-\infty}^{\infty}\frac{\mid I_{(left)}+I_{(well)}+I_{(right)}\mid^2 dq_z}{N_U N_B}$	5.26
Polar Phonon	$\sum_{h=1}^{2}\sum_{h'=3}^{4} \frac{1}{2}\int_{-\infty}^{\infty}\frac{2\pi\mid M(q_z)\mid^2}{\sqrt{q_z^4+2(k_\parallel^2+k_\parallel'^2)q_z^2+(k_\parallel^2-k_\parallel'^2)^2}}dq_z$	5.27

However, superimposed upon this simple behaviour are a series of peaks in the capture matrix elements which can be associated with the presence of transmission resonances into the well. Clustered about these are intermediate values, which are due to capture from states just off the resonance condition, but with a significant fraction of the incident wave amplitude being transmitted into the well. The transmission of the barrier wave into the well region largely dictates the strength of an unbound-bound transition; the mixing between the subbands, and the consequent variation of the hole envelope functions with $k_\parallel$ appears to
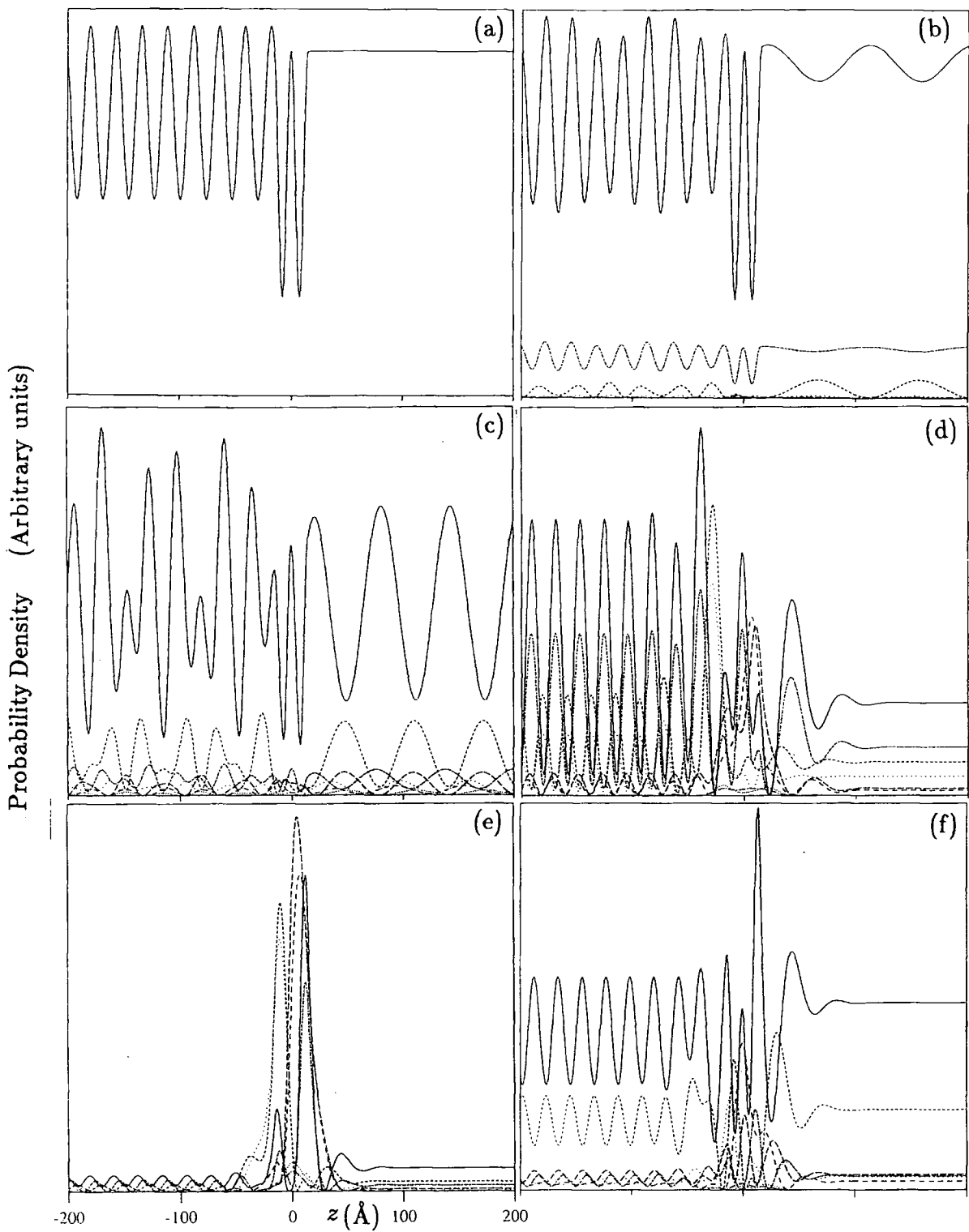
Figure 5.23 Unbound states derived from the heavy hole band of InGaAsP, at an energy of -0.36 eV, showing the transition to a transmission resonance at $k_{\parallel} = 0.09\text{Å}^{-1}$. (a) $k_{\parallel} = 0\text{Å}^{-1}$, (b) $k_{\parallel} = 0.02\text{Å}^{-1}$, (c) $k_{\parallel} = 0.06\text{Å}^{-1}$, (d) $k_{\parallel} = 0.085\text{Å}^{-1}$, (e) $k_{\parallel} = 0.09\text{Å}^{-1}$, (f) $k_{\parallel} = 0.095\text{Å}^{-1}$. The resonance condition corresponds to the largest scattering matrix elements into the LH1 subband by optical phonon emission (figures 5.9b and 5.10b).
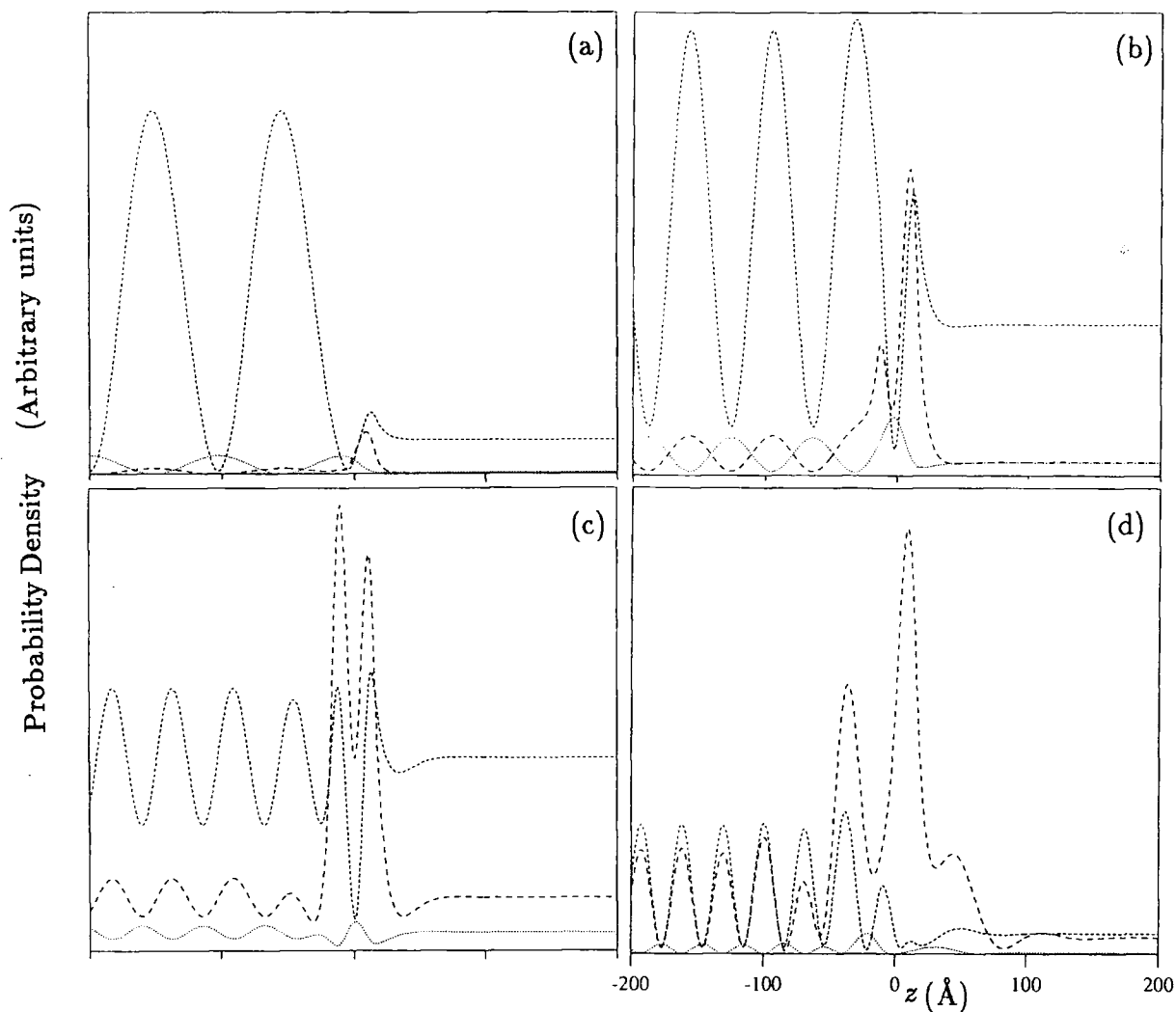
Figure 5.24 Probability densities for unbound states derived from the light hole band of InGaAsP with $k_{\parallel} = 0$, at energies (a) -0.25 eV, (b) -0.30 eV, (c) -0.35eV and (d) -0.43 eV. The curve ... represents the envelope for the conduction band Bloch function, - - - the light hole component and $--$ the spin split-off part. The quantum well is centred at $z = 0$.

be much less significant.

Figure 5.23 shows the probability density of barrier waves derived from the heavy hole band of InGaAsP with energy -0.36 eV (relative to valence band edge of the well material), incident from the left hand barrier with increasing $k_\parallel$ in the range $0 - 0.095\,\text{Å}^{-1}$. In the case $k_\parallel = 0$, the reflected wave amplitude at the left hand barrier interferes with the incident wave. For $k_\parallel \neq 0$, the heavy hole states mix with the conduction, light hole and spin split-off bands (the off diagonal elements of the k.p Hamiltonian (figure 5.1) are non-zero), hence the heavy hole envelope functions contain contributions from these other Bloch components. At $k_\parallel = 0.09\text{Å}^{-1}$ (e), the wavevector transverse to the well k_z, is such that the transmission probability tends towards unity. There is a small reflected amplitude, and the probability density of the heavy hole state becomes localised about the well region. This example corresponds to the sharp resonance condition for scattering into the LH1 subband by optical phonon emission (figures 5.9b and 5.10b).

Figures 5.13-5.22 show the scattering matrix elements for scattering from unbound states derived principally from the light hole band of bulk InGaAsP. Note the extra sequence of values on each of these figures, occuring at larger $k_\parallel^{unbound}$. These are additional matrix element values derived from the heavy hole bulk band, and are shown on the same sets of axes for comparison. Recall from figure 5.4 that at large $k_\parallel^{unbound}$, two magnitudes for k_z are possible owing to the warping of the heavy hole band. These values represent transitions from heavy hole states with the smaller values of k_z, and hence are small due to the lower trans-

mission into the well. At a given energy and $k_{\parallel}^{unbound}$, light hole barrier waves possess smaller transverse wavevectors than corresponding heavy hole states, and they are less readily transmitted into the well. This implies that light holes are less readily captured than heavy holes. Furthermore, little resonant structure is observed in the matrix elements, and for the most part the matrix elements show a monotonic increase with increasing unbound state energy.

However, for scattering into states of the HH1 and LH1 subbands at the larger values of $k_{\parallel}$ considered, the matrix elements decrease. This is a result of the significant conduction and spin split-off band zone centre basis state components in the barrier light hole band states (light hole states are coupled with these bands, even at $k_{\parallel} = 0$). With increasing hole energy, the light hole states in the barrier possess an increasing contribution from the zone centre spin split-off basis state component (since the energy lies closer to the spin split-off band edge). This increase is at the expense of that for the zone centre light hole basis state component. Therefore at large $k_{\parallel}$, the contribution to the scattering matrix elements from the envelopes of the spin split-off Bloch components of the bound and unbound states is important. Since the bound state wavefunction is largely a function of the heavy and light hole Bloch parts (recall chapter 3), the matrix elements for transitions of this type will generally be smaller than those for scattering from lower energy barrier waves.

The only evidence for resonant transitions from light hole states into this particular quantum well structure is for optical phonon emission into the highest bound state on the HH2 subband, from a state with $k_{\parallel} = 0$. This unbound state

of energy $E = -0.43\,\mathrm{eV}$ (relative to the valence band edge of the well material) is depicted in figure 5.24d. It does not show the same level of enhancement of probability density as the bound states derived from the heavy hole bulk band of InGaAsP, but nonetheless, there is relatively large transmission into the well, compared to light hole barrier waves of similar energy (figures 5.24b, c).

The capture rate per unit area of the well per unit incident particle current density (the capture probability) is determined by the product of the scattering matrix element and the density of final states, divided by the flux (equation 5.30). This flux is proportional to the local carrier velocity or the local gradient of the bulk band with respect to k_z, $\frac{\partial E}{\partial k_z}$. Hence the flux associated with both heavy and light hole barrier waves, whatever $k_{\parallel}^{unbound}$, increases monotonically at higher energies in the valence band. The scattering rates from Fermi's Golden Rule are proportional to the density of final states. As a result of anticrossing between the subbands due to mixing, the density of states decreases for states farthest out in $k_{\parallel}$ along each subband (figure 5.3).

Apart from the resonant transitions, the matrix elements generally increase with increasing unbound state energy, as discussed above. However, the density of final states and the flux both act to reduce the capture probability for transitions from states higher in the valence band. The result is that the local capture probability is largest when a transition is made into a state at intermediate $k_{\parallel}^{bound}$. The capture resonances are still observed, but their resolution is screened by the flux and density of final states. Hence, contrary to the predictions of simple models for carrier capture incorporating parabolic bands, the capture probability into

the well is not found to be greatest for transitions made into states lying nearest the continuum edge. Thus, although the subband mixing does not have a strong influence on carrier capture through its effect on scattering matrix elements, it is important as a result of the effect on subband curvatures.

The capture probabilities $p(k_\parallel, k_z)$ for alloy and phonon scattering from heavy hole unbound states are shown in figures 5.25-5.33. The probability of alloy scattering into the HH1 and LH1 subbands exceeds that for capture by acoustic scattering as a result of the nature of the matrix elements. For transitions from virtual bound states, the fastest capture by elastic scattering is found to be that for alloy scattering into the HH1 subband. Across the range of energies and wavevectors considered, the capture probability is generally small, being on average 1-2%. The capture probabilities for optical phonon absorption are an order of magnitude smaller than those for phonon emission. This is due to the phonon occupancy factor $\frac{n_q}{(n_q+1)} \sim 0.5$ at $T_L = 300\,\mathrm{K}$, and the fact that scattering by phonon absorption must be made into states of larger $k_\parallel^{bound}$, thus with a smaller density of final states. From the previous study of bound-bound transitions (chapter 3), the rates for polar optical phonon scattering were greater than those for non-polar optical phonon scattering. This is not found to be the case for hole capture since the denominator of the matrix element for this process increases as a function of the difference between $k_\parallel^{bound}$ and $k_\parallel^{unbound}$. Therefore, with regard to the virtual bound heavy hole state of figure 5.23e, the probability of capture by non-polar optical phonon emission is 90%, whereas that for polar optical phonon scattering is 50%.

Summing over all twelve scattering processes, the total capture rate per unit incident particle flux is on average about 10 %. However, at a transmission resonance, the cumulative capture probability can exceed 100 % (for instance the example discussed above). Clearly it is not physically possible to capture a greater current density than that which is incident upon the well. Such instances represent a breakdown of the perturbation theory, and also reflect the fact that the reflected and transmitted particle currents are not solved self-consistently with the captured current density.

Figures 5.34-5.42 depict the probabilities for alloy and phonon capture from light hole (and additional heavy hole) unbound states. Across all scattering processes, the capture probability is small ($\sim 2\%$), but this is comparable to those for heavy hole-bound transitions, if the transmission resonances are ignored. The reason for this is that the light hole particle flux is less than that associated with a heavy hole barrier wave.

An accurate picture of the carrier capture process could be obtained once this microscopic capture data is incorporated into an ensemble Monte Carlo simulation. However, by assuming that the heavy and light hole barrier states are distributed in k-space according to a Maxwell-Boltzmann distribution, it is possible to estimate the average capture rate per unit area of the well plane for each scattering mechanism (equation 5.31). Tables 5.5 and 5.6 list the average capture rates per unit area into the three subbands of figure 5.1, from heavy and light hole barrier states, respectively.

Table 5.5 Average capture rates $A^{-1} < P >$ for heavy holes into a 30 Å

$In_{0.7}Ga_{0.3}As$-$In_{0.75}Ga_{0.25}As_{0.55}P_{0.45}$ quantum well.

Lattice Temperature $T_L = 300$ K

Capture Process	$A^{-1} < P > \; (\times 10^{15} \mathrm{m}^{-2} \mathrm{ps}^{-1})$		
	HH1	LH1	HH2
Alloy scattering	8.936	6.611	4.672
Acoustic phonons	3.795	2.789	1.825
Non-polar phonon emission	7.877	4.830	5.914
Non-polar phonon absorption	1.485	1.198	0.2794
Polar phonon emission	4.964	5.066	14.27
Polar phonon absorption	0.6714	0.9618	0.3761

Table 5.6 Average capture rates $A^{-1} < P >$ for light holes into a 30 Å

$In_{0.7}Ga_{0.3}As$-$In_{0.75}Ga_{0.25}As_{0.55}P_{0.45}$ quantum well.

Lattice Temperature $T_L = 300$ K

Capture Process	$A^{-1} < P > \; (\times 10^{15} \mathrm{m}^{-2} \mathrm{ps}^{-1})$		
	HH1	LH1	HH2
Alloy scattering	1.739	1.980	1.116
Acoustic phonons	0.700	0.789	0.428
Non-polar phonon emission	1.555	1.126	1.273
Non-polar phonon absorption	0.348	0.373	0.0637
Polar phonon emission	0.895	1.134	2.903
Polar phonon absorption	0.1432	0.2918	0.0823

A comparison of the average capture rates listed in table 5.5 with those of table 5.6 shows that for all scattering mechanisms, heavy holes are more efficiently captured than light holes. In both tables, it is evident that the optical phonon absorption rates are an order of magnitude smaller than the equivalent rates for phonon emission. This result is consistent with the observations made on the capture probabilities (discussed earlier in this section). Optical phonon absorption is the least important capture process.

It is apparent that heavy holes are most effectively captured into the HH2 subband by polar optical phonon emission, but this process does not appear to be the dominant mechanism for hole capture into the HH1 and LH1 bands. For these subbands, the largest capture rates are those for alloy and non-polar optical phonon emission. This difference can be explained by the fact that capture into the HH1 and LH1 bands involves scattering into bound states which lie farther out in $k_\parallel$-space than those on the HH2 subband, and so the polar optical phonon scattering matrix elements are smaller. Acoustic phonon scattering is less important, but the capture rates are of similar magnitude to the polar optical phonon emission rates (with the exception of heavy hole capture into the HH2 subband).
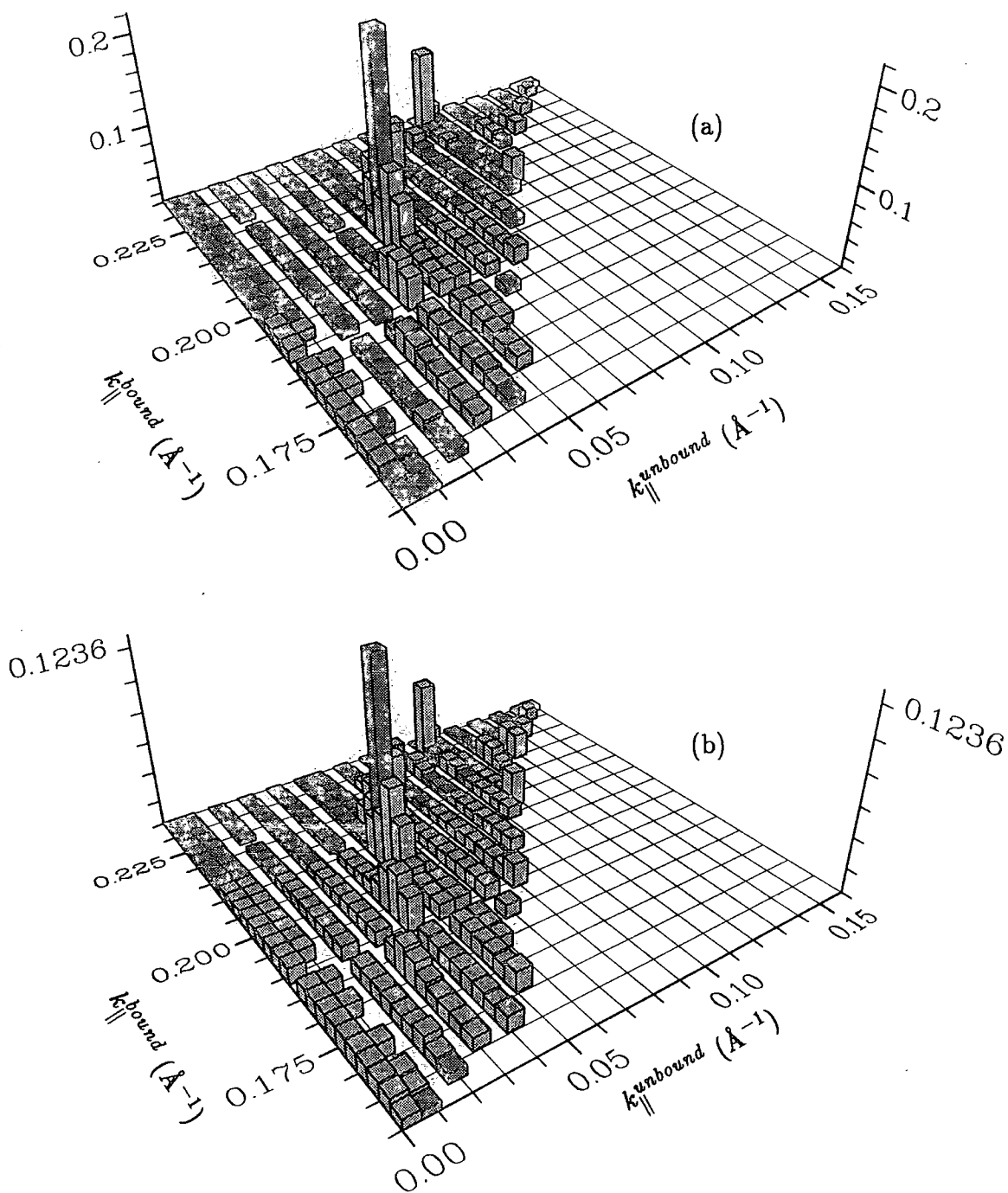
Figure 5.25 Capture probabilities per unit area of the well plotted against $k_{\parallel}^{bound}$ and $k_{\parallel}^{unbound}$ for (a) alloy, and (b) acoustic phonon scattering from heavy hole unbound states into the HH1 subband of figure 5.2.
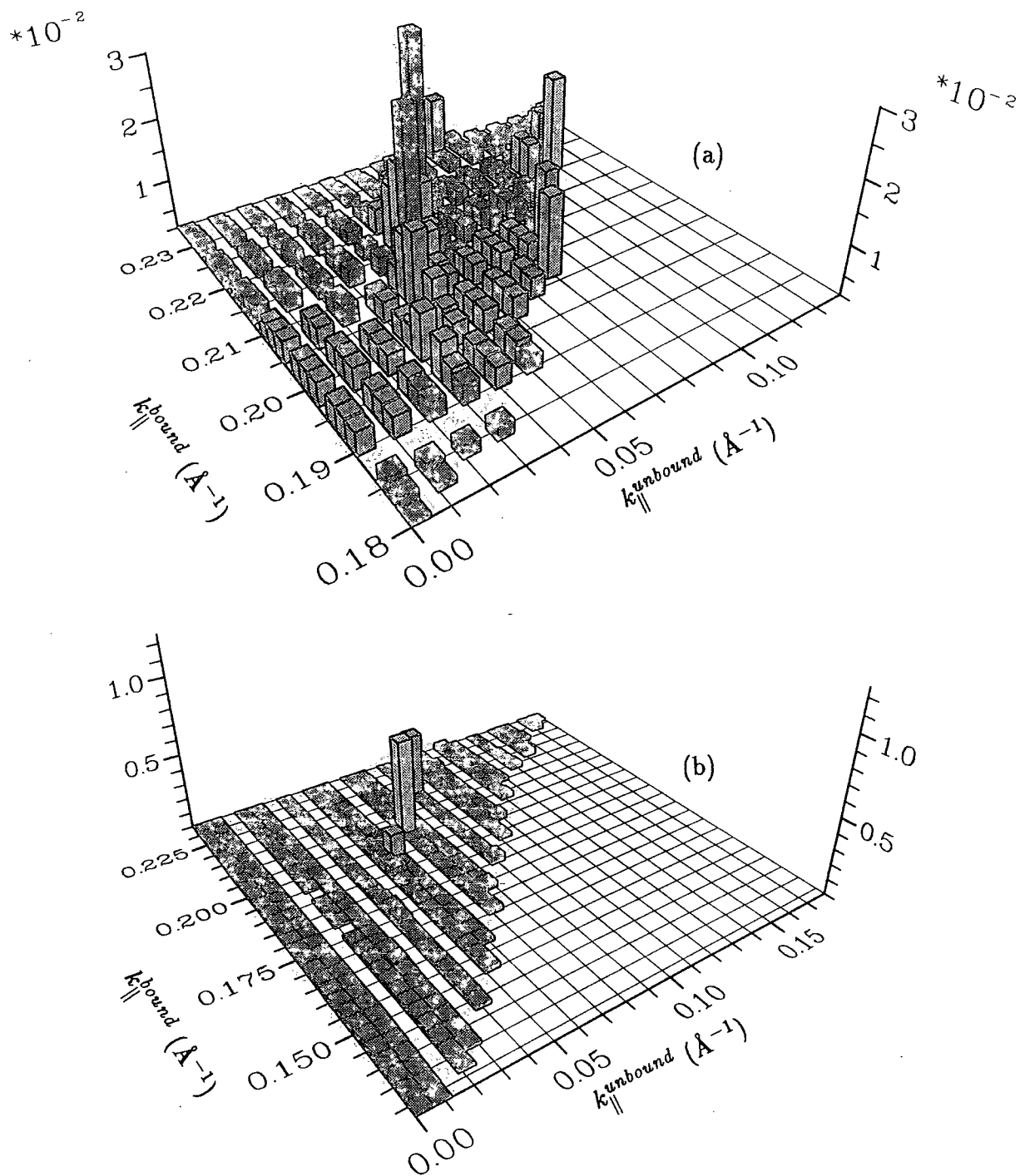
Figure 5.26 Capture probabilities per unit area of the well plotted against $k_\parallel^{bound}$ and $k_\parallel^{unbound}$ for (a) non-polar optical phonon absorption, and (b) non-polar optical phonon emission from heavy hole unbound states into the HH1 subband of figure 5.2.
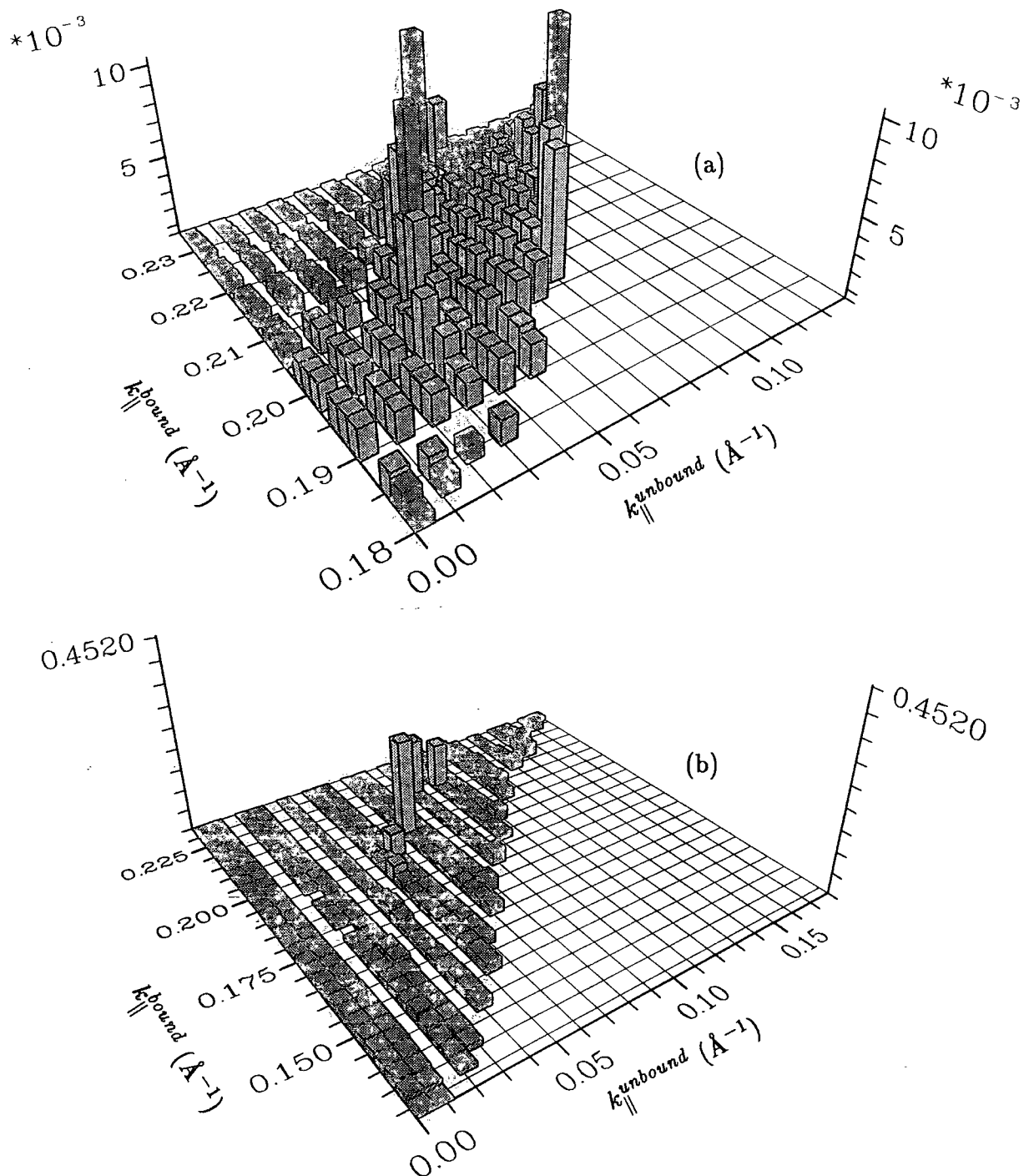
Figure 5.27 Capture probabilities per unit area of the well plotted against $k_\parallel^{bound}$ and $k_\parallel^{unbound}$ for (a) polar optical phonon absorption, and (b) polar optical phonon emission from heavy hole unbound states into the HH1 subband of figure 5.2.
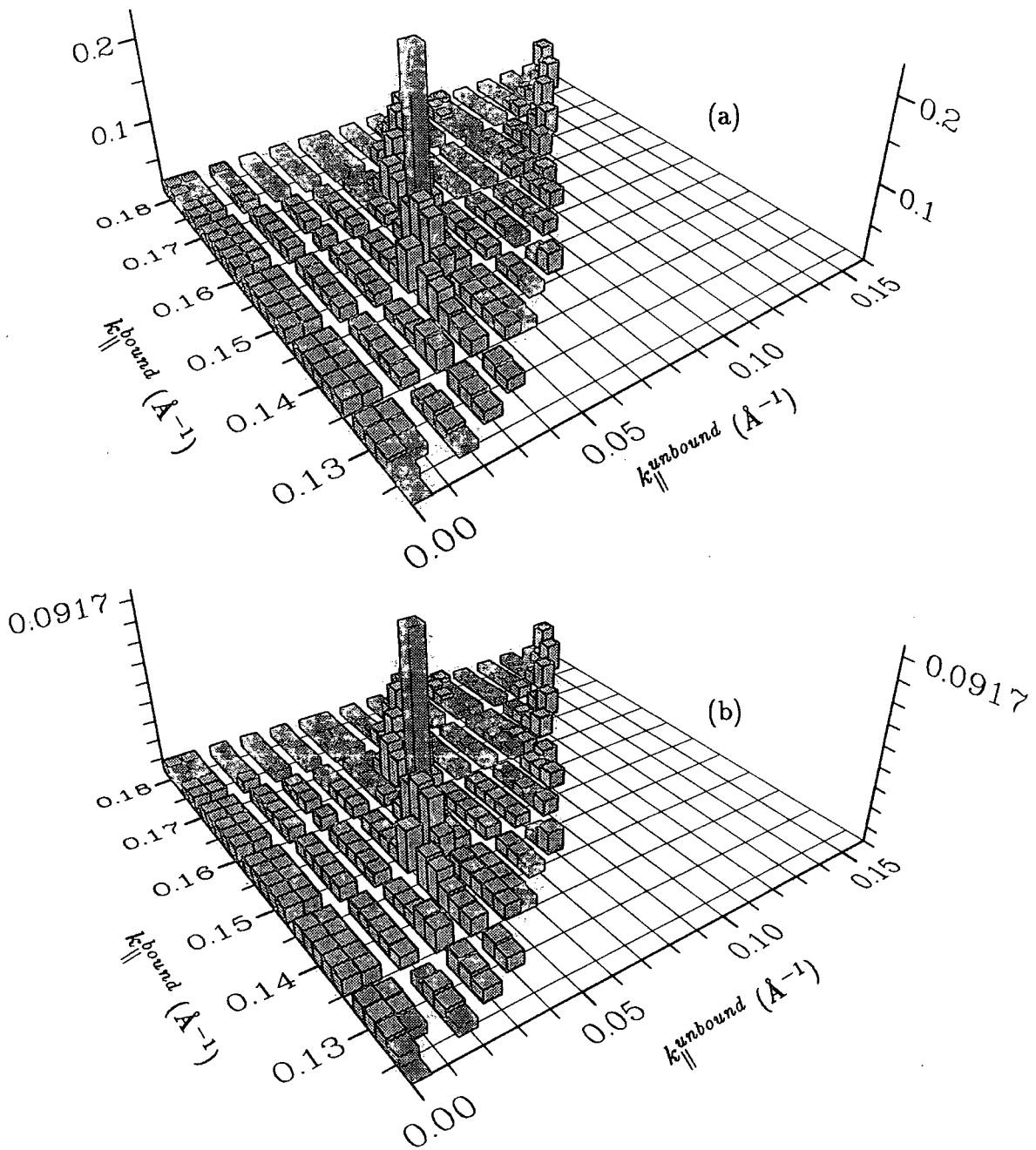
Figure 5.28 Capture probabilities per unit area of the well plotted against $k_{\parallel}^{bound}$ and $k_{\parallel}^{unbound}$ for (a) alloy, and (b) acoustic phonon scattering from heavy hole unbound states into the LH1 subband of figure 5.2.
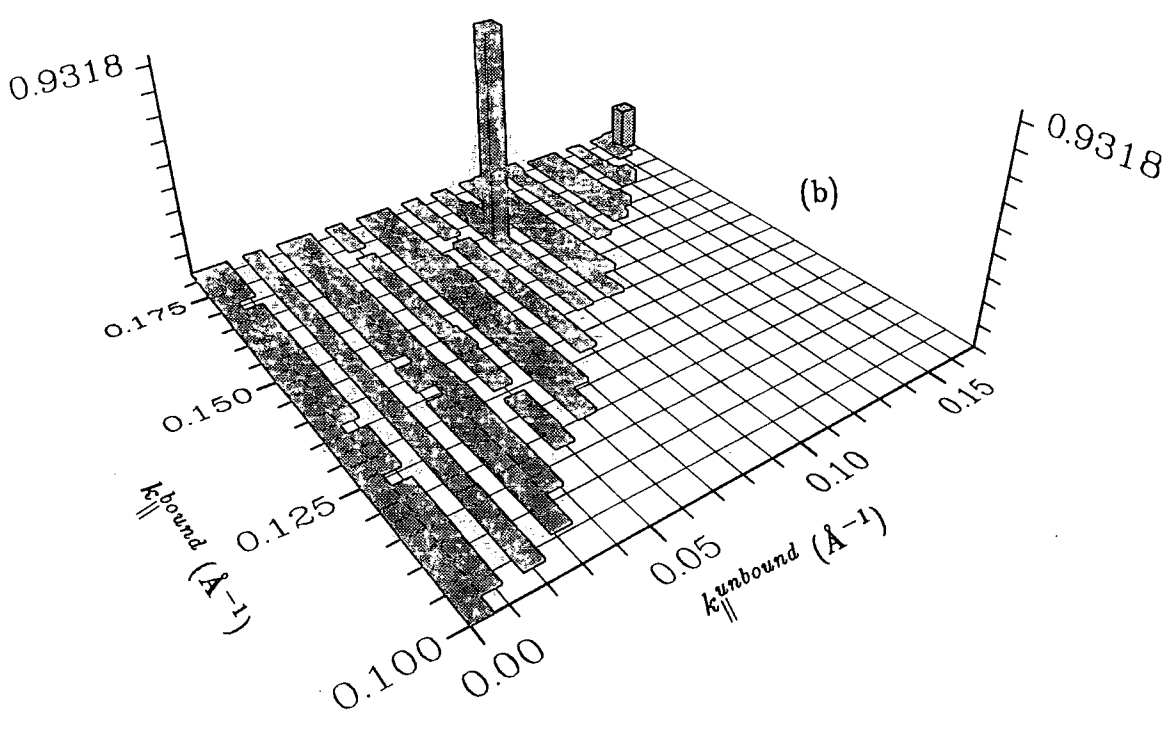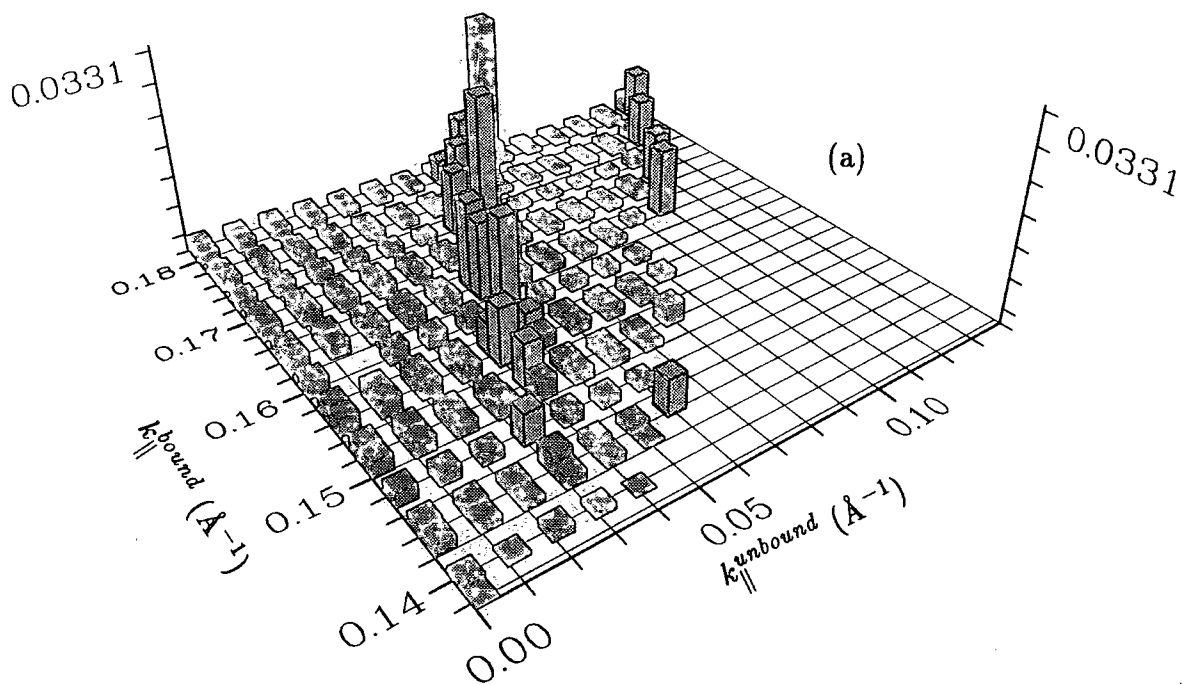
Figure 5.29 Capture probabilities per unit area of the well plotted against $k_\parallel^{bound}$ and $k_\parallel^{unbound}$ for (a) non-polar optical phonon absorption, and (b) non-polar optical phonon emission from heavy hole unbound states into the LH1 subband of figure 5.2.
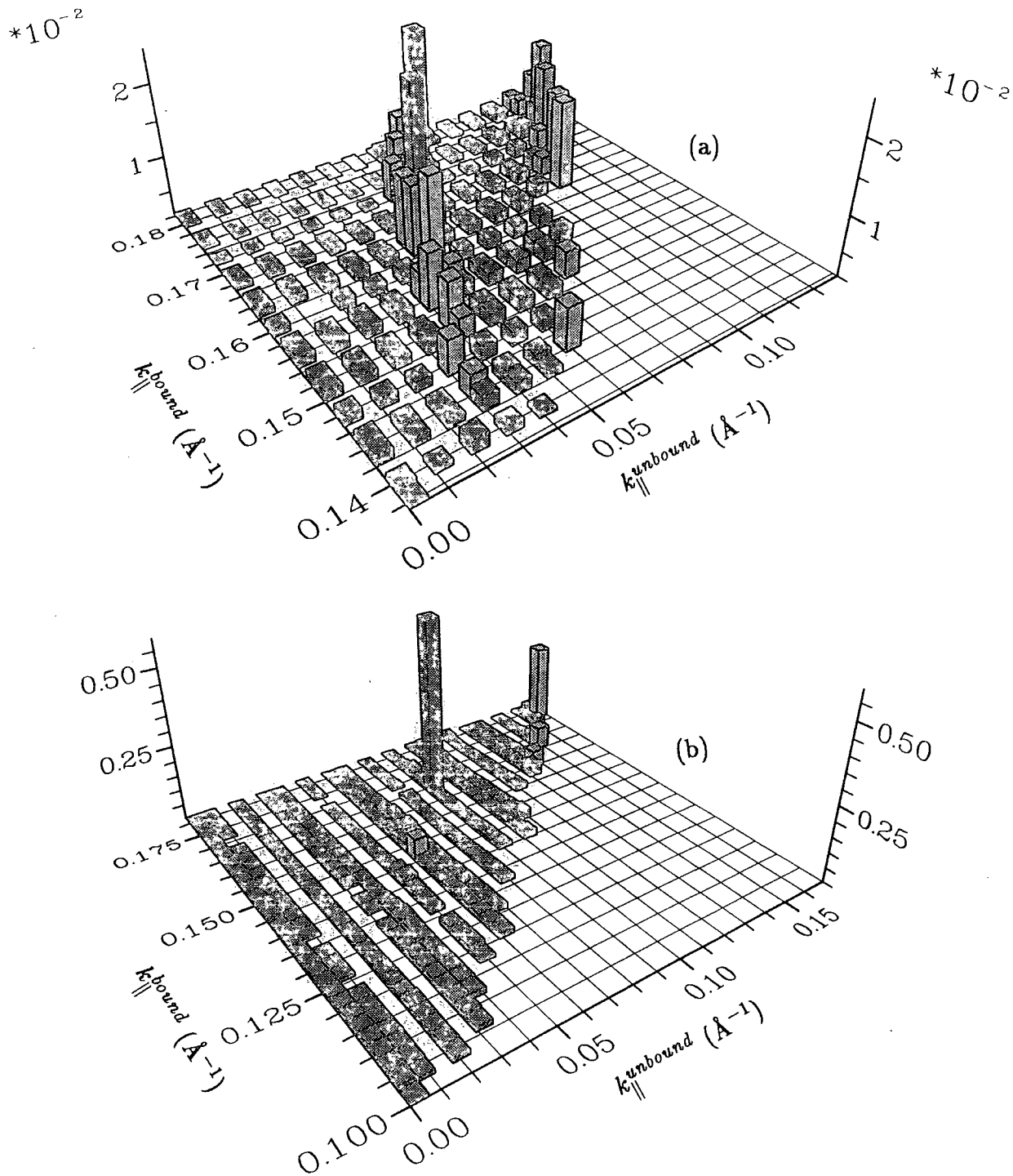
Figure 5.30 Capture probabilities per unit area of the well plotted against $k_{\parallel}^{bound}$ and $k_{\parallel}^{unbound}$ for (a) polar optical phonon absorption, and (b) polar optical phonon emission from heavy hole unbound states into the LH1 subband of figure 5.2.
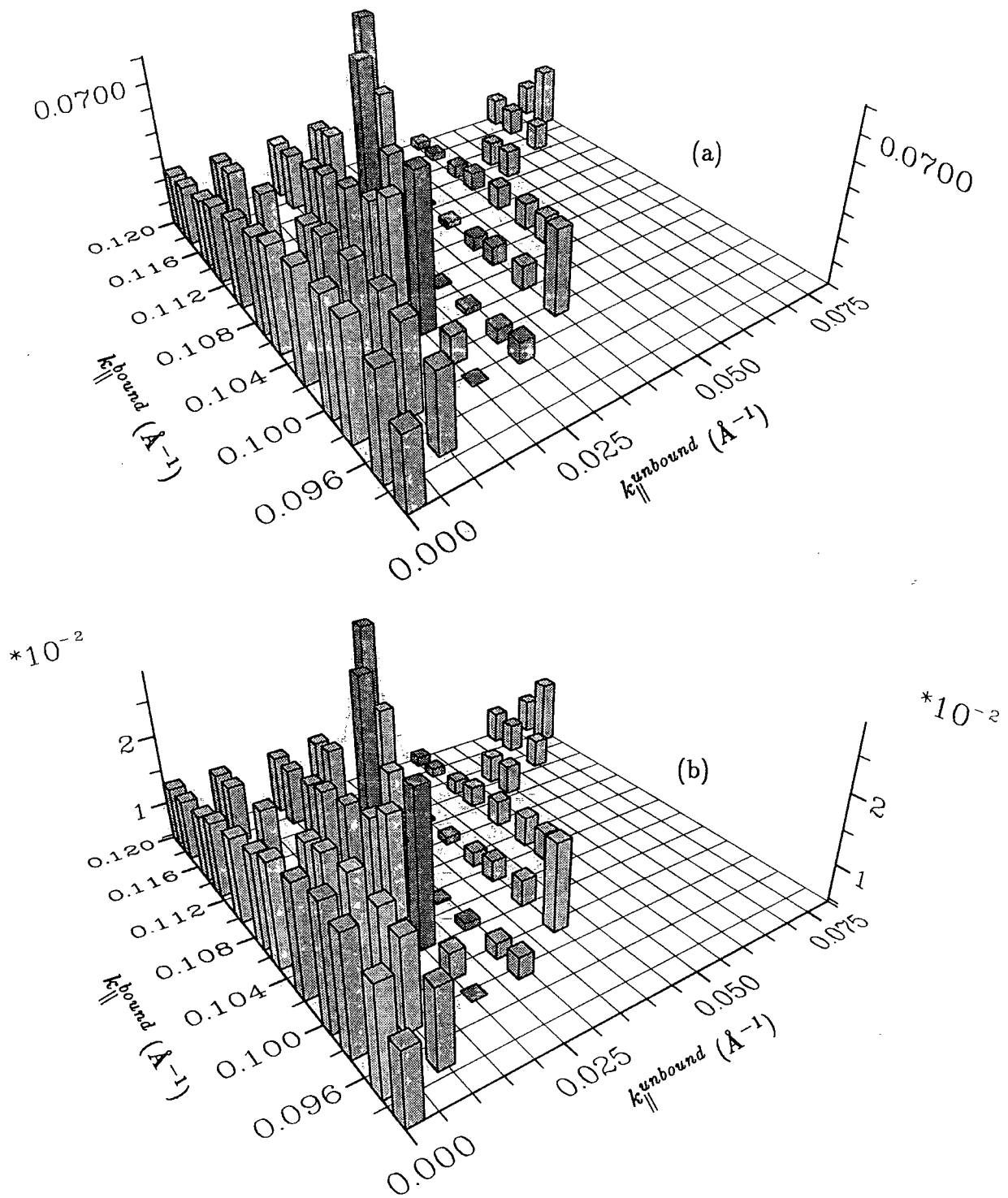
Figure 5.31 Capture probabilities per unit area of the well plotted against $k_\parallel^{bound}$ and $k_\parallel^{unbound}$ for (a) alloy, and (b) acoustic phonon scattering from heavy hole unbound states into the HH2 subband of figure 5.2.
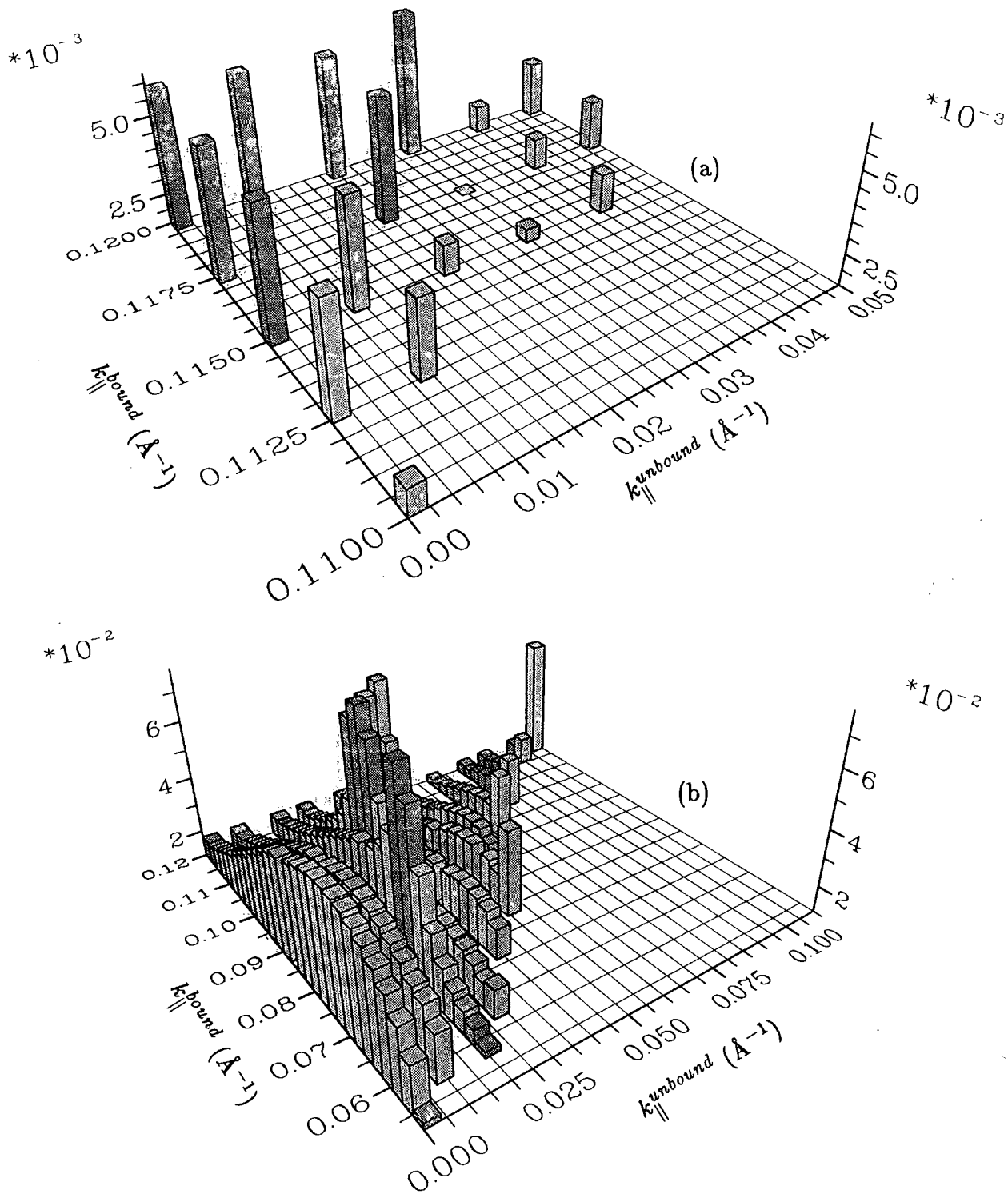
Figure 5.32 Capture probabilities per unit area of the well plotted against $k_{\parallel}^{bound}$ and $k_{\parallel}^{unbound}$ for (a) non-polar optical phonon absorption, and (b) non-polar optical phonon emission from light hole unbound states into the HH2 subband of figure 5.2.
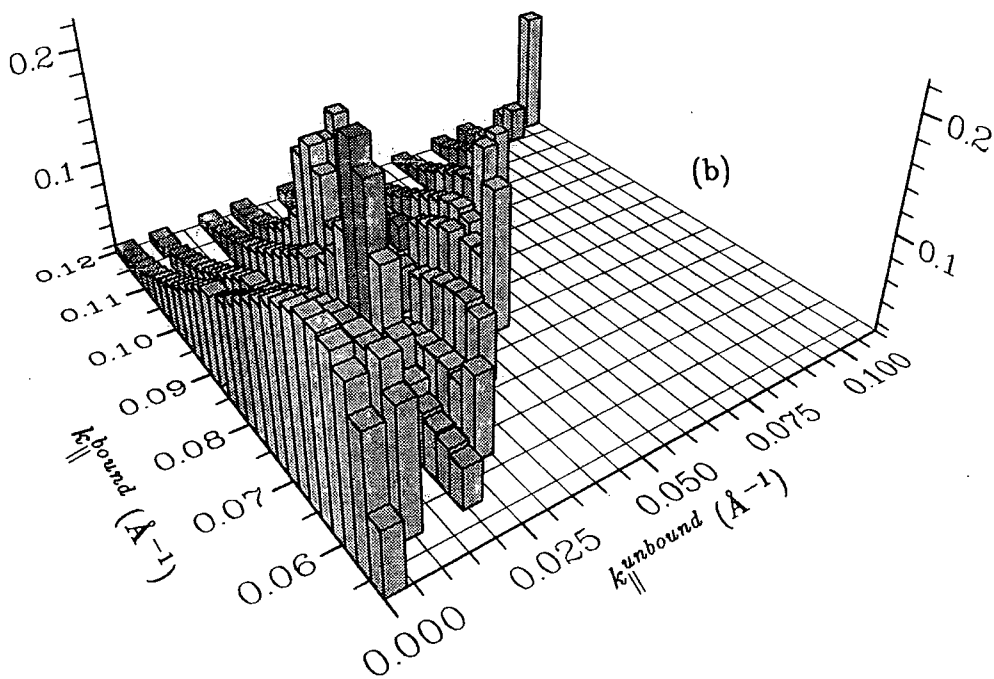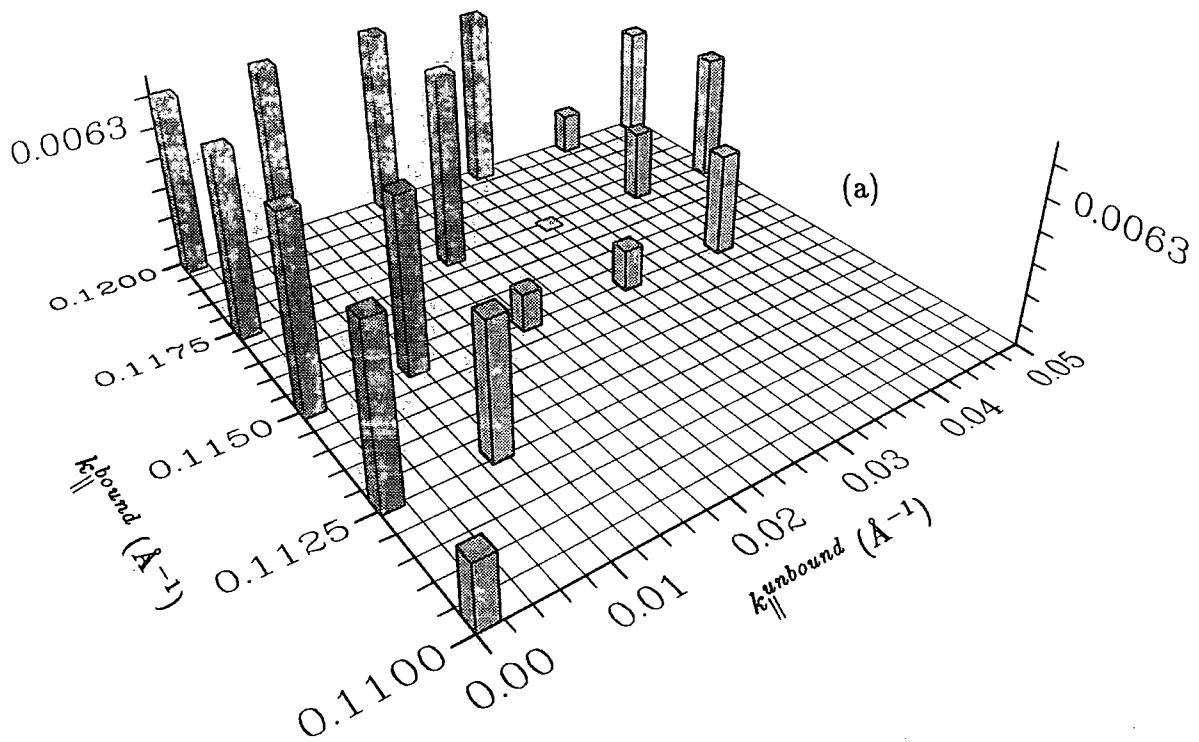
Figure 5.33 Capture probabilities per unit area of the well plotted against $k_\parallel^{bound}$ and $k_\parallel^{unbound}$ for (a) polar optical phonon absorption, and (b) polar optical phonon emission from light hole unbound states into the HH2 subband of figure 5.2.
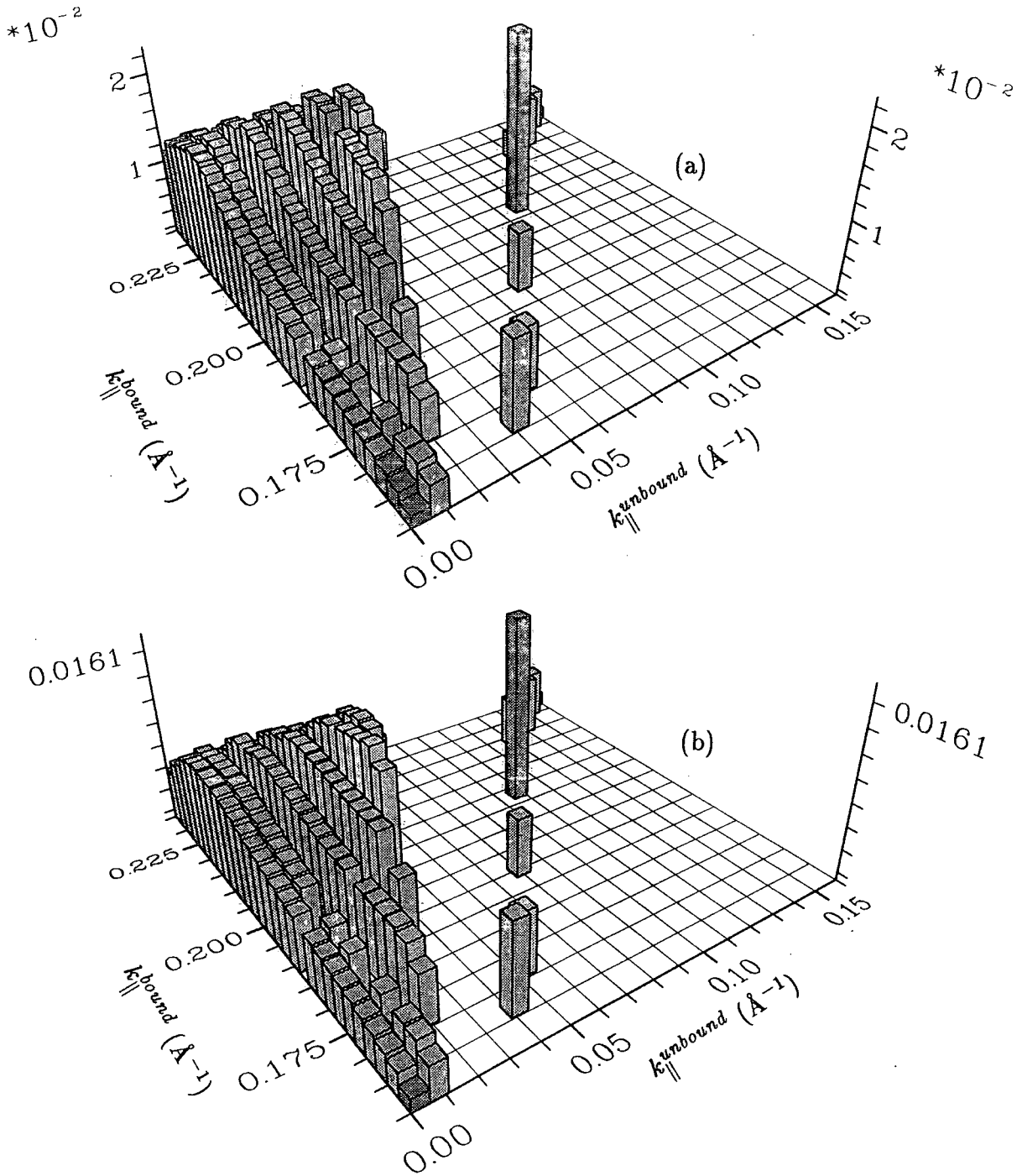
Figure 5.34 Capture probabilities per unit area of the well plotted against $k_{\parallel}^{bound}$ and $k_{\parallel}^{unbound}$ for (a) alloy, and (b) acoustic phonon scattering from light hole unbound states into the HH1 subband of figure 5.2.
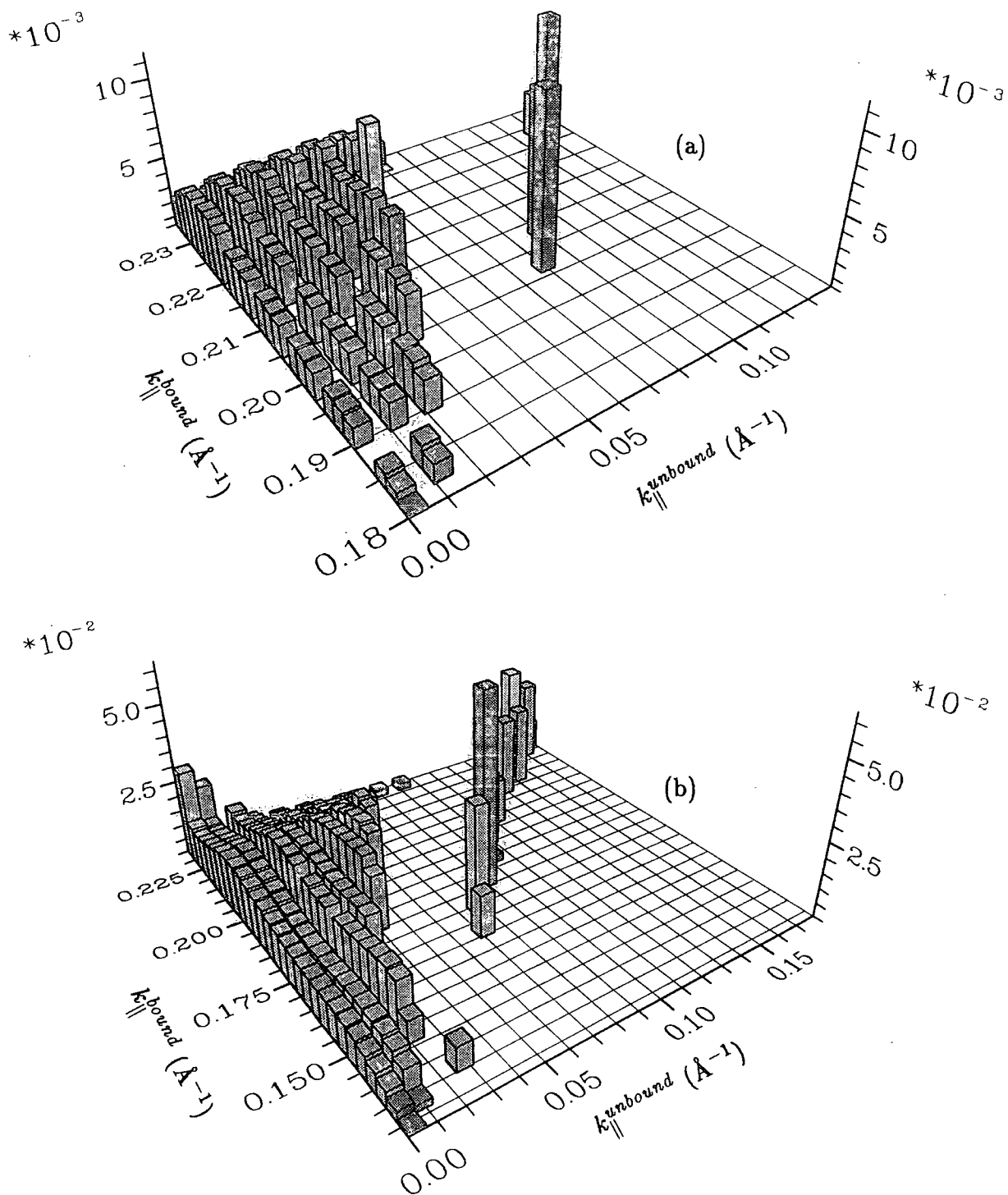
Figure 5.35 Capture probabilities per unit area of the well plotted against $k_{\parallel}^{bound}$ and $k_{\parallel}^{unbound}$ for (a) non-polar optical phonon absorption, and (b) non-polar optical phonon emission from light hole unbound states into the HH1 subband of figure 5.2.
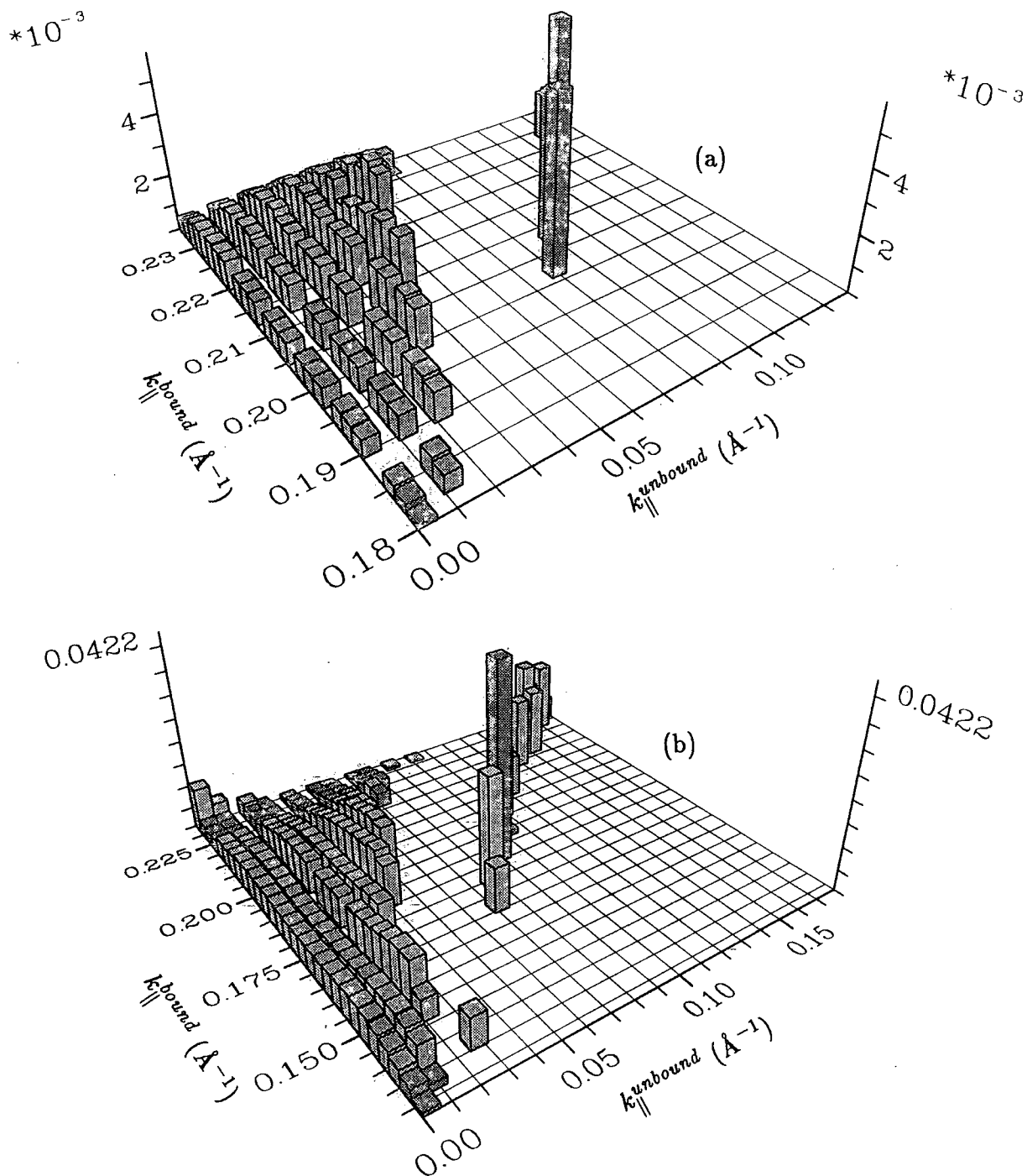
Figure 5.36 Capture probabilities per unit area of the well plotted against $k_{\parallel}^{bound}$ and $k_{\parallel}^{unbound}$ for (a) polar optical phonon absorption, and (b) polar optical phonon emission from light hole unbound states into the HH1 subband of figure 5.2.
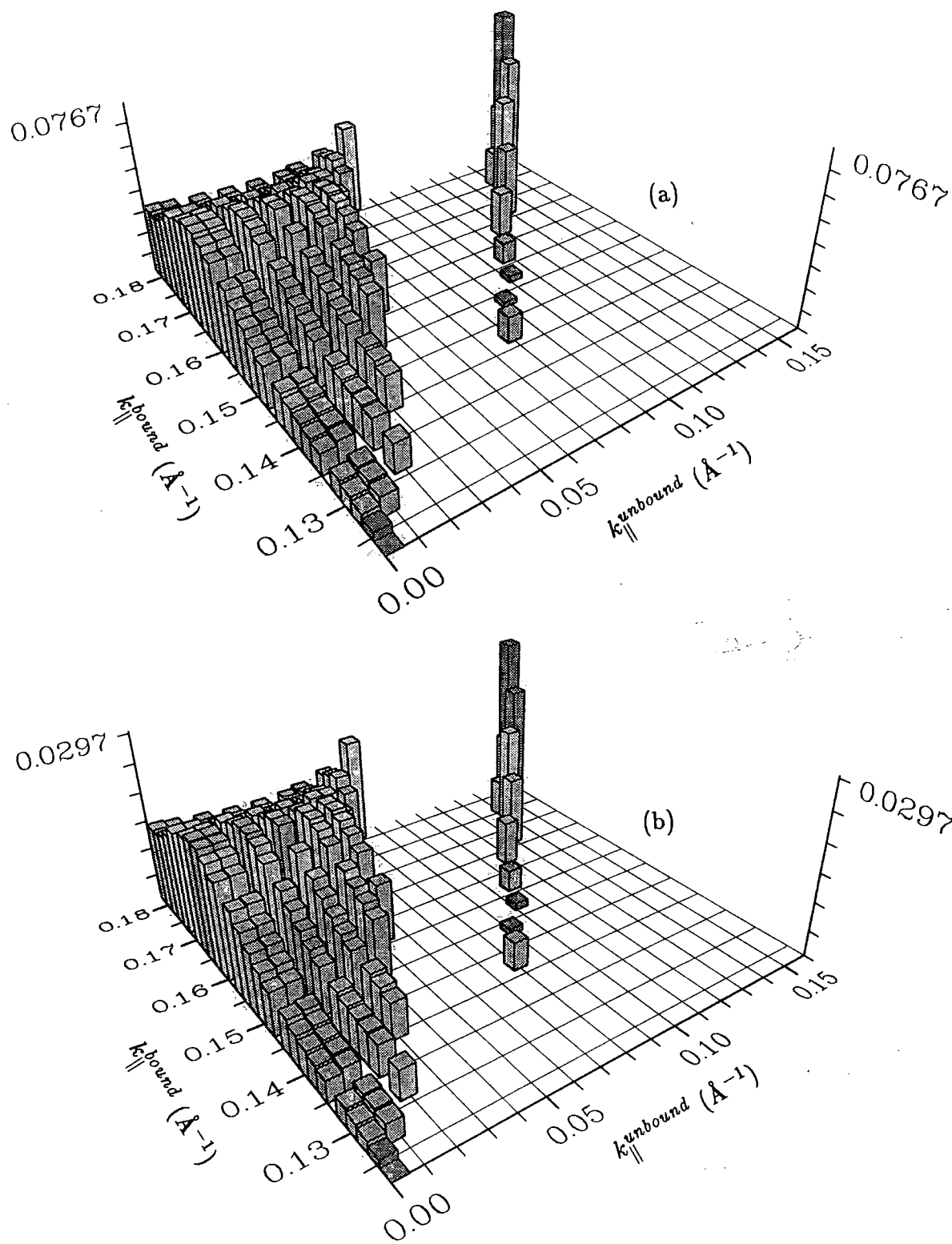
Figure 5.37 Capture probabilities per unit area of the well plotted against $k_\parallel^{bound}$ and $k_\parallel^{unbound}$ for (a) alloy, and (b) acoustic phonon scattering from light hole unbound states into the LH1 subband of figure 5.2.
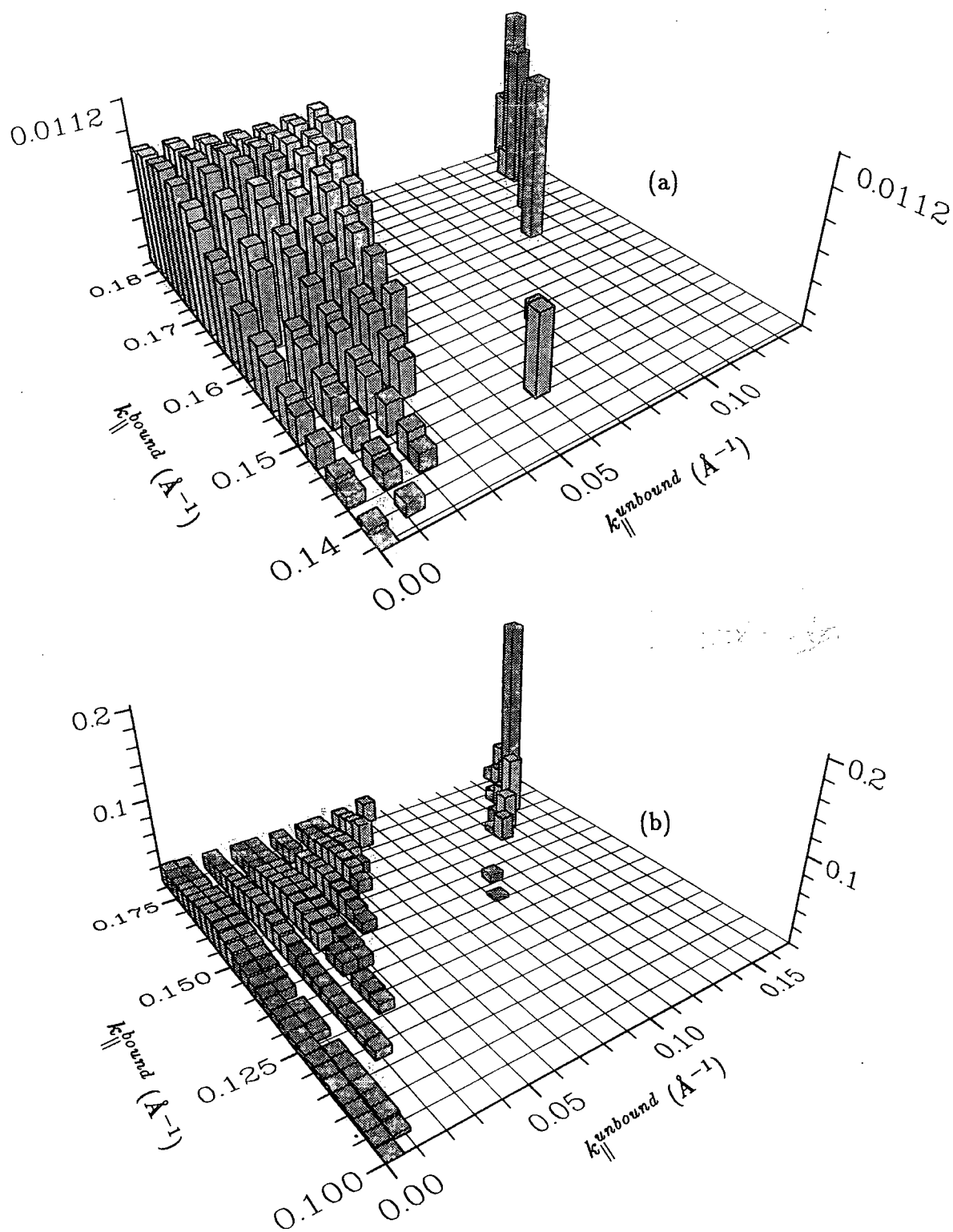
Figure 5.38 Capture probabilities per unit area of the well plotted against $k_{\parallel}^{bound}$ and $k_{\parallel}^{unbound}$ for (a) non-polar optical phonon absorption, and (b) non-polar optical phonon emission from light hole unbound states into the LH1 subband of figure 5.2.
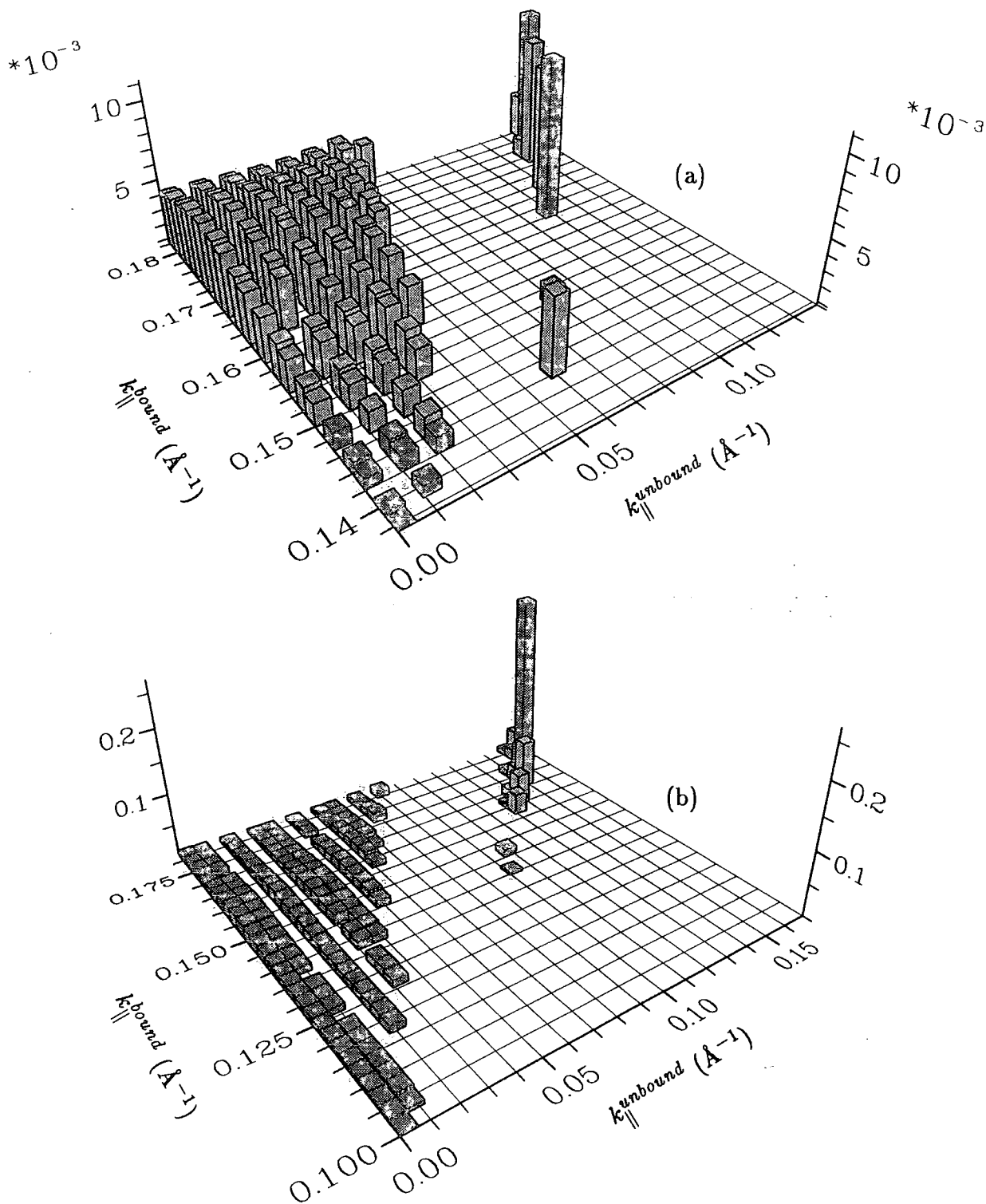
Figure 5.39 Capture probabilities per unit area of the well plotted against $k_{\parallel}^{bound}$ and $k_{\parallel}^{unbound}$ for (a) polar optical phonon absorption, and (b) polar optical phonon emission from light hole unbound states into the LH1 subband of figure 5.2.
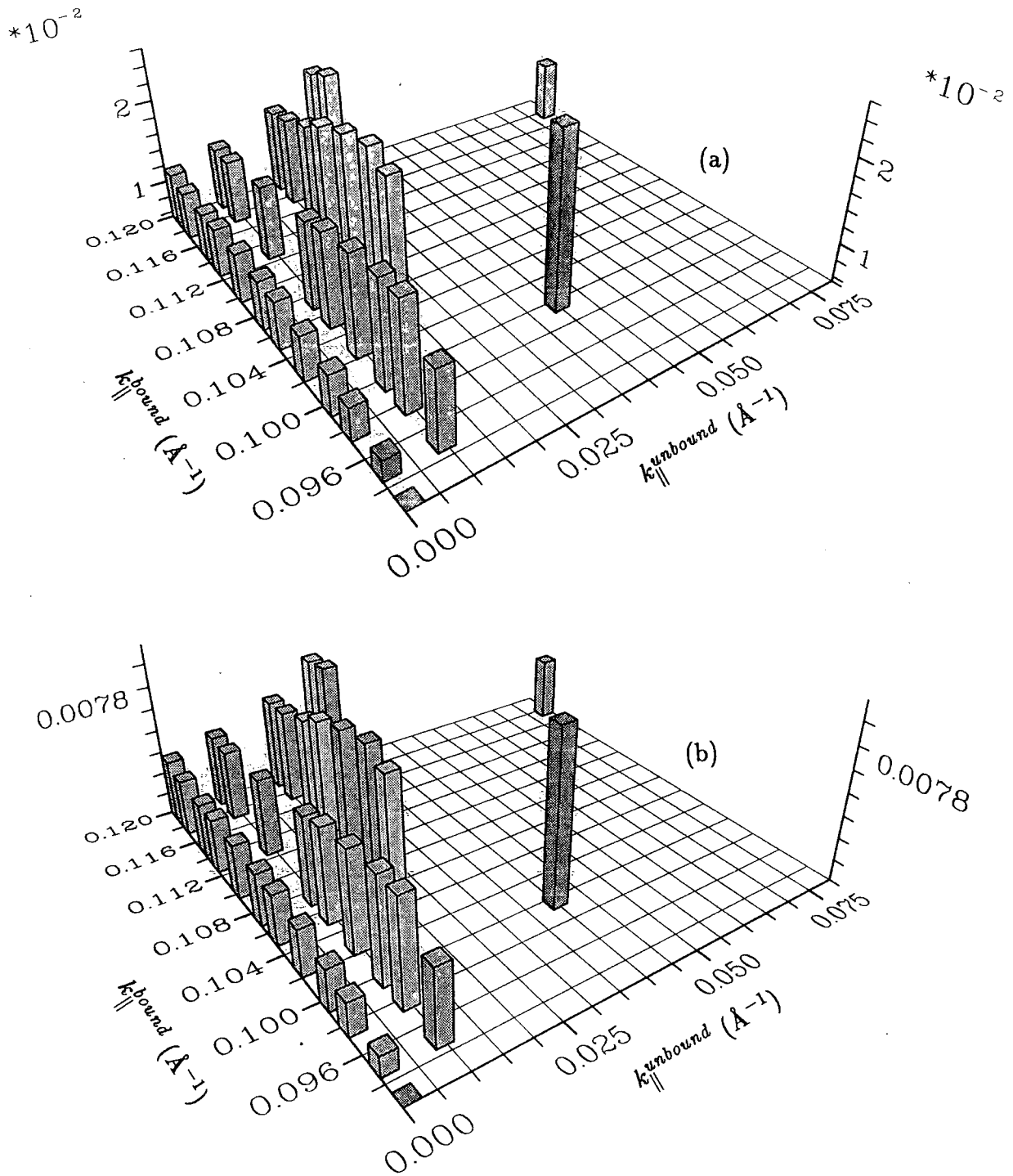
Figure 5.40 Capture probabilities per unit area of the well plotted against $k_{\parallel}^{bound}$ and $k_{\parallel}^{unbound}$ for (a) alloy, and (b) acoustic phonon scattering from light hole unbound states into the HH2 subband of figure 5.2.
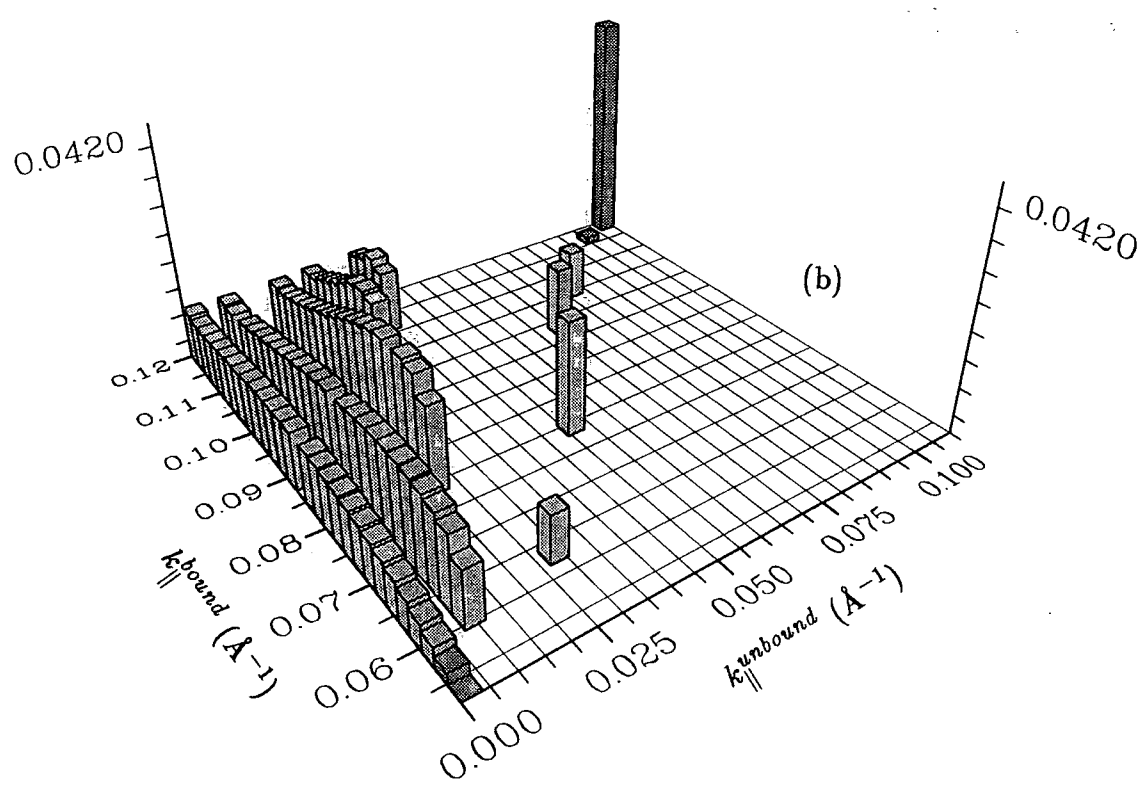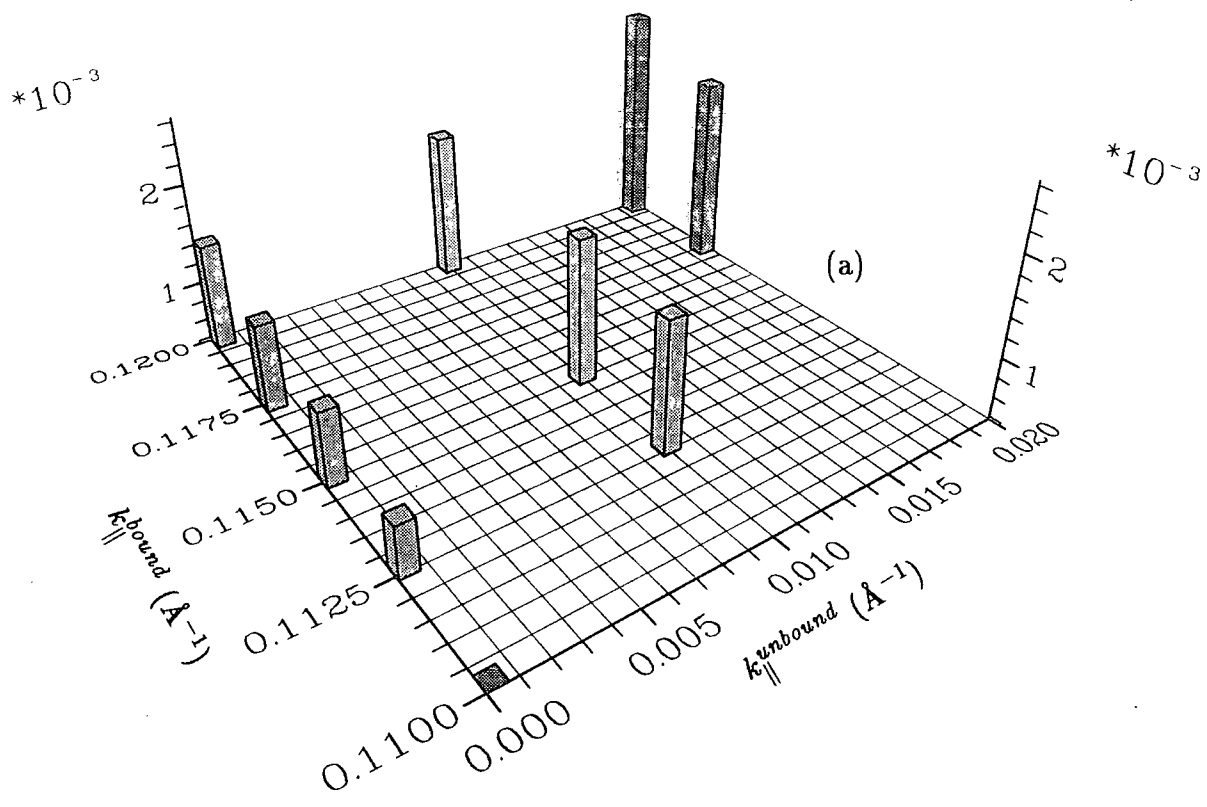
Figure 5.41 Capture probabilities per unit area of the well plotted against $k_\parallel^{bound}$ and $k_\parallel^{unbound}$ for (a) non-polar optical phonon absorption, and (b) non-polar optical phonon emission from light hole unbound states into the HH2 subband of figure 5.2.
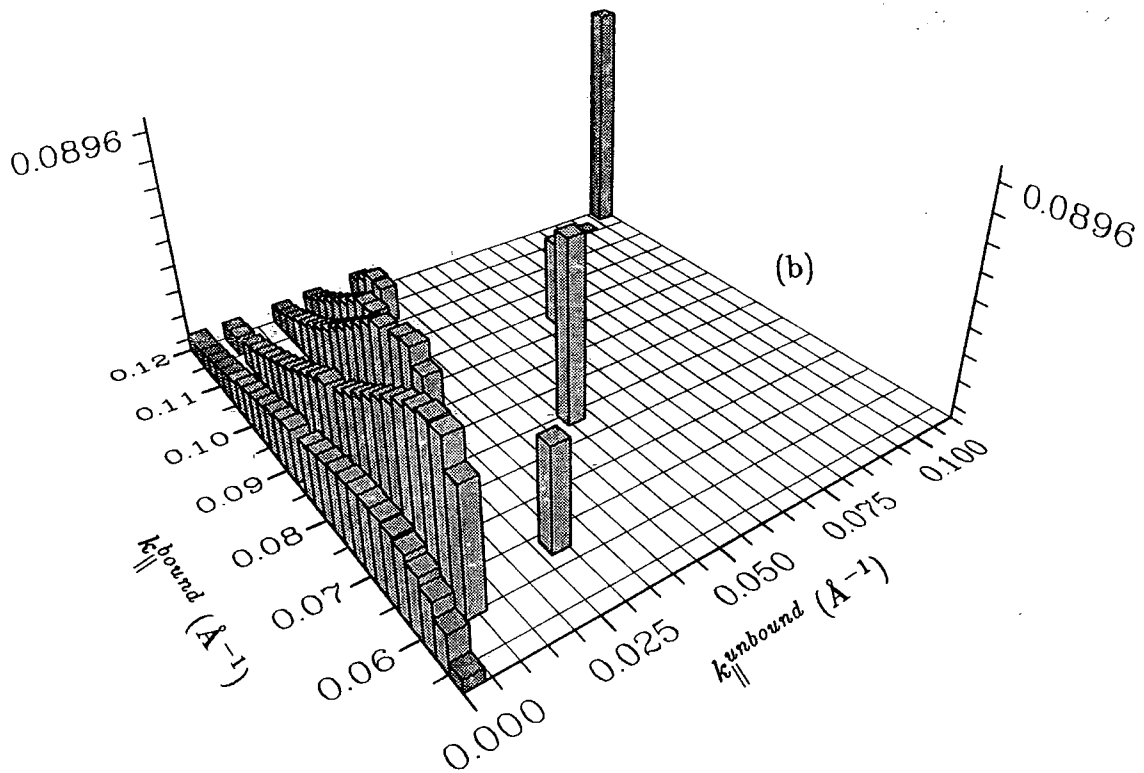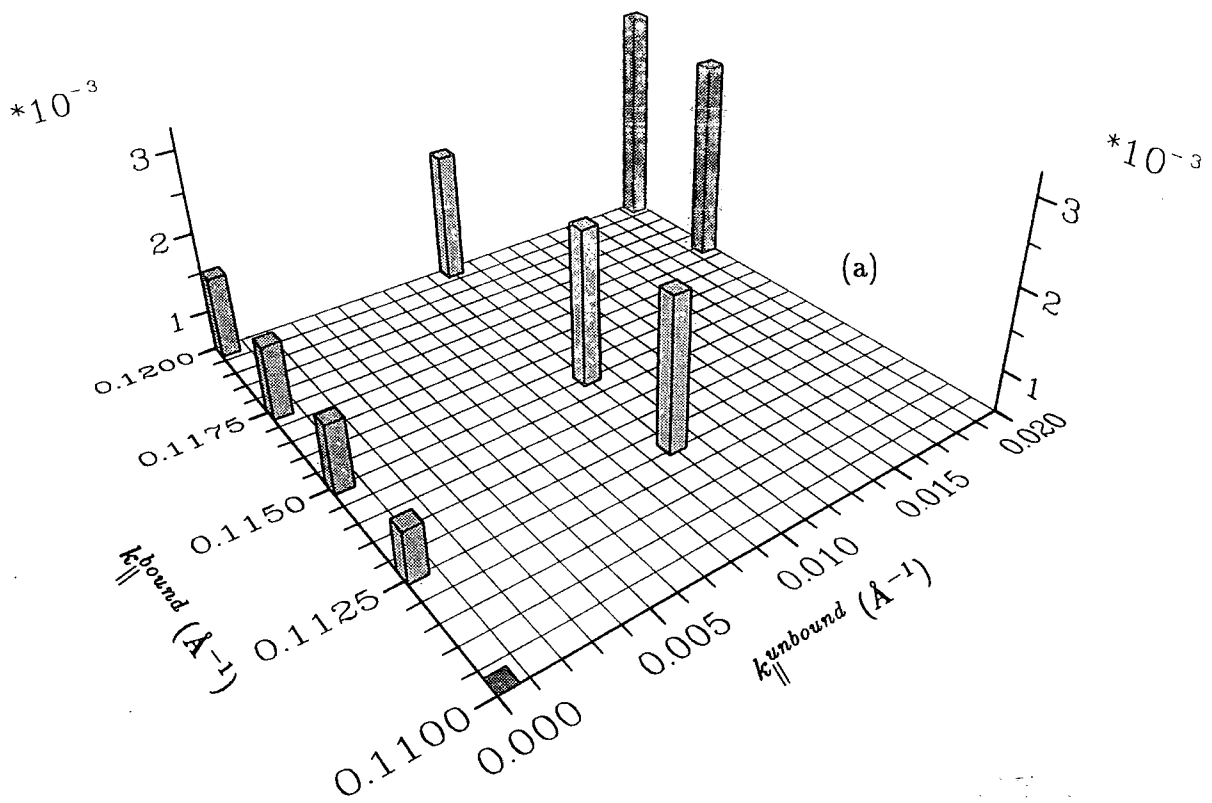
Figure 5.42 Capture probabilities per unit area of the well plotted against $k_{\parallel}^{bound}$ and $k_{\parallel}^{unbound}$ for (a) polar optical phonon absorption, and (b) polar optical phonon emission from light hole unbound states into the HH2 subband of figure 5.2.

5.7 Summary

The hole capture model presented in this chapter is in several respects similar to existing capture models [2, 8, 12]. For example, it has been assumed that at the instant of capture, the unbound barrier states can be represented by coherent wavefunctions which span the confinement region, and that Fermi's Golden Rule defines the capture rate. The standard form of the Golden Rule requires that the unbound and bound states are normalised to the confinement volume, hence the capture rate is roughly inversely proportional to the confinement width.

However, in contrast to other calculations which used the parabolic band approximation [1, 2, 3], this model makes use of k.p bandstructure. Realistic valence subband dispersions are produced, since band mixing effects are included. The transition rates have been adapted to create capture data which are *local* to the quantum well. By writing the capture rate in terms of the incident particle flux, the capture *probabilities* for barrier states with a range of energies and momenta have been determined. In this context, the *probability* describes the fraction of the incident particle current which is trapped by the well. Such data can only give a complete description of the capture properties of a quantum well once they are included in a many-particle transport simulation. However, by assuming that heavy and light hole barrier states can be represented by a Maxwell-Boltzmann distribution, the average capture rate per unit area of the well plane can be estimated for each scattering mechanism. This provides some idea of the most important capture processes. Furthermore, it is possible to identify those subbands into which holes are more readily captured.

References

[1] Bastard G and Brum J A 1986 *Phys. Rev. B* **33** 1420

[2] Kozyrev S V and Shik A Y 1985 *Sov. Phys. Semicond.* **19** 1024

[3] Brum J A and Bastard G 1987 *Superlatt. and Microstruct.* **3** 51

[4] Nagarajan R, Ishikawa M, Fukushima T, Geels R S and Bowers J E
    1992 *IEEE Journ. Quantum Elec.* **28** 1990

[5] Nagar R, Tessler N, Abraham D, Eisenstein G, Koren U and Raybon G
    1992 *Appl. Phys. Lett.* **60** 1788

[6] Shichijo H, Kolbas R M, Holonyak N, Dupuis R D and Dapkus P D
    1978 *Solid State Comm.* **27** 1029

[7] Tang J Y, Hess K, Holonyak N, Coleman J J and Dapkus P D
    1982 *J. Appl. Phys.* **53** 6043

[8] Kuhn T and Mahler G 1989 *Solid State Elec.* **32** 1851

[9] Bastard G, Ziemelis U O, Delalande C, Voos M, Gossard A C and
    Wiegmann W 1984 *Solid State Comm.* **49** 671

[10] Deveaud B, Shah J, Damen T C and Tsang W T
     1988 *Appl. Phys. Lett.* **52** 1886

[11] Hirayama H, Yoshida J, Miyake Y and Asada M
     1992 *Appl. Phys. Lett.* **61** 2398

[12] Kuhn T and Mahler G 1988 *Physica Scripta* **38** 216

[13] Brum J A, Weil T, Nagle J and Vinter B 1986 *Phys. Rev. B* **34** 2381

[14] Ru G and Li A 1993 *Superlatt. and Microstruct.* **13** 289

[15] Eppenga R, Schuurmans M F H and Colak S 1987 *Phys. Rev. B* **36** 1554

[16] Smith D L and Mailhiot C 1986 *Phys. Rev. B* **33** 8345

[17] Wood A C G 1990 *Ph.D Thesis (Dunelm)*, not published

[18] Landholt-Börnstein Neue Serie 1982 *Physics of Group IV
     Elements and III − V Compounds*, Springer-Verlag

[19] Dutta N K and Nelson R J 1982 *J. Appl. Phys.* **53** 78

[20] Walmsley M 1993 *Ph.D Thesis (Dunelm)*, not published

[21] Littlejohn M A, Hauser J R, Glisson J H, Ferry D K and Harrison J W
     1978 *Solid State Elec.* **21** 107

Chapter 6

Bound-Bound Transition Rates For

Holes In A 30Å In$_{0.7}$Ga$_{0.3}$As Quantum Well

6.1 Introduction

Once carriers have become trapped into bound states of a quantum well they can relax within the well by phonon emission and other scattering processes between states of the same and other subbands. In this chapter, the relaxation process is considered and the intra- and inter- subband scattering rates for holes are presented for the 30Å In$_{0.7}$Ga$_{0.3}$As-InGaAsP structure described in chapter 5. The rates have again been determined by applying Fermi's Golden Rule. A short description of the matrix elements for bound-bound transitions by phonon and alloy scattering is provided in section 6.2. Although similar to those described in chapter 3, here the hole eigenstates are described using an eight rather than a two-term set of basis Bloch functions, and the quantum well is finite. A brief analysis of the matrix elements and scattering rates is given in section 6.3. Some possible paths for the cooling of holes within this particular quantum well are discussed in section 6.4.

6.2 Scattering matrix elements in the eight band k.p scheme

6.2a Subband mixing

Figure 6.1 depicts the non-parabolic valence subbands of the quantum well, clearly showing anticrossing between the HH1 and LH1 subbands. The LH1
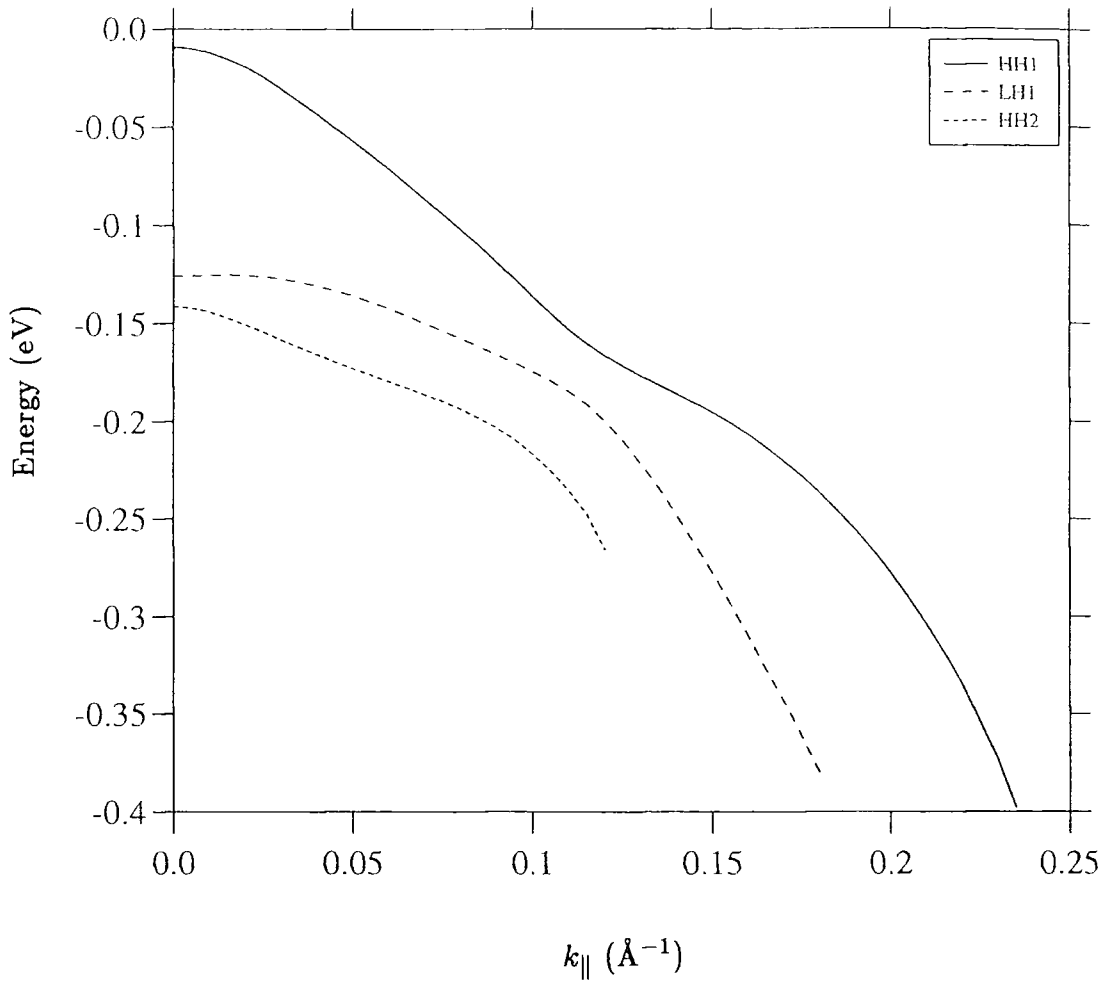
Figure 6.1 The valence subband dispersions for a 30Å $In_{0.7}Ga_{0.3}As$-$In_{0.75}Ga_{0.25}As_{0.55}P_{0.45}$ quantum well.

The biaxial compressive strain in the well is 1.2%.
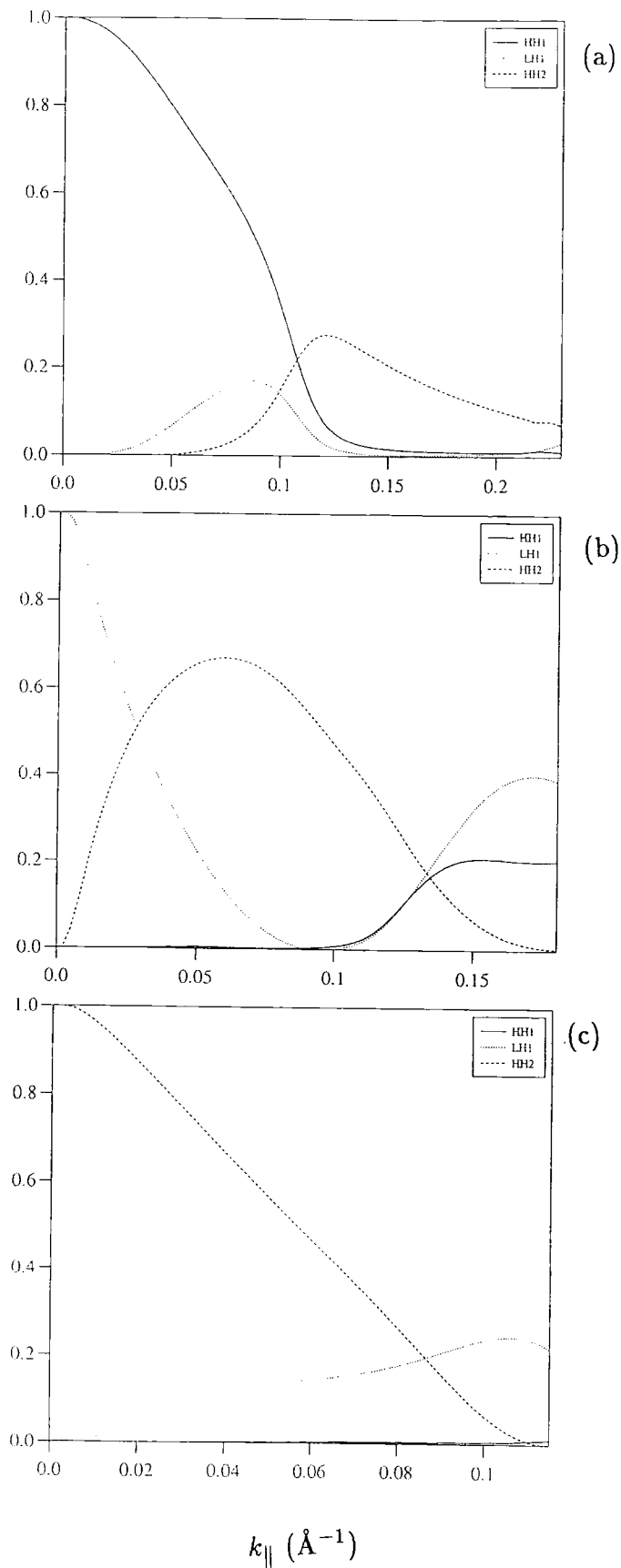
Figure 6.2 The fractional character of states on the (a) HH1, (b) LH1 and (c) HH2 subbands as a function of in-plane wavevector $k_{\parallel}$.

subband possesses a maximum at $k_\parallel \sim 0.015\text{Å}^{-1}$ away from the zone centre. Therefore, for both elastic and inelastic scattering into states on the LH1 subband, allowance must be made for the fact that at certain energies, there will be transitions to states on either side of this subband maximum, and intraband 'cross-valley' scattering is also possible. Overlap integrals between states on a particular subband and the possible zone centre eigenfunctions reveal the nature of the subband mixing. The k.p Hamiltonian matrix for $k_\parallel = 0$ (chapter 5), shows that Bloch states $|\,1\rangle .. \,|\,4\rangle$ are decoupled from states $|\,5\rangle .. \,|\,8\rangle$. Furthermore, Bloch states $|\,2\rangle$ and $|\,6\rangle$ which are heavy in the growth direction do not interact with any other such states at $k_\parallel = 0$. The Bloch functions for the conduction, spin split-off and light hole bands are always coupled, however. Hence the LH1 subband is not simply a function of the light hole Bloch states at the zone centre.

Figures 6.2a..c show the fraction of the HH1, LH1 and HH2 zone centre eigenfunctions which exist in states on the HH1, LH1 and HH2 subbands of the quantum well. At small wavevectors, states on these subbands are, to a good approximation, just admixtures of the HH1, LH1 and HH2 zone centre eigenfunctions. However, this is not true at larger $k_\parallel$, where higher order interactions are important. Figure 6.2a reveals that states on the HH1 subband retain much of their zone centre character up until the anticrossing with the LH1 subband at $k_\parallel \sim 0.1\text{Å}^{-1}$, at which the HH1 nature is almost lost. Figure 6.2b shows the strong mixing between the LH1 and HH2 subbands, which results in the off-centre band maximum in the LH1 band (figure 6.1). The loss of LH1 character is matched by a gain of HH2 character for $k_\parallel < 0.05\text{Å}^{-1}$. At larger $k_\parallel$, these states

are mostly a mixture of LH1 (40%) and HH1 character (20%). For states on the HH2 subband, the decrease in HH2 content with $k_{\parallel}$ is almost linear, and virtually none of the original character remains at the point of the subband reaching the continuum edge (figure 6.2c).

Consider the transition between a bound state $\Psi^i_{(n,k_{\parallel})}$ on subband n at in-plane wavevector $k_{\parallel}$, and some final state $\Psi^f_{(n',k'_{\parallel})}$. The three valence subbands are doubly degenerate owing to the fact that the Bloch functions are Kramer's degenerate [1]. Choosing spin indices 1, 2 to represent the degenerate eigenfunctions describing the initial state Ψ^i, and indices 3, 4 for Ψ^f, the mean matrix element connecting Ψ^i and Ψ^f (including the extra factor of two in the density of final states) is

$$| M |^2 = \frac{| M_{13} |^2 + | M_{23} |^2 + | M_{14} |^2 + | M_{24} |^2}{2}. \tag{6.1}$$

Using similar notation to chapter 5, the quantum well eigenfunctions in the well and barrier ('left' and 'right') layers can be written as follows:

$$\Psi^i_{(left)} = \sum_{j=1}^{8} \sum_{i=1}^{8} \alpha^B_{ijh} e^{ia^B_i z} e^{ik_{\parallel} \cdot r_{\parallel}} \mid j \rangle, \qquad h = 1, 2 \qquad z < -\frac{l}{2} \tag{6.2a}$$

$$\Psi^i_{(well)} = \sum_{j=1}^{8} \sum_{i=1}^{16} \alpha^W_{ijh} e^{ia^W_i z} e^{ik_{\parallel} \cdot r_{\parallel}} \mid j \rangle, \qquad h = 1, 2 \qquad \mid z \mid \leq \frac{l}{2} \tag{6.2b}$$

$$\Psi^i_{(right)} = \sum_{j=1}^{8} \sum_{i=9}^{16} \alpha^B_{ijh} e^{ia^B_i z} e^{ik_{\parallel} \cdot r_{\parallel}} \mid j \rangle, \qquad h = 1, 2 \qquad z > \frac{l}{2} \tag{6.2c}$$

$$\Psi^f_{(left)} = \sum_{j'=1}^{8} \sum_{i'=1}^{8} \beta^B_{i'j'h'} e^{ib^B_{i'} z} e^{ik_{\parallel} \cdot r_{\parallel}} \mid j' \rangle, \qquad h' = 3, 4 \qquad z < -\frac{l}{2} \tag{6.3a}$$

$$\Psi^f_{(well)} = \sum_{j'=1}^{8} \sum_{i'=1}^{16} \beta^W_{i'j'h'} e^{ib^W_{i'} z} e^{ik_{\parallel} \cdot r_{\parallel}} \mid j' \rangle, \qquad h' = 3, 4 \qquad \mid z \mid \leq \frac{l}{2} \tag{6.3b}$$

$$\Psi^f_{(right)} = \sum_{j'=1}^{8} \sum_{i'=9}^{16} \beta^B_{i'j'h'} e^{ib^B_{i'} z} e^{ik_\parallel \cdot r_\parallel} \mid j'\rangle. \qquad h' = 3,4 \qquad z > \frac{l}{2} \qquad (6.3c)$$

Indices h and h' define the degenerate eigenfunctions. The wavefunctions are normalised across unit area in the well plane and the confinement region defined in chapter 5 (width $L = 1\mu m$). For the initial state,

$$N_I = \int_{-\frac{L}{2}}^{-\frac{l}{2}} \mid \Psi^i_{(left)}(z) \mid^2 dz + \int_{-\frac{l}{2}}^{\frac{l}{2}} \mid \Psi^i_{(well)}(z) \mid^2 dz + \int_{\frac{l}{2}}^{\frac{L}{2}} \mid \Psi^i_{(right)}(z) \mid^2 dz, \quad (6.4)$$

and for the final state,

$$N_F = \int_{-\frac{L}{2}}^{-\frac{l}{2}} \mid \Psi^f_{(left)}(z) \mid^2 dz + \int_{-\frac{l}{2}}^{\frac{l}{2}} \mid \Psi^f_{(well)}(z) \mid^2 dz + \int_{\frac{l}{2}}^{\frac{L}{2}} \mid \Psi^f_{(right)}(z) \mid^2 dz. \quad (6.5)$$

6.2b Alloy scattering

In the case of bound-bound transitions by alloy scattering, it is the contribution to the scattering rate from the well which is dominant, since the envelope functions are evanescent in the barriers. The expression for the alloy scattering rate can be written in the same form as equation 3.13, and the matrix element squared $\mid M_{AL} \mid^2$ is

$$\mid M_{AL} \mid^2 = \frac{1}{N_I N_F} \sum_{h=1}^{2} \sum_{h'=3}^{4} \frac{1}{2} \sum_{j,j'=1}^{8} \sum_{i,i'=1}^{16} \sum_{m,m'=1}^{16} \beta^{W*}_{ijh'} \alpha^W_{i'jh} \beta^W_{mj'h'} \alpha^{W*}_{m'j'h}$$

$$\times \begin{cases} l & a^W_{i'} + b^W_m - a^{W*}_{m'} - b^{W*}_i = 0; \\ \frac{2 sin(a^W_{i'} + b^W_m - a^{W*}_{m'} - b^{W*}_i)\frac{l}{2}}{(a^W_{i'} + b^W_m - a^{W*}_{m'} - b^{W*}_i)} & a^W_{i'} + b^W_m - a^{W*}_{m'} - b^{W*}_i \neq 0. \end{cases} \qquad (6.6)$$

6.2c Phonon scattering

The scattering rate equations for phonon scattering in the quantum well are similar to those described in chapter 3 (equations 3.24, 3.33), the essential differences being in the matrix elements. In the case of deformation potential scattering (acoustic and non-polar processes), the scattering matrix element is

$$
\mid M_{AC/NPO}\mid^2 = \frac{1}{N_I N_F} \sum_{h=1}^{2} \sum_{h'=3}^{4} \frac{1}{2} \int_{-\infty}^{\infty} \mid I_{(left)}(q_z) + I_{(well)}(q_z) + I_{(right)}(q_z) \mid^2 dq_z
$$

(6.7)

and for polar optical phonon scattering:

$$
\mid M_{POP}\mid^2 = \frac{2\pi}{N_I N_F} \sum_{h=1}^{2} \sum_{h'=3}^{4} \frac{1}{2} \int_{-\infty}^{\infty} \frac{\mid I_{(left)}(q_z) + I_{(well)}(q_z) + I_{(right)}(q_z) \mid^2 dq_z}{\sqrt{q_z^4 + 2(k_\parallel^2 + k_\parallel'^2)q_z^2 + (k_\parallel^2 - k_\parallel'^2)^2}},
$$

(6.8)

where

$$
I_{(left)} = \sum_{j=1}^{8} \sum_{i'=1}^{8} \alpha_{ijh}^{B} \beta_{i'jh'}^{B*} \frac{e^{-i(a_i^B - b_{i'}^{B*} \pm q_z)\frac{l}{2}} - e^{-i(a_i^B - b_{i'}^{B*} \pm q_z)\frac{L}{2}}}{i(a_i^B - b_{i'}^{B*} \pm q_z)},
$$

$$
I_{(well)} = \sum_{j=1}^{8} \sum_{i'=1}^{16} \alpha_{ijh}^{W} \beta_{i'jh'}^{W*}
\begin{cases}
l & a_i^W - b_{i'}^{W*} \pm q_z = 0; \\
\frac{2\sin(a_i^W - b_{i'}^{W*} \pm q_z)\frac{l}{2}}{(a_i^W - b_{i'}^{W*} \pm q_z)} & a_i^W - b_{i'}^{W*} \pm q_z \neq 0.
\end{cases}
$$

$$
I_{(right)} = \sum_{j=1}^{8} \sum_{i'=9}^{16} \alpha_{ijh}^{B} \beta_{i'jh'}^{B*} \frac{e^{i(a_i^B - b_{i'}^{B*} \pm q_z)\frac{L}{2}} - e^{i(a_i^B - b_{i'}^{B*} \pm q_z)\frac{l}{2}}}{i(a_i^B - b_{i'}^{B*} \pm q_z)}.
$$
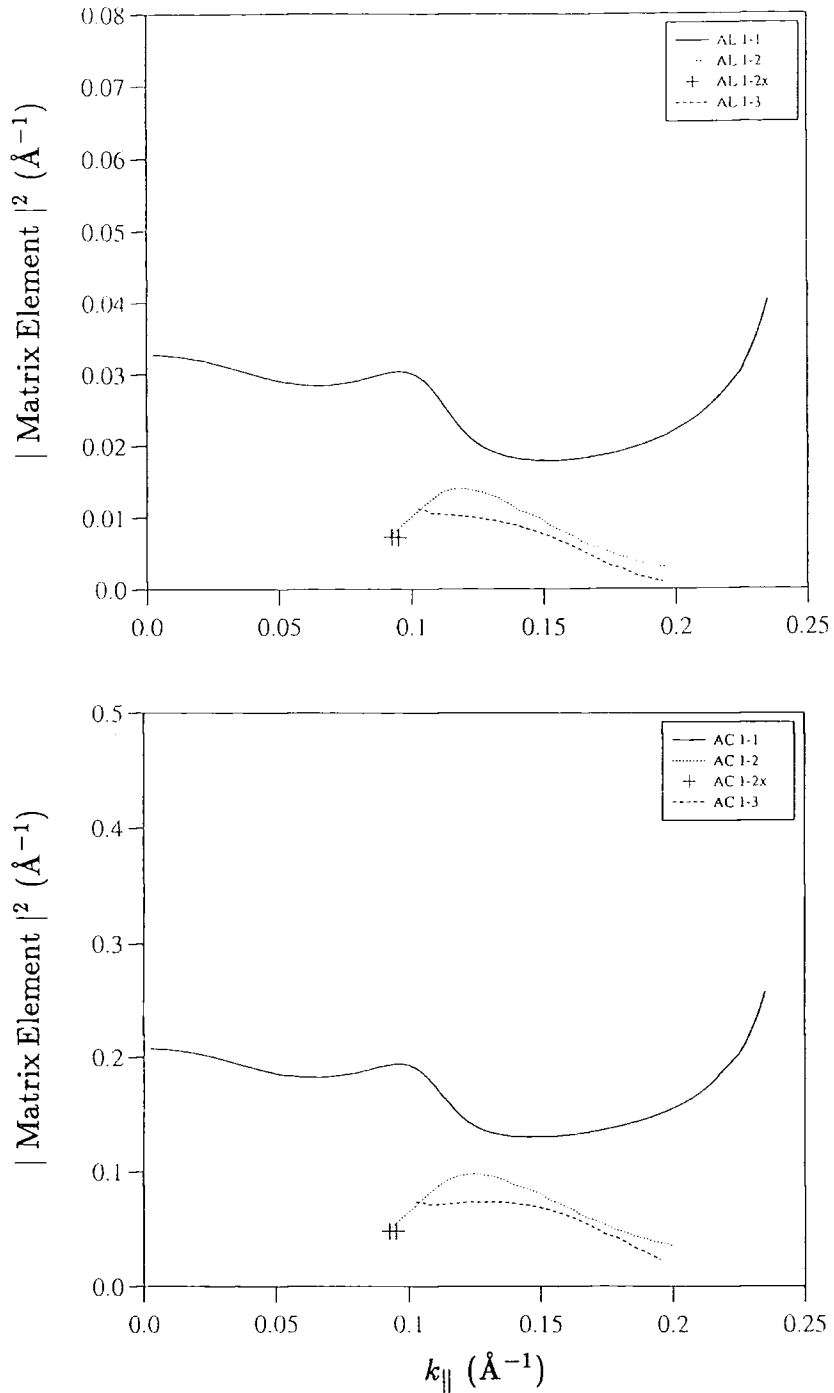
Figure 6.3 Matrix elements for alloy (AL) and acoustic phonon (AC) scattering from the HH1 subband as a function of in-plane wavevector. (In the key the label '1' represents the HH1 band, '2' the LH1 subband and '3' denotes states on the HH2 subband. All transitions marked '-2x' represent scattering into states on subband 2 lying between the zone centre and the off-centre maximum of that subband. This convention is maintained across subsequent diagrams).
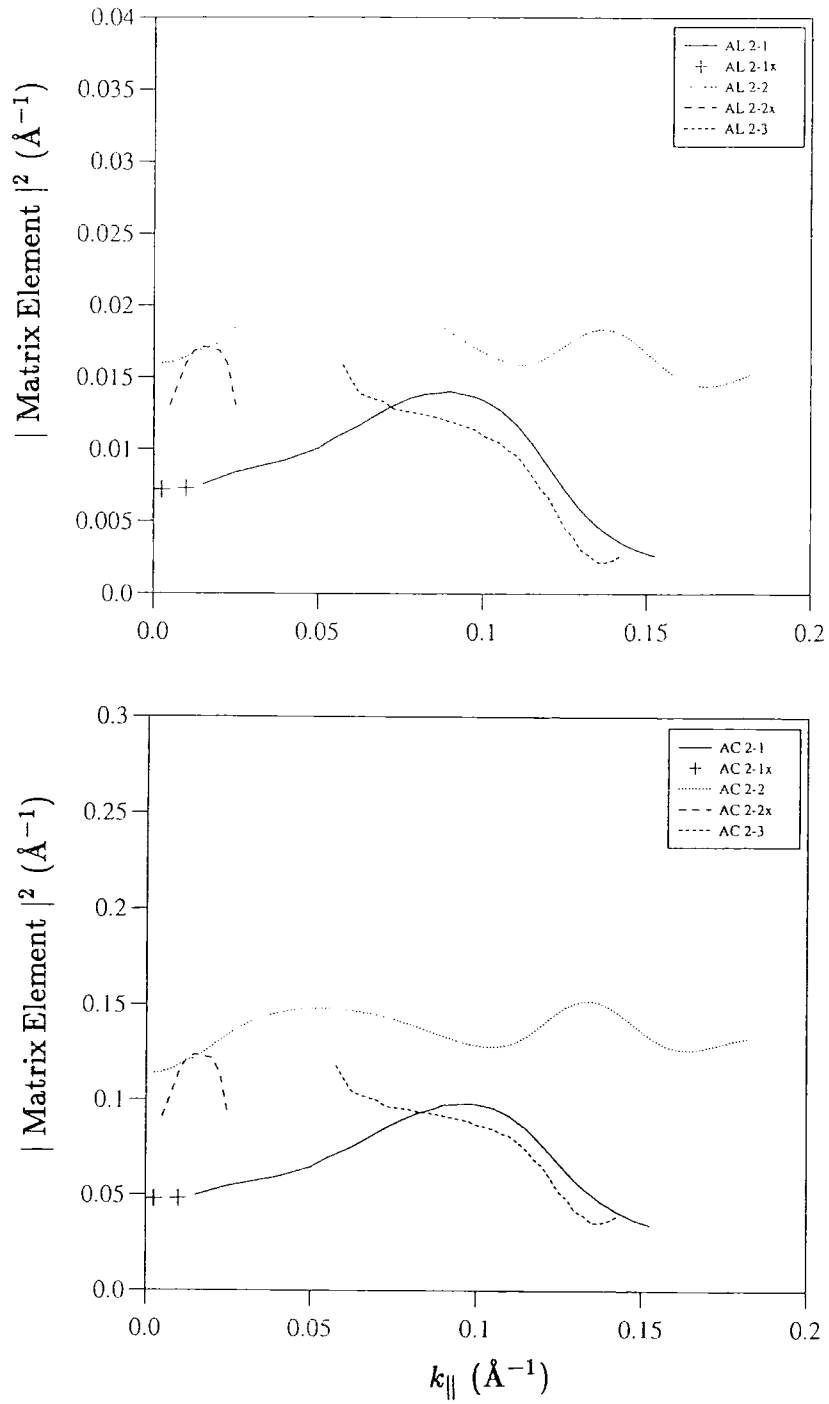
Figure 6.4 Matrix elements for alloy (AL) and acoustic phonon (AC) scattering from the LH1 subband as a function of in-plane wavevector.
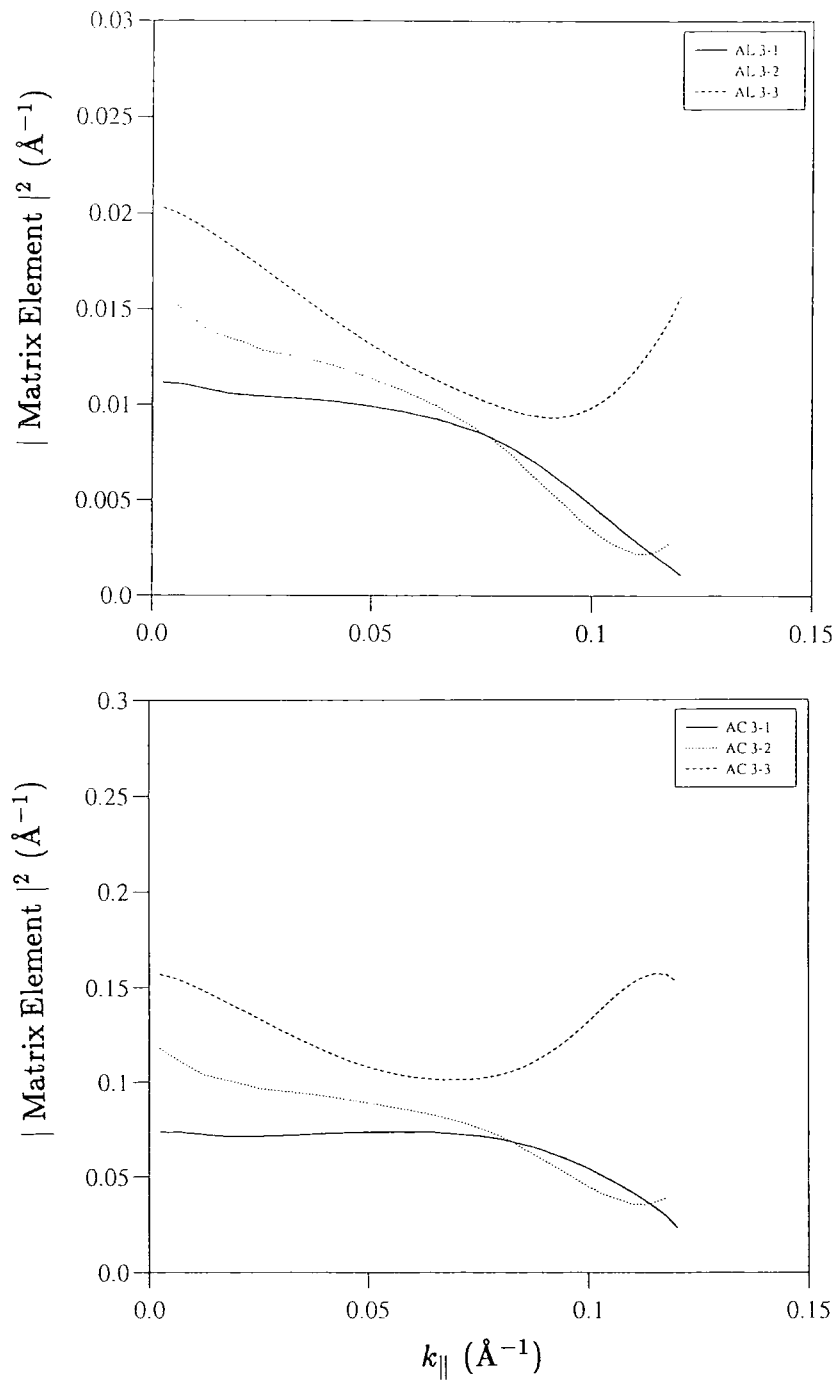
Figure 6.5 Matrix elements for alloy (AL) and acoustic phonon (AC) scattering

from the HH2 subband as a function of in-plane wavevector.

6.3 Features of the bound-bound transitions

Figures 6.3-6.5 show the squared matrix elements for alloy (AL) and acoustic phonon (AC) scattering as a function of in-plane wavevector. For each subband, the graphs for both processes follow similar trends. Matrix elements for non-polar (NP) and polar optical (PO) phonon scattering from states in the HH1 and LH1 subbands are shown in figures 6.6 and 6.7. For the inelastic processes, the salient feature is the large matrix element for polar optical phonon scattering connecting states on the HH1 and LH1 subbands in the vicinity of the anticrossing point ($k_\parallel \sim 0.1 \text{Å}^{-1}$). It so happens that the subband separation is close to the optical phonon energy in this region of $k_\parallel$-space. Hence HH1-LH1 optical phonon absorption and LH1-HH1 optical phonon emission occur between states posessing similar $k_\parallel$. Since the denominator of the polar phonon matrix element is reduced for states with a small separation in wavevector, the matrix elements show a sharp peak. Intersubband non-polar optical phonon matrix elements also reach a maximum in this region of $k_\parallel$-space, but for a different reason. These matrix elements are influenced by the degree of overlap between the envelopes of the initial and final states. Figure 6.8 illustrates that in the vicinity of the anticrossing region, states on the HH1 and LH1 possess similar character, because of subband mixing. The subband separation for $k_\parallel \sim 0.03 \text{Å}^{-1}$ is also close to the optical phonon energy, hence the polar optical phonon matrix element connecting states on the LH1 and HH2 subbands is relatively large, being comparable to that for HH2-HH2 polar phonon scattering (figure 6.9).

Figures 6.10-6.12 depict the total scattering rates as a function of in-plane

wavevector for the three subbands of figure 6.1, showing scattering thresholds and also the wavevectors at which phonon absorption processes switch off in the vicinity of the continuum edge. The scattering rate prefactors are appropriate to a lattice temperature of 300 K, in common with the results of chapter 5. At this temperature, the factor for phonon absorption n_q is approximately half that for phonon emission $(n_q + 1)$, and optical phonon absorption rates are roughly half those for the inverse emission process.

In all three subbands, polar optical phonon scattering is the dominant mechanism followed by alloy then non-polar optical phonon scattering. Acoustic phonon scattering is the least important, but for these the relaxation time is still only ~ 200 fs. The scattering rates are largest for states occupying the LH1 subband. This is mainly due to the large density of states, but is also a result of the subband mixing. The peak rate for polar optical phonon LH1-HH1 emission is around 170 ps^{-1}. In the vicinity of the off-centre subband maximum of the LH1 subband, the scattering rates for intrasubband acoustic and alloy scattering increase sharply, because the density of states diverges for $\frac{\partial E}{\partial k_{\parallel}} \to 0$.

Carrier cooling in the well is concerned with the relaxation of carriers from states just beneath the continuum edge at relatively large $k_{\parallel}$, to states at the subband edges. In the case of holes that have been captured into the HH2 subband, the calculated scattering rates suggest that the carriers are likely to undergo rapid polar optical phonon emission into both the LH1 and HH1 subbands, on a timescale ~ 50 fs.
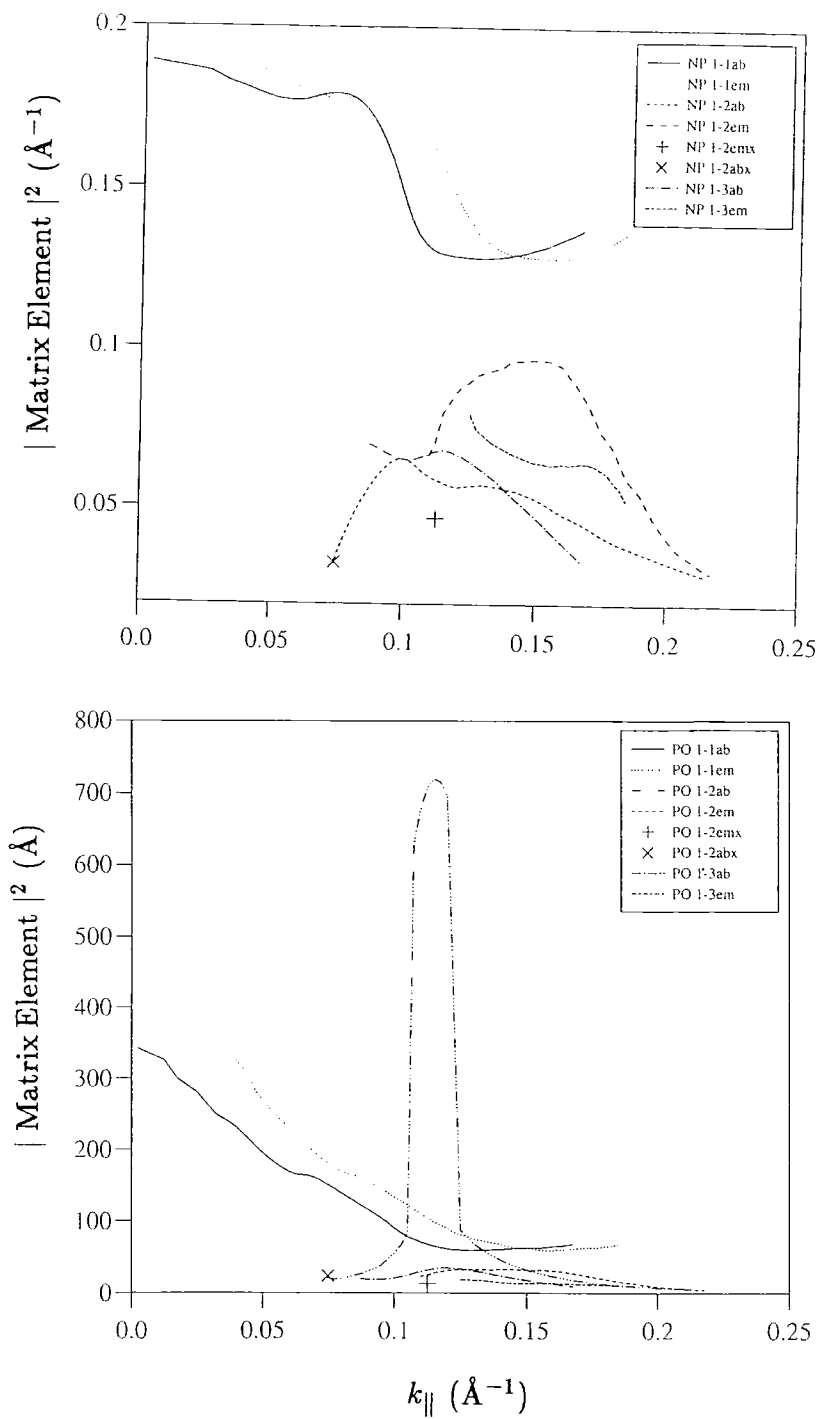
Figure 6.6 Matrix elements for non-polar (NP) and polar optical (PO) scattering from the HH1 subband as a function of in-plane wavevector.
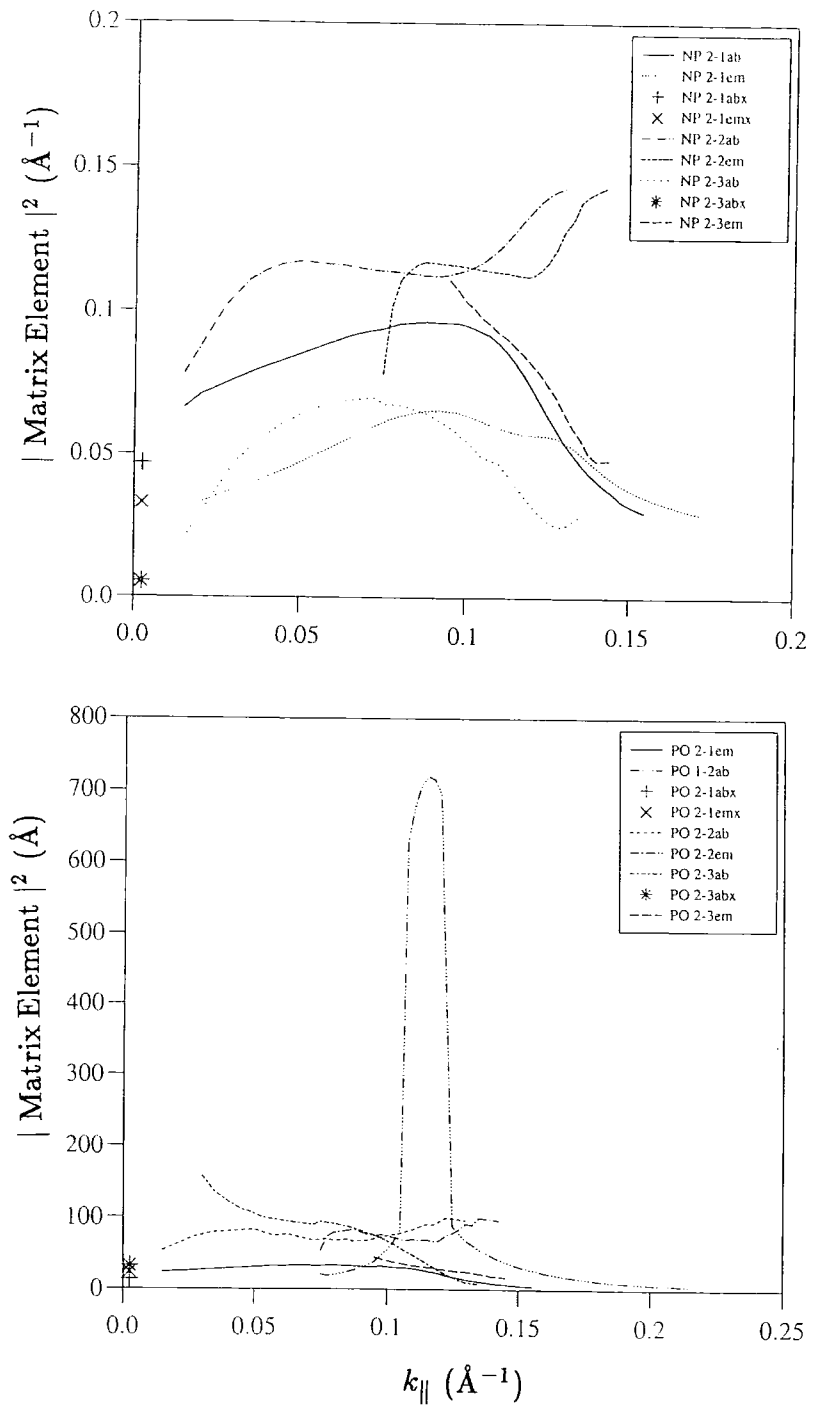
Figure 6.7 Matrix elements for non-polar (NP) and polar optical (PO) scattering from the LH1 subband as a function of in-plane wavevector.
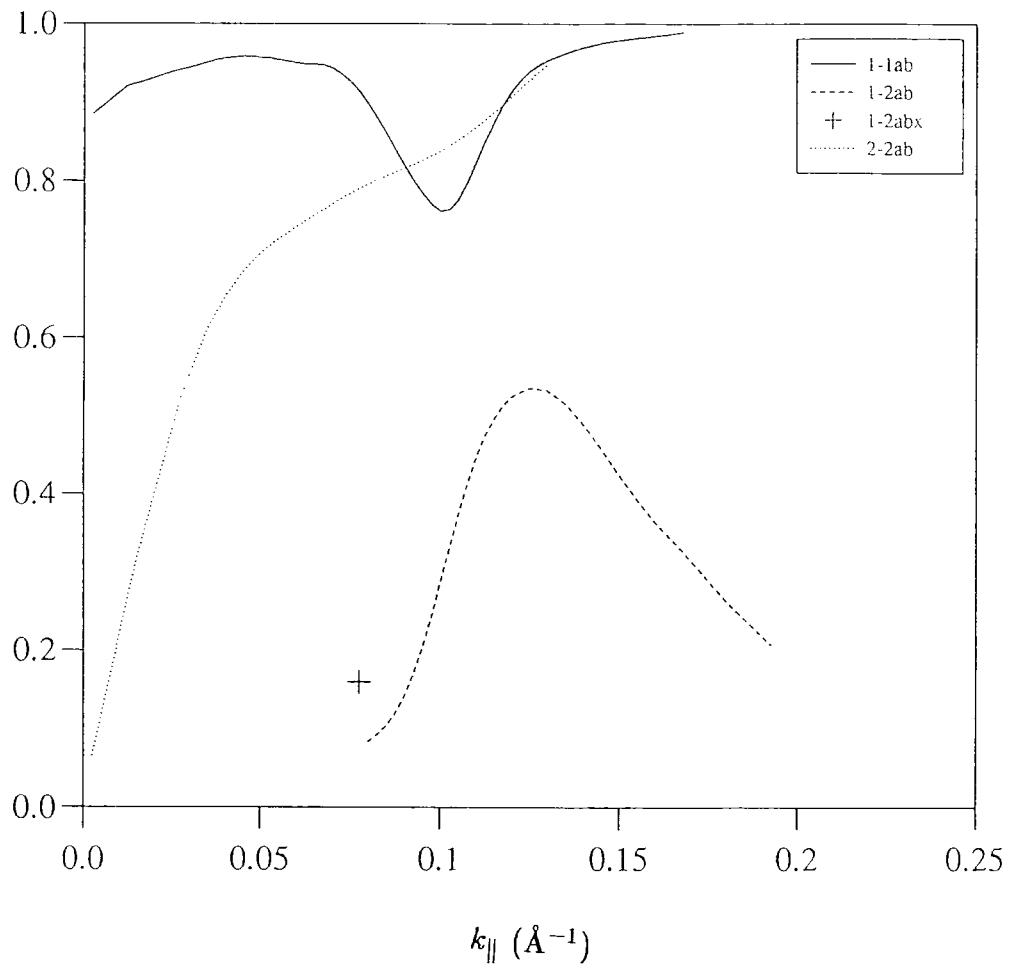
Figure 6.8 Overlap Integrals between states on the HH1 (1) and LH1 (2) subbands which correspond to transitions involving optical phonon absorption.
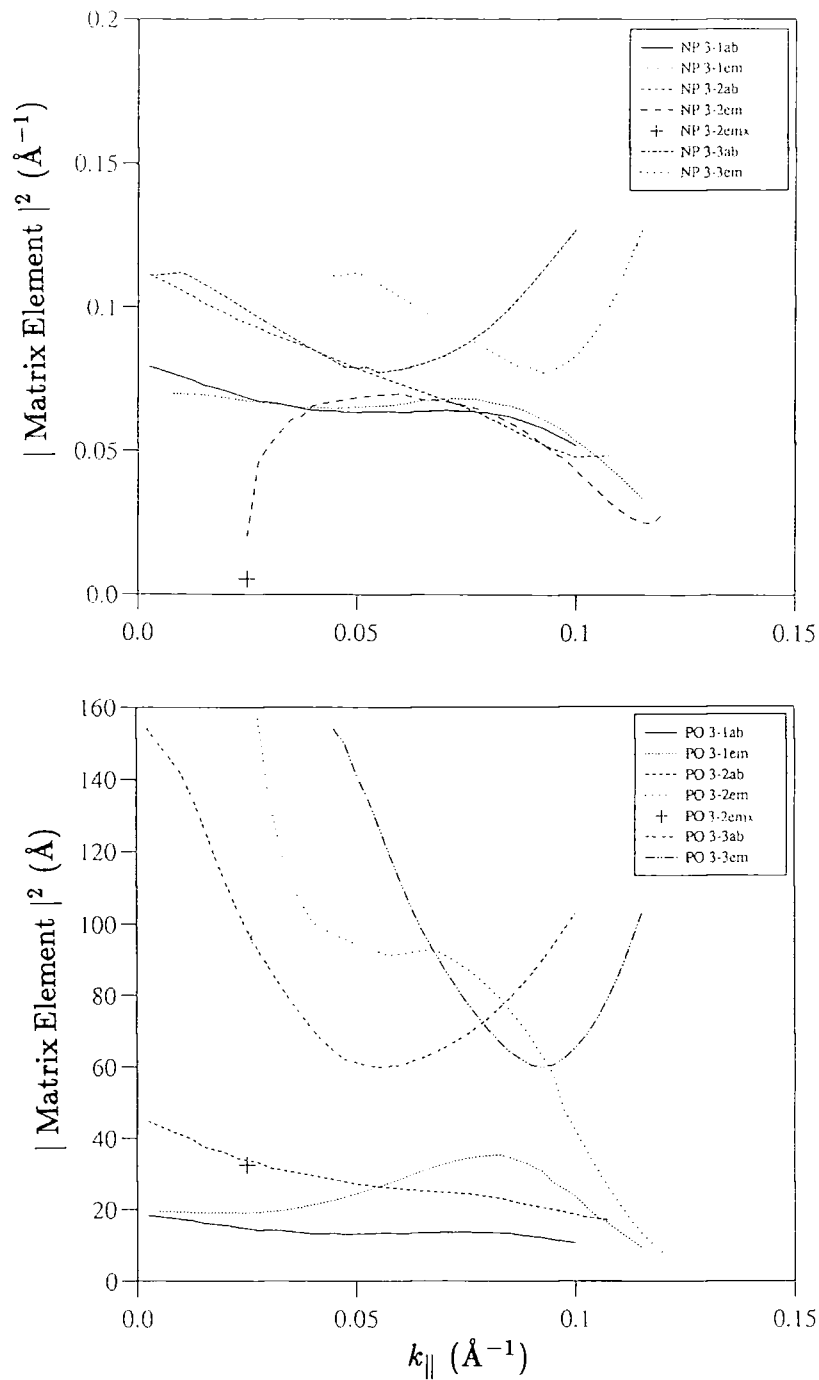
Figure 6.9 Matrix elements for non-polar (NP) and polar optical (PO) scattering from the HH2 subband as a function of in-plane wavevector.
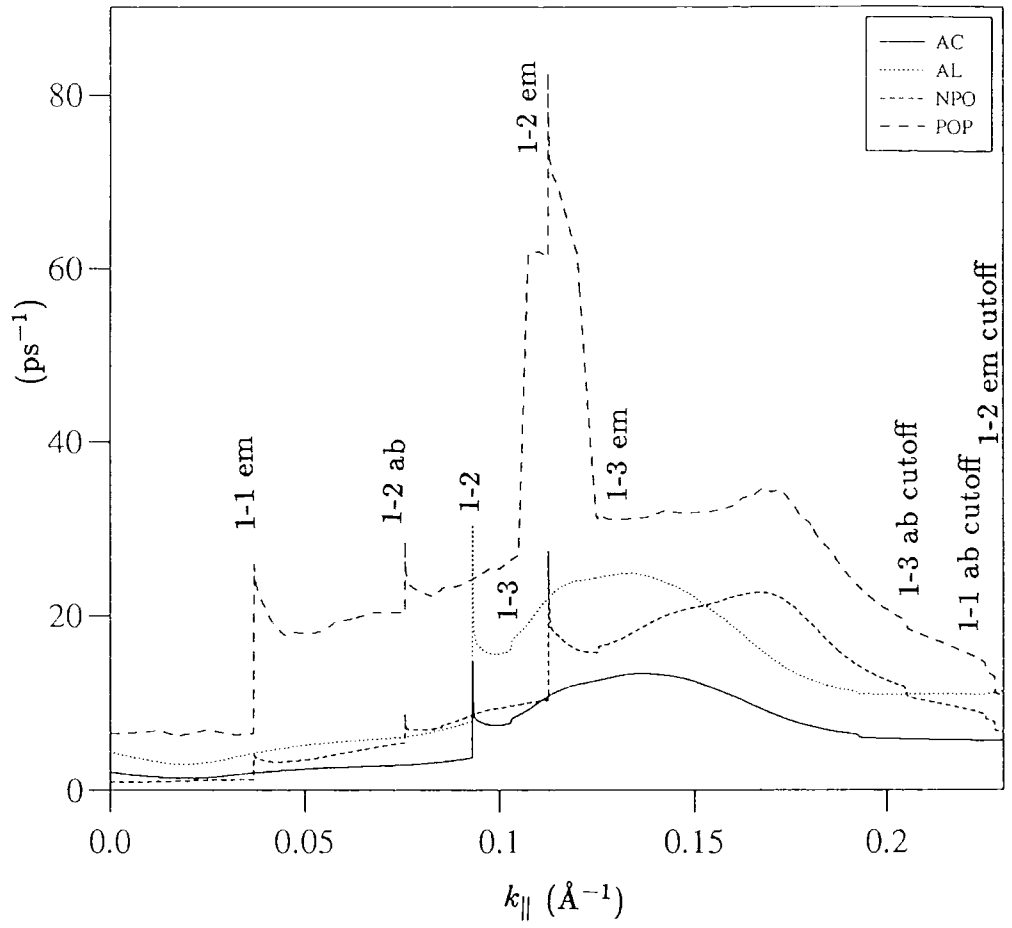
Figure 6.10 Total alloy (AL), acoustic (AC), non-polar (NPO) and polar optical phonon (POP) scattering rates for states in the HH1 subband as a function of in-plane wavevector, showing the thresholds for different scattering processes.
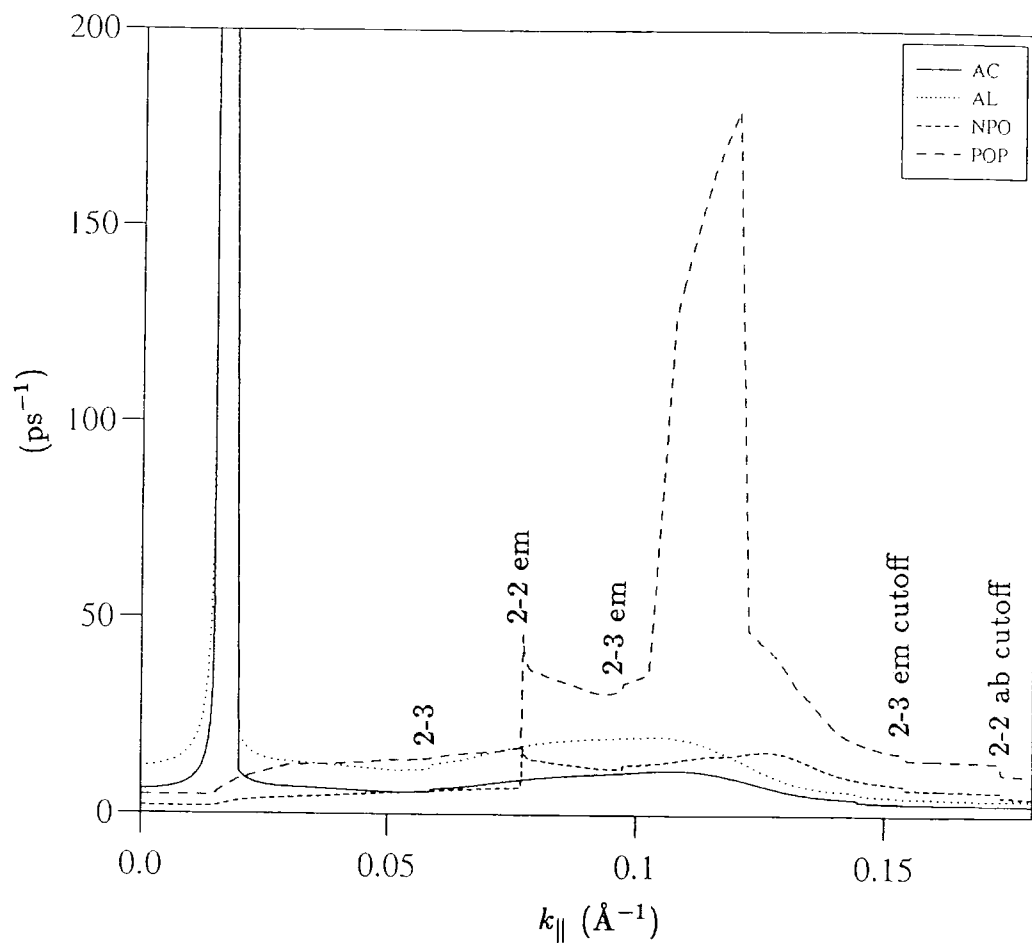
Figure 6.11 Total alloy (AL), acoustic (AC), non-polar (NPO) and polar optical phonon (POP) scattering rates for states in the LH1 subband as a function of in-plane wavevector.
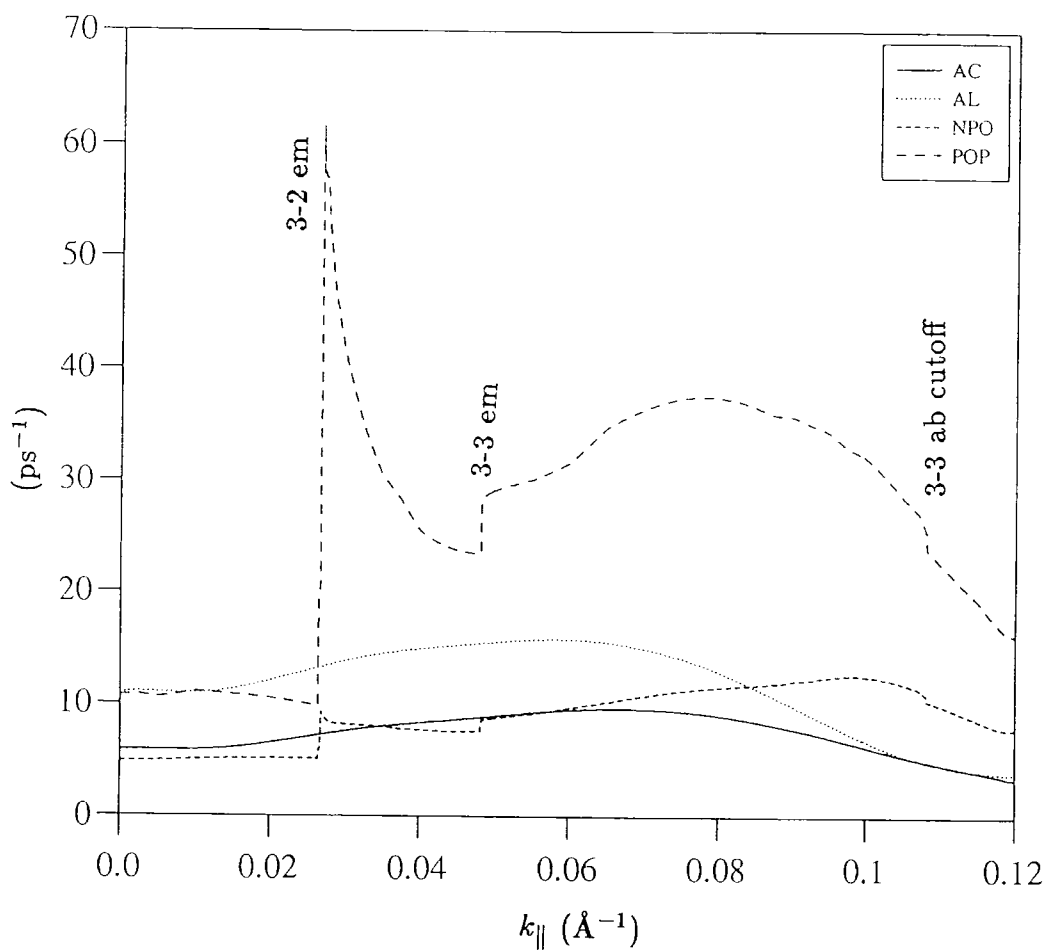
Figure 6.12 Total alloy (AL), acoustic (AC), non-polar (NPO) and polar optical phonon (POP) scattering rates for states in the HH2 subband as a function of in-plane wavevector.

6.4 Summary

In this chapter preliminary calculations have been presented as the first stage in a study of carrier cooling within the subbands of a 30Å $In_{0.7}Ga_{0.3}As$-InGaAsP (matched InP) quantum well. The possibility of carrier escape by phonon absorption has not been considered. These scattering rates suggest relaxation times on the scale of a few hundred femtoseconds. A complete description of hole cooling within this system can only be given by a detailed calculation of the carrier dynamics which, for instance, can be achieved with the ensemble Monte Carlo method [2]. However, the calculations described here can suggest the important scattering paths that holes will follow, once captured into the well. Polar optical phonon scattering will be most significant, and it has been predicted that holes which become trapped into states high within the LH1 subband will undergo rapid intraband optical phonon emission. On reaching the scattering rate maximum ($170\,ps^{-1}$) these will scatter into the HH1 subband and then undergo intraband cooling on a timescale of $100\,fs$. However, there will be a bottleneck for carriers that become trapped in the vicinity of the off-centre maximum of the LH1 subband. This is certainly possible for carriers captured into the HH2 subband. The HH2-LH1 polar phonon emission rate into states near the minimum is around $60\,ps^{-1}$. Carriers which become trapped into the HH1 subband appear likely to undergo intraband cooling. The HH1-LH1 polar phonon absorption rate is large ($70\,ps^{-1}$), but the rate for the reverse process is more than double that magnitude, hence many carriers which do undergo the HH1-LH1 transition will be scattered back rapidly.

It should also be pointed out that if this quantum well were part of a laser structure, the carrier densities within the well would be high ($> 10^{18}\,\mathrm{cm}^{-3}$). As a consequence, the subbands would be quite full, and the cooling of captured holes would be restricted by the lack of available states to scatter into. For an accurate assessment of carrier thermalisation within a laser structure, this factor would have to be considered.

References

[1] Kane E O 1956 *Journ. Phys. Chem. Solids* 1 82

[2] Kelsall R W, Taylor R I, Wood A C G and Abram R A
1989 *Superlatt. and Microstruct.* 5 207

Chapter 7

Conclusions And Suggestions

For Further Calculation

A simplified k.p method for obtaining the approximate valence bandstructure of a strained type I quantum well was presented in chapter 2. The essential simplification was the assumption that the holes were confined by an infinite square well potential, but the model took account of mixing between the heavy and light hole Bloch states. The main limitation of the infinite well approximation is that it is only appropriate for solving the valence subbands of wide band gap systems with a large valence band offset, in which the spread of the hole wavefunctions into the barriers is small.

However, this bandstructure model did provide an adequate description of the mixing between the uppermost heavy and light hole subbands, requiring only a few input parameters. Furthermore, the output wavefunction data was simplified since a unitary operation on the k.p Hamiltonian split it into two decoupled upper and lower block matrices (which produced identical bandstructure). In this way, each hole eigenfunction could be described completely in terms of just two, instead of four, basis Bloch states. Hence each hole eigenfunction could be represented by two envelope functions, one defining the heavy hole character, the other the light hole component. The chief advantage of solving for the valence subband dispersions in this way was that the model contained the necessary basic physical features whilst simplifying the calculation of intra- and inter-subband hole scattering rates which were sufficiently accurate for application in

simulations of parallel hole transport in the quantum well.

In chapter 3, it was shown how the bandstructure model could be applied to the calculation of acoustic and optical phonon, alloy and remote impurity scattering rates for holes for $In_x Ga_{1-x}As$-AlGaAs wells of varied geometry and alloy composition. The subband dispersions and scattering rates were then incorporated into single particle Monte Carlo simulations of low field ($< 10^5 \, Vm^{-1}$) hole transport in a quantum well, with the aim of identifying the competing factors which act to increase or limit the hole mobility.

A study of the low field transport of holes in 90 Å $In_x Ga_{1-x}As$-AlGaAs ($0.10 \leq x \leq 0.25$) quantum wells at 77 K predicted an increase in the mobility with increasing indium in the well, despite the increase in alloy scattering. This was due to a reduction in the in-plane effective mass of the highest HH1 subband (a combination of the fact that the heavy hole effective masses are lower in bulk InAs than GaAs and hence in the alloy, and the effect of biaxial compressive strain in the well).

In a second investigation, the transport properties of holes were studied in $In_{0.18}Ga_{0.82}As$ wells of different width (50-150 Å). The results suggested that the hole mobility increases with increasing well width, largely because of the well width dependence of the scattering matrix elements. However, a local minimum in the hole mobility was observed for wells ~ 120 Å thick. Comparison of this behaviour with that for simulations in which inter-subband scattering was neglected, revealed that this phenomenon could be explained by the combination of the effects of significant scattering into the second HH2 subband and the

relatively large effective mass of that band.

The infinite well model produces subbands with associated hole effective masses which are artificially light, as a result of the total confinement. This was discussed in chapter 4. As a consequence, the estimated hole mobilities from the Monte Carlo simulations were found to be consistently larger than experimental data for similar quantum wells. Better quantitative agreement with experiment could be obtained by using a finite well bandstructure model, but still assuming that mixing is between the heavy and light hole bands, alone. The bandstructure calculation is clearly less straighforward, because of the need to calculate the wavefunctions in the barrier layers and their matching to those in the well, but would not significantly complicate the hole scattering rate expressions.

An attempt at devising a k.p model to calculate the capture rates for holes into a quantum well was described in chapter 5. In common with existing effective mass models for carrier capture, it was assumed that at the instant of capture, unbound holes in the barriers could be represented by coherent wavefunctions which spanned the confinement region. This is a dubious assumption since in reality, carrier-carrier and carrier-phonon scattering will modify the barrier states. However, by treating the trapping process like a transmission problem through a potential barrier, it is possible to reinterpret the standard form of Fermi's Golden Rule, and express the capture rates in terms of the associated incident particle flux. That way, *local* information about the capture efficiency into the well can be obtained.

The model was applied to the calculation of the hole capture rates into a

30 Å $In_{0.3}Ga_{0.7}As$-$In_{0.75}Ga_{0.25}As_{0.55}P_{0.45}$ quantum well by acoustic and optical phonon processes, and also alloy scattering. Calculation of the capture rates for holes of different energies and momenta (both parallel and transverse to the well plane) revealed significant structure in the capture rates. This was partly due to the presence of transmission resonances into the well, giving an enhanced capture rate, but also a result of subband mixing, which causes the subbands to be highly non-parabolic and affects the density of final states.

By summing over the individual capture rates for barrier states of different energies, the average hole capture rates per unit area of the well plane were determined for each scattering mechanism. It was found that alloy scattering and non-polar optical phonon emission are likely to be the most important capture processes for this particular quantum well. This is contrary to bound-bound scattering, where polar optical phonon scattering is generally more important than non-polar optical phonon scattering. The reason for this is that the denominator of the polar optical phonon scattering rate expression is dependent upon the difference between the in-plane wavevectors of the initial and final states. Since capture involves scattering into states lying high within the well, and thus far out along the subbands in $k_{\parallel}$-space, this difference is generally large, and acts to reduce the capture rate. Accompanying calculations of the phonon and alloy scattering rates for captured holes between the bound states in the subbands of the quantum well were presented in chapter 6. However, a complete picture of the trapping and thermalisation properties of holes into a quantum well can only be provided by a transport model, for example, an ensemble Monte Carlo simulation.

A possible extension of the model would be to consider quantum wells which cannot be represented by a square well potential, for example when the carrier density in the well is high. The capture model will eventually be used in a Monte Carlo simulation of a quantum well laser, but can be applied to any device where unbound-bound scattering is important. In the first instance, the aim will be to investigate the influence of carrier (in particular *hole*) diffusion across the optical confinement region upon the modulation bandwidth of the laser. Initially, the details of carrier trapping will be ignored, and the quantum wells will instead be treated as a simple sink for carriers. However, the simulation will be developed to include carrier trapping and thermalisation within the well. The calculations reported in chapters 5 and 6 will provide information on the microscopic hole processes to be incorporated in the model.

Monte Carlo simulations of low-field hole transport in strained InGaAs quantum wells

G C Crow, R W Kelsall and R A Abram

Department of Physics, University of Durham, South Road, Durham DH1 3LE, UK

Abstract. We report on Monte Carlo simulations of low-field hole transport at 77 K in InGaAs–AlGaAs quantum wells of different widths and alloy compositions. The valence subband structure is obtained using a $k \cdot p$ method within the infinite well approximation, which accounts for mixing between heavy and light hole states. The effects of alloy, impurity and phonon scattering are included in the transport simulations. Although the infinite well approximation is only expected to be reliable for barriers with an aluminium fraction greater than about 0.4, for which the heavy hole well is sufficiently deep, the results show good agreement with experimental measurements for a finite 90 Å $In_{0.18}Ga_{0.82}As$–GaAs quantum well. A study of hole transport in 90 Å $In_x Ga_{1-x}As$ wells ($0.10 \leqslant x \leqslant 0.25$) predicts a mobility which increases with indium concentration since the reduction in the effective mass of the highest HH1 valence subband due to strain more than compensates for the greater alloy scattering rate. An analysis of wells with 18% indium content and widths in the range 50–150 Å indicates a general increase in hole mobility with well width but with a local minimum around 90 Å due to intersubband scattering from the HH1 subband to the heavier HH2 subband.

1. Introduction

It is well known that III–V quantum well heterostructures, with compressive biaxial strain in the well layer, can produce a ground state valence subband with a reduced in-plane hole effective mass and thus the prospect of a higher hole mobility for parallel transport. However, experimental results at 77 K for a 90 Å $In_{0.18}Ga_{0.82}As$–GaAs quantum well [1] have indicated that the hole transport is little improved over similar unstrained GaAs–AlAs quantum wells, and theoretical studies [2, 3] suggest that alloy scattering is important in removing the possible enhancement to the hole mobility. In fact, a proper assessment of the efficacy of strained quantum wells in enhancing hole mobility requires a study of structures with a range of well widths and levels of biaxial strain. In this paper, we report on Monte Carlo simulations of hole transport for a range of InGaAs–AlGaAs quantum wells, and aim to identify the factors which may enhance or restrict the hole mobility as the indium content and well width are varied.

2. Theory

Quantum wells simulated in the paper are similar to samples grown by Fritz et al [1] except that the supply and spacer layers are of AlGaAs material instead of GaAs. The AlGaAs supply layers are doped with acceptor impurities to provide holes for the InGaAs well. The doped regions of the supply layers are separated from the well by undoped $Al_{0.4}Ga_{0.6}As$ spacer layers designed to reduce scattering by ionized acceptor impurities, which is especially important for less energetic carriers. The widths of the spacer and supply layers were chosen to be 150 Å and 125 Å respectively, with an acceptor impurity concentration of 2.0×10^{17} cm^{-3}.

Previous simulations of InGaAs quantum wells [4] have shown that holes are unlikely to be excited out of the two highest subbands at low in-plane electric fields ($\sim 10^4$ V m^{-1}), and so only those subbands are included in the model. The band structure and wavefunctions are obtained from a $k \cdot p$ model with heavy and light hole basis states [5], and the quantum well described in an infinite-well approximation in which the wavefunctions are required to vanish at the well edges. For the quantum wells considered here, the latter approximation combines a sufficiently accurate description of the two subbands with a low demand on computational resources and facilitates the consideration of many different geometries and alloy compositions. The wavefunctions for the quantum well states are written as follows:

$$\Psi(r_{\parallel},z) = \sum_{j} \Phi_j(z)\exp(ik_{\parallel}\cdot r_{\parallel})|j). \qquad (1)$$

$\Phi_j(z)$ is the quantum well envelope function associated with the bulk Bloch periodic function $|j)$, and the summation is restricted to the $|\frac{3}{2},+\frac{3}{2})$, $|\frac{3}{2},-\frac{3}{2})$, $|\frac{3}{2},+\frac{1}{2})$ and $|\frac{3}{2},-\frac{1}{2})$ states. All generated band structures feature anticrossing, a consequence of subband mixing that marks the exchange in character of states in the two doubly degenerate bands as a result of subband mixing.

Remote impurity scattering is modelled in the way described by Kelsall and Abram [2]. In calculating the hole–phonon interactions, resulting from acoustic, non-polar optical and polar optical phonons, the bulk phonon approximation has been used, as in earlier work [2–4, 6]. Alloy scattering has been described assuming a random alloy, in which the alloy scattering potential has the same symmetry as the lattice sites and a magnitude of $\Delta E = 0.267\,\text{eV}$ [2]. Scattering rates for all the processes are calculated from Fermi's Golden rule:

$$P_{(k_{\parallel}\to k'_{\parallel})} = \frac{2\pi}{\hbar}|M(k_{\parallel},k'_{\parallel})|^2 \rho(E') \qquad (2)$$

where $M(k_{\parallel},k'_{\parallel})$ is the matrix element between initial and final states, and $\rho(E')$ is the density of final states. The well width dependence of $|M(k_{\parallel},k'_{\parallel})|^2$ can be thought of as originating in two ways. First, the effect of the localized nature of the envelope functions, which is apparent in the results of Ridley [7] for phonon scattering in a *single* parabolic band in an infinite well. Second, the subband mixing, which is a function of subband separation and hence the well width. The first factor describes a clear decrease in the $|M(k_{\parallel},k'_{\parallel})|^2$ with increasing well width for inter- and intra-subband alloy, acoustic and non-polar optical phonon processes, but the variation in polar optical phonon scattering matrix elements is less obvious. Hence for this latter process, subband mixing effects are generally the dominant influence as described in section 3.2.

3. Results

3.1. Variation of hole mobility with indium concentration

Single-particle Monte Carlo simulations were performed to investigate steady-state hole transport in 90 Å $In_xGa_{1-x}As$ quantum wells at 77 K, with the five different indium fractions $x = 0.10, 0.15, 0.18, 0.20$ and 0.25. Figure 1 shows the first two valence subbands for $x = 0.10, 0.18$ and 0.25, indicating the manner in which the subbands change as the indium concentration, and hence the strain within the system, is increased. In the bulk, biaxial compressive strain splits the degeneracy at the zone centre between the heavy and light hole bands, and when holes are confined in a quantum well, the strain in the well acts to deepen the well for heavy holes and reduce it for light holes. In the infinite well
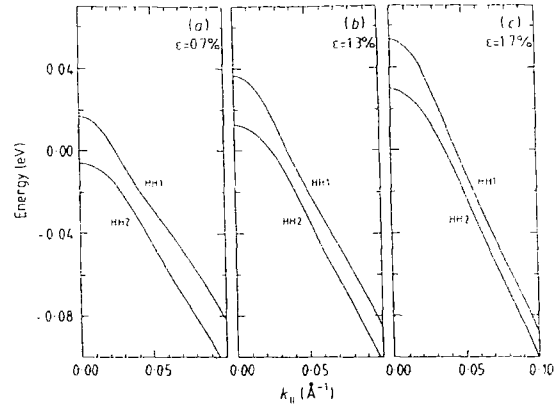
Figure 1. In-plane energy dispersions for the first two valence subbands of a 90 Å $In_xGa_{1-x}As$ quantum well: (a) $x=0.10$, (b) $x=0.18$, (c) $x=0.25$. ϵ is the biaxial strain.

approximation, the same effect causes the heavy hole subbands to be raised in energy compared with that for the unstrained system. The non-parabolicity of the HH1 and HH2 subband dispersions of figure 1 is evidence for the band mixing, and is most obvious in the case of the 10% indium concentration where the HH2 subband has a rather smaller curvature than the HH1 subband near $k_{\parallel} = 0$. It is apparent that as the indium concentration in the well is increased, the curvature of both subbands increases. This has two consequences which favour a greater hole mobility: both the density of states and the in-plane effective mass are reduced.

However, a third property which acts to reduce the mobility is a small shift of threshold wavevectors for optical phonon emission processes towards the zone centre as the compressive strain is increased. For $x = 0.10$, optical phonon HH1–HH1 emission switches on at $k_{\parallel} = 0.037\,\text{Å}^{-1}$, and at $k_{\parallel} = 0.033\,\text{Å}^{-1}$ for $x = 0.25$. Not only this, but the matrix elements for HH1–HH1 and HH2–HH2 optical phonon emission at and above threshold are larger for the higher strained systems and dominate the effects of the reduction in the density of states mentioned above, giving higher optical phonon scattering rates. As an example, the threshold polar optical HH1–HH1 emission rate for $x = 0.10$ is $\sim 7\,\text{ps}^{-1}$ compared with $11\,\text{ps}^{-1}$ for $x = 0.25$. Non-polar optical phonon scattering is less significant but the rate increases from $0.66\,\text{ps}^{-1}$ to $1\,\text{ps}^{-1}$ across the same range. Subband mixing can explain the increase in these scattering rates. For the highest strain system, the difference in wavevector between the initial and final states for a particular optical phonon transition is less than it would be for the lowest strain example, hence the transition occurs between states more alike in character and the matrix element is larger. Alloy scattering is another mechanism which acts to reduce the hole mobility as the indium content is increased. The alloy scattering rate is proportional to $x(1 - x)$ and more than doubles across the range of indium concentrations from $x = 0.10$ to $x = 0.25$.
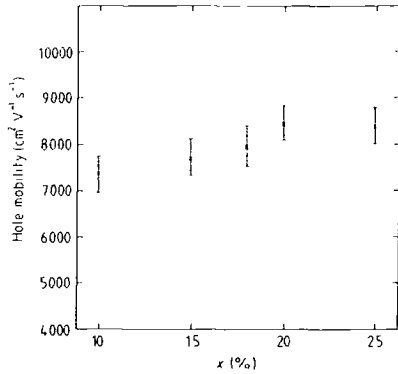
Figure 2. 77 K hole mobility versus indium fraction x for $In_xGa_{1-x}As$ quantum wells of width 90 Å.

The transport simulations for the five alloy compositions considered show that the hole mobility rises with increased indium concentration, despite increased scattering by alloy disorder and optical phonons. The results for the hole mobility are shown in figure 2. Aside from remote impurity scattering, which is important for low energy carriers near the bottom of a subband, the majority of scattering events were found to be due to polar optical phonon HH1-HH1 absorption and emission, and HH1-HH1 alloy scattering events. As expected, the rate of scattering due to alloy disorder was seen to double as the indium content was raised from 10 to 25%. However, no significant increase in the amount of polar optical phonon scattering was observed. This can be put down to the fact that, at the low electric fields considered, relatively few carriers are excited beyond the optical phonon emission threshold ($k_{\parallel} \geqslant 0.03 \, Å^{-1}$). Contrary to previous opinion [8], acoustic phonon processes were found to be the least important source of hole scattering at 77 K.

4. Variation of hole mobility with well width

In the second investigation, $In_{0.18}Ga_{0.82}As$ quantum wells with widths in the range 50–150 Å were studied. Figure 3 shows the valence band structure for three of those samples, at well widths of 50, 90 and 150 Å. It is immediately noticeable that the differences between the band structures are far greater than the changes resulting from the range of biaxial strain considered. One important property is the subband separation. For the case of the 50 Å well, the HH1 and HH2 subband edges are some 80 meV apart but for the 150 Å well the separation is only 8 meV. Also, for the 50 Å well the in-plane hole effective mass for the HH2 subband is more than three times that of the HH1 subband, whereas in the 150 Å case the effective masses of the two subbands are quite similar.

In low-field hole transport few carriers will be excited to the second subband in the 50 Å well and the greater effective mass will not be significant in reducing the average hole mobility. In contrast, the proximity of
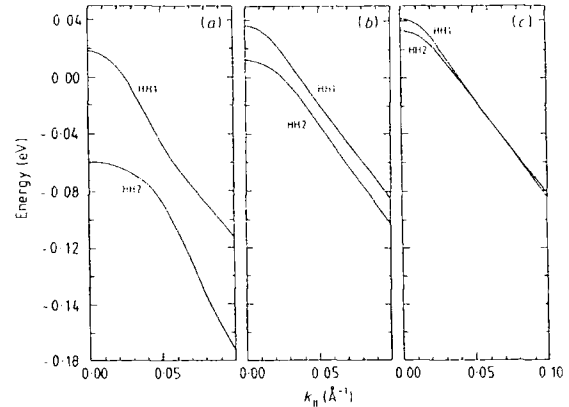
Figure 3. In-plane energy dispersions for the first two valence subbands of an $In_{0.18}Ga_{0.82}As$ quantum well: (a) well width $= 50$ Å, (b) 90 Å, (c) 150 Å. The subbands of (c) anticross although this cannot be discerned from the diagram.
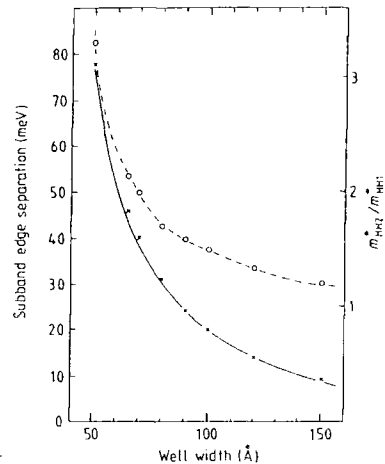
Figure 4. HH1 and HH2 subband edge separation ($\times$), and the ratio of the HH2 and HH1 zone centre effective masses (O) versus well width for $In_{0.18}Ga_{0.82}As$ quantum wells.

the HH1 and HH2 subbands for the 150 Å well implies that there will be considerable scattering into the HH2 subband. However, in this instance holes occupying the HH2 subband will possess much the same in-plane mass as those in the first subband ($m^*_{HH2}/m^*_{HH1} \sim 1.2$) and will not be much less mobile than those in the HH1 subband. Figure 4 depicts the subband edge separation and the ratios of the zone centre masses for the HH1 and HH2 subbands as a function of well width, showing how the mass ratio approaches unity as the subbands converge. The increase in the HH2 mass as the quantum well becomes narrower results in a larger density of states, which acts to increase the scattering rates to that subband and the strength of intraband scattering.

The total alloy, acoustic, non-polar optical and polar

221

optical phonon scattering rates were found to decrease with increasing well width. In the first three cases, this is due to that part of the well width dependence of the matrix elements arising from the localized envelope functions. For the polar optical phonon scattering, where that dependence is not marked, the trend can be explained by subband mixing effects. HH1–HH1 polar optical phonon scattering provides a particularly clear illustration of the effects of mixing because the dispersion of the HH1 subband changes very little as the well width is adjusted, and the density of states factor in the scattering rate does not vary significantly. Taking the extreme cases of the 50 and 150 Å wells, the position of the anticrossing region is the key factor in determining the scattering rates. The effect of bringing the subbands closer together by increasing the well width causes the anticrossing region to be shifted towards the zone centre. Hence if we consider the example of polar optical phonon absorption from a state near the HH1 subband edge in a 50 Å well, the transition is made between states of predominantly ground state character on the same side of the anticrossing region. The equivalent transition for the 150 Å well is made from a state resembling the ground state, to a mixed state at the anticrossing. The matrix elements for HH2–HH2 polar optical phonon transitions show similar behaviour. In addition the density of states in the second subband decreases with well width, and so the HH2–HH2 rate is considerably reduced for wider wells.

In contrast, the intersubband polar optical phonon scattering rates are observed to increase with well width since at greater well widths the initial and final states are in different bands but on opposite sides of the anticrossing region and therefore are similar in character. The matrix elements for intersubband polar optical phonon scattering are, however, much smaller than the intrasubband matrix elements, and so this increase has little influence upon the total polar optical phonon scattering rate.

The above analysis of the band structure and the scattering matrix elements indicates that the hole mobility should increase with well width. The mobilities obtained from simulations for the set of $In_{0.18}Ga_{0.82}As$ wells are given in figure 5 and show the expected general trend. There is, however, a local minimum in the hole mobility for wells ~ 90 Å wide, which can be explained as follows. For the narrowest well studied, there is negligible excitation of holes to the second subband because of the large energy separation of the subbands. Increasing the well width reduces the separation and then the holes are more readily scattered to the HH2 subband. Figure 6 shows the population of the second subband at each well width studied. For a 90 Å well there is a significant population ($\sim 10\%$) of the second subband. However, the important characteristic of the 90 Å case is that it combines a significant second subband population with a hole mass for that subband which is comparatively heavy at 1.6 times the mass of HH1. At larger well widths the HH2 population increases but the effective mobility of that subband also increases
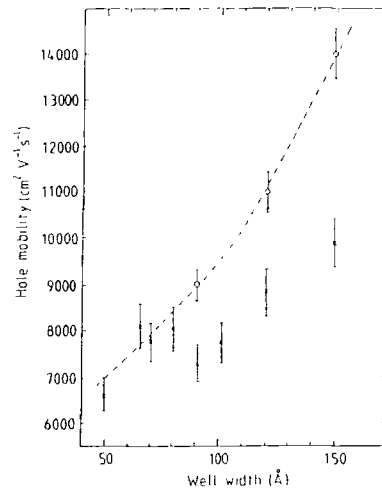
Figure 5. 77 K hole mobility versus well width for $In_{0.18}Ga_{0.82}As$ quantum wells: O, one-subband approximation; ×, two-subband approximation.
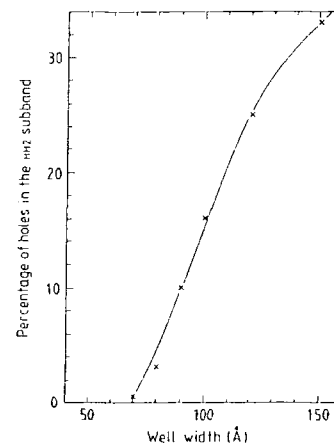
Figure 6. Percentage of holes in the HH2 subband versus well width for an $In_{0.18}Ga_{0.82}As$ quantum well at 77 K and with an applied electric field of 10^4 V m^{-1}.

due to the reduction in the hole mass as discussed earlier.

Figure 5 also shows the results of simulations that were carried out for 90, 120 and 150 Å wells using a one-subband approximation (i.e. just the HH1 subband). The aim was to see what mobilities might have been obtained if intersubband scattering was omitted and all holes had a similar in-plane effective mass. For wells less than 80 Å thick, the curves for the one- and two-subband approximations converge, indicating that the second subband plays a minor role, but for wells wider than 80 Å, where there is considerable intersubband scattering, the presence of the second subband suppresses the hole mobility. The 150 Å well width marks the limit of validity of the two-band approximation. Around this well width, scattering into the third (HH3) subband becomes likely, since it is only ~ 20 meV above the HH2 subband edge.

This well width is also near the critical layer thickness for growing dislocation-free layers of InGaAs for this level of strain. The largest practical well width is limited by the critical thickness of the strained layer, which for this system is around 150 Å according to Andersson [9] and rather less from the earlier model by Matthews and Blakeslee [10].

5. Conclusions

In this paper we have reported Monte Carlo simulations of hole transport in InGaAs–AlGaAs quantum wells of different widths and indium contents. Valence band structure for the simulations was generated using a $k \cdot p$ method in the infinite-well approximation, which accounts for mixing between heavy and light hole states. Results from the low-field hole transport simulations for 90 Å $In_x Ga_{1-x}$As–AlGaAs quantum wells ($0.10 \leqslant x \leqslant 0.25$) predict that a greater hole mobility is to be expected as the indium content is increased. This results from the reduction in the in-plane hole effective mass for the HH1 subband (due to the larger compressive biaxial strain) which more than compensates for the effects of increased alloy scattering within the well.

The variation of the hole mobility with well width shows interesting effects derived from the competing factors which enhance or reduce the hole mobility. This was illustrated by the second set of simulations in which $In_{0.18}Ga_{0.82}$As–AlGaAs quantum wells with widths in the range 50–150 Å were studied. The general trend was for the hole mobility to increase with well width, but a

local minimum in the mobility was observed for wells ~ 90 Å wide because of the combination of significant transfer into the second subband and the relatively large effective mass of that subband.

Acknowledgments

References

[1] Fritz I J, Drummond T J, Osbourn G C, Schirber J E and Jones E D 1986 *Appl. Phys. Lett.* **48** 1678
[2] Kelsall R W and Abram R A 1992 *Semicond. Sci. Technol.* **7** B312
[3] Kelsall R W, Abram R A, Batty W and O'Reilly E P 1992 *Semicond. Sci. Technol.* **7** 86
[4] Kelsall R W, Wood A C G and Abram R A 1991 *Semicond. Sci. Technol.* **6** 841
[5] Ahn D and Chuang S L 1990 *IEEE J. Quantum Electron* **26** 13
[6] Kelsall R W, Taylor R I, Wood A C G and Abram R A 1990 *Semicond. Sci. Technol.* **5** 877
[7] Ridley B K 1982 *J. Phys. C: Solid State Phys.* **15** 5899
[8] Fritz I J, Doyle B L, Schirber J E, Jones E D, Dawson L R and Drummond T J 1986 *Appl. Phys. Lett.* **49** 581
[9] Andersson T J, Chen Z G, Kulakovskii V D, Uddin A and Vallin J T 1987 *Appl. Phys. Lett.* **51** 752
[10] Matthews J W and Blakeslee A E 1974 *J. Crystal Growth* **27** 118